Functional superstructures with supramolecular nanofibers prepared by physical vapor deposition

Dissertation

zur Erlangung des akademischen Grades

eines Doktors der Naturwissenschaften (Dr. rer. nat.)

in der Bayreuther Graduiertenschule für Mathematik und Naturwissenschaften

(BayNAT)

der Universität Bayreuth

vorgelegt von

Dennis Schröder

Geboren in Köln

Bayreuth, 2025

Die vorliegende Arbeit wurde in der Zeit von Februar 2021 bis Oktober 2024 in Bayreuth am Lehrstuhl Makromolekulare Chemie I unter Betreuung von Herrn Professor Dr. Hans-Werner Schmidt angefertigt.

Vollständiger Abdruck der von der Bayreuther Graduiertenschule für Mathematik und Naturwissenschaften (BayNAT) der Universität Bayreuth genehmigten Dissertation zur Erlangung des akademischen Grades eines Doktors der Naturwissenschaften (Dr. rer. nat.).

Form der Dissertation: Kumulative Dissertation

Dissertation eingereicht am: 21.03.2025

Zulassung durch das Leitungsgremium: 23.04.2025

Wissenschaftliches Kolloquium: 23.07.2025

Amtierender Direktor: Prof. Dr. Jürgen Köhler

Prüfungsausschuss:

Prof. Dr. Hans-Werner Schmidt   (Gutachter)
Prof. Dr. Andreas Greiner   (Gutachter)
Prof. Dr. Nella Vargas Barbosa   (Vorsitz)
JProf. Dr. Hannah Kurz

I. List of Publications

The most important results of my thesis are summarized and presented in the form of four manuscripts. Three have been published and one is accepted in peer-reviewed journals. The following papers are the subject of this thesis:

[I]   Dennis Schröder, Jannik Thanner, Klaus Kreger, and Hans-Werner Schmidt
        Hierarchical Glass Fiber Superstructures with Supramolecular Nanofibers for the Nucleation of Isotactic Polypropylene
        Published in *Macromol. Mater. Eng.* **2024**, 310, 2400389.
        DOI: 10.1002/mame.202400389

[II]   Dennis Schröder, Klaus Kreger, and Hans-Werner Schmidt
        Mesostructured polymer and glass microfiber nonwovens with supramolecular 1,3,5-benzenetrisamide nanofibers for air filtration
        Published in *ACS Appl. Mater. Interfaces.* **2025**, 17, 14569-14577
        DOI:10.1021/acsami.4c22310

[III]   Dennis Schröder, Klaus Kreger, Ulrich Mansfeld, and Hans-Werner Schmidt
        Controlled Surface Decoration with Functional Supramolecular Nanofibers by Physical Vapor Deposition
        Published in *Adv. Mater. Interfaces* **2024***, 11, 2400259.* DOI: 10.1002/admi.202400259

[IV]   Dennis Schröder, Christian Neuber, Ulrich Mansfeld, Klaus Kreger, and Hans-Werner Schmidt
        Mesostructured Nonwovens with Supramolecular Tricycloquinazoline Nanofibers as Heterogenous Photocatalyst
        Published in *Small Sci.*, **2024**, 4, 2300160. DOI: 10.1002/smsc.202300160

During my thesis, I was involved in a collaboration and co-authored the following peer-reviewed publication. As this publication is not part of this thesis, it will not be discussed further:

[V]   Jonas De Breuck, Michael Streiber, Michael Ringleb, Dennis Schröder, Natascha Herzog, Ulrich S Schubert, Stefan Zechel, Anja Traeger, Meike N Leiske
        Amino-Acid-Derived Anionic Polyacrylamides with Tailored Hydrophobicity–Physico-chemical Properties and Cellular Interactions
        Published in *ACS Polymer AU*, **2024**, 4, 222-234

Summary

II. Summary

Supramolecular chemistry provides the opportunity to efficiently produce nanofibers by self-assembly of molecular building blocks via secondary interactions. Particularly in combination with woven or nonwoven fabrics, mesostructured superstructures can be obtained with applications ranging from filtration to catalysis. However, straightforward preparation methods that facilitate full control over all dimensions remain a challenge. In contrast to most self-assembly processes, this work focuses on a *solvent-free process to produce superstructures with defined nanofibers by physical vapor deposition (PVD)*.

The first part aimed for the development of superstructures with nanofibers of 1,3,5-benzene trisamides (BTA) capable of *nucleating isotactic polypropylene* (iPP). Therefore, various evaporable BTA building blocks with cycloaliphatic and branched substituents known to nucleate iPP were selected. It was found that the ability to self-assemble into nanofibers on substrates strongly depends on the steric demand of the substituents. Optimal PVD conditions for the reproducible production of supramolecular nanofibers were determined by systematic investigation of the process parameters, including substrate temperature, evaporation time and rate. A key feature is that the fiber length can be controlled directly via the evaporation time. Suitable glass fiber (GF) nonwovens, which are used as a reinforcing material in GF/polymer composites, were selected for superstructure preparation. In this way, *mesostructured nonwovens* with tailored bottlebrush morphology were obtained. These mesostructured nonwovens were embedded between iPP films and yielded composites with improved mechanical properties, namely increased tensile strength and modulus. This improvement was achieved by locally controlling the heterogeneous nucleation of iPP on the BTA/GF leading to a superior interfacial adhesion.

The second part aimed to prepare superstructures with tailored bottlebrush morphology as *air filtration medium*. As a starting point, a polymer nonwoven was uniformly decorated with supramolecular nanofibers based on a BTA with peripheral tert-butyl groups. Key parameters such as filtration efficiency and pressure drop were determined and evaluated for superstructures with varying nanofiber length. It was found that these superstructures or stacks of superstructures exhibited comparable filtration efficiencies of up to 94% for particles of 1 µm in size, as previously described, but had a much lower pressure drop. In a second step, glass fiber nonwoven suitable for air filtration at elevated temperatures was chosen and superstructures were

produced in the same way. With these structures, filtration efficiencies of 99 % for 1 µm particles and 93 % for 0.3 µm particles were achieved with reasonable pressure drops. More importantly, the *heat resistance* of the superstructures was investigated at 200 °C for 24 hours, as the BTA nanofibers exhibit excellent thermal stability. It was found that all key filtration parameters remained unchanged, demonstrating the suitability of such superstructures for air filtration processes at elevated temperatures that cannot be achieved with most polymer systems used.

The third part of the thesis aimed at the preparation of superstructures for the *immobilization of gold nanoparticles* (AuNPs) and their subsequent use as *heterogeneous catalysts*. Thus, a BTA with peripheral tertiary amino groups was selected as functional building block. A single-layer polyamide fabric was used to produce the superstructures by PVD. The supramolecular nanofibers with the functional periphery on the polymer support enabled the efficient immobilization of AuNPs from aqueous solution. Various electron microscopy methods confirmed a uniform loading of AuNPs with negligible leaching during catalysis. Using the well-investigated reaction of 4-nitrophenol to 4-aminophenol as model reaction, a conversion of 95 % within 4 minutes and a reaction rate constant of 1.16 min^{-1} was found, which is significantly higher than previously reported for similar systems. Moreover, it was shown that the superstructure retained its morphology and catalytic activity over several cycles, demonstrating its durability and reusability.

The fourth part aims to produce superstructures for the *photocatalytic degradation of organic pollutants*. For this, tricycloquinazoline (TCQ), a heterocyclic discotic aromatic molecule, was selected as a building block due to its high chemical stability and visible light absorption. Glass fiber nonwovens suitable for aqueous media were selected as substrate. The bottlebrush morphology could be adjusted by the evaporation time with respect to the TCQ fiber length and therefore the optical density. High photochemical stability of these superstructures was demonstrated under harsh UV conditions, showing no structural or chemical degradation. The photocatalytic activity of the chromophore was studied by using organic model pollutants such as Rhodamine B. During the photocatalytic degradation it was found that 92% of Rhodamine B was decomposed within four hours under visible light irradiation. More detailed studies during irradiation of the superstructure revealed that superoxide radicals were the primary reactive

species supported by photogenerated holes. The mechanical stability of these superstructures allows them to be used in continuous flow mode and reused for multiple runs.

In conclusion, this thesis presents a straightforward, solvent-free approach to produce mesostructured superstructures comprising supramolecular nanofibers by PVD. These super-structures can be variably tailored to specific applications by properly selecting the building block with distinct functionality.

VI

III. Zusammenfassung

Die supramolekulare Chemie bietet die Möglichkeit, Nanofasern durch Selbstorganisation molekularer Bausteine über sekundäre Wechselwirkungen effizient herzustellen. Insbesondere in Kombination mit gewebten oder nicht gewebten Stoffen lassen sich mesostrukturierte Überstrukturen herstellen, deren Anwendungen von der Filtration bis zur Katalyse reichen. Einfache Präparationsmethoden, die eine vollständige Kontrolle über alle Dimensionen ermöglichen, bleiben jedoch eine Herausforderung. Im Gegensatz zu den meisten Selbstorganisationsverfahren konzentriert sich diese Arbeit auf ein *lösungsmittelfreies Verfahren zur Herstellung von Superstrukturen mit definierten Nanofasern durch physikalische Gasphasenabscheidung (PVD)*.

Der erste Teil zielte auf die Entwicklung von Überstrukturen mit Nanofasern aus 1,3,5-Benzoltrisamiden (BTA) ab, die in der Lage sind, *isotaktisches Polypropylen (iPP) zu nukleieren*. Daher wurden verschiedene verdampfbare BTA-Bausteine mit cycloaliphatischen und verzweigten Substituenten ausgewählt, von denen bekannt ist, dass sie iPP nukleieren. Es wurde festgestellt, dass die Fähigkeit zur Selbstorganisation zu Nanofasern auf Substraten stark von den sterischen Anforderungen der Substituenten abhängt. Optimale PVD-Bedingungen für die reproduzierbare Herstellung von supramolekularen Nanofasern wurden durch systematische Untersuchung der Prozessparameter, einschließlich Substrattemperatur, Verdampfungszeit und -rate, ermittelt. Ein wesentliches Merkmal ist, dass die Faserlänge direkt über die Aufdampfzeit gesteuert werden kann. Geeignete Glasfaservliese (GF), die als Verstärkungsmaterial in GF/Polymer-Verbundwerkstoffen eingesetzt werden, wurden für die Herstellung der Überstrukturen ausgewählt. Auf diese Weise wurden *mesostrukturierte Vliese mit maßgeschneiderter Bottlebrush-Morphologie* erhalten. Diese mesostrukturierten Vliese wurden zwischen iPP-Folien eingebettet und führten zu Verbundwerkstoffen mit verbesserten mechanischen Eigenschaften, insbesondere einer höheren Zugfestigkeit und einem höheren Modul. Diese Verbesserung wurde durch die lokale Steuerung der heterogenen Keimbildung von iPP auf dem BTA/GF erreicht, was zu einer besseren Grenzflächenhaftung führte.

Der zweite Teil zielte darauf ab, Überstrukturen mit maßgeschneiderter *Bottlebrush*-Morphologie als *Luftfiltrationsmedium* herzustellen. In einem ersten Schritt wurde ein Polymervlies gleichmäßig mit supramolekularen Nanofasern auf der Basis eines BTA mit peripheren

Zusammenfassung

tert-Butylgruppen dekoriert. Schlüsselparameter wie Filtrationseffizienz und Druckabfall wurden für Überstrukturen mit unterschiedlicher Nanofaserlänge bestimmt und bewertet. Es zeigte sich, dass diese Überstrukturen oder Stapel von Überstrukturen vergleichbare Filtrationseffizienzen von bis zu 94 % für Partikel mit einer Größe von 1 μm aufwiesen, wie zuvor beschrieben, aber einen wesentlich geringeren Druckabfall hatten. In einem zweiten Schritt wurde ein Glasfaservlies ausgewählt, das für die Luftfiltration bei erhöhten Temperaturen geeignet ist, und es wurden auf die gleiche Weise Überstrukturen hergestellt. Mit diesen Strukturen wurden Filtrationseffizienzen von 99 % für 1 μm große Partikel und 93 % für 0,3 μm große Partikel bei angemessenen Druckverlusten erreicht. Darüber hinaus wurde die Hitzebeständigkeit der Überstrukturen bei 200 °C für 24 Stunden untersucht, da die BTA-Nanofasern eine ausgezeichnete *thermische Stabilität* aufweisen. Es wurde festgestellt, dass alle wichtigen Filtrationsparameter unverändert blieben, was die Eignung solcher Überstrukturen für Luftfiltrationsprozesse bei erhöhten Temperaturen zeigt, die mit den meisten verwendeten Polymersystemen nicht erreicht werden können.

Der dritte Teil der Arbeit zielte auf die Herstellung von Überstrukturen für die *Immobilisierung von Goldnanopartikeln* (AuNPs) und deren anschließende Verwendung als *heterogene Katalysatoren*. Dazu wurde ein BTA mit peripheren tertiären Aminogruppen als funktioneller Baustein ausgewählt. Zur Herstellung der Überstrukturen durch PVD wurde ein einlagiges Polyamid Gewebe verwendet. Die supramolekularen Nanofasern mit der funktionellen Peripherie auf dem Polymerträger ermöglichten die effiziente Immobilisierung von AuNPs aus wässriger Lösung. Verschiedene elektronenmikroskopische Methoden bestätigten eine gleichmäßige Beladung der AuNPs mit vernachlässigbarer Auslaugung während der Katalyse. Anhand der gut untersuchten Reaktion von 4-Nitrophenol zu 4-Aminophenol als Modellreaktion wurde eine Umwandlung von 95% innerhalb von vier Minuten und eine Reaktionsgeschwindigkeitskonstante von 1.16 min^{-1} gefunden, die deutlich höher ist als die zuvor für ähnliche Systeme berichteten. Darüber hinaus wurde gezeigt, dass die Überstruktur ihre Morphologie und katalytische Aktivität über mehrere Zyklen beibehielt, was ihre Haltbarkeit und Wiederverwendbarkeit belegt.

Der vierte Teil zielt auf die Herstellung von Überstrukturen für den *photokatalytischen Abbau von organischen Schadstoffen* ab. Hierfür wurde Tricycloquinazolin (TCQ), ein heterozyklisches diskotisches aromatisches Molekül, aufgrund seiner hohen chemischen Stabilität und Absorption von sichtbarem Licht als Baustein ausgewählt. Als Substrat wurden für wässrige Medien

geeignete Glasfaservliese gewählt. Die *Bottlebrush*-Morphologie konnte durch die Verdampfungszeit in Bezug auf die TCQ-Faserlänge und damit die optische Dichte eingestellt werden. Die hohe photochemische Stabilität dieser Überstrukturen wurde unter harten UV-Bedingungen nachgewiesen, wobei keine strukturelle oder chemische Degradation auftrat. Die photokatalytische Aktivität des Chromophors wurde anhand von organischen Modellschadstoffen wie Rhodamin B untersucht. Während des photokatalytischen Abbaus wurde festgestellt, dass 92 % des Rhodamins B innerhalb von vier Stunden unter Bestrahlung mit sichtbarem Licht zersetzt wurden. Genauere Untersuchungen während der Bestrahlung der Überstruktur ergaben, dass Superoxidradikale die primären reaktiven Spezies waren, die durch photogenerierte Löcher unterstützt wurden. Die mechanische Stabilität dieser Überstrukturen erlaubt es, sie im kontinuierlichen Flussmodus zu verwenden und für mehrere Durchläufe wiederzuverwenden.

Zusammenfassend wird in dieser Arbeit ein einfaches, lösungsmittelfreies Verfahren zur Herstellung mesostrukturierter Überstrukturen aus supramolekularen Nanofasern durch PVD vorgestellt. Diese Überstrukturen können durch die richtige Auswahl der Bausteine mit unterschiedlicher Funktionalität variabel auf spezifische Anwendungen zugeschnitten werden.

x

Table of Content

1 Introduction

1.1 Preparation of nanofibers using physical vapor deposition

Vapor deposition has undergone remarkable development in recent decades and has become a fundamental process in modern materials science and engineering. It enables the precise control and production of thin films and coatings with tailored properties that are critical in a wide range of applications.[1] This technique has played an important role in organic light emitting diodes,[2] batteries,[3,4] biomedicine,[5,6] and many other fields.

In general, there are two different types of vapor deposition methods, *chemical vapor deposition* (CVD) and *physical vapor deposition* (PVD). The different principles of the deposition processes are illustrated in **Figure 1**. In CVD, a gaseous precursor compound A reacts with the substrate in a chemical reaction and forms a layer of the chemical reaction product B. So, whenever the deposited product has a different chemical composition to the starting material, the process is called CVD.[7] The chemical transformation is often triggered by a catalytic impact of the substrate material. The chemical reaction that leads to the deposition of the layer of material B generally takes place at high substrate temperatures, as these make the underlying reaction possible in the first place. Prominent chemical reactions in CVD encompass various processes. One such reaction involves *pyrolysis*, notably observed during the deposition of pyrolytic graphite from methane.[8] Moreover, employing multiple gaseous precursors enables *reduction reactions*. For instance, silicon deposition occurs through hydrogen reduction of silicon tetrachloride, typically at about 1000 °C.[9] Additionally, *oxidation reactions* occur by incorporating oxygen as a reactive gaseous precursor. An example includes the deposition of silicon dioxide through the oxidation of silane.[10]

In contrast, within *physical vapor deposition* processes, material A undergoes vaporization from a solid or liquid source, emerging as atoms or molecules. It then traverses as vapor through a vacuum or low-pressure gaseous (or plasmatic) environment to the substrate, where it eventually condenses into a layer of material A.[7]

Introduction
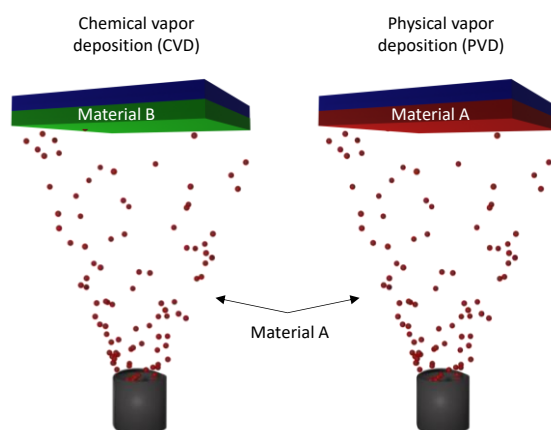
Figure 1. Schematic illustration of chemical vapor deposition (left) and physical vapor deposition (right) processes.

PVD Setup

In the simplest case, a PVD system consists of a vapor deposition chamber in which a vacuum is created, a vaporization source, and a substrate holder that contains the substrate. To ensure a good coverage of the substrate material with the vaporized target material the strength of the vacuum should be adjusted that the distance between the source and the substrate is smaller than the mean free path of the vapor. The typical range for the strength of the vacuum for organic molecules is around 10^{-3}-10^{-6} mbar, when distance between the source and the substrate is in the range of tens of cm.[7] In contrast, "microspacing in air sublimation" reduces the distance to several micrometers which allow the operation under ambient pressure.[11–16]

The source, that vaporizes the target material, can do this either thermally or physically. Thermal sources can consist of different heating techniques including, resistive heating, high energy e-beams, low energy e-beams, and inductive heating.[7] Each heating technique has its advantages and disadvantages and are suitable for different kind of materials. Resistive heating sources can be easily controlled via the current that is applied to them and is beneficial for organic materials. There are different configurations of the source like boats, crucible or for precise evaporation effusion cells. Physical sputtering, is based on the vaporization of atoms from a surface by momentum transfer from bombarding energetic atomic-sized particles, especially used for metals like platinum.

The substrate, where the vaporized target material is deposited can be a variety of materials, including silicon wafer, glass slides or polymeric materials. In some cases that substrate holder

is equipped with thermoelements, that control the substrate temperature. To monitor the PVD process quarzcrystal micro balances (QCM) are often used to detect the evaporation rate.

Additional elements can be added to a PVD setup to expand the possibilities, for instance several sources can be used to give rise of the possibility to deposit several target materials at the same time or subsequently. Furthermore, masks and shutters can be used to access structured substrates or to perform combinatoric experiments.[1]

In **Figure 2** the PVD setup of the Macromolecular Chemistry I, that was used during this work is depicted. The setup consists of a vacuum chamber that is attached to a glovebox to handle air sensitive samples and an electronic control unit that allows the precise adjustment of the source temperature. The vacuum chamber is equipped with three effusion cells, that are all equipped with a QCM sensor, additionally two QCM sensors in close proximity to the substrate are installed to monitor the evaporation rate more precisely. The substrate is placed into a substrate holder that can be turned in 90° increments during operation. Beneath the substrate holder a shutter mask is installed that can move stepwise or gradually. Between the shutter and the substrate different masks can be selected from a mask sampler.

Figure 2. PVD setup in the Macromolecular Chemistry I at the University of Bayreuth. A) The setup consists of a vacuum chamber (framed in dashed blue lines) that is attached to a glovebox and an electronic control unit. B) The vacuum chamber is equipped with three effusion cells, that are all equipped with a QCM sensor, additionally two QCM sensors in the close proximity to the substrate and a rotatable substrate holder (framed in dashed orange lines). C) The rotatable substrate holder consists of a positionable substrate holder that can be turned in 90° increments during operation, a shutter mask, and a mask sampler. Source: University of Bayreuth, Macromolecular Chemistry I.

Introduction

Combinatorial physical vapor deposition

The specific PVD setup in our group, through the installed shutters and masks, allows the use of these combinatorial techniques to rapidly produce gradients and sectors on the same substrate in a combinatorial experiment without breaking the vacuum or opening the chamber. The movable shutter mask beneath the substrate was used to prepare a *linear gradient* of one evaporated substance on the substrate when the movement was continuous, or a *step gradient* when the movement was stepwise (**Figure 3**).[1] Under optimized PVD conditions an uniformity of better than 3% over the whole substrate 76 x 76 mm, which corresponds to a layer thickness variation of less than 3 nm for a film of 100 nm, could be achieved.[1] This demonstrates the accuracy of the PVD process and allows different sectors on a substrate to be compared with each other.
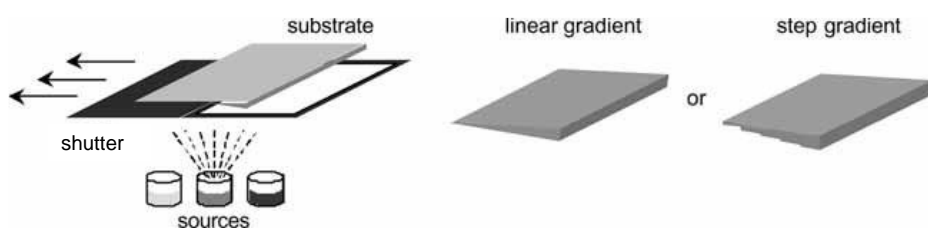
Figure 3. Schematic illustration of the preparation of linear or step gradient using a combinatorial approach by exploiting a movable shutter. Reprinted with permission of Ref.[1]© 2007 AIP Publishing.

Sector libraries can be prepared using masks that cover a certain area of the substrate. Turning the substrate by 90° increments allow the preparation of even more complex sectors. Additionally, several depositions steps can be performed with different target materials allowing the preparation of multi material films with different layer sequences (**Figure 4**).
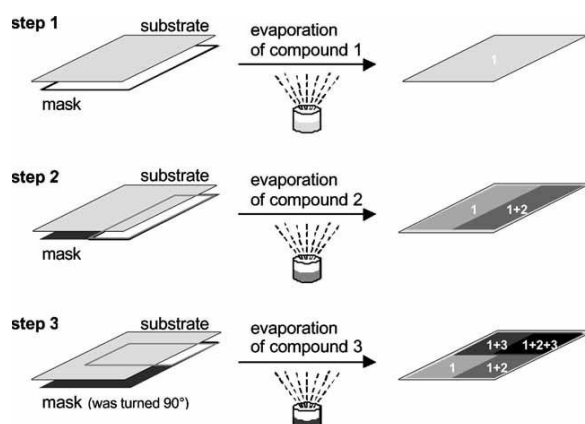
Figure 4. Schematic representation of the sequential preparation of a four sector library with different layer sequences by using either three different masks or two masks and rotating the substrate 90° before the last step. Reprinted with permission of Ref.[1] © 2007 AIP Publishing.

This kind of combinatorial approach allows the fabrication of organic light emitting diodes or organic solar cells.[2,17–24] Furthermore the PVD technique can be used to deposit photoresists with subsequent use in lithography.[25–30] In addition, simultaneously evaporation of more than one target material leads to the formation of thin films with a homogenous distributed composition. This can be utilized for preparation of polyimides via physical vapor deposition polymerisation, where the prepared films are subsequently tempered in an inert atmosphere to achieve polymerisation.[31,32]

Growth modes

There are three major modes by which thin films grow in an epitaxial fashion on a surface, namely FRANK-VAN DER MERWE-growth, VOLMER-WEBER-growth and STRANSKI-KRASTANOW-growth.[33] In **Figure 5** the three different growth modes are depicted schematically. In FRANK-VAN DER MERWE-growth, also known as layer-by-layer growth, the deposited layer grows atom by atom or molecule by molecule on the substrate. An even and continuous layer is formed before the next layer begins. This growth mode occurs when the interaction between the atoms of the substrate and the atoms of the growing layer is stronger than the interaction between the atoms of the deposited layer itself.[34,35]

In VOLMER-WEBER growth, also known as island-growth, small islands or clusters initially form on the surface of the substrate, which can eventually grow together to form a continuous layer. This mode occurs when the interaction between the atoms of the growing layer is stronger than the interaction between the atoms of the layer and the substrate. The result is a three-dimensional, island-like structure.[36]

The STRANSKI-KRASTANOW-growth, also known as layer-plus-island growth, is a combination of the first two growth modes, i.e. this mode involves a two-step process, first a thin film forms in a layer-by-layer fashion until a critical layer height is reached, sometimes called wetting layer, before the growth transitions to the nucleation and coalescence of adsorbate islands.[37]

| Frank–van der Merweer (layer-by-layer) | Volmer-Weber (island) | Stranski–Krastanov (layer-plus-island) |
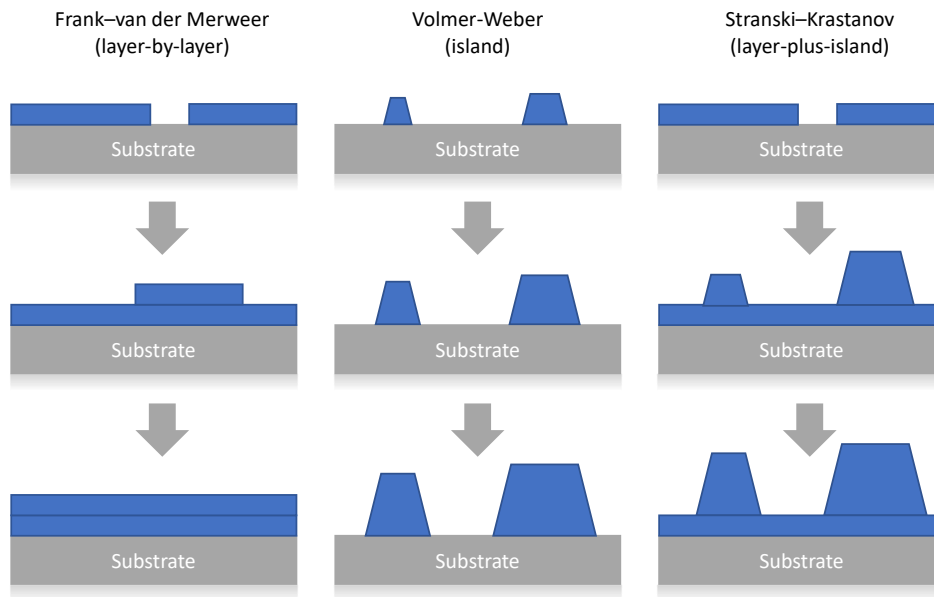
Figure 5. Schematically illustration of the three major growth modes of epitaxial growth by FRANK-VAN DER MERWE-growth, VOLMER-WEBER-growth and STRANSKI-KRASTANOW-growth.

Nanoobject formation

Vapor deposition techniques can not only result in thin films but also in nanoobjects like nano-fibers, nanobelts, or nanoflowers. To realize this several approaches including templated, nu-cleated and self-nucleated nanofiber formation were introduced (**Figure 6**). The first approach uses a porous template, that after vapor deposition can be removed, resulting in nanoobject that have the shape, the void of the template had.[38–40] The second approach uses seeds, that are placed onto the surface before PVD, so that these seeds can act as nucleation sites and initiate nanofiber formation.[41,42] By placing the seeds in a targeted manner, even complex pat-terns on surfaces can be decorated with supramolecular nanofibers.[42] The third approach in-volves no pretreatment of the substrates surface, which is why this approach will be called self-nucleated. Here, the material that is deposited on the substrate forms nuclei that initiate growth of supramolecular nanofibers. Especially VOLMER-WEBER and STRANSKI-KASTANOV growth modes enable the formation of one dimensional architectures.[43,44]
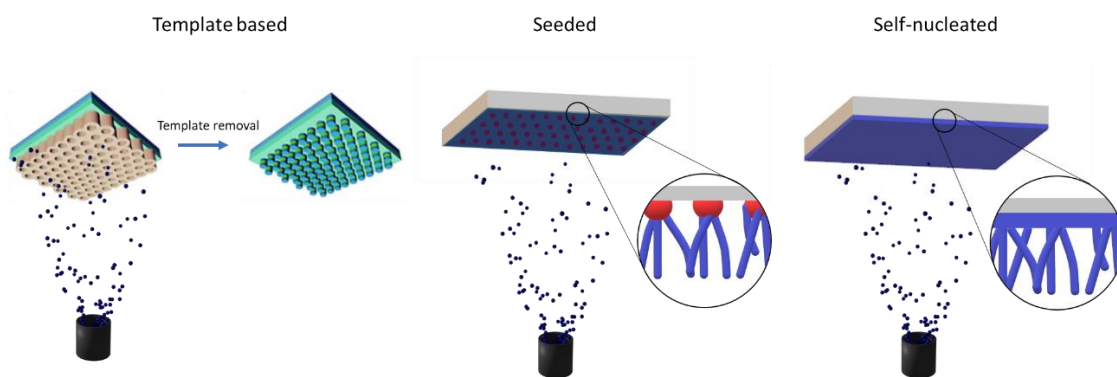
Figure 6. Schematic illustration of the three different approaches for the preparation of supramolecular nanofibers via PVD.

The morphology of supramolecular nano-objects from vapor is strongly influenced by several parameters, including the molecular structure, the evaporation rate, the substrate temperature and the substrate material (**Figure 7**).
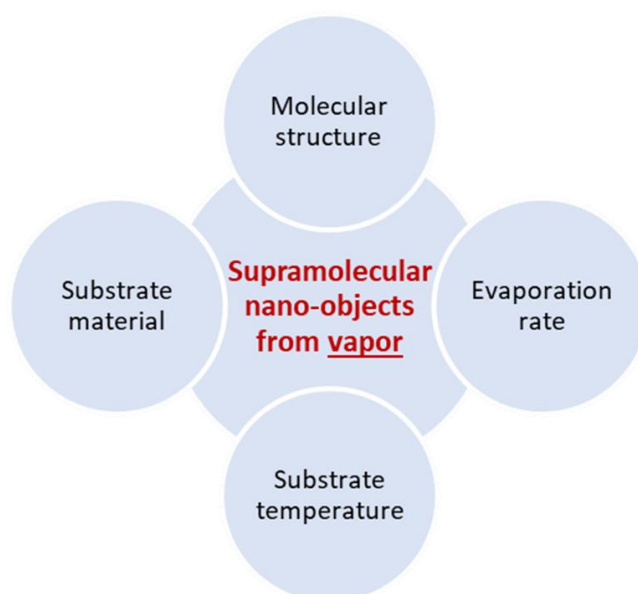
Figure 7. Influence parameter for the morphology of supramolecular nanoobjects from vapor.

Among them are the *molecular structure*, where small changes can result in drastic differences in the morphology while using a fixed set of PVD conditions.[45] Suitable molecules have to possess high temperature stability, evaporate without decomposition and self-assemble into nanofibers via defined secondary interactions. In particular a lot of aromatic motifs fulfill these requirements like perylene bisimides,[40,42,46–52] porphyrins,[41,53–59] phthalocyanines[39,60–67] among others.[38,68–72] In addition, small peptide sequences also fulfill these requirements and

can be successfully assembled to nanofibers via PVD.[43,45,73–81] Furthermore, it is also possible to co-vaporize several building blocks, resulting in more complex fiber architectures.[13,15,82]

For a given molecule, optimal PVD conditions have to be found to ensure nanofiber formation. Among the parameters the *evaporation rate*, can influence the degree of uniformity. A low evaporation rate leads to a low vapor flux, which allows a uniform formation of nuclei and consequently a uniform growth of the nanofibers. In contrast a high evaporation rate leads to high vapor flux resulting in the formation of polydisperse nuclei and consequently in a polydispersive growth of nanofibers.[68]

Another parameter that influences the morphology is the *substrate temperature*. Here an optimal temperature window has to be identified. When the substrate temperature is too cold, no nanofiber formation occurs but amorphous film formation. When the substrate temperature is too hot, the adsorption-desorption equilibrium is shifted towards the desorption site hence, little to no material is deposited on the substrate. Especially molecules, that need a high source temperature often need 50-70% of that as substrate temperature to enable nanofiber formation.[44,46,54,65]

Additionally, not only the temperature but the *substrate material*, in general can influence the nanofiber morphology. In particular, the surface of the materials is of great consequence in the nucleation process, whereby a specific degree of roughness provides an adequate number of sites for the nucleation of fibers. Furthermore, the polarity of the surface exerts an influence on the orientation of the molecules and, consequently, on the growth.[39,51,56,58,61,64]

Exemplary SEM images of supramolecular nanofibers produced by PVD from different building blocks are depicted in **Figure 8**. A wide range of fiber morphologies, thicknesses and lengths can be achieved by using suitable PVD conditions.
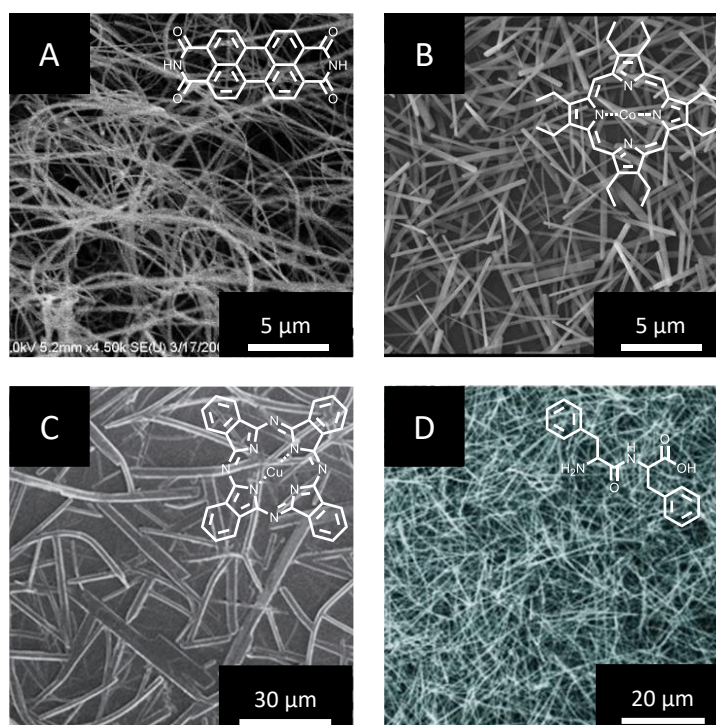
Figure 8. SEM images of supramolecular nanofibers prepared via PVD based on A) perylene bisimide (Adapted with permission of ref.[48] © 2008, American Chemical Society), B) porphyrin (adapted with permission of ref.[55] © 2009 American Chemical Society), C) phthalocyanine (adapted with permission of ref.[62] © 2015 IOP Publishing), and D) peptides (adapted with permission of ref.[78] © 2011 WILEY-VCH Verlag GmbH & Co. KGaA).
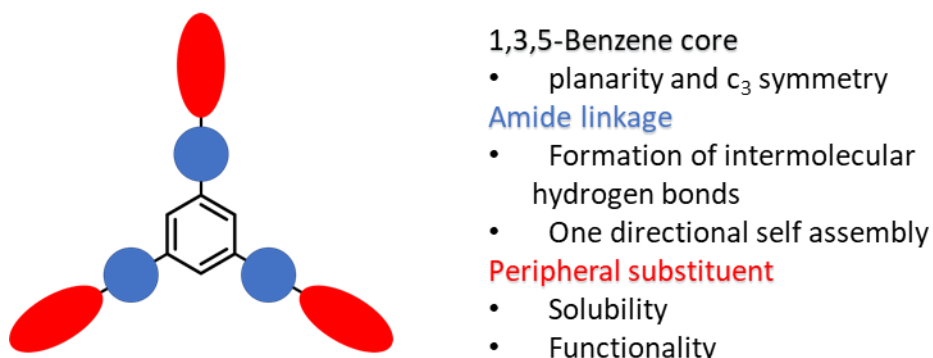
Due to the wide range of molecules available in the PVD process, supramolecular nanofibers can be produced for just as many different applications. Among other things, these fibers have been used in the field of organic electronics i.e. photoelectric devices,[38,55,66,67,74,75] transistors,[14,52,63,66,70,83,84] sensors,[47,49] battery [50] or supercapacitor anode materials,[77] and piezoelectric energy harvesting.[43]

1.2 Materials

1.2.1 1,3,5-Benzenetrisamides (BTAs)

Self-assembly to supramolecular nano-objects

Supramolecular chemistry enables the self-assembly of molecular building blocks into supra-molecular nano-objects by utilizing non-covalent interactions, also known as secondary inter-actions. These include van der Waals forces, π-π interactions, hydrogen bonds, dipole-dipole interactions, ion-dipole interactions, ion-ion interactions, and coordination bonds of complex transition-metal ions with ligands. One of the best-studied substance classes for self-assembly in nano-objects are 1,3,5-benzene trisamides (BTAs). The general design is based on a benzene core that is substituted in 1, 3, and 5 position with amide groups, which form the link to periph-eral substituents (**Figure 9**). The benzene core and the substitution pattern provide planarity and C_3 symmetry. The amide groups serve to form intermolecular hydrogen bonds, which ena-ble one-dimensional self-assembly. The peripheral substituents influence the solubility and function of the nano-objects.

1,3,5-Benzene core
- planarity and c_3 symmetry

Amide linkage
- Formation of intermolecular hydrogen bonds
- One directional self assembly

Peripheral substituent
- Solubility
- Functionality

Figure 9. General molecular design of 1,3,5-benzene trisamides.

The most widely used nucleus for C_3 symmetrical trisamides is by far benzene, as its starting materials are readily available. In addition, there are other cores such as cyclohexanes,[85,86] carbonyl-bridged triarylamines, [87,88] heptazines, [89] triarylamines, [90] or triphenylenes [91] that were used to prepare the corresponding trisamides. The three amide groups can form hydrogen bridge bonds with non-covalent bond energies of 4-120 kJ mol^{-1} each, which as a sum are similar in strength to covalent C-C bonds with a bond energy of 350 kJ mol^{-1}.[92,93] The amide groups can be attached to the benzene core in two different ways: either via the carbon atom (C-cen-tered) or via the nitrogen atom (N-centered). Alternatively, a mixed attachment is possible,

which gives rise to four possible stereo isomers (**Figure 10**). The selection of peripheral substituents attached to the amide groups can impact the thermal properties, solubility, self-assembly behavior, and ultimately, the function. Typically, three identical peripheral substituents are attached to the core, resulting in a C_3 symmetry. However, unsymmetrical BTA derivatives with varying substituents at the amide groups have also been documented.
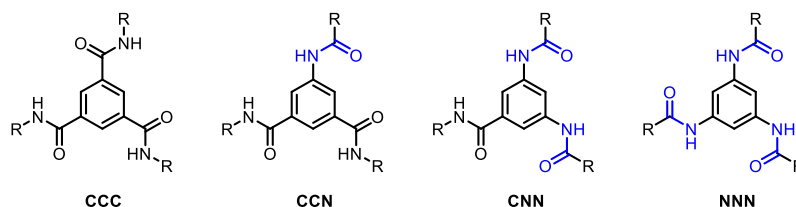
Figure 10. Chemical structures of 1,3,5-benzenetrisamides derivatives with different C- and N-centered amide linkage. Based on 1,3,5-benzenetricarboxylic acid core all amide units are C-centered (CCC). Based on 5-aminoisophthalic acid core one amide linkage is inverted (CCN). Based on 3,5-diaminobenzoic acid core two amide linkages are inverted (CNN). Based on 1,3,5-triaminobenzene core all amide groups are N-centered (NNN).

Trisamide synthesis often follows the SCHOTTEN-BAUMAN reaction, using either trimesic acid chloride with an excess of amine or triaminobenzene with an excess of acid chloride in the presence of an acid scavenger such as triethylamine or pyridine. Since the resulting trisamides often have low solubility, high-boiling solvents such as *N*-methyl-2-pyrrolidone are used. Alternatively, trisamides can also be produced via the aminolysis of methyl trimesic acid ester with an excess of amines and elimination of methanol.
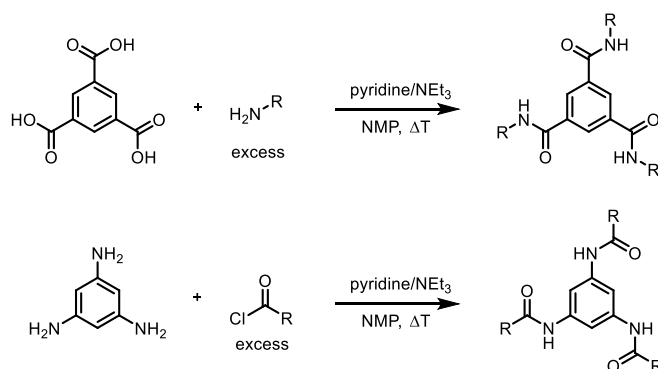
Figure 11. General reaction scheme for 1,3,5-benzene trisamides using a SCHOTTEN-BAUMAN reaction starting from trimesinic acid (top) or triamino benzene (bottom). As acid scavenger pyridine or triethylamine are typically used. Since BTAs show a low solubility, high boiling solvents like N-methyl-2-pyrrolidone (NMP) are used.

It is known that BTAs have capabilities to form supramolecular columns in both bulk and solution states. The peripheral substituents have been demonstrated to influence a number of properties, including solubility behavior, thermal properties, as well as packing behavior and crystal structure in the solid state. It was found that in bulk the subsequent molecule is typically

co-facially stacked and rotated by 60°, resulting in three strands of helical hydrogen bonds, which leads to the formation of supramolecular columns.[94–96] The dipole moments of the directed hydrogen bonds are additive over the length of a column, leading to the formation of a macrodipole moment. This can be compensated for by the antiparallel alignment of further columns, which leads to the formation of bundles (**Figure 12**).[94–97] Depending on the peripheral substituents, thermotropic liquid crystalline behavior manifests itself in BTAs. Several different phases, both nematic and smectic, can be realized.[85,98–100]
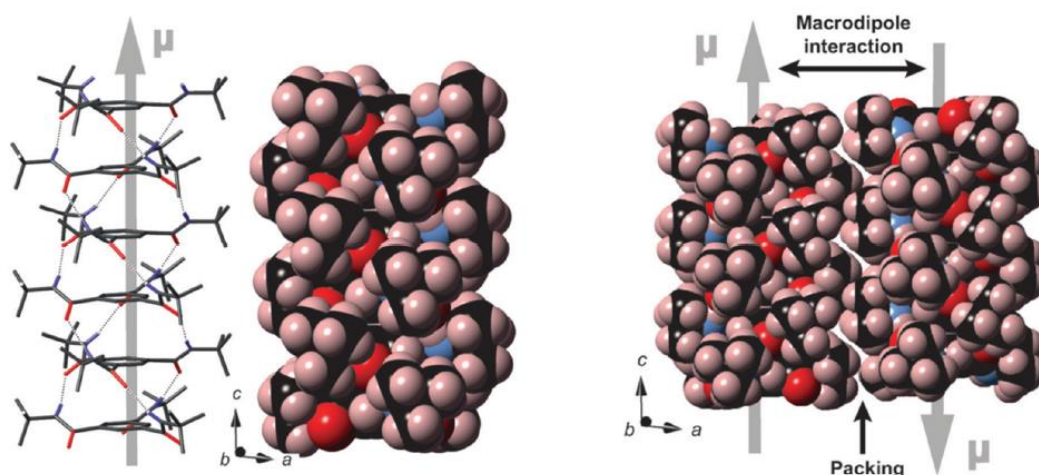
Figure 12. Side view of a columnar stack of six benzenetrisamides molecules which builds up a macrodipole along a single supramolecular column (left). Side-view of two benzenetrisamides columns with antiparallel alignment to compensate the macrodipole (right). The macrodipoles are highlighted with the help of grey arrows. Adapted from Ref.[97] used under a Creative Commons CC—BY license.

The self-assembly of BTAs into one-dimensional supramolecular structures can be stimulated by external factors under specific conditions, such as changes in temperature, concentration, solubility, or pH. For this to occur, the BTA must first be molecularly dissolved in a medium like a polymer melt or solvent (**Figure 13**). An external trigger initiates the self-assembly process, causing the molecular building blocks to aggregate into single supramolecular columns. Subsequent compensating of the macrodipole results in the formation of bundles of supramolecular columns. This process is fully reversible due to the involvement of non-covalent interactions.
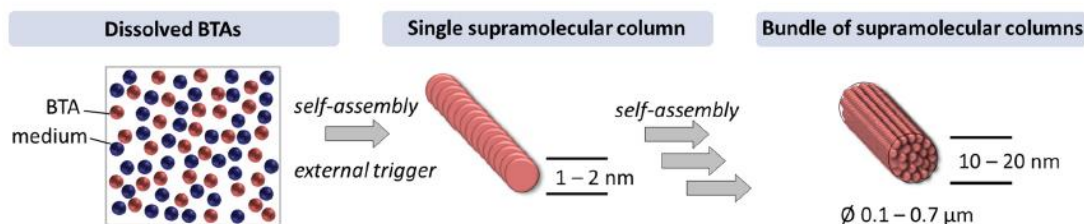
Figure 13. Schematic illustration of a solution based self-assembly process of BTAs. The BTA (red), which has to be molecularly dissolved into a medium like solvent or polymer melt (blue), undergoes self-assembly into single supramolecular columns upon an external trigger like changes in temperature, concentration or pH. To compensate the macrodipole of the single supramolecular BTA column bundles of such supramolecular columns are formed. Source: University of Bayreuth; Macromolecular Chemistry I.

The morphology of supramolecular nano-objects upon cooling at constant concentration using the temperature change as trigger can be controlled by various parameters during the self-assembly process. The most important parameters, which are shown in **Figure 14**, include the molecular structure, the concentration of the BTA, the cooling rate and the solvent.

The peripheral substituents of the BTAs significantly influence the polarity and solubility of the compound, for this reason, it is necessary to determine the appropriate processing window for all BTAs. As a general rule regarding concentration, the diameter of the supramolecular nanofibers increases as the concentration increases. In terms of cooling rate, slow cooling results in a larger fiber diameter, while rapid cooling leads to thinner fiber diameters.[101] The solvent plays a crucial role during the self-assembling process. Different morphologies can be realized by the appropriate choice of solvent. For example, for a BTA with terpyridine groups as a peripheral substituent, both spherical nanoparticles and nanofibers could be selectively produced. The spherical nanoparticles were prepared from a solution with 0.1 wt% BTA from 6:4 (w/w) ethanol/H_2O and the nanofibers from a solution with 0.1 wt% BTA in 9:1 (w/w) propanol/H_2O.[102]
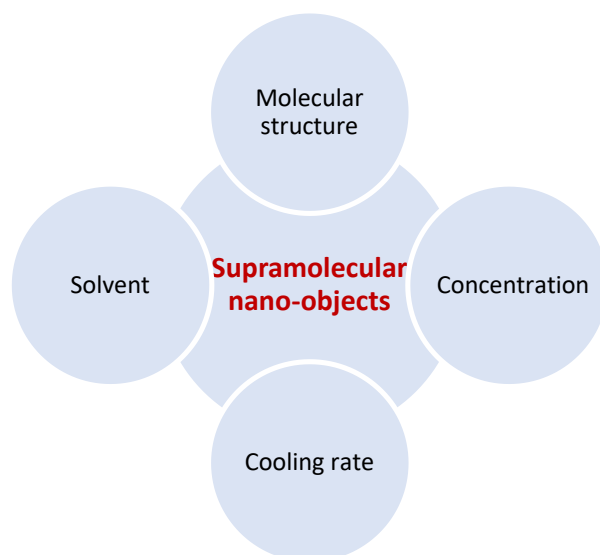
Figure 14. Important self-assembly parameter that influences the morphology of supramolecular nano-objects, in particular the molecular structure of the used building block, the concentration, the cooling rate and the used solvent.

Not only cooling of a molecularly dissolved BTA can lead to the initiation of self-assembly but also heating. It has been shown for BTAs with peripheral tertiary *N,N*-dialkyl-ethylamino groups that they form supramolecular microtubes when heated from water.[103] Another trigger for the initiation of self-assembly of molecularly dissolved BTAs is the change in pH. BTAs with peripheral *p*-carboxylphenyl groups completely dissolved in aqueous sodium hydroxide solution by forming the corresponding sodium salt. Decreasing the pH value to acid conditions by adding a proton source, self-assembly is initiated and thus the BTA assemble to nanofibers, which results in the formation of a hydrogel.[104,105] In addition, electro gelation can be used to produce protons near an electrode surface, which leads to an deposition of supramolecular nanofibers on that surface.[106,107]

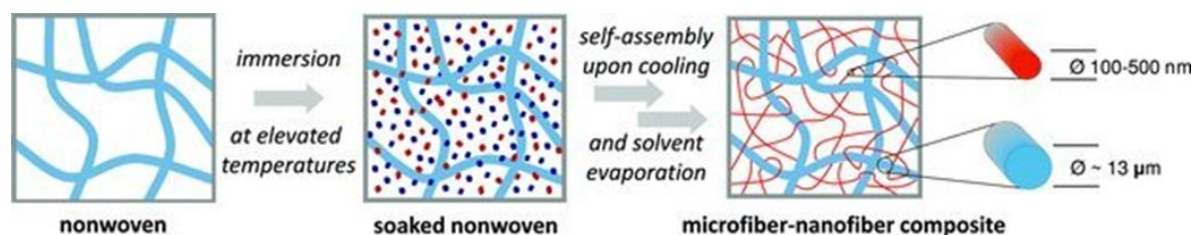**Application of supramolecular BTA nanofibers**

The large number of available peripheral substituents allows a wide range of applications for supramolecular BTA nanofibers. For example, trisamides can be dissolved in polymer melts and form supramolecular fibers during cooling via self-assembly. By carefully selecting the periphery, an epitaxial match can be achieved between the supramolecular BTA fiber and the polymer crystal structure, which leads to nucleation of the polymer. In this context, the crystallization temperature and the crystal structure and size can be influenced by the BTA used.[108–114] A more detailed description of the nucleation process of polymers in bulk is described in **Chapter 1.3.1**.

In addition to their use as a nucleating agent for bulk polymers, BTAs can also be employed as nucleating agents for polystyrene foams. The underlying concept is depicted in **Figure 15**. Depending on the concentration and the processing temperature, BTA with a tertbutyl group can be homogeneously dissolved in the polystyrene melt. Upon cooling, the BTA self-assembles into finely dispersed, solid supramolecular nano-objects, which subsequently act as nucleating sites for foam cell formation. At a concentration of 0.2 wt% BTA, the cell sizes were significantly reduced by a factor of 35, from 632 to 18 mm, in comparison to those of a neat extruded polystyrene foam.[115,116]
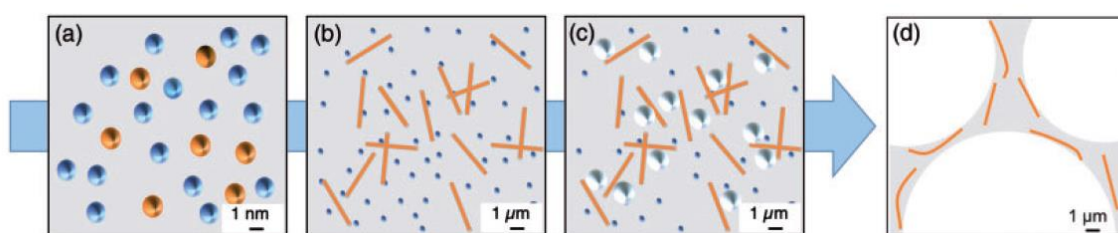

Figure 15. Concept and processing steps of the morphology control of PS foams with supramolecular additives: (a) Dissolution of BTA (orange) and blowing agents (blue) in PS melt (gray), (b) self-assembly of the BTA upon cooling into supramolecular nano-objects, (c) foam nucleation on the surface of the nano-objects, and (d) PS foam cell structure with BTA nano-objects.[115] Reprinted with permission from Ref.[115]© 2019 Sage Publications.

One advantage of self-assembly processes is that the formation of supramolecular nanofibers can be performed in porous media, thereby enabling the fabrication of interpenetrating networks. This has been utilized in the fabrication of polymer microfiber/supramolecular nanofiber composites as it is shown in **Figure 16**. Here, the polymer nonwoven was immersed in a hot solution containing dissolved BTA with peripheral alkyl substituents. Following this, the soaked polymer nonwoven was removed from the BTA solution and, upon cooling and solvent evaporation, self-assembly to supramolecular nanofibers occurred. This resulted in an interpenetration network of polymer fibers and supramolecular nanofibers. The microfiber/nanofiber composites were subsequently employed as air filtration media for particulate matter, exhibiting effective filtration efficiency and minimal pressure drop.[117,118]

Figure 16. Schematic illustration of the *in situ* preparation process of a microfiber-nanofiber composite composed of supramolecular BTA nanofibers (red fibers) within a nonwoven (blue fibers). For this, the nonwoven was immersed in a molecularly dissolved BTA solution (blue dots: solvent, red dots: molecular BTA units). Upon cooling and solvent evaporation, the microfiber-nanofiber composite was obtained. Reproduced with permission from Ref.[117] © 2013 WILEY-VCH Verlag GmbH & Co. KGaA.

The selective filtration of heavy metal ions and particles may be addressed by the use of BTAs with sulfur-containing peripheral substituents. As illustrated in **Figure 17**, two distinct BTAs were dissolved in a hot organic solvent and poured into a sand filling. One BTA possessed alkyl substituents, which ensured mechanical stability, while the other BTA had sulfur-containing groups, which enabled the adsorption of heavy metal ions/particles. Upon cooling, self-assembly of core shell nanofibers occurred, with the sulfur-containing BTA forming the shell layer. Subsequent exchange of the organic solvent with aqueous heavy metal ions/particles resulted in selective adsorption on the supramolecular nanofibers.[119,120]
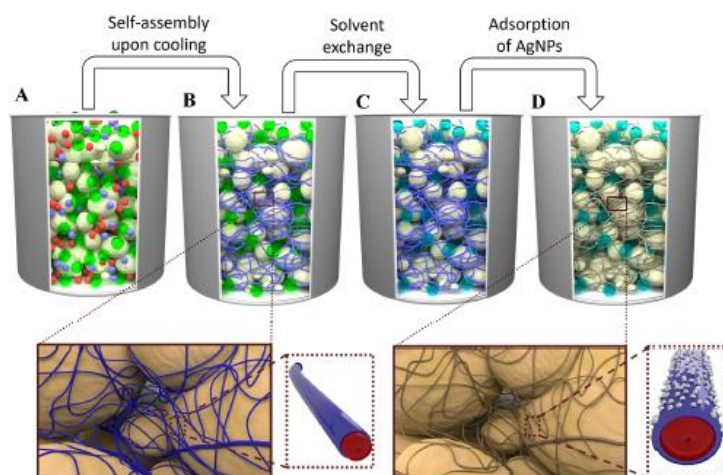
Figure 17. Schematic representation of the self-assembly process of co-assembled supramolecular filter-sea-sand-composites. **A**: A container filled with a defined amount of sea sand is immersed into a clear BTA-mixture solution at elevated temperatures until the sand is fully soaked (red spheres: aliphatic BTA; blue spheres: functional BTA; green spheres: solvent). **B**: The system is cooled down to initiate the formation of supramolecular nanofibers within the voids of the granulate material. At first, the aliphatic BTA forms supramolecular fibers. Subsequently, the sulfur-containing BTA starts to assemble on the fibers of the aliphatic BTA. Thus, core-shell fibers can be formed (blue lines: core-shell fibers). A schematic representation of such a core-shell fiber is shown on the bottom side of the sketch. **C**: The solvent is exchanged with a non-solvent like water (light transparent blue spheres: non-solvent). **D**: Silver nanoparticles (AgNP) can be adsorbed on the surface of functional supramolecular fibers. These AgNPs are immobilized on the surface of the fibers (bronze lines: fibers with AgNPs). A schematic representation of such a core-shell fiber with adsorbed AgNPs is shown on the right side of the sketch.[120]

A further potential application for supramolecular BTA nanofiber is the immobilization of gold nanoparticles (AuNPs) for use as a catalyst carrier in heterogeneous catalysis. To obtain a mechanically stable composite, electrospun polymer short fibers and supramolecular nanofibers based on a BTA with peripheral terpyridine groups were combined using a wet laid process. The composite was dipped into an aqueous solution of Au(III) ions and subsequently immersed into a NaBH$_4$ solution, resulting in the reduction of the bound Au(III) ions to AuNPs (**Figure 18**). The AuNP-decorated composite was subsequently employed as a heterogeneous catalyst in the catalytic reduction of 4-nitrophenol to 4-aminophenol. It was demonstrated that the composite is both mechanically resistant and exhibits only minimal leaching of AuNP. This allows the composite to be used as a catalyst without reactivity impairment during repeated use.[102,121]
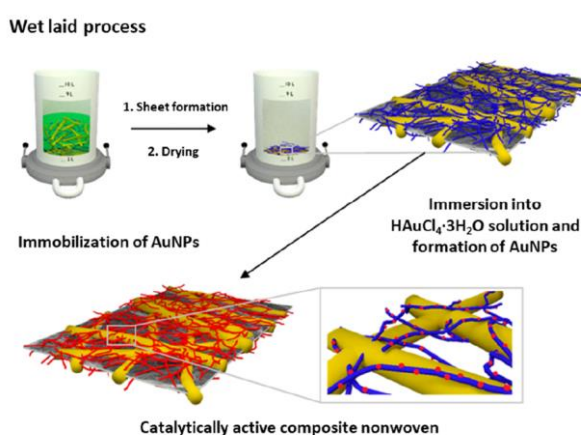
Figure 18. Schematic representation to prepare catalytically active composite nonwoven. Short electrospun polyacrylonitrile (PAN) fibers (yellow fibers) were mixed with a functional terpyridine-based BTA as supramolecular motif (blue nanofibers) and prepared with the wet-laid process. After immersion into a HAuCl$_4$ · 3H$_2$O solution and formation of AuNPs (red dots), a stable catalytically active composite nonwoven is observed. Adapted with permission from Ref.[121]© 2021 American Chemical Society.

Introduction

Hierarchical superstructures

The field of supramolecular chemistry is not limited to the creation of low-dimensional structures but is able to develop architectures of higher-order, which are known as hierarchical superstructures. One method for creating such superstructures is to combine coaxial electrospinning with a self-assembly process from solution (**Figure 19**). During the electrospinning process, BTA seeds are formed as a shell layer on top of the polystyrene core. When immersing these fibers in a solution of the same dissolved BTA, the seeds act as nucleation sites, from which a self-assembly process is triggered, resulting in a structure that resembles a penguin downy feather. A nonwoven consisting of these penguin-downy-feather-like fibers, was used as an air filtration medium for particulate matter. By varying the density of the supramolecular fibers via adjusting the seed concentration, a filter could be produced that has very high filter efficiency and a very low pressure drop.[122]
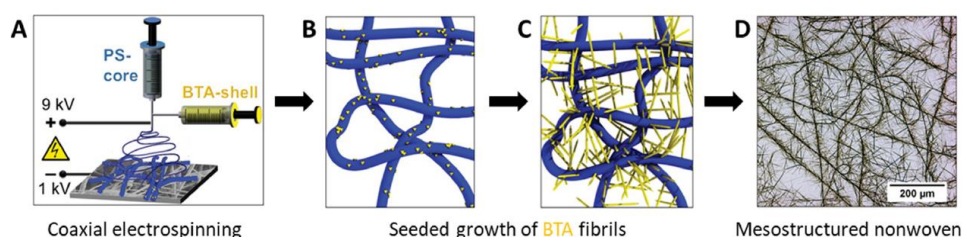
Figure 19. Schematic illustration to prepare mesostructured nonwovens with a special morphology. A) Coaxial electrospinning of polystyrene (PS) fibers (colored in blue) with BTA seeds (colored in yellow). B) Resulting BTA seeds on top of the PS fibers. C) Mesostructured nonwoven composed of polymer and supramolecular BTA fibers after seeded growth of the BTA fibers. D) The corresponding optical micrograph of the mesostructured nonwoven. Adapted with permission from Ref.[122]© 2019 WILEY-VCH Verlag GmbH & Co. KGaA.

Another way to obtain hierarchical superstructures is to combine crystallization driven self-assembly and molecular self-assembly. For this purpose, polystyrene was decorated with micelles using coaxial electrospinning as described in **Figure 20**. These micelles were obtained from a triblock co-polymer using crystallization driven self-assembly. After immersion of these fibers in a solution of dissolved BTA, and subsequent drying results in the formation of a superstructure rendering a fir-tree like morphology. The chemical match between the peripheral substituent of the trisamide and the functional group of the triblock co-polymer is of crucial importance; in the absence of this match, the superstructure is not formed. This superstructure is suitable for the immobilization of palladium nanoparticles due to the tertiary amine group, which may facilitate their use in heterogeneous catalysis or filtration.[123–125]
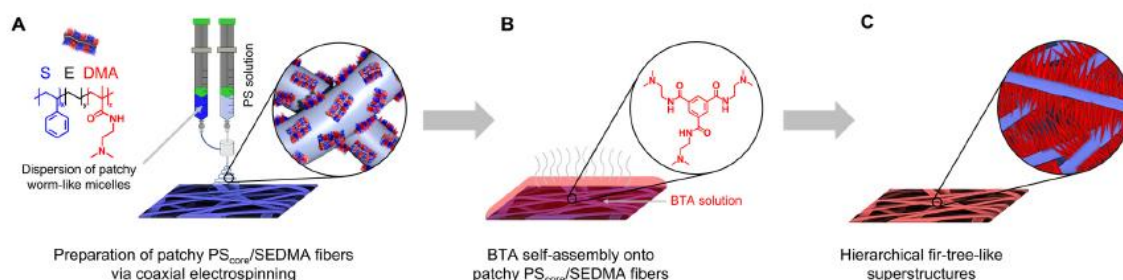
Figure 20. Schematically illustration for the preparation of hierarchical superstructures. A) The dispersion of patchy worm-like polystyrene-block-polyethylene-block-poly(*N,N*-dimethylaminoethyl methacrylamide) (SEDMA) triblock terpolymer micelles were coaxial electrospun on supporting polystyrene (PS) fibers to prepare patchy PS core/SEDMA fibers. B) The prepared patchy polymer fibers were immersed into an aqueous solution containing the BTA with *N,N*-dimethyl groups. Subsequent evaporation leads to the patch-mediated molecular self-assembly of the BTA onto the patchy polymer fibers and C) results in a hierarchical fir-tree-like superstructure. Reproduced from Ref.[123] used under a Creative Commons CC—BY license.

Special self-assembly techniques even make it possible to mimic nature. Exploiting the capillary forces of vertically aligned polyamide microfibers serving as a structuring substrate for the site-specific self-assembly of a specific BTA with tertiary amines as peripheral substituent from solution (**Figure 21**). The morphology of the supramolecular spines resembles that of a cactus and extends over several hierarchical levels, eventually leading to a conical shape with elongated self-assembled microgrooves and a super hydrophilic surface. Like its natural model, the supramolecular cactus has also been shown to be able to transport water droplets unidirectionally via these hierarchical conical microstructures.[126]
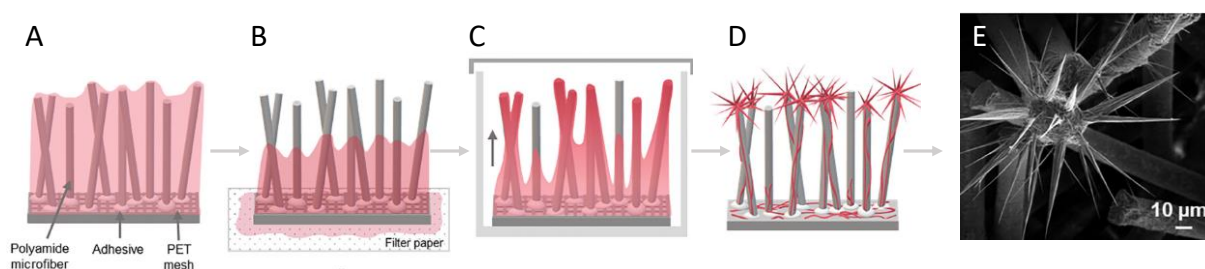

Figure 21. Schematic illustration of the preparation of artificial supramolecular spines on top of polyamide microfibers. A) Polyamide flock consisting of vertically aligned polyamide microfibers fixed onto a polyethylene terephthalate (PET) mesh. The PA flock is immersed into a BTA solution. B) The soaked polyamide flock is then placed on a filter paper for a dedicated time to partially remove the BTA solution. C) During the drying process in a covered petri dish capillary forces of the Polyamide microfibers transport the BTA solution toward the polyamide head and evaporation of the solvent occurs and self-assembly is initiated at the polyamide head. D) Polyamide microfibers decorated with supramolecular BTA spines. E) SEM micrograph of Polyamide microfibers decorated with supramolecular BTA spines. Adapted from Ref.[126] used under a Creative Commons CC—BY license.

1.2.2 Tricycloquinazoline

Tricycloquinazoline (TCQ) is an electron-poor nitrogen-containing heterocycle with the molecular formula $C_{21}H_{12}N_4$ (**Figure 22**). The molecule geometry is planar with a triple axis of rotation perpendicular to the plane of the molecule, resulting in a C_3 symmetry.

In the following, the synthesis and properties of TCQ and its derivatization will be discussed. Furthermore, the use and properties of TCQ and its derivatives in applications like discotic liquid crystals, covalent organic frameworks, and metal-organic frameworks will be summarized.
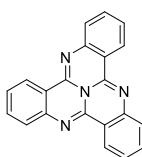

Figure 22. Molecular structure of tricycloquinazoline (TCQ).

TCQ can be produced from various reactants via a condensation reaction with elimination of water or ammonia by trimerization (**Figure 23**). The synthesis of TCQ was first described by Jacobsen and Huber in 1908. They heated indazole with two equivalent copper powders and obtained TCQ with a yield of 30 % by splitting off ammonia.[127] However, they proposed a linear arrangement of three benzene rings, two pyridine rings and one pyrazole ring for the molecular structure. The correct structure of TCQ was first proposed by Kozak and Kalmus in 1933, who synthesized TCQ by reacting o-aminobenzaldehyde with ammonium chloride in 22 % yield.[128] The proposed structure was finally confirmed by Iball and Motherwe through the crystal structure.[129,130] The salt of o-aminobenzonitrile and p-touloulsulfonic acid also produces TCQ in 26 % yield when heated to 210 °C.[131] Yoneda and Mera showed that TCQ can also be prepared from antranil and ammonium acetate in refluxing sulfolane : acetic acid solvent mixture in 51 % yield.[132] The yield could be increased to 75 % starting from o-aminobenzonitrile and catalytic amounts of $ZnCl_2$ in refluxing α-chloronaphthalene.[133] Omitting an organic solvent and using a $ZnCl_2$ melt instead gave TCQ in up to 97% yield.[134]

TCQ is extremely temperature stable and has a melting point of 319°C.[127] In addition, it is also very chemically stable, as it can neither be acetylated nor methylated, is oxidant resistant and stable against strong bases.[135] It is insoluble in water, ether, alcohol, aqueous alkaline solutions

and dilute acids. However, it is soluble in concentrated sulphuric acid and concentrated hydrochloric acid, but precipitates again in needle form when diluted. It is very soluble in either hot aniline or pyridine.[127,128]
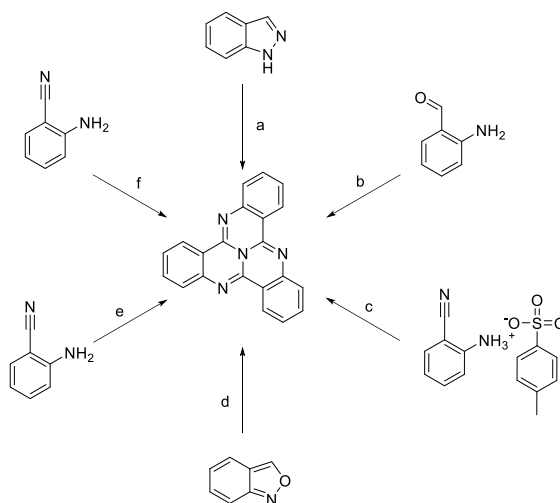
Figure 23. Synthetic routes towards TCQ. Reaction conditions: a) Cu-powder 2 eq., 290°C, 6 h, 30% yield;[127] b) NH₄Cl, 22% Yield;[128] c) 210°C, 0.25 h, 26% Yield;[131] d) NH₄AcO 2 eq., sulfolane:AcOH 3:1, 170°C, 10 h, 51% yield;[132] e) ZnCl₂ 0.01 eq., α-chloronaphthalene, 290°C, 8 h, 75% yield;[133] f) ZnCl₂ 1 eq., 350°C, 24 h, 97% yield.[134]

Synthesis of TCQ derivatives

The low solubility in organic solvents prevents the possibility of carrying out chemical transformations on TCQ, with some exceptions. For example, nitration reactions can be conducted with nitric acid; here, the degree of nitration can be controlled by the concentration of nitric acid.[128,132,135,136] In addition to nitration, TCQ dissolved in acetic acid can also be converted to trichloro-TCQ by adding chlorine.[128] Hydroxylation under Fenton conditions can be used to produce 3-hydroxy-TCQ in 14% yield starting from H₂O₂ and FeSO₄ and TCQ.[137]

Since the preparation of substituted TCQ derivatives from TCQ is only feasible to a limited extent, the substituents can also be attached prior to trimerization. Thus, trichloro-TCQ, tribromo-TCQ, trimethoxy-TCQ and hexamethoxy-TCQ could be prepared from substituted anthranils.[138]

**Liquid crystals based on TCQ as discotic core**

The intrinsic C_3 symmetry of TCQ makes it interesting as a core for liquid crystalline discotic mesogens. A whole series of 2,3,6,7,10,11-hexa(thioalkoxy)tricycloquinazolines have been synthesized via the nucleophilic substitution of C_3-symmetric hexachloro-TCQ with linear thioalkanes.[138] The resulting compounds featured aliphatic side chains varying from three to 18 carbon atoms. Thermal analysis of these compounds revealed a broad temperature range of liquid crystalline behavior. Structural elucidations of the mesophases revealed hexagonal columnar arrangements for all compounds.[138] Spectroscopic investigations of thin films based on hexa(heptylthio)tricycloquinazoline show, that the crystalline form has rich vibronic structure, indicating Frank-Condon excitation of individual molecules. After heating above mesophase transition temperature and consequently transforming it into a columnar phase the absorption bands broadens and the features are blue-shifted 5 to 16 nm compared to the crystalline phase.[139] In addition, 2,3,6,7,10,11-hexa(thioalkoxy)tricycloquinazolines with long aliphatic side chains can form monolayers on gold substrates, due to the six thioether moieties. The orientation of the core was found to be face-on, whereas the alkyl chains do not lay flat on the gold surface but are folded upwards, shielding the aromatic core as indicated by atomic force microscopy, infra-red spectroscopy as well as scanning tunnel microscopy.[140,141]

Another class of TCQ-based mesogens are 2,3,6,7,10,11-hexaalkoxytricycloquinazolines, that can be synthesized by a Williamson ether synthesis using hexahydroxy-TCQ or hexaacetoxy-TCQ and alkylbromides.[142,143] Mesogenic behavior is observed from a length of the aliphatic side chain of at least four linear carbon atoms. Using branched aliphatic chains the mesogenic behavior is destroyed, when the branching is close to the TCQ core. Introducing sidechains where the branching is located farer from the core, leads to a drastic decrease in the isotropic temperature, compared to the linear isomer.[144] For all linear and branched peripheral sidechain compounds a columnar mesogenic phase is reported.[142,144] Lamellar liquid crystalline phases can be achieved by using either linking the hexa-deprotonated hydroxy-TCQ to didodecyldimethylammonium salt via ionic self-assembly or by six cyanobiphenyl moieties that are connected to the TCQ core via oligo ethylene glycol spacers.[145,146] Latter, can also be processed to Langmuir-Blodgett films, where the compound are aligned edge-on.[147] Using oligo ethylene glycol chains as peripheral substituent of hexahydroxy-TCQ, also yields a discotic mesogen, that features a

broad mesophase from the temperature range of 77 °C-233 °C and shows a hexagonal columnar mesophase.[148] This TCQ based liquid crystal is fluorescent and was successfully employed as a molecular probe for fluorescence imaging of other discotic liquid crystals.[149] Furthermore, the electrical conductivity of this columnar liquid crystal was investigated after n-doping with 10 wt% potassium and revealed a conductivity of $\sigma_{\parallel} = 1.1 \times 10^{-3}$ S m^{-1}. This is an increase of two orders of magnitude in conductivity compared to n-doped TCQ based liquid crystal with an aliphatic side chain.[150] The increase is attributed to the oligo ethylene glycol sidechains, that can stabilize the resulting potassium cation and hence allow a higher degree of n-doping.[148] Furthermore, Langmuir monolayers where prepared using LANGMUIR–BLODGETT techniques and their structural alignment was elucidated. The monolayer exhibits a gas phase, a low density liquid phase, where the molecule orientation is face-on, and high density liquid phase, where the molecule orientation is both edge-on and face-on.[151,152]

Covalent organic frameworks and metal-organic frameworks based on TCQ

More recently, the structural motif of TCQ has gained attention in the field of *covalent organic frameworks* (*COFs*) and *metal-organic frameworks* (*MOFs*) (**Figure 24**). In 2019, BUYUKCAKIR *et al.* presented the first synthesis of TCQ-based COFs, also known as covalent quinazoline networks (CQN) using an ionothermal polymerization of 2,5-diaminoterephthalonitrile in a melt of ZnCl$_2$.

COF-1: R=H
COF-2: R=F

MOF-1: M=Cu^{2+}
MOF-2: M=Ni^{2+}
MOF-3: M=Mg^{2+}
MOF-4: M=Co^{2+}
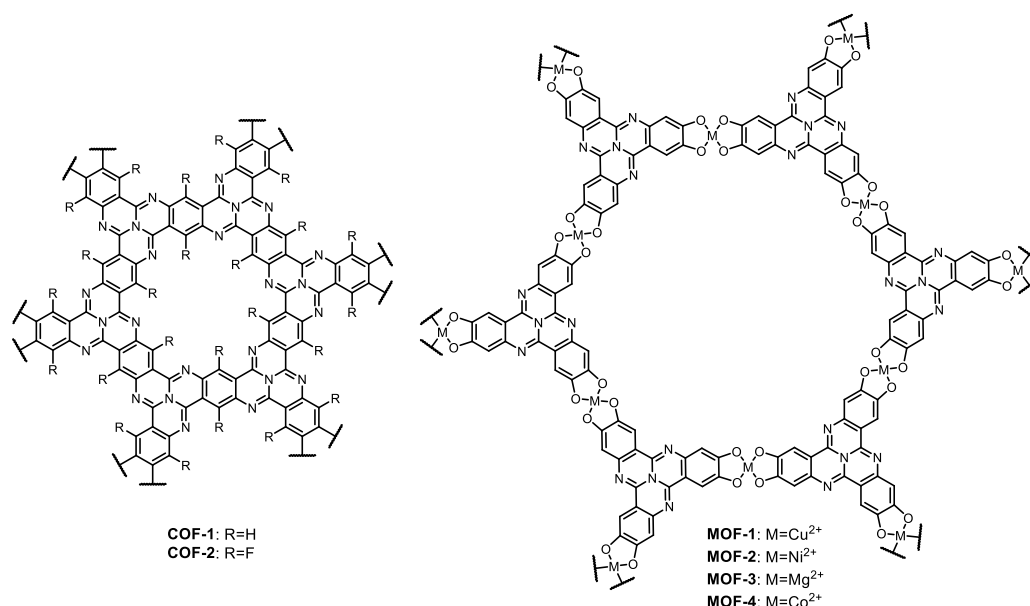
Figure 24. Chemical structure of TCQ-based covalent COFs and MOFs.

Introduction

This COF-1 showed a remarkable surface area of more than 1800 $m^2\,g^{-1}$ together with large pore volumes of up to 0.93 $cm^3\,g^{-1}$, which enabled its application as a promising CO_2 adsorbent with a CO_2 uptake capacity of 7.16 mmol g^{-1} (31.5 wt%) at 273 K and 1 bar.[134] Furthermore, the influence of microstructuring on TCQ-based polymers on their porosity and performance in the electrochemical hydrogen evolution reaction (HER) was investigated. For this purpose, the 2-dimensional COF-1 was compared with a 3-dimensional tricycloquinazoline conjugated porous polymer prepared by oxidative coupling polymerization of TCQ using $FeCl_3$. It was shown that the 3-dimensional polymer has a higher surface area with a broadly distributed pore size distribution in contrast to the periodically ordered COF-1 which has a smaller surface area but a very narrowly distributed pore size. Furthermore, it was shown that this periodically ordered pore architecture leads to open 1-dimensional channels. The conductivity of the electron/mass transfer through the π-conjugate plane and the open 1-dimensioal channel is ultimately more favorable to boost the electrochemical catalytic activity in the HER for COF-1 compared to the 3-dimensional TCQ-polymer.[153]

The incorporation of fluorinated 2,5-diamino-3,6-difluoro-terephthalonitrile in the ionothermal synthesis results in CQN-2, which can be used as an electrocatalyst in the electrocatalytic reduction of CO2 to ethylene with a Faradaic efficiency of ethene production (FE_{C2H4}) of 61.1% at -1.07 V (versus reversible hydrogen electrode [RHE]).[154] COF-2 can also be used as an organic cathode material in lithium-ion batteries, where it delivers good performance with a high capacity (250 mA h g^{-1} at 0.1 A g^{-1}), high rate capability (105 mA h g^{-1} at 5.0 A g^{-1}) due to its 2-dimensional extended conjugated architecture and layered structure. The intrinsic chemical stability of COF-2 is reflected in a remarkable cycling stability of 95.8% retention rate after 2000 cycles at 2.0 A g^{-1} together with a high coulombic efficiency of 99.95%.[155]

In addition to covalent organic networks, the TCQ structural motif has also been used in organometallic networks. Here, the building block hexahydroxy-TCQ is combined with different metals (M= Cu^{2+}, Ni^{2+}, Mg^{2+}, or Co^{2+}) to create 2-dimensional MOFs with tunable electronic properties and high electrical conductivity. This precise control over the electronic properties of the resulting MOFs could pave the way for the next generation of hybrid electronics.[156]

Hexahydroxy-TCQ is very suitable due to a large, electron-poor ligand core with reduced electron density at the metal binding site, which leads to a more pronounced reversibility of the

metal-ligand bond and a higher in-plane crystallinity for the production of single crystalline conductive 2D-MOFs. Latter is difficult because in-plane growth (that is, growth in the ab plane) requires continuous formation and breakage of strong metal–ligand bonds, whereas growth normal to the covalent sheets (that is, in the c direction) is governed by much weaker π-stacking interactions. Because the latter are much more reversible, they usually dominate growth but are too weak to enforce long-range translational symmetry, causing severe stacking disorder. Consequently, these materials exhibit long needle- or thread-like morphology, with severely stunted in-plane growth such that the ab dimensions of typical MOF crystallites rarely exceed several hundred nanometers. Dou et al. were able to produce a series of single crystalline MOFs with sizes up to 200 μm and determine two crystal structure types that have analogous 2D honeycomb-like layers but different packing modes and pore contents.[157,158] For MOF-1, the π-π distance was determined to be 3.19 Å, which is less than in any other 2D MOF and also less than the distance of graphene layers in graphite.[159] Furthermore, the in-plane and out-of-plane conductivities were determined, showing that MOF-1 has an in-plane conductivity of ~100 S m^{-1} and an out-of-plane conductivity of ~9 S m^{-1} at room temperature. The former is thus one of the highest reported conductivities for 2D MOFs.[160]

Due to the conductive properties of TCQ based MOFs, MOF-1 and MOF-2 were investigated as electrocatalyst for CO_2 reduction. For both MOF-1 and MOF-2 the only products from CO_2 saturated 1M $KHCO_3$ aqueous solution was hydrogen and methanol. For latter, the faradaic efficiency for methanol at -0.4 V vs. RHE was 53.6% using MOF-1 which is a remarkable yield. MOF-2 had its highest faradaic efficiency for methanol at -0.3 V vs. RHE 5.4%. Furthermore, a good durability of the faradaic efficiency could be shown, over a time period of 10h continuous operations.[161]

In addition, the redox activity of the TCQ core in MOF-1 was used as a lithium storage material. This enables the transport of Li^+/e^- and guarantees a robust electrode. The result is a high capacity of 657.6 mAh g^{-1} at 600 mA g^{-1}, which exhibits remarkable high-rate capability and impressive cyclability.[162]

Flexible photodetectors based on thin films of MOF-1 on flexible substrates show a broad photoresponse in a range from UV to mid-infrared (370-3400 nm) due to the small bandgap and broadband light absorption. Furthermore, these photodetectors can act as an optical synapse and feature excellent data recognition accuracy in artificial neural networks.[163]

Lastly MOF 1 was used as a hole extraction layer in a perovskite solar cell, where it provides an ultra smooth surface for perovskite film growth, an excellent photocarrier extraction capability, and defect passivation on the perovskite surface. The power conversion efficiency of a flexible perovskite solar cell using MOF-1 as hole extraction layer was determined to be 20.3%, while a reference with a state of the art hole extraction layer NiO_x only exhibit a power conversion efficiency of 18.3%.[164]

1.3 Applications

1.3.1 Nucleation of isotactic polypropylene

Polypropylene (PP) is a thermoplastic polyolefin, which is obtained by polymerization of propylene. After polyethylene it has the highest annual production of all plastics. To put this into perspective, assuming a density of polypropylene of $1g/cm^3$ the annual productions equals the size of 24 Khufu's great pyramid at Giza. The ever-increasing demand for polypropylene is primarily due to its outstanding properties. PP has the lowest density of all plastics, good thermal stability, chemical resistance, mechanical strength, and low cost of only 1$ a kilogram.[165]

In contrast to ethylene or other vinyl monomers, PP cannot be produced via radical polymerization, as propylene can stabilize the radical through its mesomeric boundary structure.[166] For a long time, PP was therefore considered unpolymerizable until NATTA used ZIEGLERS olefin polymerization catalyst system of $TiCl_4/Al(C_2H_5)_3$ for propylene.[167] Since the carbon atom to which the methyl group is attached is chiral, this leads to an ordered sequence of configuration repeating units in the main chain, also known as tacticity.[168] The possible tacticities for PP are depicted in **Figure 25**. The stereostructure of the polypropylene chain is described using the terms meso (m) and racemo (r), which indicate whether neighboring methyl substituents have the same (m) or different (r) configurations. For isotactic polypropylene (iPP) the neighboring methyl groups are dominantly meso positioned, where as in syndiotactic polypropylene (sPP) the methyl groups dominantly raceme positioned. For atactic polypropylene (aPP), the sequence of the methyl group is random.
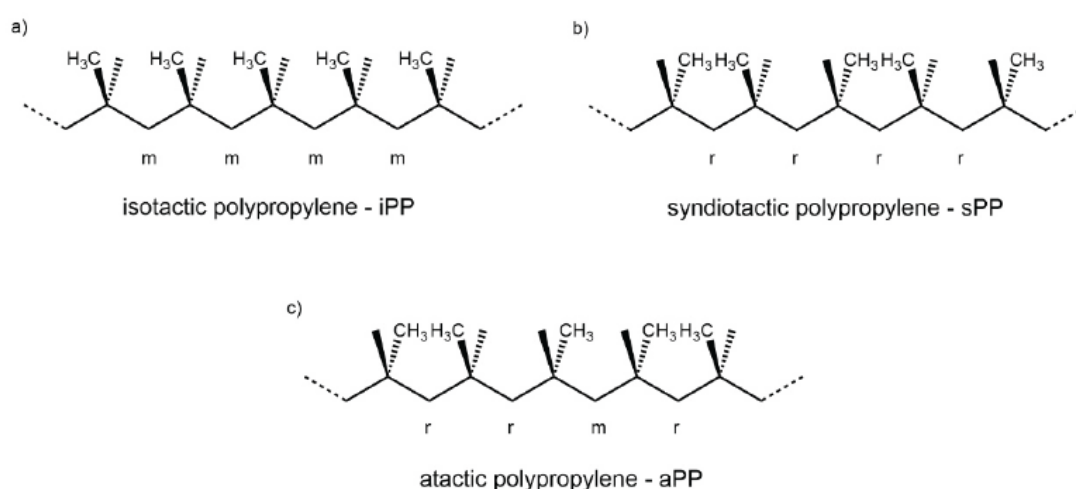

Figure 25. Molecular structures of the three different chain architectures of polypropylene; a) isotactic polypropylene - iPP, b) syndiotactic polypropylene - sPP and c) atactic polypropylene - aPP.

Isotactic polypropylene is capable of existing in at least three distinct crystalline forms, namely the monoclinic α-, the trigonal β-, and the orthorhombic γ-phases, which are depicted in **Figure 26**. In all cases, the chains are arranged in a left- or right-handed threefold (3_1) -helix conformation, with all methyl groups oriented either upwards or downwards. The most common and under normal processing conditions thermodynamically stable alpha modification has the following unit cell parameters of the unit cell: a = 6.65 Å, b = 20.96 Å, c = 6.5 Å, α = γ = 90°, β = 99°80.[169] Since the length of a and c is almost the same, the α-modification of PP leads to the formation of lamellae with a unique tendency to organize in a "cross-hatched" pattern. The α-form spherulites consist of radial (mother) lamellae, which are the predominant direction of growth, and tangential (daughter) lamellae, which are oriented almost perpendicular to the radial direction. This severely restricts the mobility of the segments and therefore results in a material with comparatively high strength and stiffness and a rather brittle behavior.

The metastable β-phase of polypropylene can be produced under specific crystallization conditions, such as high-shear rates, a large temperature gradient, or the use of β-nucleating agents. The β-phase exhibits a trigonal unit cell with the lattice parameters (a) = (b) = 11.0 Å,(c) = 6.5 Å and β = 120°. Compared to the alpha modification, the beta modification does have an increased impact strength, making it the modification of choice for applications requiring higher toughness.[165]

The γ-phase exhibits an orthorhombic unit cell with the lattice parameters (a) = 8.54 Å, (b) = 9.93 Å and (c) = 42.41 Å. It is formed using homogenous metallocene catalysts, or for high molecular weight iPP at high pressures. The gamma modification has no relevant industrial application.[165]
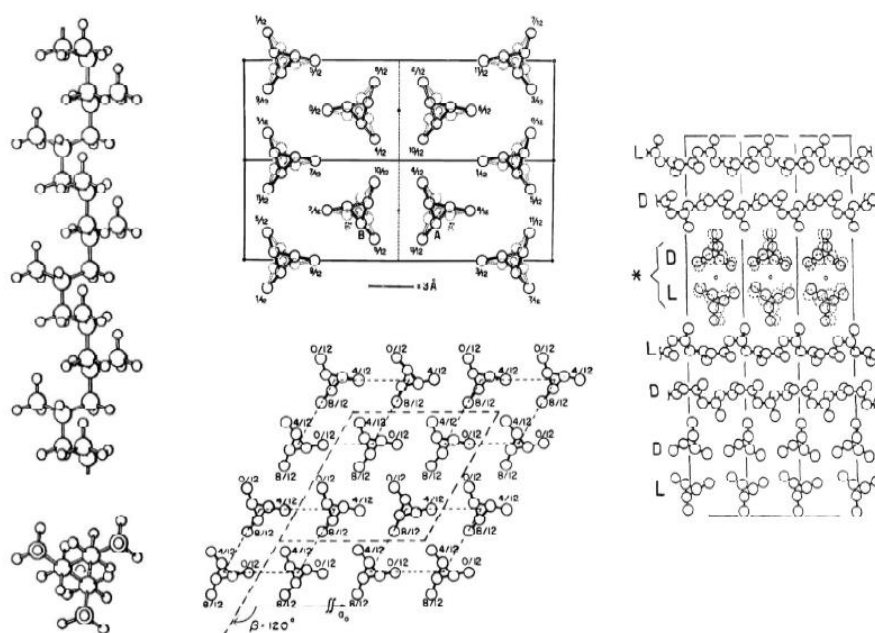
Figure 26. Left: Side- and top view of the conformation of an isotactic polypropylene macromolecule. Adapted from ref.[170] Center, top: Crystal structure of the α- phase of iPP. Center, bottom: Crystal structure of the β-phase of iPP. Adapted from ref.[170] Right: Crystal structure of the γ-phase, with its 80° tilt between adjacent layers of isochiral helices. Adapted from ref.[169] All three structures are presented in the a-b plane.

In order to optimize the material properties of PP for the respective application, it is crucial to understand the crystallization process. In general, any system tries to move towards the energetically favored state. Importantly, the free enthalpy of the amorphous state and the crystalline state have different temperature dependencies due to their different entropies (**Figure** 27).[171] Therefore, a specific temperature exists, where the free enthalpies of both states is identical – the melting point. Above this temperature, the amorphous or molten state is energetically favored and below this point, the crystalline state is energetically favored. A temperature change crossing the melting point, hence, creates an energetical driving force for a phase transition.[171]
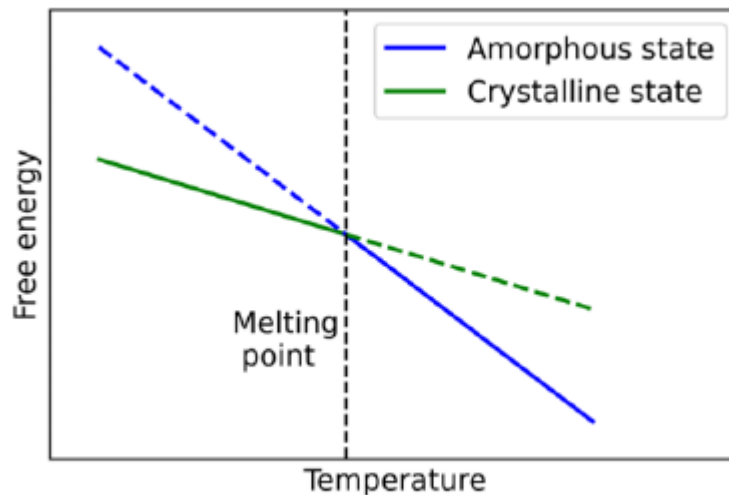
Figure 27. Schematic representation of the free energy in a polymeric system. At high temperatures, the free energy of the amorphous state (blue) is lower while at lower temperatures the free energy of the crystalline state is preferred.[172]

The formation of a crystal is dependent on two terms related to free enthalpy (**Figure 28**). Firstly, energy is required for the incorporation of another molecule into an existing cluster during the process of crystallization. This energy (ΔG_c) must be consumed in the form of surface energy, as a boundary surface between two phases (solid cluster vs. liquid outside) must be overcome. On the other hand, there is the free enthalpy that is released by the change in volume when molecules transform from the liquid phase into the solid phase (ΔG_v). Both terms depend on the radius of the nucleus, but the surface-related term scales with the square of the crystal size, and the volume-related term scales with the cube of the crystal size. This leads to a maximum of ΔG at r_c, which is the critical radius for nucleus formation. The critical radius r_c describes the minimum size of a nucleus that must be formed before it is stable in the polymer melt. Hence, nuclei with a smaller radius than r_c are unstable and redissolve into the polymer melt.[171]
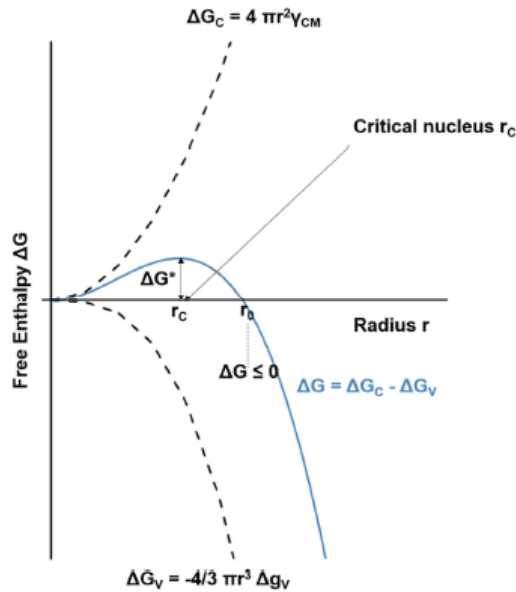
Figure 28. Free enthalpy of formation ΔG (blue), as a function of the interfacial energy ΔG_C and the volume energy ΔG_V, plotted vs the nucleus radius. At the critical radius rc the free enthalpy of formation ΔG possesses its highest value. At the radius r_0 the free enthalpy of formation ΔG becomes zero, leading to growth of the nucleus. Reprinted from ref.[173] under a Creatives Common CC – BY.

The energy barrier ΔG* that must be overcome to initiate crystal growth can be reduced in heterogeneous nucleation. Here, the energy barrier towards nucleation is lowered compared to homogeneous nucleation due to a lower surface energy penalty for the formation of a nucleus. The surface energy cost of forming a solid is dependent on the contact angle Θ to the surface (e.g. surface of nucleating agent). While for homogeneous nucleation a contact angle of Θ = 180° exists, leading to a high surface energy, the contact angle for heterogeneous nucleation is much smaller. A comparison of the free enthalpy of nucleus formation ΔG for the cases of homogeneous and heterogeneous nucleation is depicted in **Figure 29**. While the critical radius r_c remains the same, the nucleation barrier is lowered in the case of the heterogeneous nucleation. Also, the radius at which the free enthalpy of formation reaches zero remains the same for both heterogeneous and homogeneous nucleation.[171,174]
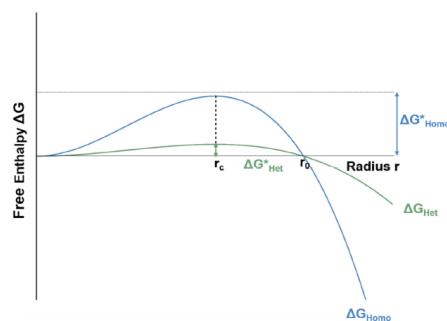
Figure 29. Comparison of the free enthalpy of nucleus formation for homogeneous and heterogeneous nucleation. The nucleation barrier is lowered in the case of heterogeneous nucleation compared to homogeneous nucleation. The critical radius r_c, however, remains the same. Reprinted from ref.[173] under a Creatives Common CC – BY.

Since heterogeneous nucleation is dependend on the surface angle between the polymer melt and the nucleating agent, developing efficient nucleating agents with an appropriate surface is therefore desirable. Heterogeneous nucleation with nucleating agents takes place at higher temperatures compared to homogeneous nucleation.[171,174] This effect is shown in **Figure 30**, where the heating and cooling curves of a pure iPP and an iPP with a nucleating agent, measured with differential scanning calorimetry is depicted. The crystallization peak of the nucleated iPP $T_{c,nuc}$ shifts to higher temperatures in comparison to the respective unnucleated polymer $T_{c,neat}$. Generally, the addition of nucleation agents does not increase the crystallinity.[175]
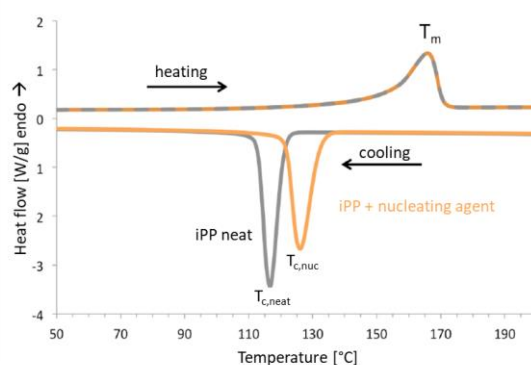

Figure 30. Illustration of a heating and cooling curve from a DSC measurement of an iPP with melting temperature T_m and the crystallization temperatures of the unnucleated iPP $T_{c,neat}$ and the nucleated iPP $T_{c,nuc}$. Adapted from ref.[176] under a Creative Commons CC – BY license.

Although some classes of materials can nucleate iPP, sorbitol derivatives and 1,3,5-benzene trisamides are the most widely used industrial nucleating agents.[108,111,177,178] The latter work according the principle shown in **Figure 31**. The BTA dissolves homogenously in the iPP melt, without decomposition. Upon cooling, self-assembly to supramolecular BTA nanofibers takes place above the crystallization temperature of iPP. These nanofibers act as a nucleation site for the iPP. Upon initial nucleation on the supramolecular nanofibers polymer crystallites can grow.
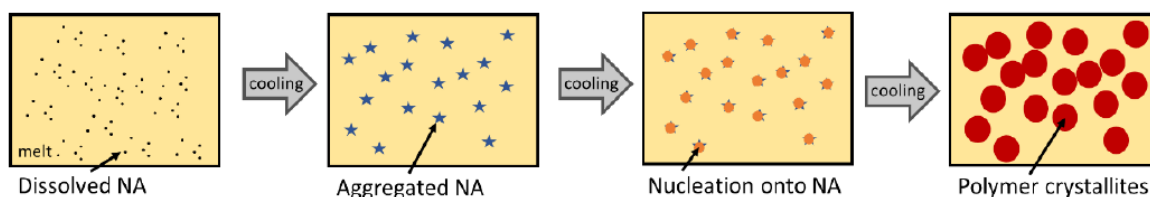
Figure 31. Schematic illustration of the functional principle of supramolecular nucleating agents for iPP. The nucleating agent dissolves homogenously in the iPP melt, without decomposition. Upon cooling supramolecular nanofibers are formed above the crystallization temperature of iPP. iPP starts to nucleate from these formed nanofibers and polymer crystallites are formed. Reprinted from ref.[172] under a Creative Commons CC − BY license.

To guarantee optimal nucleation, it is crucial that the surface of the supramolecular BTA fiber exhibits an epitaxial match with the crystal structure of iPP. 1,3,5-tris(2,2-dimethylpropionylamino)benzene, a commercial nucleating agent also known as Irgaclear® XT386 from BASF SE, crystallizes in an orthorhombic unit cell (a = 14.9 Å, b = 24.05(8) Å, c = 6.80(2) Å).[179] It has been determined that with a repeat distance of 6.80 Å in the c-direction, the epitaxial mismatch with the corresponding periodicity in isotactic polypropylene is less than 5%. This has been shown to facilitate epitaxial growth. **Figure 32** depicts a schematic of the nucleation of a polypropylene chain on the crystal surface of one trisamide column of Irgaclear® XT386.
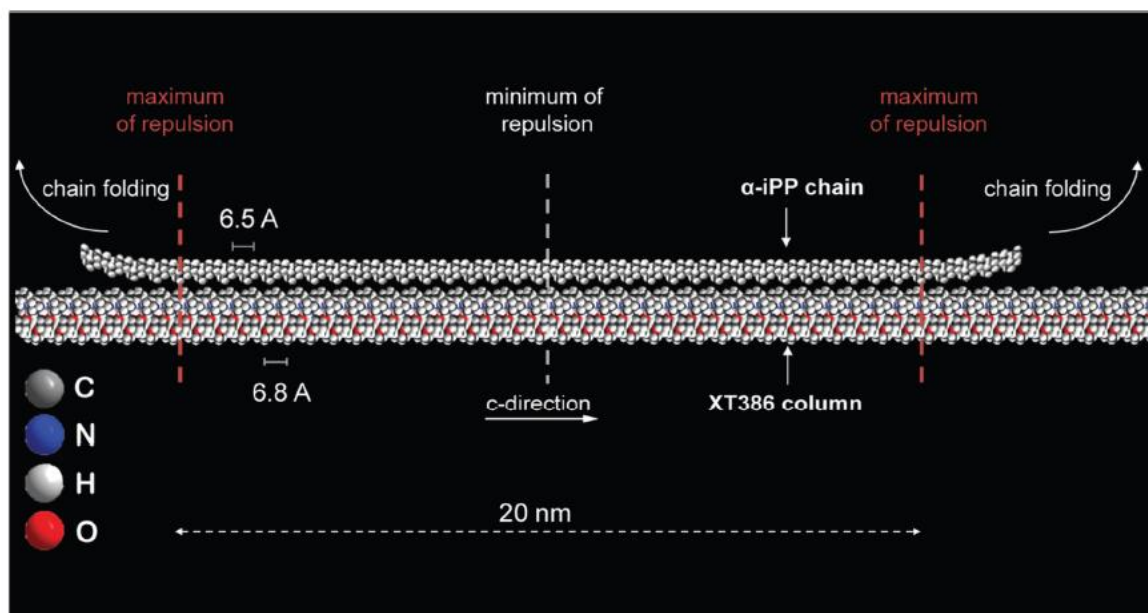
Figure 32. Schematic of epitaxial growth of an isotactic polypropylene chain on the column surface of 1,3,5-tris(2,2-dimethylpropionylamino)benzene (Irgaclear® XT386). The small epitaxial mismatch of 5% between polypropylene and Irgaclear XT386 leads to a maximum repulsion (indicated at the position of the red dashed lines) between the methyl groups of the polypropylene chain and the tert-butyl groups of the benzenetrisamide column approximately every 20 nm. This maximum in repulsion favors chain folding of the polypropylene chain. Source: Macromolecular Chemistry I, University of Bayreuth.

1.3.2 Air filtration

During the Covid 19 pandemic, everyone realized how important filter technology is for personal health protection. Scientific assessments have shown that wearing a face mask is an effective non-pharmacological measure to minimize the spread of disease in the community.[180,181] However, it is not only during a pandemic that the demand for effective filters is high. **Figure 33** shows the size of natural and artificial contaminants that pose a health risk when inhaled, such as acute respiratory infectious diseases.[182–184] For personal protection or to clean industrial exhaust air streams, to mitigate artificial contaminants, it is necessary to develop efficient, sustainable and stable filters.
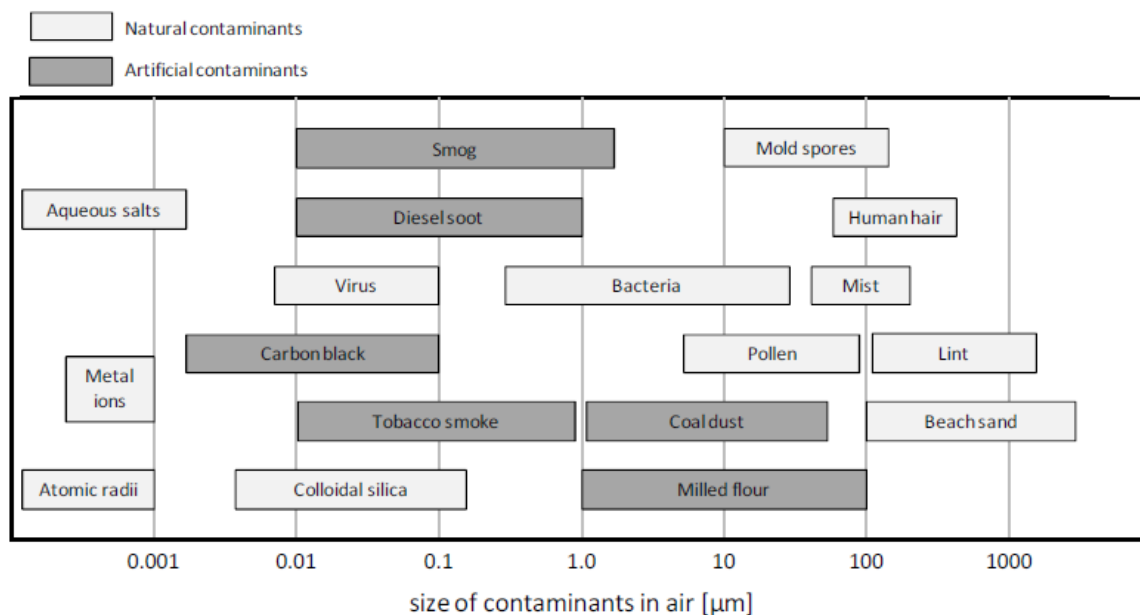

Figure 33. Size range of airborne natural and artificial pollutants. Reprinted with permission from ref.[184] © 2007 Elsevier Ltd.

In contrast to sieving, where particles that are larger than the pore size of the sieve are separated, filtration separates particles that are smaller than the pore size of the filter. There are essentially four filtration mechanisms, which are shown in **Figure 34**: *inertial impaction*, *interception*, *diffusion*, and *electrostatic attraction*.[185] Inertial impaction occurs when large particles moving along an air stream are unable to adjust their direction to the rapidly deforming streamlines. Due to the inability of the particles to deviate from previously established paths, they impact the fiber surface directly.[186] Most of submicron particles are separated via an interception mechanism. Here, streamlines that carry particles are in close proximity of the fiber surface, until attractive forces capture the particle.[187,188] For very small particles the Brownian

molecular motion, causes the deviation from the streamlines, increasing the probability of impacting the fibers surface.[186] Electrostatic attraction as a filter mechanism is based on the Coulombic forces between a charged fiber and an oppositely charged particle. when either one of the particles or fibers is in a neutral state, the charge of one polarizes the other, resulting in attraction by dielectrophoretic force.[189] Using electrostatic attraction, allows for the selective filtration of charged contaminants.[190]
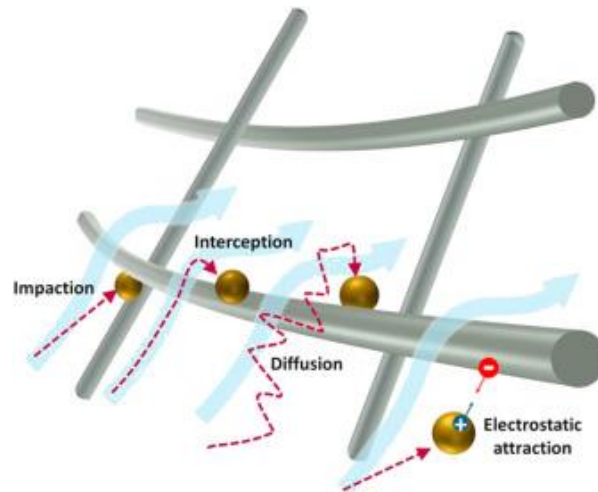
Figure 34. Schematic illustration of the four types (Impaction, Interception, Diffusion and electrostatic attraction) of particulate matter filtration mechanism. Reprinted from ref.[185] used under a Creative Commons CC – BY license.

The filter efficiencies of the various filter mechanisms depend on the particle size. **Figure 35** shows the size-dependent filter efficiencies of the different mechanisms and the resulting overall filter efficiency. This typically has a minimum at around 0.1-0.3 µm, which is called the most penetration particle size (MPPS).[191]
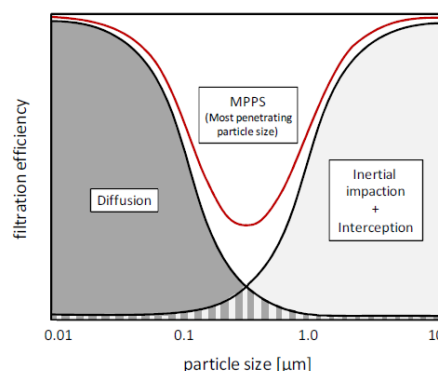
Figure 35. Schematic illustration of the overall filter efficiency dependent on the particle size (red) and the individual contribution of the diffusion filtration mechanism (dark grey) and the inertial impaction and interception (light grey). The minimum in the overall filtration efficiency is called most penetrating particle size. Reprinted from ref.[192] under a Creative Commons CC – BY license.

Introduction

The quality of filters can be measured using various indicators such as filter efficiency η and pressure drop Δp. The filter efficiency indicates the percentage of a certain particle size that is separated by the filter medium.[117] **Equation 1** is used to calculate the efficiency, where N corresponds to the number of particles that penetrated the filter medium and N_0 refers to the number of all particles that were applied to the filter.

$$\eta = \left(1 - \frac{N}{N_0}\right) * 100\%$$
Equation 1

Since the filter efficiency is measured for a specific particle size, the PM_x notation has been established, where PM corresponds to particulate matter and x corresponds to the particle size in μm.

A second important indicator for filters is the pressure drop Δp. This is generally caused by air molecules hitting the fibers. According to DARCY's law, the pressure drop Δp can be expressed by **Equation 2**, where Q corresponds to the volumetric flow rate, μ corresponds to the dynamic viscosity of the fluid, L corresponds to the filter thickness, k corresponds to permeability of filter and A to the area of the cross-section of the filter.[193]

$$\Delta p = -\frac{Q\mu L}{kA}$$
Equation 2

A filter should therefore be equipped with a small fiber diameter, sufficiently porous channels and a low thickness so that the air flow can pass through with little resistance. The greater the pressure drop, the more energy has to be expended to filter a contaminated air mass, which is the reason why a lower pressure drop is desirable. Since filter efficiency and pressure drop are in conflict with each other, the quality factor (QF) was introduced for a more comprehensive assessment of a filter's performance.[194–196] This is calculated from **Equation 3** based on the filter efficiency and the pressure drop.

$$QF = \frac{ln(1-\eta)}{\Delta p}$$
Equation 3

As the pressure drop and therefore the quality factor is proportional to the flow velocity, it is important to only compare filters with similar test conditions.

Nanostructured nonwoven filtration media based on nanofibers have proven to be an promising strategy, approaching ideal filters with high filtration efficiency across the entire range of particle sizes and a low pressure drop.[197] An overview of various morphologies that have been

produced by modifying polymer fibers can be seen in **Figure 36**. By exploiting the RALEIGH instability during the electrospinning process, graphene oxide polyacrylonitrile composite nanofiber-based membranes with a structure like a string of olive-shaped beads were realized (**Figure 36A**). These composites exhibit a filtration efficiency of 99.97% for $PM_{2.5}$ with an 8 Pa pressure drop, tested by a flow velocity of 5.31 cm s^{-1}.[198] Electrospun nanofibers with a wrinkled morphology (**Figure 36B**) were produced from polycaprolactone/polyethylene oxide fibers by a solvent annealing process with acetone.[199] Such wrinkled fiber exhibit a filter efficiency of 80.01 % for $PM_{2.5}$.[200] Porous nanofibers were prepared by electrospinning of a mixture of polylactic acid and zeolitic imidazolate framework-8 (**Figure 36C**). These porous nanofibers exhibit a filtration efficiency for $PM_{2.5}$ of around 95% and a pressure drop of 37 Pa.[201] Fibrillated para-aramid fibers with off-standing nanofiber branches mimicking a downy feather-like morphology, were prepared by surface fibrillation of Kevlar fibers in either sodium hydroxide or phosphoric acid immersion baths (**Figure 36D**).[202,203] These fibrillated fibers exhibit a filtration efficiency of around 70% for $PM_{0.3}$, with a pressure drop of only 3.8 Pa.[202]
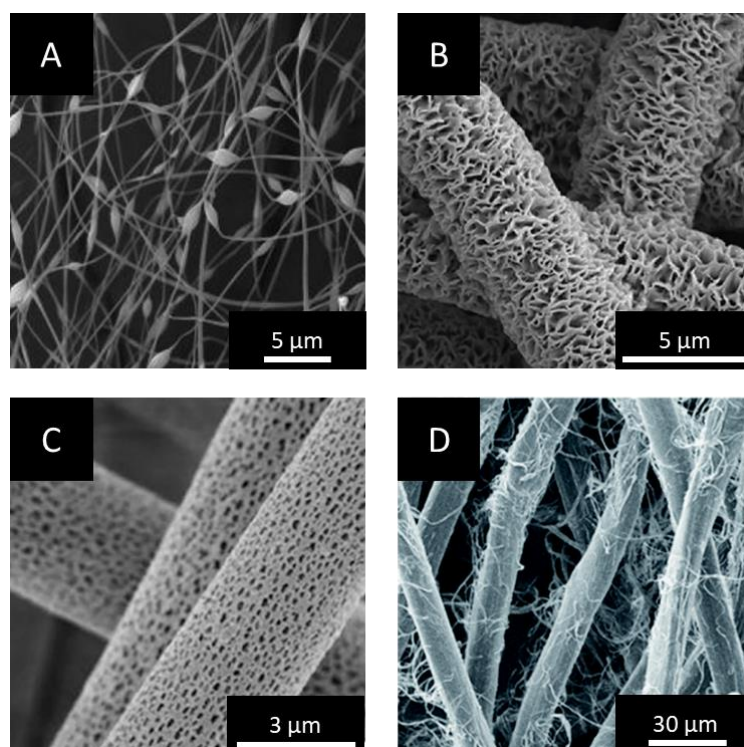
Figure 36. SEM images of nanostructured nonwoven filter media. A) graphene oxide polyacrylonitrile composite nanofiber-based membranes with a structure like a string of olive-shaped beads. Adapted with permission of ref.[198] © 2018 Elsevier B.V, B) electrospun nanofibers with a wrinkled morphology. Adapted from ref.[199] under a Creative Commons CC – BY license, C) Electrospun porous nanofibers. Adapted with permission of ref.[201]© 2018 Elsevier B.V, D) Fibrillated para-aramid fibers with off-standing nanofiber branches mimicking a downy feather-like morphology. Adapted with permission from ref.[203]© 2020 Royal Society of Chemistry.

Introduction

An emerging approach for realizing more complex morphologies for air filtration medium is based on the combination using bottom-up and top-down fiber strategies (**Figure 37**). Polymer microfiber / supramolecular nanofiber composite could be produced by immersing polymer microfiber nonwoven in solutions of BTA and subsequent drying (**Figure 37A**). During the evaporation of the solvent, the BTA assembles into supramolecular nanofibers that entangle with the polymer nonwoven, resulting in a mechanical stabile composite.[117] The filtration efficiency of these composite is dependent on the BTA used, the concentration and the solvent in which it is immersed.[117,118] Under optimized conditions a filtration efficiency of 95% for 0.2 µm particles and approximately 100% for 2.0 µm particles at an average pressure drop of 1529 Pa using a flow velocity of 25 cm s^{-1}.[118]

A similar approach was conducted with 1,3:2,4-di(3,4-dimethylbenzylidene) sorbitol as molecular building block, that formed a network of supramolecular nanofibers penetrating a polyacrylonitrile nonwoven (**Figure 37B**). This resulted in hierarchical dual-nanonets, that showed remarkable filtration efficiencies of 99.999 for $PM_{0.3}$ and a pressure drop of 32 Pa measured at flow velocities of 0.75 cm s^{-1}.[204]

Mesostructured nonwovens with a penguin downy feather-like morphology (**Figure 37C**), were realized by coaxial electrospinning, decorating the core polystyrene fiber with BTA seeds. These seeds can act as nucleation sites, when immersed and subsequently removed from a BTA solution leading to hierarchical superstructures with off-standing supramolecular nanofiber branches. The density of the nanofibers can be tailored by the concentration of the seeds and the concentration of the BTA dissolved in the immersion solution. Using optimized conditions, these mesostructured nonwoven exhibit a filter efficiency of 99.8%% for 0.3 µm particles and approximately 100% for 1.0 µm particles at an average pressure drop of 22 Pa using a flow velocity of 5 cm s^{-1}.[122]
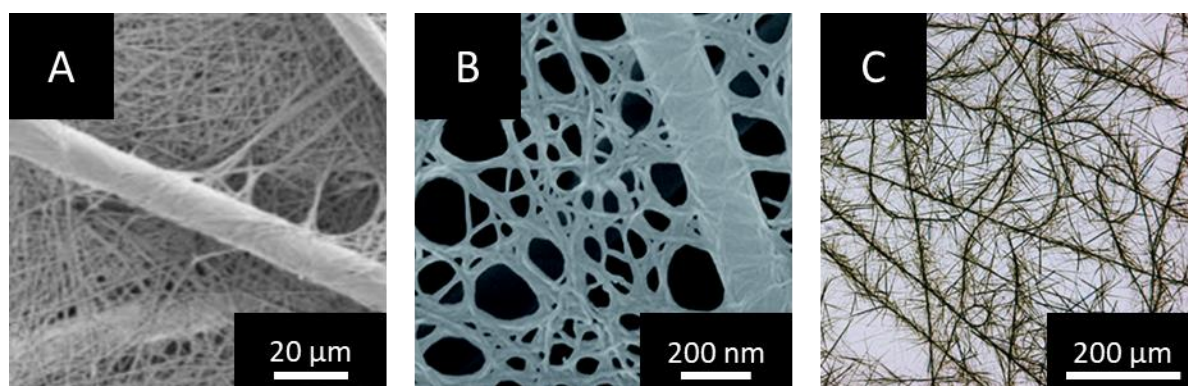
Figure 37. Complex morphologies for air filtration medium. A) SEM image of Polymer microfiber / supramolecular nanofiber composite. Adapted with permission of ref.[118]© 2016, American Chemical Society B) SEM image of hierarchical dual-nanonets. Adapted with permission of ref.[204]© 2021 Royal Society of Chemistry., C) Optical micrograph of a mesostructured nonwoven with a penguin downy feather-like morphology. Adapted with permission from ref.[122] © 2019 WILEY-VCH Verlag GmbH & Co. KGaA.

Although multi-structured polymer-based filters have resulted in very good filtration efficiencies and low pressure drops, this type of filter typically does not have sufficient thermal stability required for filtration at elevated temperatures, such as those found in typical industrial exhaust streams. Temperature-stable, mesostructured filters for air filtration at elevated temperatures therefore remain an open field of research in which innovative solutions are urgently needed.

1.3.3 Nanoparticle loading and catalysis

Metal nanoparticle

The history of gold nanoparticles (AuNPs) began as early as 1857 with FARADAY's work on colloidal gold, which he was able to produce by reducing tetrachloroauric(III) acid with phosphorus. Although analytical capabilities were severely limited at the time, the characteristic ruby red color of gold nanoparticles could already be observed at that time.[205] Since then, the research field of (gold) nanoparticles has expanded remarkably. On the one hand, this is due to the continuous technical progress that has advanced the characterization of NPs, which ultimately leads to a deeper understanding of NPs.[206–211] On the other hand, the field of research has become more attractive due to its promising potential in numerous application areas e.g. medicine[212–214] or (photo)catalysis.[215–217]

Metallic NPs typically have a size of 1-100 nm, which leads to a large surface-to-volume ratio. This results in a significant change in chemical and physical properties compared to the bulk material. Compared to bulk materials, where surface atoms make up only a small percentage of the total atom count, nanoparticles (NPs) have a much higher proportion of surface atoms. Due to their large curvature, the atoms in NPs exhibit a strong affinity for the surface, meaning nearly all of them are either close to or directly on it. Therefore, the coordination number decreases in NPs compared to the bulk material, which results in a higher reactivity.[218]

A further distinctive attribute of metal NPs is the phenomenon of localized surface plasmon resonance (LSPR). This occurs at a specific wavelength and is dependent on the dimensions, morphology, and local refractive index of the NPs in question.[219] LSPR is defined as the collective oscillation of electrons in metallic NPs caused by the electromagnetic interaction between the metal NPs and the incident light of a specific wavelength. The plasmon resonance model is based on the assumption that positively charged metal atoms are locally fixed and that free valence electrons can move around these metal atoms. In the event that the wavelength of the incident light is greater than the dimensions of the metal NPs, an interaction occurs between the electromagnetic field produced by the incident light and the free valence electrons. Depending on the metal, the LSPR features an absorption maximum at different wavelengths. This LSPR can change the optical appearance of a metal quite drastically. For instance, bulk gold with its characteristic metallic golden color, appears in the colloidal form as dark red to violet, due

to the LSPR the absorption maximum shifts from 520 to 570 nm for spherical particles with an increase in diameter from ~10 to ~100 nm (**Figure 38**).[220]
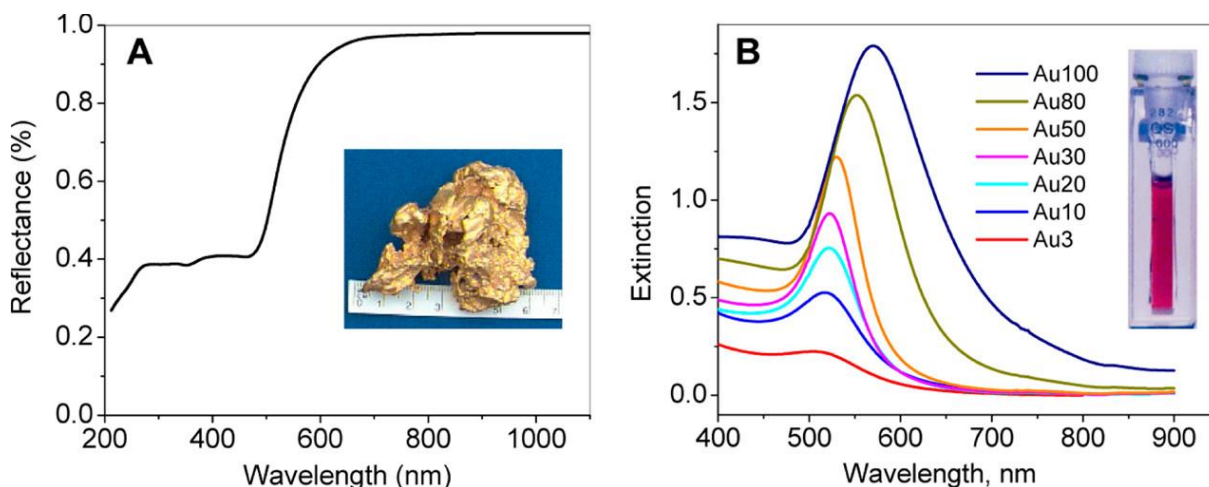
Figure 38. A) Optical reflectance spectrum of bulk gold. B) Optical extinction spectra of gold colloids (3–100-nm diameters, see legend). Inset: Photograph of 10-nm Au colloid. Reprinted with permission from ref.[220] © 2016 American Chemical Society.

In order to exploit the superior properties of AuNPs for possible applications, it is essential that the NPs do not agglomerate and form larger clusters. However, this is precisely what occurs with small NPs, which possess high surface energy and attempt to compensate for this by agglomerating. The theory that describes the agglomeration of NPs is the DLVO theory, named after DERJAGUIN, LANDAU, VERWEY, and OVERBEEK. This theory considers the balance between attractive van der Waals forces and repulsive electrostatic forces acting on colloidal particles.

By plotting the force acting on a particle—arising from van der Waals forces, electrostatic forces, as well as their sum—against the distance to a second particle, it becomes evident that attractive van der Waals forces dominate at short distances, whereas electrostatic forces prevail at longer distances (**Figure 39**). To avoid agglomeration of NPs strategies must be used that either strengthen the repulsive forces or reduce the attractive forces. Generally, van der Waals interactions can be decreased by increasing the size of the NP.
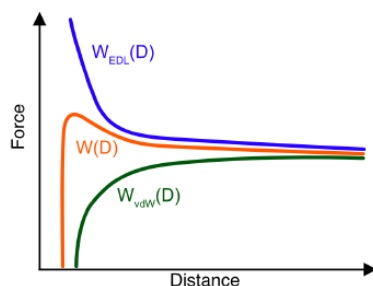
Figure 39. Schematic illustration of the force acting on a particle, i.e. attractive van der Waals forces (green), repulsive electrostatic forces (blue) and their sum, the resulting DLVO force (orange) against the distance to another particle.

These strategies must already be considered during the synthesis of AuNPs. With regard to the synthesis itself, there have been few changes compared to the methodology that FARADAY employed. In general, AuNPs are produced from a gold precursor (often $HAuCl_4$), a reducing agent, and a stabilizer to suppress agglomeration.[221] The two most commonly used methods for the production of stabilized AuNP are the TURKEVICH method and the BRUST-SCHIFFRIN method.[209] In the original TURKEVICH method, $HAuCl_4$ is boiled with sodium citrate, whereby the citrate is oxidized to the corresponding dicarboxyacetone. This then acts as a stabilizing ligand for the reduced Au^0.[222] In this case, the size of the AuNPs can be modified by adjusting the concentration of sodium citrate and the pH value.[223,224] Due to the limited reducing power of sodium citrate, the synthesis of AuNP can be optimized by adding the reducing agent $NaBH_4$. Another advantage is that the reaction can be carried out at room temperature, which enables the formation of AuNP with a smaller size than in the conventional TURKEVICH method.[225] The BRUST-SCHIFFRIN method is based on the observation, that AuNPs can be stabilized by sulfur containing ligands i.e. thiolates.[226,227] As reduction agent also $NaBH_4$ was used. In particular the BRUST-SCHIFFRIN method allows the functionalization/stabilization of AuNPs with disulfides,[228] xanthates,[229] and thioacetates,[230] which give rise to a lot of different surface modified AuNPs. Other AuNP ligands are oxygen (phenol and carboxyl groups),[231–233] nitrogen (amines)[234–236] or phosphorus (phosphine)[237,238] based and are typically introduced via ligand exchange reactions. In addition to small molecular ligands, polymers and macromolecules are becoming an important class of ligands to stabilize and functionalize AuNP, hence they feature various advantages, i.e. long-term stability, adjustability of the solubility, tunable surface density of brushes and processability.[239] There are two major strategies of decorating AuNPs with polymeric ligands, "grafting to" and "grafting from".[240,241] Latter uses a small molecular ligand, that has a polymerizable functional group, e.g. a vinyl group, where polymerization occurs after a

(radical) initiator is added.[242] In the "grafting to" approach a polymer, that has either stabilizing groups attached in the backbone, e.g. poly (vinylalcohol) or poly (vinylpyrrolidone),[243,244] or is end-capped with stabilizing groups, e.g. thiolate endcapped polymers.[240,245,246] Often these polymer-stabilized NP are produced via ligand exchange reactions in which small molecular ligands are exchanged for polymeric ligands, which is entropically triggered.

All the stabilization methods described above refer to AuNP dispersions. However, for catalytic reactions in particular, it is desirable to immobilize the nanoparticles on a heterogeneous support, which increases reusability. Silicon dioxide, aluminum oxide, MOFs, graphene or other forms of carbon, as well as various types and architectures of polymers have been used as carrier materials with different techniques.[247–251] In particular, polymer fibers are very popular as carrier materials due to their versatile functionality, straightforward processability and low cost. A commonly employed technique for immobilizing NPs onto a support material is known as the deposition method. In this approach, NPs are first synthesized separately and then immobilized by depositing them onto a support. The colloidal deposition process involves immersing the support in an aqueous or organic NP dispersion, followed by various purification steps such as centrifugation, filtration, or multiple washings.[252] The immobilization depends on electrostatic interactions and the possibility of forming chemical bonds between the NP surface and the functional groups of the support material, hence polymers with the earlier mentioned functional groups are ideal to immobilize AuNPs.[253–255] Polymers that do not intrinsically carry suitable functional groups to immobilize AuNPs, such as polystyrene, can be modified by surface modifications to overcome this issue.[256–260] In addition to covalent, polymeric fibers, metallic NPs can also be immobilized on non-covalent, supramolecular fibers. For example, the class of 1,3,5-benzene trisamides can be immobilized by selecting the appropriate peripheral substituent.[121,125,261–263]

Among the numerous applications of AuNPs, research was particularly focused on their use in catalysis.[216,264–266] AuNPs have been shown to catalyze an extensive range of diverse chemical transformations, including CO oxidation, alcohol oxidation, and nitroarene Reduction. This thesis will focus on the catalytic reduction of 4-nitrophenol (4-NP) to 4-aminophenol (4-AP), a reaction that has been extensively studied due to the toxicity and carcinogenicity of nitro compounds and the importance of amino products as precursors in the production of analgesic and

antipyretic drugs such as paracetamol. **Figure 40A** describes the reaction equation of the reduction of an aqueous 4-NP solution to 4-AP in the presence of NaBH$_4$ catalyzed by AuNPs. The reaction is particularly suitable as a model reaction to test the catalytic activity of catalyst systems due to the simple reaction control by in situ UV/Vis measurements. **Figure 40B** illustrates the typical absorption spectrum of the solution as a function of time. The peak at 400 nm is attributed to the 4-nitrophenolate, the concentration of which decreases with time, while a new peak emerges at 300 nm, the intensity of which increases with time. This peak can be assigned to the 4-aminophenolate. The reaction follows a first-order reaction so that the apparent rate constant K$_{app}$ can be determined via the slope of the linear correlation of ln(A/A$_0$) over time.
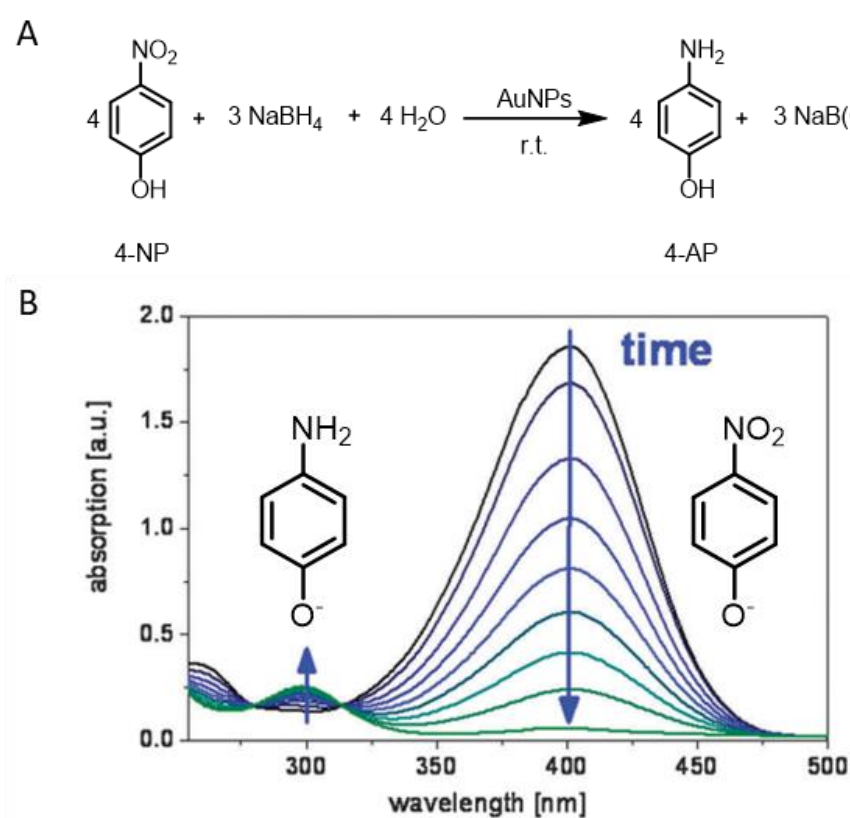

Figure 40. A) Reaction equation of the reduction of an aqueous 4-NP solution to 4-AP in the presence of NaBH$_4$ catalyzed by AuNPs B) Representative absorption spectra of the reaction solution as a function of time. The time between two consecutive curves is 2 minutes. Full conversion takes place in 20 minutes. The main peak at 400 nm (nitrophenolate ions) decreases as reaction time proceeds, whereas a second peak at 300 nm, referring to the product aminophenol, slowly increases (see arrows). Two isosbestic points are visible at 280 nm and 314 nm and indicate that only one product is formed during this reaction. Adapted with permission from.[265]© 2012 Royal Chemical Society.

The mechanism of the reduction of 4-NP is described by the Langmuir-Hinshelwood model, which is illustrated in **Figure 41.** The initial stage of the process involves the adsorption of the 4-NP and the borohydride ions onto the surface of the AuNP, coupled with the hydrolysis of the

NaBH₄. Given the relatively rapid progression of this process, the rate-determining step is the reduction of surface-bound 4-NP by surface-hydrogen species. The final step of the catalytic cycle, namely the desorption of the product 4-AP, is once again rapid and results in the regeneration of an active site.

The apparent rate constant is dependent on various factors including the size, shape, crystallinity, and the used ligand of the AuNPs. Furthermore, the reaction is dependent on more general reaction conditions, i.e. pH, temperature, and dissolved oxygen concentration.
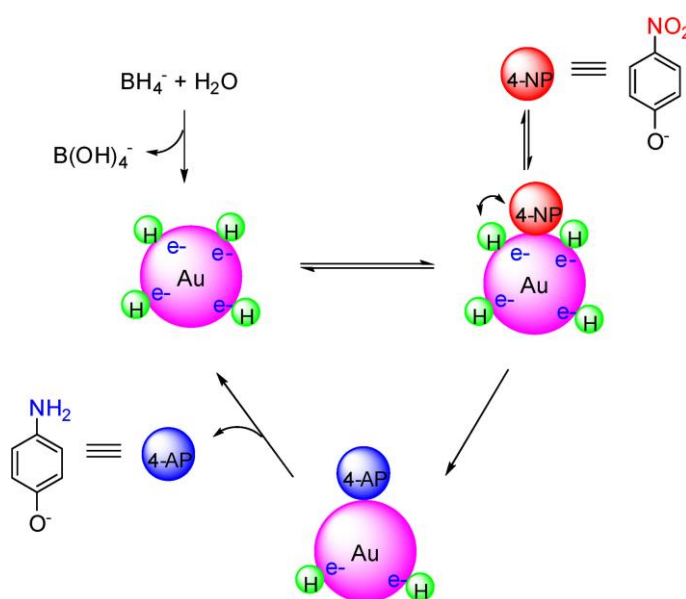
Figure 41. Mechanistic model of Langmuir–Hinshelwood mechanism for the reduction of 4-NP to 4-AP catalyzed by AuNPs in the presence of NaBH₄. Adapted with permission from Ref.[267] © 2015 Elsevier B.V.

Although many efforts have been made to optimize catalytic systems based on AuNPs, the development of new architectures that ensure good accessibility of the nanoparticles and prevent leaching of the NPs into the reaction solution is necessary, especially for AuNPs immobilized on support materials.

1.3.4 Photocatalysis

Photocatalytic degradation of organic pollutants

In addition to conventional metal-based catalysis, photocatalysis has emerged as a major field of research in recent decades. It aims to address some of humanity's greatest challenges, including the development of sustainable energy sources and ensuring access to fresh water for all. For the latter, it is essential to convert polluted water into clean water using environmentally friendly, inexpensive technologies. In the following chapter, the degradation of organic contaminants by the advanced oxidation process will be discussed, with a particular focus on the photocatalytic degradation of organic pollutants.

Advanced oxidation process (AOP)

AOPs are defined as those that involve the *in situ* generation of strong oxidants such as hydroxyl radicals, superoxide radicals, or photogenerated holes in sufficient quantities to decontaminate polluted water.[268,269] These strong oxidizing agents transform organic contaminants into environmentally friendly carbon dioxide, water and additionally, if heteroatoms are present, into the corresponding mineral acids e.g. hydrochloric acid, sulfuric acid or nitric acid.[270,271]

The various AOPs can be classified according to the trigger used to convert an oxidizing precursor into the oxidizing agent. Probably the longest known variant is the chemical AOP, which was introduced in 1894 by FENTON and his investigations on the degradation of tartaric acid by hydrogen peroxide in the presence of iron (II) salts.[272] Later mechanistic studies showed that FENTON reagents, as the iron is oxidized, lead to the release of hydroxyl radicals, which then oxidize and decompose the organic matter.[273,274] Even though FENTON's discovery was over 130 years ago, industrial wastewater is still treated using this process today.[275] Another chemical variant of AOP is peroxonation, in which ozone and hydrogen peroxide together form hydroxyl radicals.[276] Here the hydrogen peroxide supports the decomposition of ozone in the aqueous medium.[277]

The photochemical AOP represents an improvement because the conversion of the oxidizing precursor into the oxidizing agents can be significantly accelerated by using light as an additional trigger. The splitting of hydrogen peroxide homolytically into two hydroxy radicals can be achieved through the irradiation of the latter with ultraviolet light in the wavelength range of 200-300 nm.[278] However, due to the low absorption coefficient and the absorption maximum of hydrogen peroxide, a high concentration of hydrogen peroxide and very high energy light are

required for this process. One potential disadvantage of low absorption can be avoided by using ozone instead of hydrogen peroxide, as the absorption coefficient of ozone is approximately 200 times higher than that of hydrogen peroxide.[269,279] The classic FENTON process can also be improved by irradiation with UV light, where the additional trigger light leads to an accelerated conversion of hydrogen peroxides to hydroxy radicals.[280] In addition, irradiation with UV light offers the advantage that the iron (III) ions generated from iron (II) salts can be reduced back to its original form, which enables the catalytic use of iron salts instead of the stoichiometric use as is the case with the conventional FENTON process.[281,282] Despite all these improvements in photochemical AOPs, the need for high-intensity UV irradiation and the addition of oxidizing precursors such as hydrogen peroxide or ozone to polluted waters limit the AOP.

These disadvantages can be overcome by using a photocatalytic variant of the AOP. In this process, oxidizing species can be directly generated from water in the presence of a semiconductor that acts as a photocatalyst. Photocatalysis is defined as follows:

"Change in the rate of a chemical reaction or its initiation under the action of ultraviolet, visible or infrared radiation in the presence of a substance—the photocatalyst—that absorbs light and is involved in the chemical transformation of the reaction partners."[283]

The general mechanism for any heterogenous photocatalysis can be divided into four steps (**Figure 42**). i) Absorption/Excitation, ii) Energy Transport, iii) Reduction and Oxidation-Reactions (redox) and iv) Product formation/Catalyst recovery. The photocatalyst absorbs a photon with an energy larger than its band gap. This promotes an electron from a ground state to an excited state, which leads to the formation of an electron-hole pair, a so-called exciton. These excitons can either decay under radiation of light, decay over a non-radiative pathway or separate into free charges. Reactions only take place on or near surfaces, so the free charges have to be transferred within their diffusion limit to the surface. On the surface the electrons and holes respectively will be transferred to the substrates where a redox-reaction takes place and generates charged intermediates. The last step is the formation of the products by these charged intermediates.
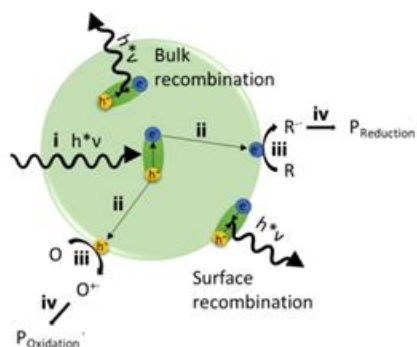
Figure 42. General photocatalytic steps for a particle including i) absorption/excitation, ii) charge transfer, iii) redox reaction and iv) product formation.

During photocatalytic AOP, superoxide radicals and hydroxyl radicals are predominantly involved as reactive oxidative species.[284] Superoxide radicals are generated by the reduction of oxygen dissolved in water, whereas hydroxyl radicals are formed by the oxidation of water with photogenerated holes h^+.[284] The necessary redox potentials of these reactions are shown in **Table 1**. In order to generate superoxide radicals from oxygen dissolved in water, the photocatalyst must have a sufficiently negative reduction potential. Specifically, the conduction band potential of the photocatalyst should be -0.16 V or more negative (compared to the standard hydrogen electrode, SHE).[285,286] This is the potential required at pH 7 to donate electrons to molecular oxygen and reduce it into the superoxide radical. On the other hand, a photocatalyst must have a strong positive oxidation potential to generate hydroxyl radicals from water. The generation of hydroxyl radicals requires that the oxidation potential of the photocatalyst is at least +2.32 V (relative to SHE).[285,286]

**Table 1.** The redox potentials for reactive oxygen species associated redox couples at pH=7.[285,286]

Half-reaction	Redox couple	Redox potential (E_0) [V]
$O_2 + e^- \rightarrow O_2^{\bullet-}$	$O_2/O_2^{\bullet-}$	-0.16
$H_2O + h^+ \rightarrow H^+ + \bullet OH$	$H_2O/\bullet OH$	2.32

Photocatalysts

To ensure efficient AOP, the photocatalysts used must have a number of properties. These include a suitable absorption spectrum, appropriate redox potentials, chemical and photostability, ease of processing, and scalable, low-cost quantities. For the absorption spectrum, it is desirable to absorb in the visible range so that resources and energy-saving light sources (such as the sun) can be used. In addition, it must meet the redox potentials for the generation of at

least one of the reactive oxygen species. Due to the harsh oxidative conditions during AOP, it is necessary that photocatalysts have sufficient chemical stability so that they do not self-destruct during the process. This is particularly challenging for organic photocatalysts. However, the photocatalytic efficiency is not only determined by the material properties, but also by the morphology of the photocatalyst. Basically, as already described in the definition of photocatalysis, the reaction only takes place at or near the surface of the photocatalyst, so it is desirable to increase the surface area of the catalysts using suitable processing techniques.

Figure 43 shows the redox potentials of common photocatalysts. It is notable that only TiO_2 and ZnO have a sufficiently positive redox potential to generate hydroxyl radicals directly from water. In contrast, organic photocatalysts in particular have a sufficient negative reduction potential to generate superoxide radicals from oxygen dissolved in water.
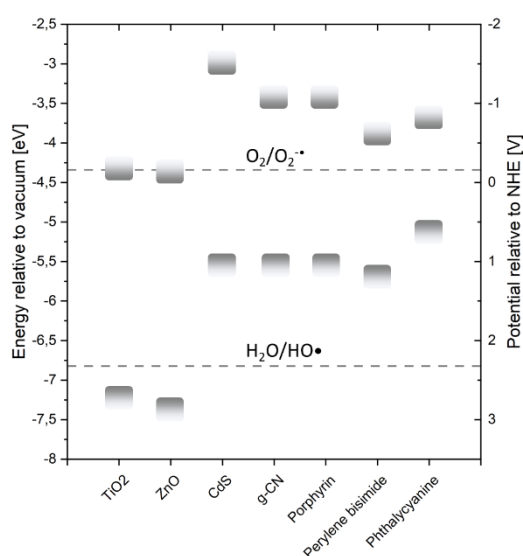
Figure 43. Redox potentials of represantitive inorganic semiconductor (TiO2, ZnO, CdS) and organic semiconductors (porphyrin, perylene bisimide, Phthalcyanine). The dotted vertical lines indicate the redox potential of $O_2/O_2^{-\bullet}$ and $H_2O/HO\bullet$.

Examples of inorganic photocatalysts that are widely used in the literature are mainly metal oxides or sulfides.[287,288] For example, TiO_2 or ZnO, which can generate both hydroxyl radicals and superoxide radicals due to their high band gap, are suitable, but the band gap also limits the usable light to high-energy UV radiation, as a reference only 5% of the sun irradiation is in the UV range.[289–291] Furthermore, both materials are inexpensive and are characterized by high chemical and photostability.[292,293] In addition, there are enough processing techniques that

allow specific shapes and dimensions for the photocatalyst, such as the sol-gel technique,[294,295] hydrothermal growth,[296,297] or spray pyrolysis technique.[298,299]
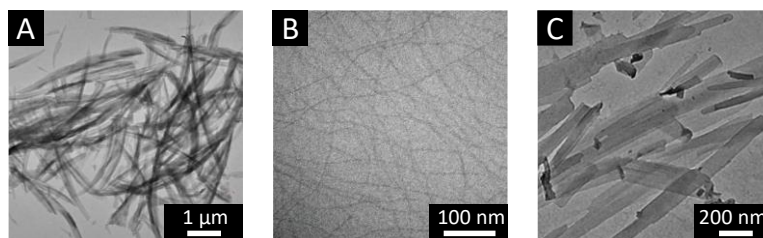
Organic photocatalysts

Inorganic photocatalysts often have large band gaps, which requires the use of UV light. One advantage that organic photocatalysts offer is that their molecular design can be adapted so that their absorption spectrum can absorb a large proportion of the light emitted by the sun. Especially heptazine based materials such as graphitic carbon nitrides (g-CN),[300–304] porphyrins,[305–307] perylene bisimides,[308–312] phthalocyanines,[313–315] ullazines,[316] and quinacridone[317] (**Figure 44**) are of interest due to their broad absorption in the visible light range as well as the high stability these chromophores show against harsh oxidative conditions during AOP.

heptazine   porphyrin   perylene bisimide   phthalocyanine   ullazine   quinacridone
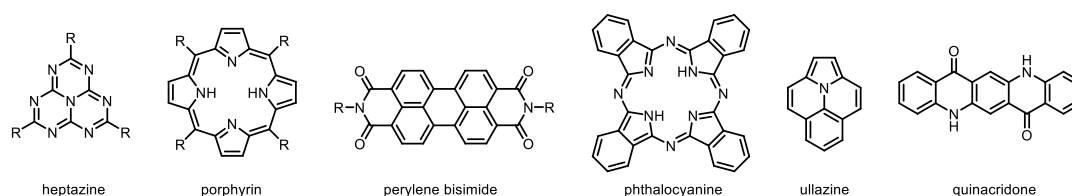
Figure 44. Molecular structures of prominent chromophores found in organic photocatalysts that absorb in the range of visible light.

These photocatalysts can be self-assembled via supramolecular chemistry, in particular by exploiting hydrogen bonding or π-π stacking, to 1D nanostructures i.e. nanofibers, nanorods or nanobelts (**Figure 45**). These nanoobjects feature a high surface area, which is beneficial for adsorption of organic pollutants to the photocatalyst. In addition, organic chemistry, allows for introduction of peripheral substituents that either promote self-assembly or to modify the electronic structure of the photocatalyst and thus promoting charge-separation to enhance the photocatalytic performance.[310]

Figure 45. TEM images of supramolecular photocatalysts based on A) perylene bisimides, adapted with permission of ref.[309] © 2016 WILEY-VCH Verlag GmbH & Co. KGaA, B) ullazines, adapted with permission of ref.[316] © 2022, American Chemical Society and C) quinacridone, adapted with permission of ref.[317] © 2020 Royal Chemical Society.
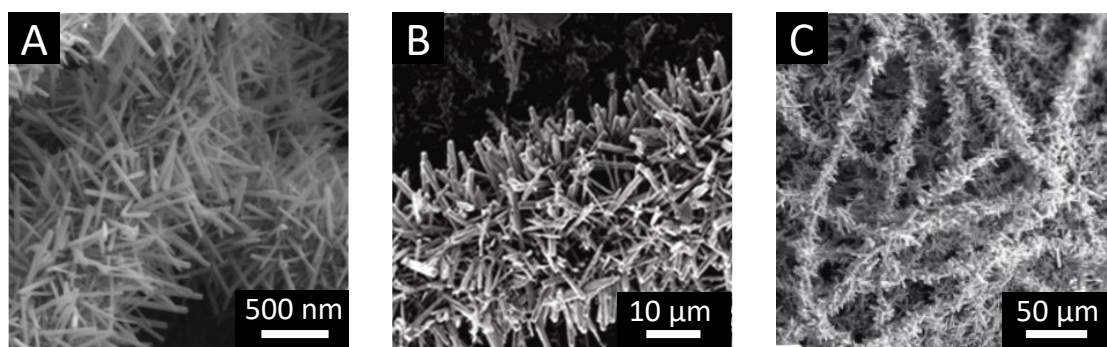
Immobilized photocatalysts

In all the examples mentioned so far, the photocatalysts were used in the form of low-dimensional geometries, i.e. 0D quantum dots, nanoparticles or noble metal atoms, 1D nanotubes, nanorods or nanowires, or 2D nanofilms or nanowires, which were dispersed in polluted water and then illuminated. This has the advantage that the photocatalysts have a large surface area due to their size in the nanometer range. However, these dispersions have the problem that they are not stable and the photocatalysts agglomerate and thus lose their high surface area and consequently their catalytic reactivity.[318] Furthermore, the separation/recovery of the photocatalyst is tedious or energy intensive due to the size of the photocatalyst.[318]

These disadvantages can be avoided by immobilizing the photocatalysts on a macroscopic support material.[319] In addition to preventing agglomeration of the photocatalyst and easy separation/recovery from the water,[320,321] other synergistic effects, such as the support material adsorbing pollutants, can lead to an increased concentration of pollutants in the near vicinity of the photocatalysts, thus accelerating degradation.[322,323] Furthermore, the surface polarity can be controlled by selecting the appropriate support material, thereby tailoring the selective adsorption of organic pollutants.[324–326] Additionally, the choice of support material can influence the electronic environment of the photocatalyst. For example, a highly conductive support can facilitate the rapid separation of photogenerated electron-hole pairs while slowing their recombination, thereby enhancing photodegradation efficiency.[327,328]

Among macroscopic support materials, fibrous materials are of particular interest, due to the fact that the mechanical properties of the support material can be controlled by the choice of material. Organic polymer fibers can be designed to have a flexible character, whereas inorganic fibers such as glass or steel fibers are inherently very stiff.[329,330] Particular glass fibers can be stably present in the harsh oxidative environment during the AOP, further are glass fibers permeable for light.[330,331] In addition, fibrous materials provide high aspect ratio, which ensures that more photocatalyst can be immobilized on the support surface; thus, more active sites are provided for photocatalytic reaction.[327,332] Furthermore, the production methods of fibers are very well established, which makes the production of fibers very inexpensive and scalable.

The photocatalysts can be immobilized using different techniques such as dip-coating,[326,333,334] chemical vapor deposition,[331,335,336] or hydrothermal techniques.[330,337,338] By cleverly selecting the processing methods, it is possible not only to immobilize the photocatalyst on the macro-

scopic support, but also to create a mesostructured architecture and thus a hierarchical super-structure, which, for example, has additional properties such as an increased surface area. In **Figure 46** SEM images of hierarchical superstructures that were used as photocatalyst in AOP are depicted. Here, ZnO nanofibers, -wires and -rods were radially grown from either inorganic glass fibers or organic electrospun fibers via a hydrothermal method.[330,337,338] Creating hierarchical superstructures based on organic photocatalysts remains an ongoing challenge and is desirable to generate novel, efficient heterogenous photocatalysts for photocatalytic degradation of organic pollutants.

Figure 46. SEM images of immobilized photocatalyst on a macroscopic fibrous support rendering a hierarchical superstructure. A) ZnO nanofibers prepared via hydrothermal method on electrospun polyacrylonitrile fibers, adapted with permission from ref.[338] © 2014 Elsevier B.V., B) ZnO nanorods prepared via hydrothermal method on glass fibers, adapted with permission from ref.[337] © 2010 The American Ceramic Society, and C) radially grown ZnO nanowires on flexible polylactide fibers.[337] Adapted from ref.[330] under a Creative Common CC – BY license

2 Aim of this thesis

Mesostructured superstructures particularly based on woven or nonwoven fabrics with defined supramolecular nanofibers have great potential to be used in wide range of applications due to their high aspect ratio including filtration to catalysis. However, the preparation of superstructures, which enables full control over all dimensions of the supramolecular nanofibers remain a challenge. Moreover, this work aims to focus on a solvent-free straightforward process to produce superstructures with defined nanofibers by physical vapor deposition (PVD) in contrast to typical solution-based self-assembly procedures. This thesis aims to address these challenges in four parts.

The *first part* will deal with the development of a *solvent-free process to prepare supramolecular nanofibers via PVD*. A first requirement to be used in PVD is the ability of the material to vaporize without thermal decomposition. In particular, selected BTAs, which are known to sublime and have the capability to nucleate iPP, shall be investigated. The morphology of the deposited BTAs will be investigated using scanning electron microscopy. The influence of the process parameters, i.e. substrate temperature, evaporation time, and evaporation rate on the fiber morphology will be comprehensively studied on solid substrates for the most promising BTA. After establishing the optimal PVD conditions, the *preparation of mesostructured nonwoven* will be realized using a fibrous support. Here a distinct glass fiber (GF) nonwoven will be selected, which can also be used as reinforcement material for polymers. Since the BTAs are selected in a way that the supramolecular BTA nanofibers can also act as nucleating agents for iPP, this will allow one to study the *nucleation potential of the mesostructured nonwovens* for iPP. Finally, this shall lead to an improved adhesion between the GF structures and the iPP and influence the mechanical properties of the final composite.

The *second part* of this thesis aims to prepare *mesostructured polymer nonwovens* decorated with defined supramolecular BTA nanofibers for the *potential use in air filtration applications*. Here, a model polymer nonwoven, which was already recently used in our group will be selected allowing a comparison with previous results. The preparation of superstructures with supramolecular nanofibers shall be performed by PVD and characterized by electron microscopy. The influence of the length of decorated supramolecular nanofibers shall be investigated with respect to filtration characteristics. For this a filter test rig and ISO fine test dust as particulate matter will be used to determine filtration efficiency and pressure drop. An intriguing aspect of

BTAs is the relatively high thermal stability. This opens the way to fabricate more *temperature resistant superstructures* to be used at temperatures, which cannot be realized based on commodity and engineering polymers. For this purpose, the polymer nonwovens will be replaced by thermally stable glass fiber nonwovens. Here the aim is to investigate how the decoration with supramolecular nanofibers in *mesostructured glass fiber nonwovens* will improve the filtration performance. After preparation of such mesostructured glass fiber nonwovens with defined supramolecular BTA nanofibers by PVD process, filtration characteristics and temperature resistance shall be investigated.

The *third part* of this thesis will deal with the preparation and use of *mesostructured superstructures*, which provides additional functionality in the periphery of the BTA nanofibers. The functional BTA nanofibers prepared by PVD shall be able to *immobilize gold nanoparticles (AuNPs)* and the so-formed AuNP-decorated superstructures shall be acting as heterogeneous catalyst. For this, a BTA with peripheral tertiary amino groups will be selected as a functional building block. A single-layer polyamide fabric will be used to produce a highly porous superstructure, which can be easily permeated by solutions. After determination of all parameters for superstructure formation by PVD and the characterization with electron microscopy, AuNPs will be prepared and immobilized on the superstructures from aqueous solutions. Ultimately, the potential of the *AuNP-loaded superstructures as supported heterogenous catalysis* will be assessed and evaluated in aqueous solutions using standard model reactions for catalysis. This also includes catalytic performance, stability and reusability of the AuNP-loaded mesostructured woven.

The *fourth part* of this thesis will deal with the preparation and use of *mesostructured superstructures*, in which the supramolecular nanofibers themselves act as *heterogeneous photocatalysts*. In contrast to the chapter above, this requires a photocatalytically active building block. For this, tricycloquinazoline (TCQ), which is a heterocyclic discotic aromatic molecule, will be selected as a building block due to its high chemical stability and visible light absorption. After synthesis and molecular characterization by common analytical techniques, suitable processing conditions for PVD will be established to enable the formation of supramolecular nanofibers during evaporation. Mesostructured superstructures based on suitable glass fiber nonwovens and supramolecular TCQ nanofibers will be prepared, and their morphology and optical properties will be characterized. Additionally, these mesostructured nonwovens will be

tested to determine whether they can withstand the harsh conditions encountered during irradiation. Ultimately, the application of these *mesostructured nonwovens as heterogeneous photocatalysts in the photocatalytic degradation* of two model compounds including the dye Rhodamine B and the antibiotic Tetracycline will be demonstrated, both in batch and under continuous flow conditions. The degradation mechanism of the pollutants, the reusability of the photocatalyst, and its leaching behavior will be evaluated.

3 Synopsis

3.1 Overview of the thesis

Porous mesostructured superstructures, which are based on woven or nonwoven support structures on which supramolecular nanofibers with a high aspect ratio are firmly attached have great potential to be used in wide range of applications including filtration to catalysis. However, the precise preparation of supramolecular nanofibers leading to defined and tailored superstructures remains a challenge. To achieve full control over all dimensions of supramolecular nanofibers, this thesis focusses on evaporable molecular building blocks, which can be processed by physical vapor deposition (PVD). Beneficially, PVD is a solvent-free straightforward process comprising a continuous and controllable building block feed for structure formation, which is in contrast to typical solution-based self-assembly procedures.

The main results of this thesis have been documented in four manuscripts, all of them are published in peer-reviewed journals.

A general overview of the thesis is shown in **Figure 47**. The central theme of this thesis is to make use of vapor deposition of molecular building blocks to form defined mesostructured superstructures. Both the molecular building blocks as well as the woven or nonwoven support structures were carefully selected in view of their proposed application. Thus, the first part deals with the preparation of supramolecular nanofibers by PVD based on a series of distinct benzenetrisamides (BTAs), which can also act as nucleating agents for the commodity polymer iPP. As support, a glass fiber nonwoven was selected with can be used to reinforce iPP. Such glass fiber / BTA fiber superstructures can locally induce iPP crystallization when deposited in an iPP melt improving the adhesion between matrix and superstructure. In the second part, we aim to transfer the findings realizing superstructures by depositing BTA nanofibers on polymer model nonwovens or glass fiber nonwovens, which can be used for air filtration applications. In particular the combination of the selected BTA with glass fibers allows to prepare mesostructured superstructures to be used for air filtration at elevated temperatures, which cannot be realized with commodity polymers for filtration applications. Differently to part one and two, part three makes use of a functional BTA comprising peripheral tertiary amino groups. After superstructure formation by PVD, this allows for the selective immobilization of AuNPs on the BTA nanofibers, which can be subsequently used as reuseable composite for catalytic reactions. Finally, the fourth part aims to realize superstructures suitable for photocatalytic reactions. For

this, tricycloquinazoline (TCQ), a heterocyclic discotic aromatic molecule, was selected to be used as photocatalytically active building block. Stable mesostructured superstructures, using a suitable glass fiber nonwoven, allow for the degradation of organic pollutants under continuous flow conditions.
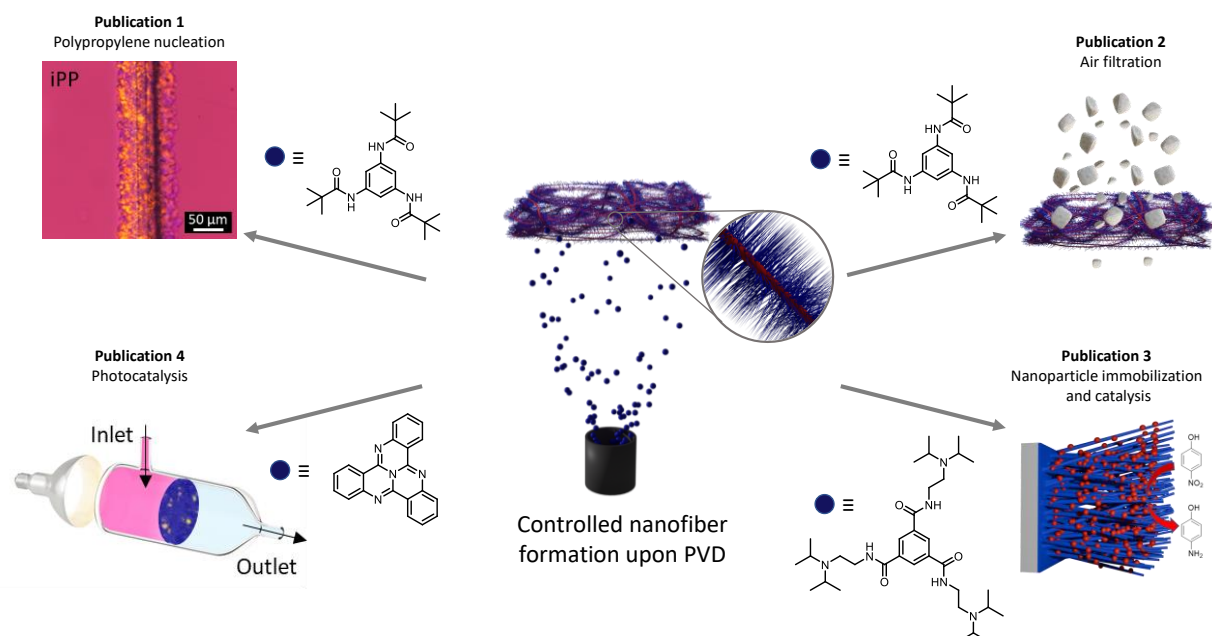
Figure 47. Overview of this thesis to prepare and make use of mesostructured superstructures for different applications. The central theme comprises the development of a PVD process using distinct molecular building blocks (blue circle) resulting in supramolecular nanofiber formation in a controlled manner. By rationally selecting the building block the application of these mesostructured materials can be tailored. In the first part several nonpolar BTAs were comprehensively studied and the preparation of mesostructured materials that can be used to nucleate iPP is demonstrated. In the second part the potential of such mesostructured materials is demonstrated as air filtration medium. The third part makes use of functional BTA building block. Those nanofibers on woven are able to immobilize gold nanoparticle, which ultimately acts as heterogenous catalyst. The fourth part introduces tricycloquinazoline (TCQ) as photocatalytically active building block, which allows the preparation of mesostructured materials to be used for the degradation of organic pollutants under continuous flow condition.

3.2 Hierarchical glass fiber superstructures with supramolecular nanofibers for the nucleation of isotactic polypropylene

The *first publication* deals with a comprehensive study using a solvent-free process, i.e. PVD, to prepare mesostructured superstructures based on a nonwoven support and supramolecular nanofibers based on 1,3,5-benzenetrisamides (BTAs). In general, BTAs are a well-known class of materials suitable to self-assemble in nanofibers from solutions. For this study, six different BTAs with cycloaliphatic and branched peripheral substituents were selected as molecular building blocks, which are known to sublime without decomposition (**Figure 48**). These BTAs are also known to act as nucleating agents for isotactic polypropylene (iPP). To study the influence of the molecular structure on the formation of supramolecular nanofibers on flat substrates by PVD, the same set of conditions were chosen for all six BTAs. This includes a substrate temperature (T_{sub}) of 25°C of the used silicon substrate, an evaporation time of 30 min and an evaporation rate of 1.4 µg s^{-1}. To achieve a constant evaporation rate of 1.4 µg s^{-1}, the source temperature (T_{source}) was set individually to 315 °C for BTA 1, 270 °C for BTA 2, 245 °C for BTA 3, 235 °C for BTA 4, 230 °C for BTA 5 and 230 °C for BTA 6.
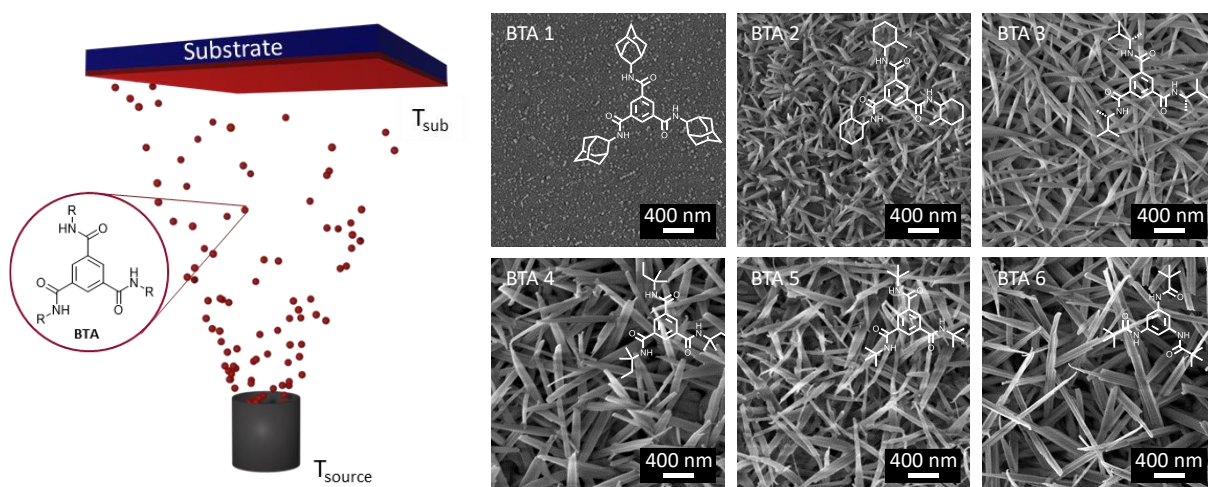
Figure 48. Left: Schematic illustration of the physical vapor deposition of benzenetrisamides (BTA). The vapor deposition depends on the physical and thermal properties of the BTA and can be controlled by the source temperature (T_{source}) and the temperature of the substrate (T_{sub}). For a general and comprehensive study, various flat substrates were used. To prepare mesostructured superstructures suitable for applications, glass fiber substrates were used. Right: SEM images of six different BTA 1-6, with cycloaliphatic and branched peripheral substituents that were investigated on flat substrates in view of the formation of supramolecular nanofibers. PVD conditions: The evaporation rate was 1.4 µg/s which was obtained by adjusting the source temperature for BTA 1 to T_{source} = 315 °C, for BTA 2 to T_{source} = 270 °C, for BTA 3 to T_{source} = 245 °C for BTA 4 to T_{source} = 235 °C for BTA 5 to T_{source} = 230 °C and for BTA 6 to T_{source} = 230 °C with an evaporation time of 30 min for all BTAs on a flat silicon substrate at 25°C T_{sub}. Adapted from Ref.[I] under a Creative Commons CC – BY license.

Scanning electron microscopy (SEM) investigations, as depicted in **Figure 48,** reveal that the capability to form supramolecular nanofibers increases with decreasing steric demand of the peripheral substituent. To systematically investigate the influence of different process parameters, namely substrate temperature, evaporation time and rate, BTA 6 was chosen as the representative BTA.

It was found that the substrate temperature influences the balance between adsorption and desorption of the molecules, which in turn influences the nanofiber formation and their morphology. Experiments with three substrate temperatures (25°C, 50°C, 100°C) on silicon wafers show that at 25°C dense nanofibers with a uniform distribution and a fiber thickness of 204 nm are formed. At 50°C, the number of nanofibers decreases and are more unevenly distributed. At the same time, they become thicker (300 nm). This indicates that the overall number of nuclei is decreased. At 100°C, the fiber formation is strongly hindered on the substrate and only a thin wetting layer is overserved. This is attributed to a shift in the equilibrium towards desorption after layer formation at higher temperatures. Therefore, for all further experiments the substrate temperature was set to 25°C.

By using combinatorial experiments, different sectors that differ in vapor deposition time could be produced on the same substrate. It is assumed, that the nanofiber formation follows a STRANSKI-KRASTANOW-growth, where in this case a critical layer height of around 200 nm must be present before supramolecular nanofiber growth can continuously proceed in a linear fashion with around 0.1 µm/min. This knowledge allows for straightforward length control representing a major advantage over solution-based self-assembly methods. Similarly, it was found that the evaporation rate, which can be adjusted by the source temperature, controls the nanofiber growth in a linear fashion.

The demonstrated length control of BTA nanofibers using PVD, encouraged us to produce and investigate hierarchical superstructures, by replacing flat substrates with glass fiber nonwoven as substrate material (**Figure 49**). The molecular building block and the PVD parameters were kept identical: BTA 6 was evaporated at a rate of 1.4 µg/s on the nonwoven at substrate temperature of 25°C. Using a combinatorial approach different sectors on the glass fiber nonwoven were created that differ in the evaporation time, i.e. 15 min, 30 min and 45 min. The SEM images of a neat glass fiber nonwoven and the superstructures are depicted in **Figure 49**. A homogeneous coverage with supramolecular nanofibers on the glass fibers was found with increasing

fiber density and length depending on the evaporation time. Thus, fiber growth and morphology develop in a similar manner as found for flat substrates, resembling a bottlebrush morphology. The average superstructure diameter (dashed lines) are found to be 13 μm (for 15 min), 19 μm (for 30 min) and 24 μm (for 45 min evaporation time). Considering an average diameter of 10 μm for a neat glass nanofiber (solid lines), the supramolecular nanofiber length is around 1.5 μm, 4.5 μm, and 7 μm for the respective evaporation time.
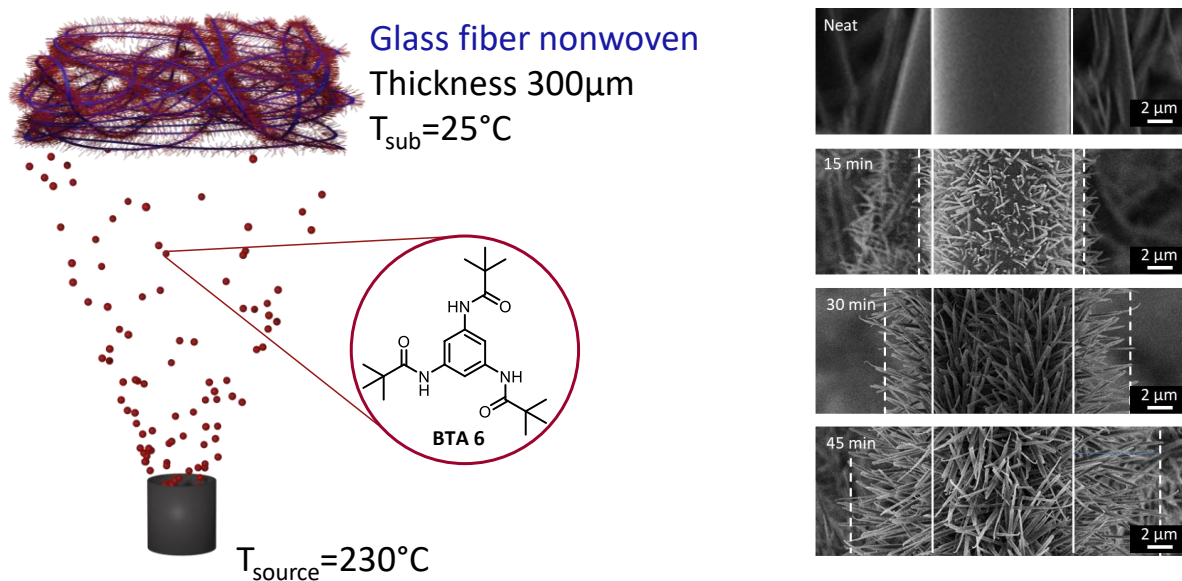

Figure 49. Schematic illustration of the controlled superstructure formation on glass fiber nonwoven (blue) with supramolecular nanofibers of BTA 6 (red) using a evaporation rate of 1.4 μg s⁻¹, a T_{sub} of 25°C and a T_{source} of 230°C. SEM images of the neat glass fiber nonwoven and hierarchical superstructures prepared via PVD of BTA 6 on the glass fiber nonwoven at different evaporation times of 15, 30, and 45 min (T_{sub} = 25 °C, evaporation rate = 1.4 μg s⁻¹). The white solid lines indicate the glass fiber diameter and the white dashed lines diameter of the bottlebrush structure including the supramolecular nanofibers. Adapted from Ref.[I] under a Creative Commons CC – BY license.

Supramolecular nanofibers of BTA 6 are known to efficiently nucleate iPP due to the epitaxial match between the crystal lattice of BTA 6 and of iPP. Powder X-ray diffraction measurements revealed that the supramolecular nanofibers prepared via PVD, exhibit the same crystallographic features as previously reported. Similarly, nanofibers scratched off from substrates after PVD and placed on top of an iPP melt provide clear evidence of trans-crystallization around the supramolecular nanofibers as the iPP melt cools at 135°C. This demonstrates that PVD-processed nanofibers exhibit the same nucleation performance as the conventional BTA nucleating agent. Based on these findings, we were interested in the investigation of nucleation capability of the BTA nanofibers present on the glass fibers with bottlebrush morphology when placed on an iPP melt. For this, a single hierarchically structured fiber was removed from the decorated

nonwoven studied using polarized microscopy. A single neat glass fiber was used as reference (**Figure 50**). As observed before, the BTA nanofibers clearly induce trans-crystallization of iPP at 134 °C, which proceeds upon further cooling in a direction perpendicular to the glass fiber featuring a dense fine-grained crystalline layer iPP of about 20 µm. At temperatures below 128°C homogenous nucleation leading to large spherulites of the iPP matrix takes place. These findings are very interesting and demonstrate a locally induced and limited nucleation suggesting an improved adhesion of the glass fiber to the iPP matrix due to the trans-crystallization, which is not the case in the reference experiment, in which only randomly formed iPP spherulites can be observed.

Based on these encouraging findings, we prepared a hierarchical superstructure with a bottle-brush morphology comprising 10 wt% BTA. Such a hierarchical superstructure was then laminated between two thin sheets of iPP by compression molding resulting in a glass fiber reinforced composite material containing about 3 wt% of glass fibers. For reference, a neat glass fiber nonwoven without the supramolecular nanofibers was laminated between two iPP sheets using the same conditions as well as the same amount of the glass fiber nonwoven. Dog bone specimens from all samples were used for mechanical testing, i.e. tensile tests. It was found that the reinforced iPP with the neat glass fiber nonwoven had an E-Modulus of 1264 ± 92 MPa and an ultimate strength of 33.0 ±2.1 MPa. The E-Modulus of the composite with the hierarchical superstructure was determined to be 1609 ± 128 MPa and the ultimate strength was determined to be 37.0 ± 1.2 MPa. These findings clearly confirm, that the supramolecular nanofibers play a beneficial role for the mechanical properties by improving the adhesion from the glass fibers to the iPP matrix due to tailored heterogeneous nucleation of iPP.

In conclusion, a robust PVD process was introduced to decorate surfaces with supramolecular nanofibers based on BTAs. Using GF nonwovens as a substrate enabled the creation of hierarchical bottlebrush-like superstructures with defined nanofiber lengths. These superstructures effectively nucleate iPP, promote trans-crystallization from the decorated glass fibers and enhance GF/iPP composite adhesion, which is reflected in improved mechanical properties. These results highlight that PVD is a viable method for producing fiber-decorated superstructures, which can be extended to other nucleating agents and semi-crystalline polymers to improve composite performance.
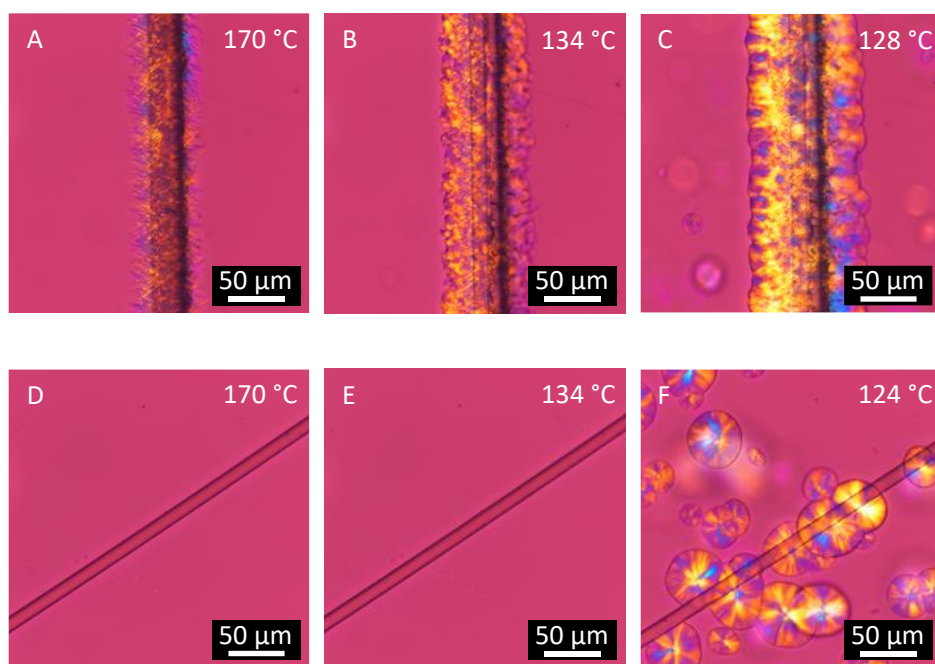
Reference experiment

Figure 50. Polarized optical micrographs of a glass fiber decorated with supramolecular nanofibers of BTA 6 prepared via PVD and placed into the melt of iPP at 170°C (A). Trans-crystallization of iPP nucleated form supramolecular nanofibers of BTA 6 starts at 134°C after cooling it with a cooling rate of 5°C/min (B&C). Melt of iPP with a neat glass fiber without any BTA at 170°C (D). Linear cooling with 5K/min, does not lead to a crystallization of PP at 134 °C (E), only further cooling to 124°C triggers the nucleation of large spherulites, indicating that the neat glass fiber does not act as nucleation side (F). All photographs taken with λ/4 plate. Adapted from Ref.[I] under a Creative Commons CC – BY license.

3.3 Mesostructured polymer and glass microfiber nonwovens with supramolecular 1,3,5-benzenetrisamide nanofibers for air filtration

Based on the findings of the first publication, the *second publication* deals with mesostructured superstructures based on either polymer or glass fiber nonwovens and supramolecular nanofibers of BTA 6 prepared via PVD, which can be used for air filter applications. An ideal filter medium should combine two major characteristics: This includes outstanding filtration efficiency while at the same time the pressure drop, being present due to the drag, should be as low as possible. With the approach used in this thesis, we aim to make use of supramolecular nanofibers to increase filtration efficiency and to control the nanofiber length to reduce drag by avoiding excessively covering pores present in the microfiber support structures. To demonstrate this proof of concept, hierarchical superstructures were prepared by using a polymer nonwoven, which were decorated with supramolecular nanofibers of BTA 6 by PVD. To study the performance systematically, different amounts of BTA ranging from 2, 5 to 10 wt% were used (**Figure 51**). The overview SEM images reveal that the polyester nonwoven is completely and homogeneously covered with supramolecular BTA nanofibers. At larger magnifications it can be observed that the nanofibers grow perpendicularly away from the substrate material, resembling a bottlebrush morphology as shown before. The average length of the supramolecular BTA fibers were determined to be 3.3±1.7 µm, 12±4.1 µm, and 20±3.4 µm for the hierarchical superstructures containing 2 wt%, 5 wt%, and 10 wt% of BTA, respectively. To ensure a homogenous coverage of both sides, the nonwovens were flipped after the first half of the evaporation time.
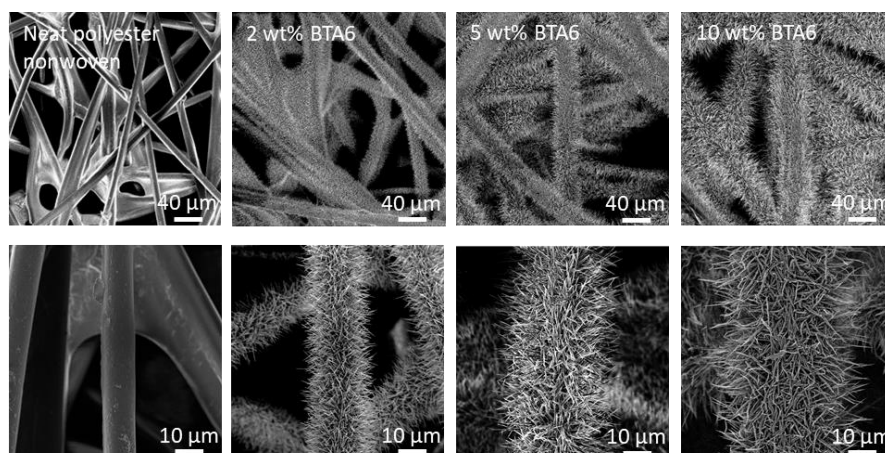
Figure 51. Comparison of SEM images overview (top row) and magnification (bottom row) of neat polyester nonwoven and mesostructured polyester nonwoven with 2 wt%, 5 wt%, and 10 wt% BTA 6. Adapted with permission from Ref.[II] © 2025, American Chemical Society.

Synopsis

Prior to filtration experiments a stability test of the filter was conducted, by applying an air flow of 0,25 m s^{-1} for 24 h. A particle analyzer did not observe any leakage or detachment of nanofibers from the filter. Additional SEM investigation before and after the stability test showed no significant change in morphology. For the filtration tests, ISO fin test dust was used as aerosol a to investigate the filtration efficiency of the hierarchical superstructures. While the neat polymer nonwoven as reference does only separate particulate matter of sizes in the range of 0.2-1.0 μm size to 5 %, the superstructure feature improved filtration efficiencies. The higher the mass fraction of supramolecular nanofibers, the better is the filtration efficiency of the specimens: In this study, filtration efficiencies of up to 87 % for 2.0 μm sized aerosol particles were achieved with the superstructure containing 10 wt% of supramolecular nanofibers (**Figure 52**). Further enhancing the filtration efficiency was achieved by using stacks of the three mesostructured superstructures leading to filter efficiencies of up to 98% for 2 μm sized particles while still a low pressure drop was maintained.
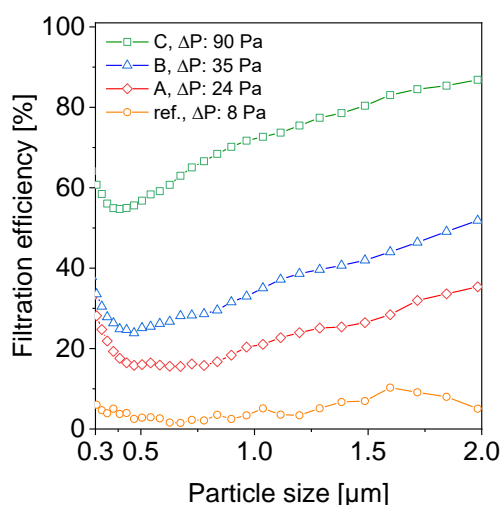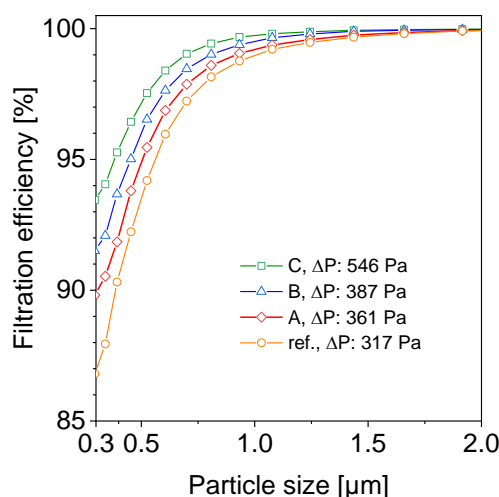

Figure 52. Filtration efficiencies of A) a mesostructured nonwoven with 2 wt.% of BTA (red diamond) exhibiting a pressure drop of 24 Pa, B) a mesostructured nonwoven with 5 wt% of BTA (blue triangle) with a pressure drop of 35 Pa, C) a mesostructured nonwoven with 10 wt% of BTA (green square) showing a pressure drop of 90 Pa. A neat nonwoven (yellow circle) was used as reference (Ref.) exhibiting a pressure drop of 8 Pa. Testing conditions: measuring time = 30 s; flow velocity = 0.25 m s^{-1}; filtration area = 28.3 cm^2, test aerosol = ISO fine test dust, upstream aerosol concentration = 30.000 particles cm^{-3}. Adapted with permission from Ref.[II] © 2025, American Chemical Society.

Since BTA 6 is known to feature a high thermal stability, this renders the use of supramolecular nanofibers based on BTA 6, as a promising candidate to realize mesostructured nonwovens which are suitable to be used for filtration applications at elevated temperatures. Since commodity polymers or engineering plastics are not suited to be used at temperatures of about

200°C, distinct glass fiber nonwovens were used to replace the polymer nonwoven and to prepare hierarchical superstructures via PVD. For the preparation, the same conditions were used as evaluated before, resulting in the same absolute amount of BTA deposited on the glass fiber. Since glass fibers exhibit a higher density than polymers, the relative amount of BTA decreased to 0.9, 1.9 and 3.3 wt%. SEM investigations of the glass fiber superstructures reveal the same bottlebrush morphology as found for the polymer analogues.

Filtration experiments show that with the BTA superstructure, the filtration efficiency of the glass fiber filter media can be improved, in particular in the region of particulate matter below 1 µm. Decoration of the glass fiber nonwoven with BTA nanofibers increase the filtration efficiency to about 99% for 1 µm sized particles and to 93% for 0.3 µm sized particles (**Figure 53**). The pressure drops were determined to be 317 Pa, 361, to 387 Pa, to 546 Pa, for neat, 0.9 wt%, 1.8 wt%, and 3.3 wt% glass fiber nonwoven, respectively.


Figure 53. Filtration efficiencies in the range of 0.3-2.0 µm of particulate matter of mesostructured glass nonwovens with A) 0.9 wt% of BTA (red triangle) with a pressure drop of 361 Pa, B) 1.8 wt% of BTA (blue triangle) with a pressure drop of 387 Pa, C) 3.3 wt% of BTA (green square) with a pressure drop of 546 Pa, and ref) a neat glass nonwoven (yellow square) with a pressure drop of 317 Pa. The inset shows a magnification of the filtration efficiencies of mesostructured glass nonwoven and the reference in the range of 0.3 – 1.0 µm. Testing conditions: measuring time = 30 s; flow velocity = 0.25 ms^{-1}; filtration area = 28.3 cm^2, test aerosol = ISO fine test dust, upstream aerosol concentration = 30.000 particles cm^{-3}. Adapted with permission from Ref.[II] © 2025, American Chemical Society.

To demonstrate the temperature stability of these mesostructured glass fiber nonwoven, filters with 3.3 wt% BTA content, where heated to 200°C for 24h. The morphology of different filters with and without the heat treatment is depicted in **Figure 54**. The SEM images show no observable change in morphology, demonstrating high temperature stability of the BTA fibers. The

heat-treated filters were also subjected to particulate matter in the filter test rig and compared to filters without heat treatment. It was found that the filtration efficiency did not change compared to untreated mesostructured glass fiber nonwoven, further evidencing the thermal stability.
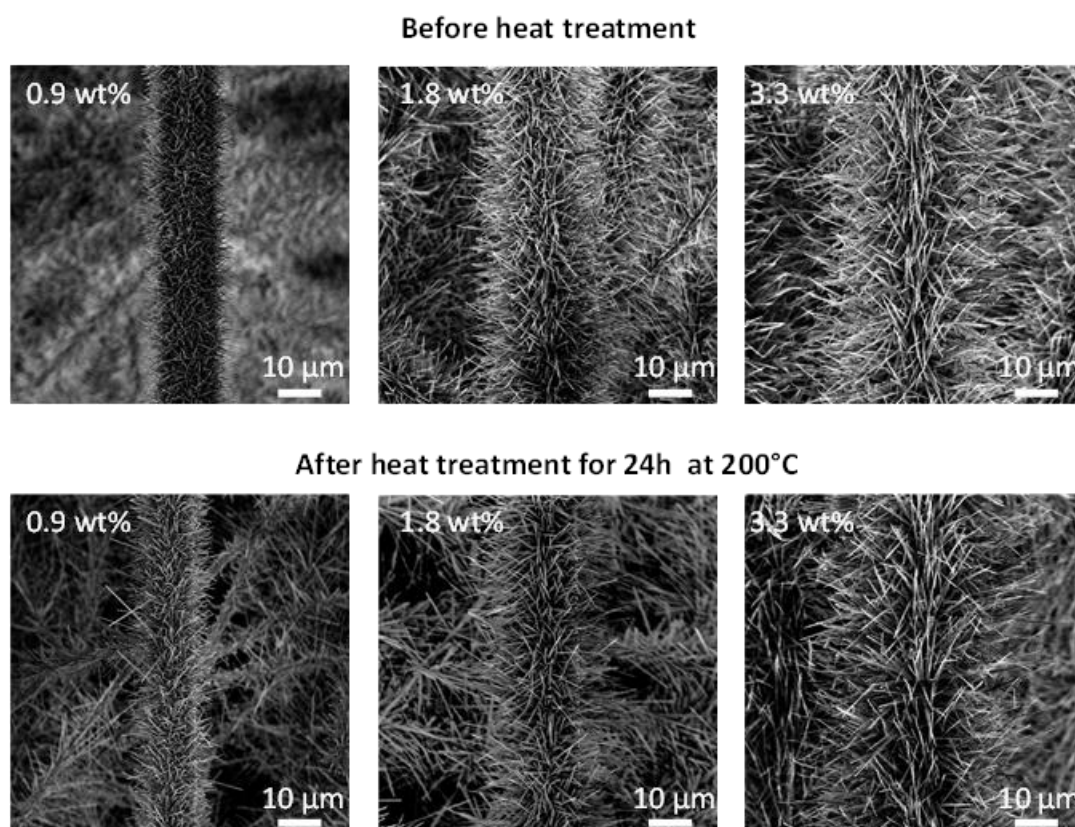
Figure 54. Comparison of SEM micrographs of mesostructured glass nonwoven with 0.9 wt%, 1.8 wt%, and 3.3 wt% of BTA before (top) and after (bottom) a heat treatment of 200°C for 24 h, showing no observable change in morphology. Adapted with permission from Ref.[II] © 2025, American Chemical Society.

In conclusion, the controlled decoration of microfiber nonwoven with supramolecular BTA nanofibers lead to improved filtration performance of the resulting mesostructured nonwoven. Choosing a suitable nonwoven allows realizing more temperature resistant filter. This approach highlights the feasibility of the post modification by PVD to enhance the performance of existing nonwoven fibrous media, potentially enabling the fabrication of mesostructured nonwovens with a broadened application window in filtration and separation.

3.4 Surface-decorated functional supramolecular nanofibers with immobilized gold nanoparticles for catalytic applications

The finding, namely the mechanical stability of PVD-deposited supramolecular nanofibers on nonwovens during air filtration, encouraged us to expand the concept and study the applicability of such mesostructured superstructures in aqueous media. Here we were also seeking to introduce functionality in the periphery of the supramolecular nanofibers by selecting BTA building block with functional groups in their periphery. For this, a BTA with tertiary amino groups was chosen, which is insoluble in water and has the potential to immobilize gold nanoparticles (AuNPs) via attractive interaction with the tertiary amine group (for chemical structure please see **Figure 47**). Combining these features allows one to prepare stable mesostructured superstructures with a high surface/volume ratio and strongly immobilized AuNPs with high catalytic activity in water, which can be used as reusable heterogeneous catalyst. The successful demonstration of this concept was the main objective of the *third publication*.

Interestingly, the selected functional BTA features a similar thermal stability of up to 300°C as the prior investigated aliphatic BTAs. Consequently, the first evaporation experiments on solid substrates revealed that similar conditions were suitable including an evaporation rate of 1.4 µg/s at a temperature of 230°C. SEM studies showed that the BTA molecules were assembled into supramolecular nanofibers on the support. These PVD-deposited supramolecular nanofibers feature a columnar arrangement driven by the helical hydrogen bonds without accompanied by-products as evidenced by IR and HPLC spectroscopy. Cross section SEM images taken after given evaporation times showed that the nanofiber growth proceeded in a linear fashion similarly as described before.

To prepare porous mesostructured superstructure, a single-layer woven polyamide fabric was chosen as substrate, in order to ensure good accessibility of the reactants during catalysis. The morphology of the vapor-deposited supramolecular nanofiber on the woven fabric was investigated by SEM. The overview image in **Figure 55A** reveals that the entire polyamide fabric is densely and homogeneously covered with supramolecular BTA nanofibers. Larger magnifications showed (**Figure 55B, C**), that the supramolecular nanofibers of the vapor-deposited building blocks were grown perpendicularly from the surface of the support structure. From these images a supramolecular fiber diameter of about 350 nm can be estimated. Due to the curved

nature of the support, the nanofiber length cannot be easily determined. However, proper superimposing of a neat woven fabric with a surface-decorated fabric allows to estimate the fiber length with a reasonable degree of accuracy (**Figure 55D-F**) yielding a length of the supramolecular BTA fibers of about 8 μm.
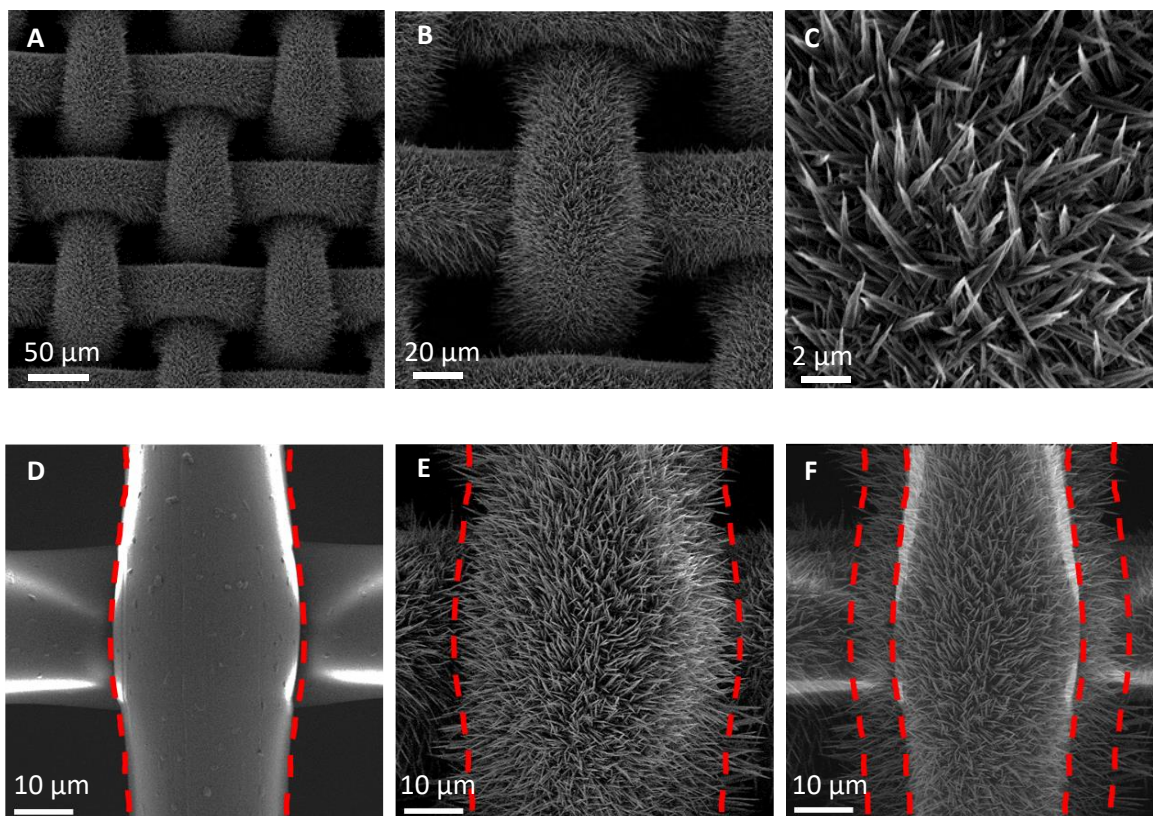
Figure 55. SEM micrographs of surface-decorated woven fabrics with defined supramolecular nanofibers. A) Overview image and B, C) different magnifications of the polyamide woven fabric with fibers of BTA. SEM micrographs of D) a neat woven fabric, E) a surface-decorated fabric and F) the corresponding superimposed image of D) and E). The red dashed lines indicate the outer border of the neat woven fabric and the surface-decorated fabric. The difference between the lines indicates the supramolecular fiber length of about 8 μm. PVD conditions: T_{source} = 230 °C, $T_{substrate}$ = 25 °C. p = 10^{-6} mbar, deposition time 120 min. Adapted from Ref.[III] under a Creative Commons CC – BY license.

Subsequently, the capability of the functional periphery of the supramolecular nanofibers to immobilize AuNPs were studied. For this an aqueous solution of dimethylaminopyridine (DMAP)-stabilized AuNPs were prepared and characterized. Dynamic light scattering (DLS) yielded a mean diameter for the AuNPs of about 10 nm and UV/vis spectroscopy a plasmon resonance at 520 nm. For the immobilization of the AuNPs, a mesostructured woven fabric was immersed into an AuNP solution for one hour. A washing step ensured the removal of unbound AuNP from the mesostructured woven. SEM investigations revealed that the morphology does not change during this immobilization process and by using a back scatter detector, clusters of AuNP can be visualized (**Figure 56**). The presence of the AuNPs was also determined by TEM

analysis of mechanically detached supramolecular nanofibers, showing the immobilization of the nanoparticles with an average diameter of 4.7 nm being somewhat smaller as determined by DLS. ICP-OES experiments showed an AuNP loading of 21 µg gold per mesostructured woven. Using a neat woven fabric as reference for the immobilization process showed that no AuNP were immobilized demonstrating the necessity of the functional periphery of the BTA fibers.
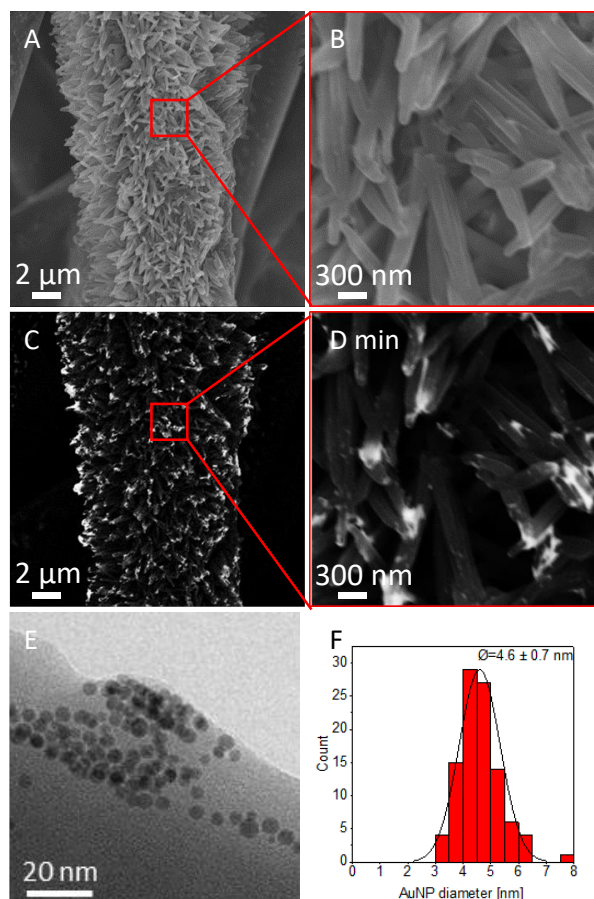
Figure 56. A,B) SEM images at different magnifications of AuNP decorated mesostructured woven using an Inlens detector. C,D) SEM images at different magnifications using the same woven and a backscatter electron detector reveal bright areas on top of the supramolecular fibers indicating the presence of gold particles. E) Distinct individual AuNPs on mechanically detached supramolecular nanofibers as revealed by TEM featuring a uniform particle size distribution. F) Corresponding histogram of the diameter of the immobilized AuNPs determined by evaluating 100 particles showing an average particle diameter of 4.6 ± 0.7 nm. Adapted from Ref.[III] under a Creative Commons CC – BY license.

The AuNP-loaded mesostructured woven fabrics were then ultimately studied with respect to the reduction of 4-nitrophenol to 4-aminophenol in the presence of $NaBH_4$ (**Figure 57**). The progress of the reaction was monitored by UV/vis spectroscopy yielding an almost complete conversion of 95% within 4 min only. Assuming first order kinetics an apparent rate constant (k) of 1.16 min^{-1} was calculated, which is an order of magnitude higher than previously reported k values for heterogeneous catalysts based on supramolecular BTA nanofibers. The reusability

was demonstrated by performing three consecutive runs, where no activity decrease could be observed. SEM characterization showed that the morphology stays intact after the catalysis and TEM analysisconfirmed that the size of the AuNP does not change. This finding was also supported by ICP-OES measurement, which revealed that only a neglectable amount of AuNP-leaches out of the mesostructured superstructure.
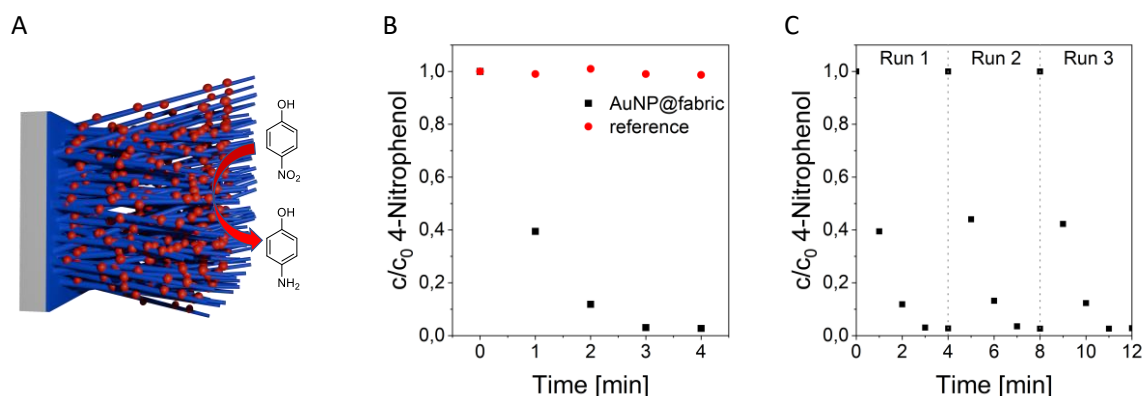
Figure 57. A) Schematic illustration of the reduction of 4-nitrophenol to 4-aminophenol using an AuNP-deposited catalyst on mesostructured woven fabric as heterogenous catalyst in the presence of $NaBH_4$. B) Decrease of the 4-nitrophenolate concentration (c_t/c_0) over time with and without AuNP-deposited catalyst on mesostructured woven fabric. C) Reusability experiments of the AuNP decorated mesostructured woven in three consecutive catalytic cycles. Reaction conditions: 1.5 mL of 0.1 mM aqueous 4-nitrophenol solution, 1.5 mL of 100 mM aqueous $NaBH_4$ and 21 µg of immobilized AuNPs on mesostructured woven fabrics. The reaction is performed at 25°C with stirring at 600 rpm. Adapted from Ref.[III] under a Creative Commons CC – BY license.

In conclusion, this approach allows for fabrication of tailored surface-decorated wovens with uniform functional supramolecular nanofibers by PVD. The functional periphery of BTA nanofibers facilitates robust AuNP immobilization, allowing efficient 4-nitrophenol reduction on the AuNP catalytic sites. These mesostructured woven fabrics with immobilized AuNPs are mechanically stable, enabling reuse without performance loss. This concept may be transferred to other BTA nanofibers and paves the way for mesostructured surfaces for other (photo-) catalytic applications.

3.5 Mesostructured nonwovens with supramolecular tricyclo-quinazoline nanofibers as heterogenous photocatalyst

A final question to be addressed in this thesis was to design mesostructured nonwovens in which the supramolecular fibers themselves can act as catalyst. Apart from conventional catalysis, photocatalysis represents an emerging field that offers promising, sustainable approaches, including water splitting or wastewater purification. Major considerations for this chapter include the use of building blocks, which (i) can form nanofibers, (ii) contains a photocatalytic active core, (iii) is highly stable in aqueous media, and (iv) omits the conventionally used peripheral side groups to ensure access to the active centers. For this, tricycloquinazoline (TCQ, for chemical structure please see **Figure 47**), an electron-poor, disc-like heterocycle that absorbs visible light was selected and synthesized.

Thermal characterizations demonstrated that the molecule exhibits temperature stability of more than 300°C. Above this temperature TCQ is able to sublime residue-free at normal pressure. Evaporation under controlled conditions i.e. pressure of 10^{-6} mbar, T_{source} of 200°C and a substrate temperature of 25°C resulted in supramolecular TCQ nanofibers. Interestingly, the diameter of the TCQ fibers is significantly thinner at 70 nm than BTA fibers that were produced via PVD previously. Similarly, the height of the fiber mat can be readily adjusted through the use of combinatorial techniques, specifically via the manipulation of evaporation time. UV/Vis investigations have demonstrated that the absorption can be specifically controlled through this straightforward process (**Figure 58**).

TCQ was subsequently evaporated onto glass fiber nonwoven, selected as the substrate due to its chemical robustness against the strongly oxidizing species formed during photocatalysis. As illustrated in **Figure 59**, hierarchical superstructures with a bottlebrush morphology were obtained as described in the previous chapters. The length and, consequently, the absorption of the supramolecular TCQ fibers can be adjusted depending on the evaporation time, which is also indicated by the increasing yellow color of the specimens.
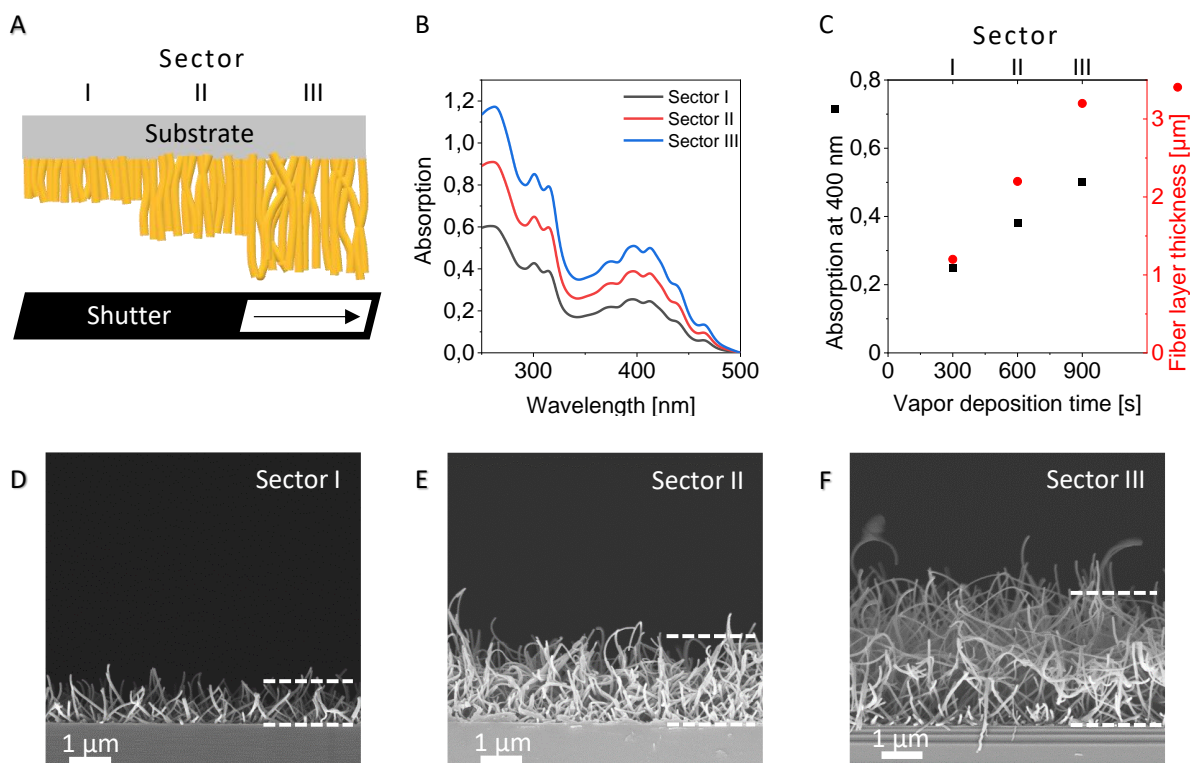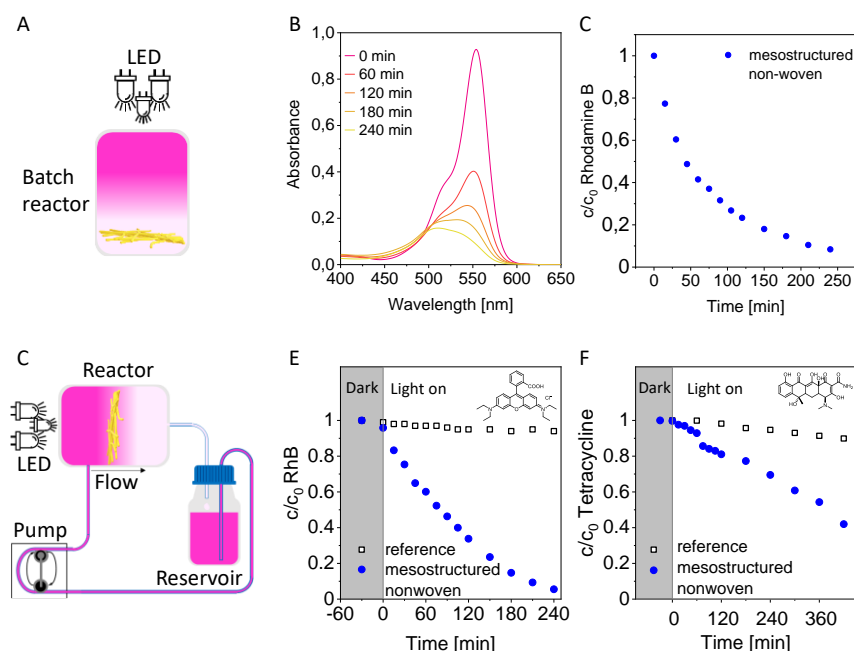
Figure 58. A) Schematic illustration of supramolecular TCQ nanofibers with increasing fiber-layer thicknesses by combinatorial vapor deposition with a shutter being moved stepwise from left to right. The vapor deposition time for sector I is 300 s, for sector II 600 s, and for sector III 900 s. B) Absorption spectra of sector I (black), II (red), and III (blue) on a quartz glass substrate. C) Absorption at 400 nm (in black) and the TCQ fiber-layer thickness (in red) as function of the vapor deposition time revealing an average fiber growth rate of 3.3 nm s^{-1}. D–F) Side-view SEM images of TCQ nanofibers for sectors I, II, and III on a silicon wafer with a fiber-layer thickness of about 1.0, 2.1, and 3.1 µm. The dotted lines are a guide to the eye to indicate the thickness. PVD conditions: T_{source} = 200 °C, p = 10^{-6} mbar, and $T_{substrate}$ = 25 °C. Adapted from Ref.[IV] under a Creative Commons CC – BY license.
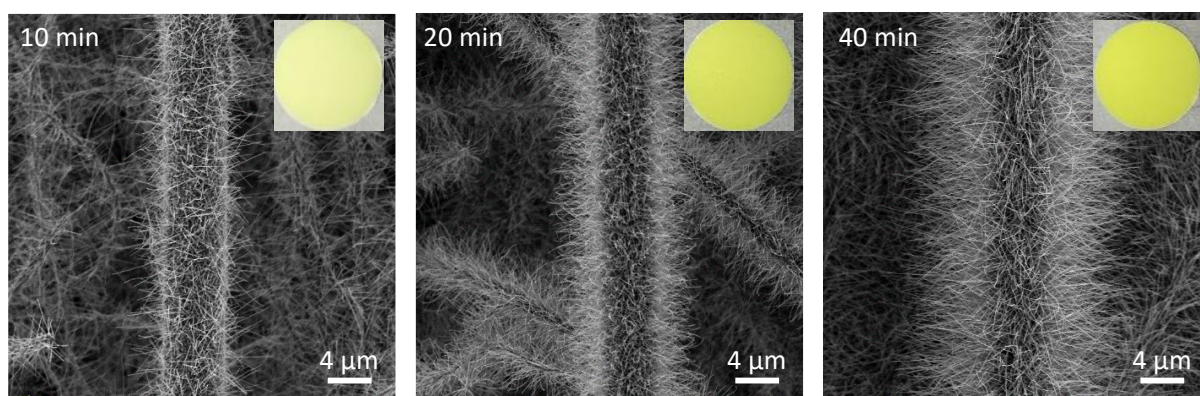
Figure 59. SEM images of supramolecular TCQ nanofiber/ glass microfiber nonwovens by PVD with increasing deposition time from 600, 1200, to 2400 seconds. The average diameter of the TCQ nanofibers for all mesostructured nonwovens were determined to be around 70 nm. The inlets show photographs of the mesostructured nonwovens with a macroscopic diameter of the specimen of 37 mm. PVD conditions: T_{source} = 200°C, $T_{substrate}$ = 25°C, p = 10^{-6} mbar, deposition time see figure, evaporation rate = 1.7 nm/s. Adapted from Ref.[IV] under a Creative Commons CC – BY license.

In order for phototactically active organic materials to be utilized effectively, it is mandatory that they show high photochemical stability under operational conditions. Therefore, we conducted UV light exposure tests using the TCQ nanofiber/glass-microfiber nonwovens under conditions that simulated harsh environments. In this experiment, a mesostructured nonwoven was immersed in deionized water, with the TCQ nanofibers facing upwards, and subjected to UV radiation at an intensity of 5 suns for 48 hours. Subsequently, the TCQ was molecularly dissolved and analyzed using high-performance liquid chromatography (HPLC). The HPLC elugrams from the solutions before and after UV exposure showed only one TCQ signal, confirming the high photochemical stability of TCQ under these conditions. Additionally, HPLC analysis of the residual water revealed that no other organic compounds are present, indicating that the TCQ remained stable under these conditions. Further evidence was provided by scanning electron microscopy (SEM) analysis before and after UV exposure, which showed that the bottlebrush-like morphology remained unchanged.

The potential of TCQ nanofiber/glass-microfiber nonwovens to be used as photocatalysts was initially assessed in a batch-type process. The setup is shown in **Figure 60A**. A 6200 K LED, which emits visible light in the range of 400 to 700 nm, was used to irradiate mesostructured nonwovens with 0.4 mg of TCQ nanofibers. This value is calculated to a loading of only 0.05 mg/cm². The nonwovens were exposed to a 10^{-5} mol/L Rhodamine B solution, and the decomposition of the dye was monitored by UV/Vis spectroscopy every 15 minutes over four hours. The absorption maximum shifted from 554 to 500 nm, indicating degradation via a *N*-deethylation pathway (**Figure 60B**). The decomposition of Rhodamine B was observed to reach 92% within four hours (**Figure 60C**). Assuming pseudo first-order reaction kinetics under constant illumination, the apparent rate constant (k') was calculated to 1.0×10^{-2} min^{-1}. SEM analysis demonstrated that the bottlebrush-like morphology of the nonwovens remained intact after photocatalysis.

Figure 60. A) Schematic illustration of photocatalytic degradation of organic pollutants using a batch-type reactor. B) Progress of the UV/Vis absorption of aqueous Rhodamine B solution during photocatalysis using a mesostructured nonwoven and a batch setup. C) Progress of photodegradation of Rhodamine B as a function of time using mesostructured nonwovens. D) Schematic illustration of photocatalytic degradation of organic pollutants using a continuous flow reactor: Organic pollutants are circulated from a reservoir solution with a flow rate of 1.5 L h^{-1}. The nanofiber/microfiber nonwoven is fixed as a heterogenous photocatalyst upon visible-light LED irradiation. E) Progress of photodegradation of Rhodamine B as a function of time without (dark) and with irradiation (light on) using mesostructured nonwovens (closed circle) and neat glass microfibers as reference (open squared). F) Progress of photodegradation of tetracycline as a function of time without (dark) and with irradiation (light on) using nanofiber/microfiber nonwovens and neat glass microfibers as reference. Adapted from Ref.[IV] under a Creative Commons CC – BY license.

To elucidate the mechanism of photocatalytic degradation of organic pollutants by TCQ, we studied the photodegradation of Rhodamine B in the presence of various scavengers, capable to identify the reactive oxygen species, i.e. hydroxyl radicals, photogenerated holes and superoxide species. Scavenging hydroxy radicals did not influence the degradation rate, constant, showing that the hydroxy radicals are not dominantly involved in the degradation of rhodamine. In contrast, scavenging photogenerated holes or superoxide radicals decreased the rate constant of 25% or 85%, respectively. Which lead to the conclusion, that holes are involved in the degradation but the main reactive species, which are formed for the degradation of rhodamine, are superoxide radicals.

In contrast to batch processes, continuous flow processes offer several advantages, including the ability to convert larger quantities of material at reduced treatment time. The efficiency of TCQ nanofiber/glass-microfiber nonwovens as photocatalysts for the degradation of Rhodamine B dye and the antibiotic tetracycline in water under continuous flow conditions was evaluated. **Figure 60D** schematically depicts the configuration of the continuous flow photoreactor,

in which the nonwoven was positioned with the TCQ nanofibers facing towards the light source. The tenfold volume, i.e. 250 mL of aqueous solution of Rhodamine B at a concentration of 10^{-5} mol/L was circulated through the reactor using a peristaltic pump. Within four hours, 95% of the dye was degraded, as illustrated in **Figure 60E**. Total organic carbon (TOC) measurements indicated that 35% of the initial Rhodamine B was converted to CO_2, while 65% was degraded into other products.

After photodegradation, we analyzed the remaining water solution for traces of TCQ using HPLC. The analysis confirmed that no TCQ leached from the mesostructured nonwoven after four hours of circulation. This led us to explore the potential for reusing the mesostructured nonwovens as photocatalysts. For this, we conducted three consecutive runs, each performed with freshly prepared Rhodamine B solutions. Throughout these tests, there was no significant loss in photocatalytic activity, indicating that the TCQ did not degrade and the nanofibers remained intact on the glass-fiber nonwoven. SEM analysis after the third run confirmed that the supramolecular TCQ nanofibers were still present on the glass-microfiber nonwoven.

Finally, the photocatalytic degradation of tetracycline, a common antibiotic found in wastewater, was investigated using supramolecular TCQ nanofiber/glass-microfiber nonwovens. The experiments were conducted with an aqueous tetracycline solution at a concentration of 10^{-4} mol/L and the same continuous flow reactor setup was used as described above. Control experiments showed no significant changes: neither the circulation of the solution in the dark with the mesostructured nonwoven nor photolysis without photocatalysts resulted in notable decomposition of tetracycline. In contrast, under illumination with the TCQ-mesostructured nonwoven (loading: 0.05 mg/cm²), 60% of the tetracycline was degraded within 7 hours (**Figure 60F**). TOC analysis of the remaining solution revealed that 40% of the degraded tetracycline was mineralized into CO_2.

In conclusion, the fabrication of mesostructured nonwoven by PVD containing supramolecular nanofibers based on TCQ as photoactive building block was successfully demonstrated. Using glass-microfiber nonwovens as a porous support leading to a bottlebrush-like morphology of fine TCQ nanofibers, which functions as a visible-light photocatalyst for degrading Rhodamine B and tetracycline under continuous flow conditions. It was shown that this approach represents a robust, reusable method for the production of functional supramolecular nanofibers with controlled morphology for (photo)catalytic applications.

4 Publications

4.1 Individual contributions to the publications

Publication I: Hierarchical Glass Fiber Superstructures with Supramolecular Nanofibers for the Nucleation of Isotactic Polypropylene

Dennis Schröder, Jannik Thanner, Klaus Kreger, and Hans-Werner Schmidt
Macromol. Mater. Eng. **2024**, 2400389. DOI: 10.1002/mame.202400389

The first publication introduces a PVD process for the preparation of mesostructured nonwovens based on supramolecular BTA nanofibers and glass microfibers to nucleate iPP.
I performed all PVD experiments and analyzed the resulting morphology using electron microscopy. Furthermore, all additional characterization, i.e. Thermal analysis, HPLC analysis and IR spectroscopy, were conducted by me. Nucleation experiments with supramolecular nanofibers prepared via PVD or mesostructured nonwoven prepared via PVD were performed by me. I prepared tensile test specimen of composites based on iPP and mesostructured nonwovens and investigated the mechanical properties of these composites. Powder XRD measurements of supramolecular nanofibers prepared via PVD were conducted by Jannik Thanner.
Hans-Werner Schmidt and Klaus Kreger were involved in scientific discussions during the project, in the interpretation of the results and in the outline of the manuscript. I prepared the figures and wrote the initial draft of the manuscript. All authors were involved in finalizing the manuscript and in the revision of the manuscript.

Publication II: Mesostructured polymer and glass microfiber nonwovens with supramolecular 1,3,5-benzenetrisamide nanofibers for air filtration

Dennis Schröder, Klaus Kreger, and Hans-Werner Schmidt
ACS Appl. Mater. Interfaces. **2025**, 17, 14569-14577, DOI: 10.1021/acsami.4c22310

The second publication focuses on the preparation of mesostructured nonwovens based on supramolecular BTA nanofibers and glass or polymer microfibers and their use as air filtration medium.
I performed all PVD experiments, prepared all the samples for the filtration experiments and analyzed the resulting morphology of the mesostructured nonwoven using electron microscopy. In addition, I analyzed the resulting mesostructured nonwoven using dynamic and isothermal thermogravimetric analysis for temperature resistance. All results from the air stream test and filtration experiments were evaluated by me. Hans-Werner Schmidt and Klaus Kreger were involved in scientific discussions during the project, in the interpretation of the results and in the outline of the manuscript. I prepared the figures and wrote the initial draft of the manuscript. All authors were involved in finalizing the manuscript and in the revision of the manuscript.

Publication III: Controlled Surface Decoration with Functional Supramolecular Nanofibers by Physical Vapor Deposition

Dennis Schröder, Klaus Kreger, Ulrich Mansfeld, and Hans-Werner Schmidt
Adv. Mater. Interfaces **2024**, 11, 2400259. DOI: 10.1002/admi.202400259

The third publication focuses on the preparation of mesostructured wovens based on supramolecular BTA nanofibers with peripheral tertiary amine groups and their use for AuNP immobilization and subsequent catalysis.

I characterized the thermal properties of the molecular building block and tested the suitability for vapor deposition. I identified optimal PVD conditions for the preparation of supramolecular nanofibers and investigated the structure using HPLC, IR and SEM. I prepared mesostructured woven and analyzed the resulting morphology using electron microscopy. I synthesized and characterized the used AuNP using UV/VIS and DLS. I developed a procedure to immobilize AuNP on the mesostructured woven and visualized the successful immobilization using SEM with a back-scatter detector. TEM images of AuNP loaded mesostructured woven were taken by Ulrich Mansfeld and I evaluated these images to receive the mean diameter of the AuNPs. All catalytic experiments were also performed by me.

Hans-Werner Schmidt and Klaus Kreger were involved in scientific discussions during the project, in the interpretation of the results and in the outline of the manuscript. I prepared the figures and wrote the initial draft of the manuscript. All authors were involved in finalizing the manuscript and in the revision of the manuscript.

Publication IV: Mesostructured Nonwovens with Supramolecular Tricycloquinazoline Nanofibers as Heterogenous Photocatalyst

Dennis Schröder, Christian Neuber, Ulrich Mansfeld, Klaus Kreger, and Hans-Werner Schmidt
Small Sci., **2024**, 4, 2300160. DOI: 10.1002/smsc.202300160

The fourth publication focuses on the preparation of mesostructured nonwovens based on supramolecular TCQ nanofibers and their use as heterogenous photocatalysts.

The synthesis and molecular characterization TCQ were performed by me. I performed PVD experiments to identify optimal PVD conditions for the generation of nanofibers with assistance of Christian Neuber. These nanofibers were evaluated using HPLC, IR and the resulting morphology with electron microscopy were conducted by me. I designed and built the flow reactor, established a procedure to reproducibly measure the photocatalytic activity and performed all photocatalytic experiments. TEM and SAED measurements were conducted by Ulrich Mansfeld.

Hans-Werner Schmidt and Klaus Kreger were involved in scientific discussions during the project, in the interpretation of the results and in the outline of the manuscript. I prepared the figures and wrote the initial draft of the manuscript. All authors were involved in finalizing the manuscript and in the revision of the manuscript.

4.2 Publication 1

RESEARCH ARTICLE

Hierarchical Glass Fiber Superstructures with Supramolecular Nanofibers for the Nucleation of Isotactic Polypropylene

Dennis Schröder, Jannik Thanner, Klaus Kreger, and Hans-Werner Schmidt*

Supramolecular additives are an established class of nucleating agents to modify and control the solid-state morphology of semi-crystalline polymers, in particular isotactic polypropylene (iPP). A widely used reinforcement material for iPP is glass fibers (GFs), which significantly improve the mechanical properties. Here, these two types of materials are combined by creating defined hierarchical superstructures composed of glass microfiber nonwovens and supramolecular nanofibers based on selected 1,3,5-benzetri-samides (BTA). The supramolecular nanofibers are prepared by physical vapor deposition (PVD), a straightforward solvent-free process. By systematically varying PVD process parameters, it is shown that supramolecular BTA nanofibers can be reproducibly prepared on flat substrates. The morphology of the supramolecular nanofibers can be controlled by substrate temperature, evaporation time, and evaporation rate. The use of GF nonwovens enables the fabrication of hierarchical superstructures with a bottlebrush morphology comprising supramolecular nanofibers of defined length. These hierarchical superstructures are capable of nucleating iPP and thus promote transcrystallization of the iPP from the decorated GFs surface, which ultimately improves the adhesion between the GFs and the iPP. Laminating decorated GF nonwovens between two iPP films clearly increases the mechanical properties of the composites in contrast to composites without nucleating agents.

1. Introduction

Nucleating agents are a crucial class of plastic additives for semi-crystalline polymers such as isotactic polypropylene (iPP), improving the polymer processing by reducing the cycling time and the polymer solid-state properties by controlling the microstructure, morphology, and crystal modification.[1–4] Among the commonly used inorganic nucleating agents such as talc, wollastonite, and mica, and organic salts such as benzoates and aromatic phosphates, supramolecular additives are a well-established class of nucleating agents.[4–6] Supramolecular nucleating agents are small molecules, which can be dissolved in the polymer melt at a distinct concentration at elevated temperatures and self-assemble upon cooling into solid supramolecular nanofibers. Upon further cooling the polymer melt, the epitaxial surfaces of the solid nanofibers provide a large number of efficient heterogeneous nucleation sites for the transcrystallization of iPP before homonucleation takes place. Two classes of compounds are technically widely used as clarifying and α-nucleating agents for iPP. These include carbohydrate-related derivatives such as sorbitol- or nonitol-based compounds[7–11] and 1,3,5-benzenetrisamide-based compounds (BTAs).[12–14] The molecular design of suitable BTAs to efficiently nucleate iPP is based on C_3-symmetric building blocks composed of a benzene core, three amide moieties, and short aliphatic or cycloaliphatic peripheral groups. During the self-assembly process, the dissolved molecular building blocks stack cofacially on top of each other due to the formation of three helical strands of hydrogen bonds between the amide groups resulting in columnar supramolecular nanofibers.[15] An important feature of these BTAs is that the peripheral substituent, located on the nanofibers surface, determines the epitaxial match between the supramolecular nanofibers and the crystal lattice of iPP and consequently the nucleation capability.[12–14,16]

A way to greatly improve the mechanical properties of iPP is the use of glass fibers (GF) with high strength and modulus.[17] Depending on the application and processing method GFs are

D. Schröder, K. Kreger, H.-W. Schmidt
Macromolecular Chemistry I and Bavarian Polymer Institute
University of Bayreuth
95447 Bayreuth, Germany
E-mail: hans-werner.schmidt@uni-bayreuth.de

J. Thanner
Inorganic Colloids for Electrochemical Energy storage
University of Bayreuth
95447 Bayreuth, Germany

The ORCID identification number(s) for the author(s) of this article can be found under https://doi.org/10.1002/mame.202400389

Publications

**ADVANCED
SCIENCE NEWS**
www.advancedsciencenews.com

[M] acro-
molecular
Materials and Engineering
Open Access
www.mame-journal.de

used in form of fibers, fiber bundles, short fibers, fabrics, and nonwovens. In these reinforced iPP/GF composites, the GFs are the main load-carrying material, while the polymer matrix transfer stresses between the fibers.[18,19] The performance of GF-reinforced iPP depends critically on the interfacial strength between the polymer matrix and the GFs.[19–21] Due to the hydrophobicity of iPP and the hydrophilicity of GFs, these materials are inherently incompatible resulting in an insufficient adhesion between the two. Therefore, several strategies were developed to enhance the adhesion of iPP to GF.[22–26] A commonly applied approach to improve adhesion is GF treatment with coupling agents. One of the most prominent classes of coupling agents is organofunctionalized silanes, providing chemical reactions of the silanes with the glass fiber surface.[19] This method also depends on a large number of parameters such as silane type, layer thickness, and application process. Another widely used approach to enhance compatibilization is based on the modification of the polymer matrix or a combination of both approaches. Matrix modification is achieved by introducing polar reactive groups in the polymer. One prominent example is maleic anhydride grafted polypropylene, which is added to the iPP matrix in the order of a few percent by weight.[20,27] The maleic anhydride groups subsequently react with functional groups on the GF and ultimately improve the compatibility. Another promising approach to improve the adhesion between the two is to modify the GFs in a way that promotes interfacial crystallization of iPP on the GFs.[28] For example, Ning et al. deposited graphene oxide on the GF surface, which led to a pronounced transcrystallization of iPP on the modified GF.[29]

In all these cases, improvement in adhesion is achieved by applying solvent-based coating techniques to establish thin layers resulting in attractive physical interactions or chemical bonding between GF and iPP. Another coating technique is physical vapor deposition (PVD) using small molecules. PVD is an established solvent-free method to fabricate thin uniform layers using thermally stable, vaporizable compounds in high vacuum. An interesting finding described recently is that with distinct small molecules under appropriate conditions, PVD can be used to prepare defined supramolecular structures such as nanofibers or nanobelts on surfaces of flat substrates with potential use for optoelectronic applications.[30] Here, often aromatic compounds such as pentacene, perylene, and porphyrin derivatives among others were used, which are able to form supramolecular aggregates on the surface via π-π-interactions of the aromatic cores.[31–38] Recently, we have also demonstrated the preparation of supramolecular nanofibers via PVD on fibrous supports to prepare functional mesostructured (non-)wovens. For example, we employed small molecules such as tricycloquinazoline to prepare supramolecular nanofibers and demonstrate their use as photocatalysts for the degradation of organic pollutants.[39] Another example is supramolecular nanofibers based on BTAs with functional side groups, which are decorated with gold nanoparticles and can be used as heterogenous catalysts for chemical reactions.[39,40]

Here we report on a systematic study to form supramolecular nanofibers by PVD using selected 1,3,5-benzenetrisamides, which are reported to act as α-nucleating agents for iPP.[12] Six different **BTA 1-6**, with cycloaliphatic and branched peripheral substituents, were investigated in view of the formation of

supramolecular nanofibers by PVD (**Figure 1**). We investigated and evaluated relevant process parameters such as substrate temperature, evaporation time, and evaporation rate to control the supramolecular fiber thickness and length on flat silicon and glass substrates. By using GF nonwovens as substrate, the fabrication of defined hierarchical GF superstructures with a bottle-brush morphology of BTA nanofibers was achieved. We demonstrate that these hierarchical glass fiber superstructures with supramolecular nanofibers can nucleate iPP and improve the mechanical properties of laminated iPP specimens in comparison to iPP specimens with a non-treated GF nonwoven.

2. Results and Discussion

2.1. Physical Vapor Deposition of BTAs and the Formation of Supramolecular Nanofibers

The formation and morphology of supramolecular nanofibers prepared via PVD are subject to the influence of the molecular structure and various PVD process parameters. Suitable molecules have to possess high temperature stability, evaporate without decomposition, and self-assemble into nanofibers via defined secondary interactions. In general, the class of 1,3,5-benzenetrisamides (BTAs) fulfills these requirements. However, target molecules have to be identified and the influence of molecular structure, substrate temperature, evaporation time, and evaporation rate on the formation of supramolecular fibers and their morphology have to be explored. The objective is to identify BTAs and PVD conditions that can be used to reproducibly prepare supramolecular nanofibers and control their length and diameters on different substrates.

2.1.1. Influence of the Molecular Structure on the Supramolecular Fiber Morphology

Apart from the considerations above, the BTAs were selected in view of their ability to nucleate iPP. In particular, BTAs with short aliphatic or cycloaliphatic peripheral groups are known to act as α-nucleating agents for iPP.[12] Thus, we selected BTAs with 2-adamantyl groups (**BTA 1**), 2-methylcyclohexyl groups (**BTA 2**), 1,2-dimethylpropyl groups (**BTA 3**), 1,1-dimethylpropyl groups (**BTA 4**) and *tert*-butyl groups (**BTA 5**) based on trimesic acid as the central core. In addition, a BTA with *tert*-butyl groups based on triaminobenzene (**BTA 6**) was chosen (see Figure 1).

All of the investigated BTAs have no melting point and have a tendency to sublime.[12] To investigate their thermal stability and vaporability without decomposition, dynamic thermogravimetric analysis (TGA) with a heating rate of 10 K min^{-1} under nitrogen was performed. The TGA results show high thermal stability for the six BTAs, with a 5% weight loss occurring in the temperature range of 340–460 °C (Figure S1, Supporting Information). The vaporability without decomposition is indicated by a steep and uniform decrease up to weight loss values of more than 95% in some cases up to 100%. PVD experiments were typically performed at a much lower temperature in the range of 230–315 °C, which is for all BTAs ≈100 °C lower than weight loss in the TGA occurs. Preliminary PVD experiments and analysis of the BTAs by high-performance liquid chromatography
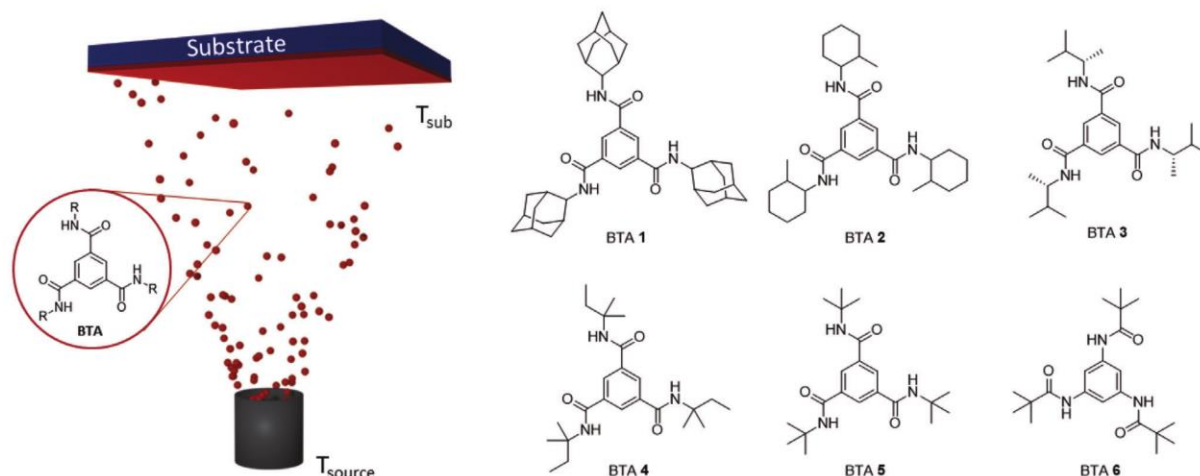
Figure 1. Schematic illustration of the physical vapor deposition of benzenetrisamides (BTA). The vapor deposition depends on the physical and thermal properties of the benzene trisamides and can be controlled by the source temperature (T_{source}), and the temperature of the substrate (T_{sub}). Substrates include flat substrates and glass fiber substrates. In this study, six different BTA 1–6, with cycloaliphatic and branched peripheral substituents were investigated in view of the formation of supramolecular nanofibers.

(HPLC) additionally prove the vaporability without decomposition. The HPLC chromatograms before and after PVD for **BTA 6** as a representative example are shown in Figure S2 (Supporting Information).

To conduct the PVD experiments, a dedicated setup was utilized, comprising an evaporation chamber equipped with effusion cells, which enable the precise control of the source temperature (T_{source}) and subsequently the evaporation rate. The evaporation rate is monitored with quartz crystal microbalances located in close proximity to the substrate.

To study the influence of the molecular structure on the formation of supramolecular nanofibers by PVD, the same set of conditions were chosen for all six BTAs. This includes a substrate temperature (T_{sub}) of 25 °C of the used silicon substrate, an evaporation time of 30 min, and an evaporation rate of 1.4 µg s^{-1}. To achieve a constant evaporation rate of 1.4 µg s^{-1}, the source temperature (T_{source}) was set individually to 315 °C for **BTA 1**, 270 °C for **BTA 2**, 245 °C for **BTA 3**, 235 °C for **BTA 4**, 230 °C for **BTA 5** and 230 °C for **BTA 6**. SEM micrographs of the silicon wafers after the PVD process are shown in **Figure 2**. With the exception of the PVD experiment with **BTA 1**, supramolecular nanofibers were formed with all other BTAs (**BTA 2–6**), which were homogeneously distributed over the entire substrate. After evaluation of the mean fiber diameter using at least 100 fibers of the trimesic acid-based BTAs, we found a mean fiber diameter of 55 nm for **BTA 2**, 84 nm for **BTA 3**, 117 nm for **BTA 4** and 123 nm for **BTA 5**. This finding seems to indicate a general trend with respect to the molecular structure, namely with decreasing the bulkiness and sterical demand of the peripheral side groups of the BTAs the nanofiber diameter increases. Another significant difference in the mean fiber diameter was found for **BTA 5** (fiber diameter: 123 nm) and **BTA 6** (fiber diameter: 204 nm). These two BTAs only differ in the connectivity of the amide linkage. The results indicate that using the same set of PVD conditions, the molec-

ular structure plays a significant role for the resulting nanofiber morphology.

2.1.2. Influence of the PVD Parameter on the Supramolecular Fiber Morphology

Since it can be expected that the fiber dimensions and morphology of supramolecular nanofibers by PVD are influenced by various process parameters such as substrate temperature, evaporation time, and evaporation rate, we focus on the use of **BTA 6** as a representative material in these studies.

Influence of Substrate Temperature: The substrate temperature largely influences the adsorption–desorption balance of the molecules. It also may impact the crystalline order of the molecules on the substrate giving rise to nuclei formation and subsequently of the nanofiber morphology. To study the influence of the substrate temperature, the fiber growth of **BTA 6** was monitored on a silicon wafer. Three different substrate temperatures were selected, namely to 25, 50 and 100 °C. The substrates were heated and the temperature was controlled using a Peltier element. The evaporation rate was 1.4 µg s^{-1} for an evaporation time of 30 min. Figure S3 (Supporting Information) shows the top and side view SEM images of the morphology at different substrate temperatures. At $T_{sub} = 25$ °C, the silicon wafer is homogeneously and densely covered with supramolecular nanofibers with an average fiber diameter of 204 nm and a fiber mat height of ≈2.20 µm. Increasing the substrate temperature to $T_{sub} = 50$ °C results in fewer nanofibers with an average fiber thickness of ≈300 nm and a smaller fiber mat height of ≈1.0 µm. The nanofibers are less homogeneously formed and unevenly distributed over the substrate. Additionally, some small circular structures are visible on top of the substrate indicating nuclei formation. Increasing T_{sub} to 100 °C largely hampers nanofiber formation and more circular and very tiny fibrous structures can be
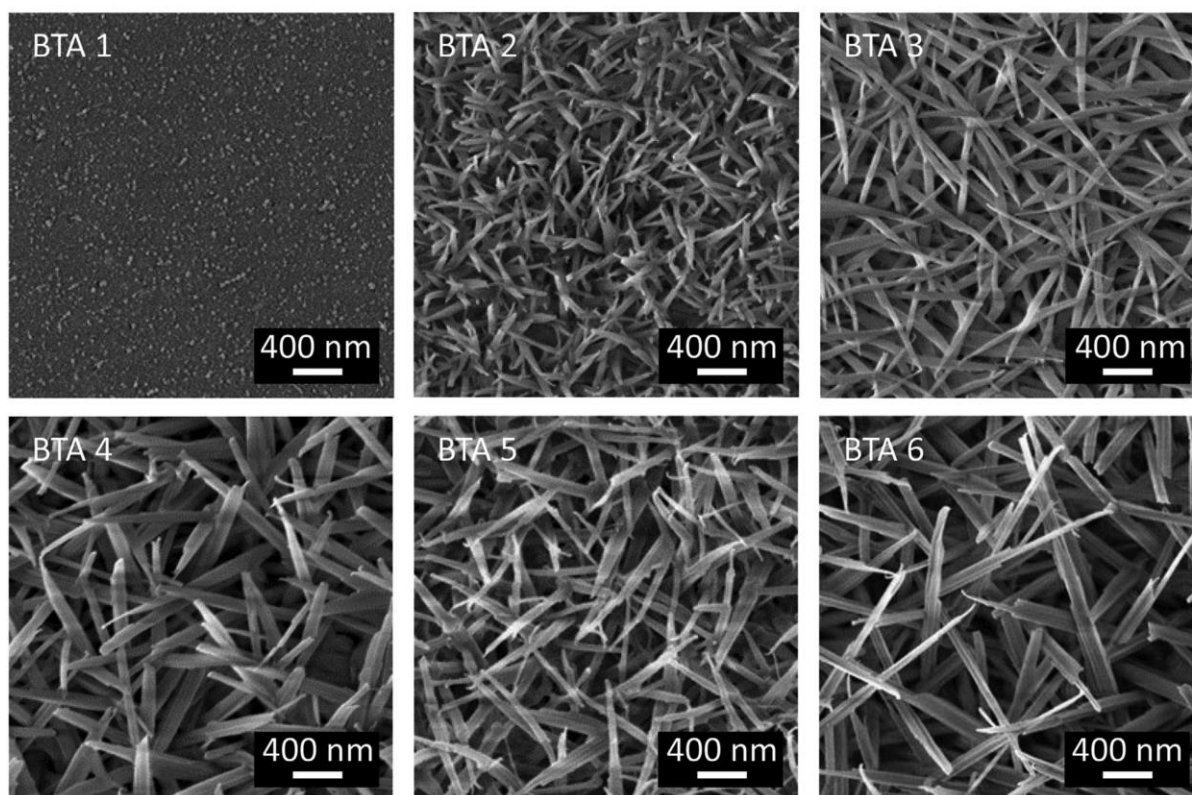
Figure 2. SEM images (top view) of supramolecular nanofibers of BTA 1 – BTA 6 prepared by physical vapor deposition on a silicon substrate with T_{sub} = 25 °C. The evaporation rate was 1.4 µg s^{-1} which was obtained by adjusting the source temperature for BTA 1 to T_{source} = 315 °C, for BTA 2 to T_{source} = 270 °C, for BTA 3 to T_{source} = 245 °C for BTA 4 to T_{source} = 235 °C for BTA 5 to T_{source} = 230 °C and for BTA 6 to T_{source} = 230 °C with an evaporation time of 30 min for all BTAs.

seen on top of the substrate. In the side view images, a thin finely structured film of ≈200 nm can be clearly seen, which is also present at lower substrate temperatures. The lack of nanofiber formation is attributed to a shift of the adsorption–desorption balance toward the desorption of the molecules from the substrate with increasing temperature, which results at 100 °C only in the formation of a wetting layer. At lower substrate temperatures, this wetting layer provide homogeneously distributed nuclei, initiating the supramolecular nanofiber formation. These findings also demonstrate that densely deposited supramolecular nanofibers of **BTA 6** can be beneficially achieved at ambient substrate temperatures without heating, which was selected for all further experiments.

Influence of Evaporation Time: Since a substrate temperature of 25 °C enables homogeneous fiber growth, the evaporation is expected to control the fiber length. To study the influence of the evaporation time on the supramolecular fiber morphology, three different evaporation times of 15, 30, and 45 min were realized on the same substrate at T_{sub} 25 °C and an evaporation rate of 1.4 µg s^{-1} using a combinatorial approach of the PVD experiment. For this, the silicon wafer was covered with a shutter preventing deposition of the BTAs on the covered area. Stepwise moving the shutter every 15 min results in three different sectors, which were

exposed to the vapor stream for 15, 30, and 45 min. In **Figure 3** the SEM top view and side view images after different evaporation times are shown. Already after 15 min of evaporation, the top view image shows a significant coverage of the silicon wafer with nanofibers to a high extent. Apparently, the coverage becomes denser and the fiber thickness larger with increasing the evaporation time from 15 to 45 min. From these SEM images, the fiber diameter was determined to increase from 186 nm after 15 min to 204 nm after 30 min and to 226 nm after 45 min evaporation time as evaluated by measuring 100 individual fibers. The side view images show the same trend, namely that the supramolecular nanofibers of **BTA 6** grow away from the substrate and become thicker in diameter with increasing evaporation time. The average height of the fiber mat was determined to be 0.9 ± 0.2 µm after 15 min, 2.2 ± 0.5 µm after 30 min, and 4.3 ± 0.5 µm after 45 min as expected.

Although for the substrate after 15 min of evaporation, the nanofibers in the top view image can be clearly seen, they cannot be easily distinguished from the wetting layer in the side view image. Therefore, we took a closer look at the initial stage of the formation and performed a more detailed combinatorial experiment. For this, the experiment was repeated with the same parameters, but the evaporation times were varied in the range

2400389 (4 of 11)
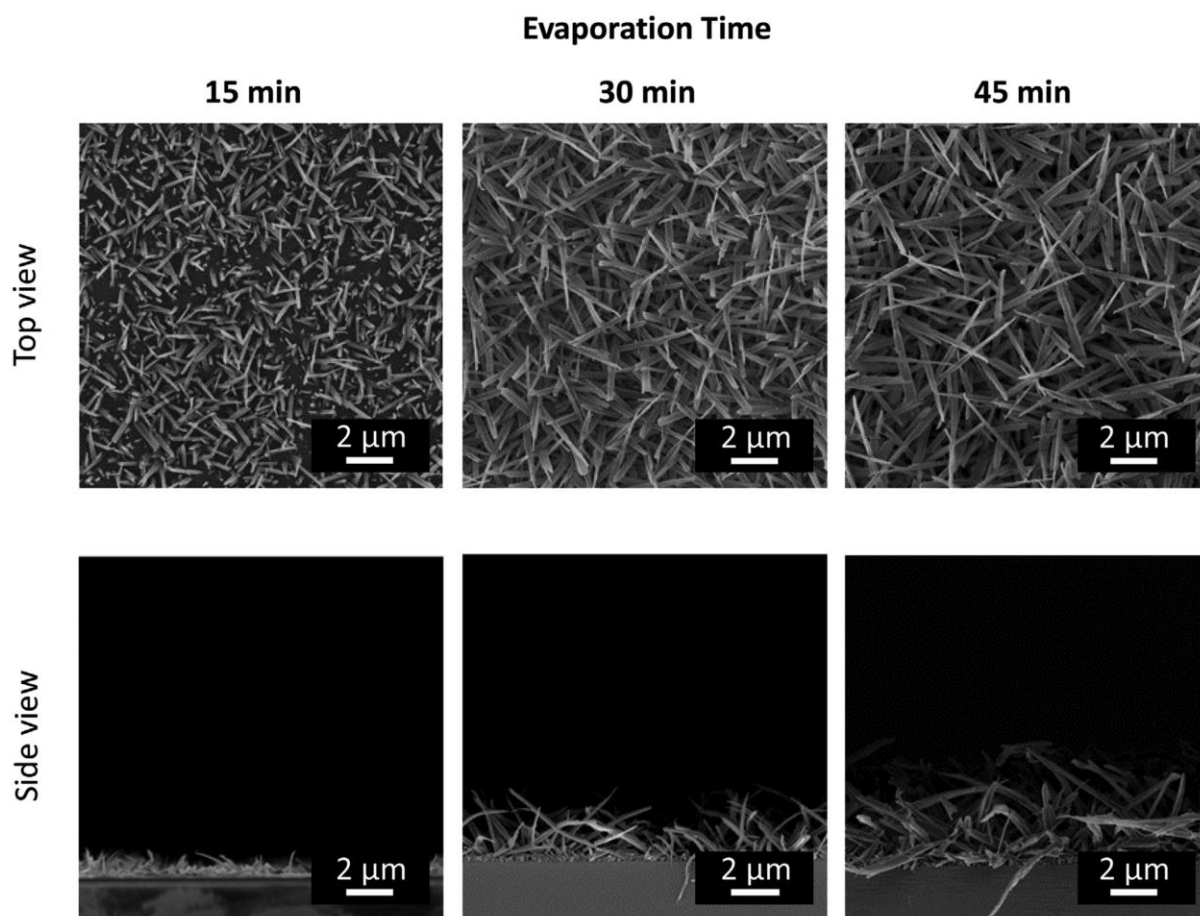
Figure 3. Top and side view SEM images of supramolecular nanofibers of BTA 6 prepared by physical vapor deposition on the same silicon wafer with $T_{sub} = 25\,°C$ depending on evaporation time at a fixed evaporation rate of $1.4\,\mu g\,s^{-1}$ as adjusted by $T_{source} = 230\,°C$. The three different vapor exposure times, i.e., of 15, 30, and 45 min, were realized in a combinatorial approach of the PVD experiment by successively covering the substrate with a shutter for the given time.

from 5, 10, 15, 30, and 45 min receiving a substrate with five different sectors. The top and side view SEM images are depicted in Figure S4 (Supporting Information). The side view images show that in the initial stage already after 5 min a wetting layer with a thickness of $\approx$200 nm is formed, which only slightly increases with time. After 10 min of evaporation first visible nuclei are formed, which are able to initiate the nanofiber growth as shown in the SEM micrograph after 15 min. After 30 and 45 min, the supramolecular nanofibers feature a similar morphology as described before, demonstrating a highly reproducible process. After the wetting layer is established and nanofiber nucleation is initiated, the growth of the fiber length and thus the fiber mat height can be plotted versus the evaporation time. We found that the fiber length growth proceeds in a linear fashion with a growth rate of $0.1\,\mu m\,min^{-1}$ as shown in Figure S5 (Supporting Information), allowing to adjust the nanofiber length by controlling the evaporation time.

Influence of the Evaporation Rate: The evaporation rate may influence the fiber morphology due to an increased heat input

upon deposition. Here, the influence of the evaporation rate on the supramolecular nanofiber morphology was studied using three different evaporation rates, namely 0.5, 1.4, and $2.8\,\mu g\,s^{-1}$ while keeping the other parameters constant. To obtain these evaporation rates, the source temperature was adjusted to $T_{source} = 220$, 230, and 250 °C, respectively. Figure S6 (Supporting Information) shows the top and side view SEM images of supramolecular nanofibers of **BTA 6** depending on the evaporation rate. The side view SEM image taken after the experiment with an evaporation rate of $0.5\,\mu g\,s^{-1}$ shows small supramolecular fibers on the substrate, which are less densely distributed on the substrate (top view image). The average fiber thickness was found to be 168 nm and the fiber mat height was $\approx$0.7 µm. This finding is similar to an increased substrate temperature or decreased evaporation rate resembling that a comparable small amount of the molecules is deposited. By increasing the evaporation rate to $1.4\,\mu g\,s^{-1}$, a densely covered substrate with an average fiber diameter of 204 nm and an average fiber mat height of 2.2 µm. Doubling the evaporation rate to $2.8\,\mu g\,s^{-1}$ increases the average fiber

82
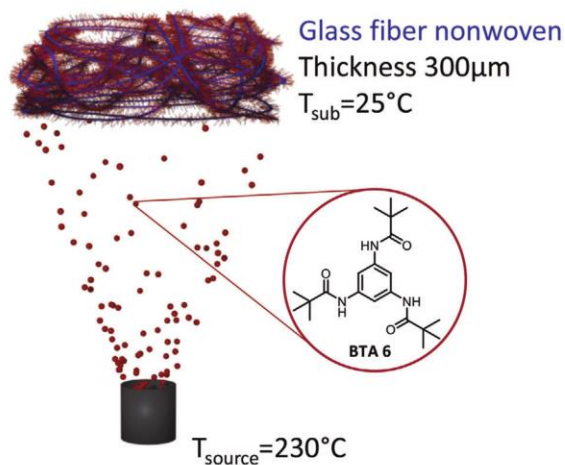
Figure 4. Schematic illustration of the controlled surface decoration of glass fiber nonwoven (blue) with supramolecular nanofibers of BTA 6 (red) resulting in hierarchical glass fiber superstructures using a T_{sub} of 25 °C and a T_{source} of 230 °C.

mat height to 4.1 µm, whereas the fiber diameter only slightly increases to 261 nm. Thus, increasing the evaporation rate mainly results in a roughly linear increase of the fiber mat height in a similar manner as it was found for the increase of the evaporation time. All these findings strongly indicate that the process to deposit nanofibers on silicon wafer is highly reproducible and largely independent on the selected PVD process parameters.

2.2. Hierarchical Superstructures of Supramolecular Nanofibers on Glass Fiber Nonwovens

Before transferring the process of supramolecular nanofiber formation on GF nonwovens, we evaluated the deposition process on the quartz glass slides and compared the resulting morphology with those found on the silicon wafers. For this, we selected an appropriate set of conditions, including a substrate temperature of 25 °C, an evaporation rate of 1.4 µg s^{-1} and evaporation rate of 30 min. The top and side view SEM images of the fiber morphologies on glass and silicon are depicted in Figure S7 (Supporting Information). The average fiber diameter on silicon was found to be 204 nm, which is 241 nm somewhat larger on the glass substrate. The average fiber mat height of 2.22 µm on silicon substrates is with a height of 2.20 µm on glass substrates very similar, which suggests that a very similar fiber morphology can be obtained on the different substrate materials.

Subsequently, the PVD process was transferred to GF nonwovens, which were then decorated with defined supramolecular nanofibers of **BTA 6**, as illustrated in **Figure 4**. Here, we selected a GF nonwoven with a thickness of 300 µm and GF diameter ranging from 8–14 µm (see Figure S8, Supporting Information). The average GF diameter was ≈10.5 µm, indicating that the GF nonwoven consists of ≈30 layers.

To prepare hierarchical glass fiber superstructures with BTA supramolecular nanofibers, square pieces of neat GF 7.6 cm × 7.6 cm were placed in the vapor deposition chamber.

The PVD process was performed in a similar manner as described before comprising at a source temperature of 230 °C and an evaporation rate of 1.4 µg s^{-1}. To ensure a complete coverage of the nonwoven with supramolecular nanofibers, the substrate was flipped by 180° after the evaporation and the process was repeated in the same manner. To evaluate the fiber growth with evaporation time, a similar combinatorial approach was chosen. Thus, we created three different sectors, which are exposed to three different evaporation times, i.e., 15, 30, and 45 min. **Figure 5** depicts excerpts of the SEM images of the resulting hierarchical superstructures after different evaporation times. The corresponding full SEM images are depicted in Figure S9 (Supporting Information). All SEM images show a homogeneous coverage with supramolecular nanofibers on the glass microfibers, with increasing fiber density and fiber length depending on the evaporation time. Thus, fiber growth and morphology develop in a similar manner as found for flat substrates, resembling in this case a bottlebrush-type morphology. From the SEM images in Figure 5 the average superstructure diameter (dashed lines) are determined to be ≈13 µm (for 15 min), 19 µm (for 30 min) and 24 µm (for 45 min) evaporation time. Assuming an average diameter of 10 µm for a neat glass microfiber (solid lines), the supramolecular nanofiber length is estimated to ≈1.5, 4.5, and 7 µm for the respective evaporation time.

Since a homogeneous and fully covered GF nonwoven is a key step for the following nucleation experiments, we repeated the PVD experiment using a GF nonwoven and evaporation time of 45 min. After the substrate was flipped and the PVD process repeated, we investigated the front and backside of the GF nonwoven by SEM and evaluated the homogeneity of the morphology. The SEMs are shown in Figure S10 (Supporting Information) demonstrating the very homogenous decoration of the front and the back side of the same GF nonwoven with supramolecular nanofibers.

2.3. Nucleation of Isotactic Polypropylene

2.3.1. Nucleation of Isotactic Polypropylene with Supramolecular Nanofibers Prepared by PVD

Supramolecular nanofibers of **BTA 6** are known to act as efficient nucleating and clarifying agents for isotactic polypropylene (iPP).[12] Powder X-ray diffraction of **BTA 6** reveals columnar arrangement of the molecules driven by three helical strands of hydrogen bonds with a space group of $P2_12_12_1$, in a orthorhombic metric of $a = 14.91(5)$ Å, $b = 24.05(8)$ Å, $c = 6.80(2)$ Å.[41] The same crystallographic features were found for nanostructures of **BTA 6** in iPP, which is close to the c-axis of the crystalline part of iPP (≈6.50 Å) providing evidence for an epitaxial match of the supramolecular nanofibers surface with iPP.[42] To verify that supramolecular nanofibers prepared by PVD have the same crystallographic features we performed a powder X-ray diffraction experiment on nanofibers scratched off Gfs slides and found a good agreement with the previously reported values (Figure S11, Supporting Information). Furthermore, we studied the nucleation capability of the PVD prepared nanofibers of **BTA 6** by placing scratched off fibers on a melt of iPP at 170 °C (Figure S12A, Supporting Information). Birefringent supramolecular nanofibers
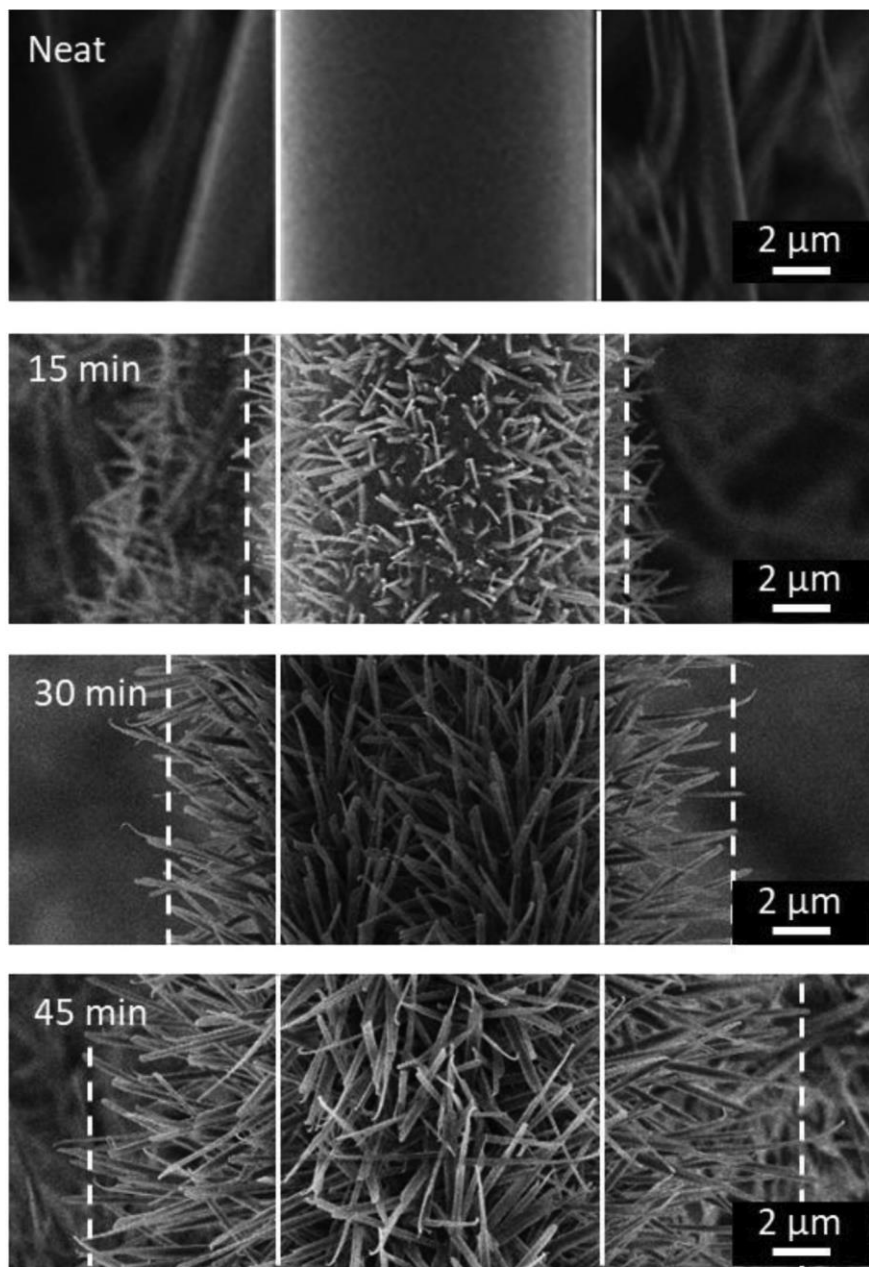
Figure 5. SEM images of the neat glass fiber nonwoven and hierarchical superstructures prepared via physical vapor deposition of **BTA 6** on the glass fiber nonwoven at different evaporation times of 15, 30, and 45 min ($T_{sub} = 25\ °C$, evaporation rate $= 1.4\ \mu g\ s^{-1}$). The white solid lines indicate the glass fiber diameter and the white dashed lines diameter of the bottlebrush structure including the supramolecular nanofibers. Full SEM images are depicted in Figure S9 (Supporting Information).

can be seen, which do not dissolve under these conditions. Upon cooling at 5 K min^{-1}, the birefringence around these fibers becomes much more pronounced at 135 °C, demonstrating the transcrystallization of iPP on the nanofibers of **BTA 6** (Figure S12B, Supporting Information). In the reference experiment, where only a neat iPP melt is studied, a homogeneous isotropic melt is observed at 170 °C (Figure S12C, Supporting Information), in which upon cooling, polymer crystallization in form of large spherulites is observed at 128 °C (Figure S12D, Supporting Information). These findings proof that supramolecular nanofibers prepared via PVD act as nucleation agents for the transcrystallization of iPP.

84
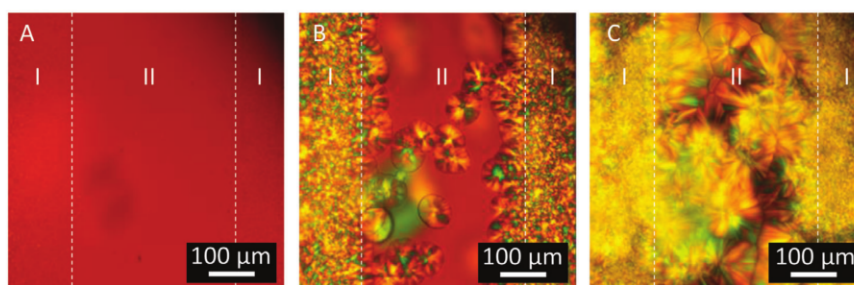
Figure 6. A) Polarized optical micrograph of iPP melt at 170 °C on top of areas alternating structures of vapor deposited BTA 6 with 300 µm feature size. The dashed white lines indicate the areas I where BTA 6 is deposited and the area II where no BTA 6 is present. B) Cooling with a rate of 5 K min^{-1} initiates the transcrystallization of the iPP melt in the areas of I at 132 °C in a homogeneous fashion. In area II without BTA 6 only some spherulites are formed. C) After further cooling, the entire iPP film is crystallized containing small-sized crystals in area I and large spherulites in area II. All micrographs are taken with $\lambda/4$ plate.

2.3.2. Nucleation of Isotactic Polypropylene on a Structured Substrate

Another interesting feature of the PVD process is that it allows the deposition of small molecules through masks, resulting in defined structured substrates. Here we used a slotted mask with a pattern of stripes and a spacing of 300 µm, which was attached close to the glass slide substrate before the PVD process took place. After vapor deposition of **BTA 6** an alternating pattern of supramolecular nanofibers of **BTA 6** was obtained on the glass slide. Figure 6A shows a molten iPP film at 170 °C with the **BTA 6** patterned glass slide on top of the polymer. Area I has a slightly grainy structure, which indicates the nanofibers, in contrast to area II, where only the neat iPP melt is present. Upon cooling the sample to 132 °C (Figure 6B), transcrystallization of the iPP is achieved selectively in area I. Interestingly, spherulitic structures are observed especially at the interface of the nucleated and non-nucleated areas, indicating homonucleation due to the heterogeneously formed polymer crystals. Upon further cooling, only spherulites are observed in area II, which ultimately leads to an alternating pattern of hetero-nucleated iPP with small crystals and homo-nucleated large spherulites (Figure 6CA).

2.3.3. Nucleation of Isotactic Polypropylene with Hierarchical Superstructures

Since we successfully demonstrated the nucleation capability of **BTA 6** nanofibers on flat glass substrates, we evaluate PVD-prepared hierarchical glass fiber superstructures with supramolecular nanofibers of **BTA 6** as a potential nucleation site for iPP. For this, we decorated a glass nonwoven with **BTA 6** nanofibers for 120 min on each side by PVD, resulting in bottlebrush structure with a supramolecular fiber mat of ≈10 µm. Subsequently, we removed individual decorated GFs by cutting. Figure 7A shows a polarized optical micrograph, in which such a hierarchical glass fiber superstructure is placed on top of an iPP melt at 170 °C. The superstructure can be clearly seen, which is homogeneously decorated with birefringent supramolecular nanofibers. The nanofibers are located perpendicular to the GF with some deviation, which is in agreement with previous findings (see **Figure 5**). Upon cooling with a rate of 5 K min^{-1},

transcrystallization of iPP on the supramolecular nanofibers occurs at 134 °C as evidenced by the pronounced birefringence (Figure 7B). Typically, transcrystallization of the polymer lamellae proceed perpendicular to the supramolecular fiber axis.[7] This means that the nucleated polymer lamellae are oriented parallel to the GF. On further cooling to 128 °C, the birefringence becomes brighter and continues to grow in a perpendicular direction to the GF featuring a crystalline layer of iPP with a width of ≈20 µm (Figure 7C). A closer look shows a spherulitic iPP growth located at the nucleated and non-nucleated interface, similar to that described before (see Figure 6). At this temperature, almost no homo-nucleation in the iPP film can be observed. To evaluate the influence of the neat GFs on the nucleation of iPP, we put a non-decorated single GF on top of the iPP melt as reference experiment (**Figure 7D**). Upon cooling, no transcrystallization from the neat GF can be observed (Figure 7E). Only at 124 °C the growth of large iPP spherulites can be observed, which is initiated randomly over the entire sample, demonstrating that no heterogeneous nucleation takes place (Figure 7F).

These findings indicate that decorating GF nonwovens with supramolecular nanofibers of **BTA 6** increases the adhesion between the GFs and the iPP matrix by establishing a surrounded dense network of fine-grained crystals of iPP, which is not the case using neat GFs. To demonstrate the beneficial role of this adhesion approach, we decorated a GF nonwoven with 10 wt.% of supramolecular nanofibers by PVD (evaporation time of 120 min per site). This hierarchical superstructure was then laminated between two sheets of iPP using a hot press that yields a GF reinforced composite material with a thickness of ≈450 µm (Figure S13, Supporting Information). For comparison, a reference was prepared by laminating a neat GF nonwoven without the supramolecular nanofibers between two iPP sheets under the same conditions. For both specimens, the amount of GF in the composite was ≈3 wt.%. Moreover, we prepared a second reference, which was based on the lamination of two neat iPP films under the same conditions resulting in the same thickness. From these specimens, dog bones were cut and used for tensile tests. We found that the neat iPP laminated specimen exhibit an E-Modulus of 1084 ± 113 MPa and an ultimate strength of 32.0 ± 2.6 MPa (stress–strain curves see Figure S14, Supporting Information). Reinforcing iPP with neat GF nonwoven increased the E-Modulus to 1264 ± 92 MPa and the ultimate strength to

ADVANCED
SCIENCE NEWS
www.advancedsciencenews.com

Macro-
molecular
Materials and Engineering
Open Access
www.mame-journal.de
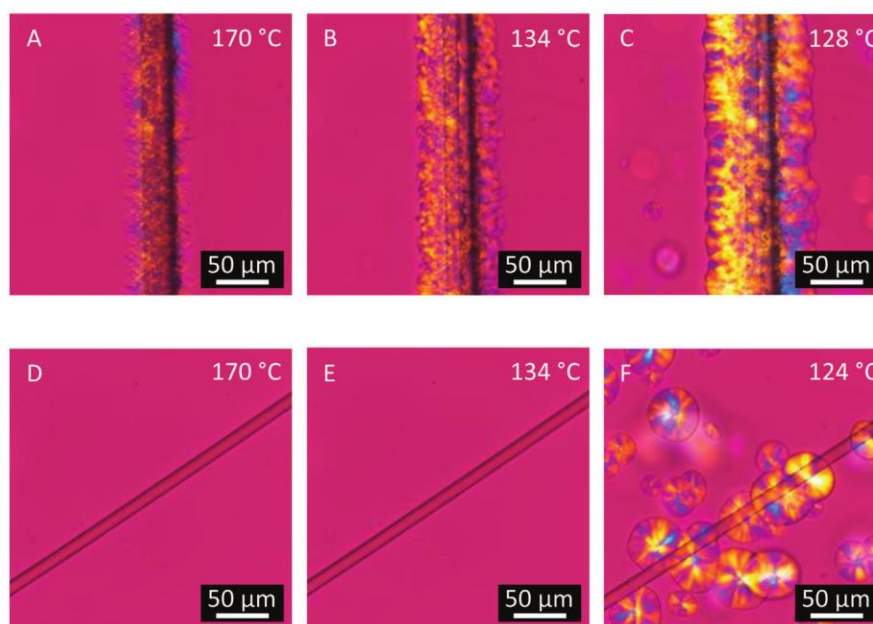
Figure 7. A) Polarized optical micrographs of a glass fiber decorated with supramolecular nanofibers of BTA 6 prepared via PVD, and placed into the melt of iPP at 170 °C. B) Transcrystallization of iPP nucleated form supramolecular nanofibers of BTA 6 at 134 °C after cooling it with a cooling rate of 5 K min⁻¹.C) The melt of iPP with a neat glass fiber without any BTA. D) Crystallization of large spherulites at 124 °C after cooling it down with a cooling rate of 5 K min⁻¹. All photographs taken with $\lambda/4$ plate.

33.0 ±2.1 MPa. The E-Modulus of the composite with the hierarchical GF nonwoven was determined to be 1609 ± 128 MPa and the ultimate strength was determined to be 37.0 ± 1.2 MPa. These findings confirm, that the supramolecular nanofibers play a beneficial role in the mechanical properties by improving the adhesion from the GFs to the iPP matrix due to tailored heterogeneous nucleation of iPP.

3. Conclusion

We demonstrated the formation of supramolecular nanofibers of 1,3,5-benzetrisamides with cycloaliphatic or branched peripheral substituents by physical vapor deposition. In particular, for **BTA 6**, a BTA with peripheral tert-butyl groups based on triaminobenzene, we systematically varied the PVD process parameters, i.e., substrate temperature, evaporation time, and evaporation rate, and show that supramolecular BTA nanofibers can be reproducibly prepared on flat substrates. The use of GF nonwovens as substrate enables the fabrication of hierarchical superstructures with a bottlebrush morphology comprising supramolecular nanofibers of defined lengths. These hierarchical superstructures are capable of nucleating iPP and thus promotes transcrystallization of the iPP from the decorated glass fibers surface. As a result, this improves the adhesion between the GF and the iPP, which is reflected by the increased mechanical properties of GF/iPP composites in contrast to composites without the nucleating agent. These findings demonstrate that the decoration of fibrous materials with supramolecular nanofibers by PVD is a

feasible approach to prepare superstructures, which can be transferred to other nucleating agents and semicrystalline polymers to achieve composites with improved mechanical properties.

4. Experimental Section

Physical Vapor Deposition of BTAs 1–6:   For physical vapor deposition of **BTA 1–6**, a modified vapor deposition chamber PLS 500 from Balzers was used.[43,44] Quartz crystal sensors were mounted near the substrate holder and used to monitor the evaporation rate. ≈500 mg of **BTA 1–6** was weighed into a quartz crucible, which was placed into an effusion cell used as a heating source. As substrate a silicon wafer, a quartz glass slide, or nonwoven made of GF was used. Applying a source temperature of T_{source} = 315 °C for **BTA 1**, T_{source} = 270 °C for **BTA 2**, T_{source} = 240 °C for **BTA 3**, T_{source} = 235 °C for **BTA 4**, T_{source} = 230 °C for **BTA 5**, and T_{source} = 230 °C for **BTA 6** at a pressure of 10^{-6} mbar, a constant apparent evaporation rate of 1.4 µg s⁻¹ was monitored by the quartz crystal sensors. For the preparation of the stepwise gradients, a combinatorial set-up was used to obtain three different sectors by moving a shutter by a distinct distance in a similar manner as described previously.[39] At the end of each experiment, the vacuum chamber was ventilated with air. For experiments with elevated substrate temperatures, a Peltier element was placed on the back side of the silicon wafer with a temperature sensor attached to the silicon wafer 2 cm away from it. A preheated copper block was put on top, which acts as a heat reservoir, allowing for a precise temperature adjustment within ±1 K. For nucleation experiments on a glass slide, a mask with 300 µm wide slits was used to produce a structured substrate with alternating areas of deposited and non-deposited nanofibers of **BTA 6**. Structured nanofibers were prepared using an evaporation rate of 1.4 µg s⁻¹ and an evaporation time of 120 min.

86

ADVANCED
SCIENCE NEWS

www.advancedsciencenews.com

acro-
molecular
Materials and Engineering
Open Access

www.mame-journal.de

Scanning Electron Microscopy: For scanning electron microscopy, samples with and without the physical vapor deposited structures on substrates were fixed via a double-sided adhesive conductive carbon tape on a SEM sample holder. For the side view SEM images, the respective samples were cut into half and clamped in a cross-section SEM holder. The samples were sputtered with platinum (1.3 nm) and SEM micrographs were recorded on a Zeiss Leo1530 FESEM.

Polarized Light Microscopy: Polarized light microscopy was performed using a polarized light microscope from Nikon (DIAPHOT 300). The optical micrographs were recorded by Nikon ACT-1 software using a digital camera (Nikon, DMX1200). Temperature-dependent measurements were performed using a hot stage (Mettler, model FP82TM). The samples were quickly heated to 170 °C and kept for 5 min at this temperature. Afterward the samples were cooled down with a cooling rate of 5 K min^{-1}. All images were recorded with a $\lambda/4$ plate.

Supporting Information

Supporting Information is available from the Wiley Online Library or from the author.

Acknowledgements

Conflict of Interest

The authors declare no conflict of interest.

Data Availability Statement

The data that support the findings of this study are available from the corresponding author upon reasonable request.

Keywords

[1] *Polypropylene Handbook. Morphology, Blends and Composites*, (Eds: J. Karger-Kocsis, T. Bárány), Springer, Cham, Switzerland **2019**.

[2] G. Wypych, *Handbook of Nucleating Agents*, 1st ed., ChemTec Publishing, Toronto, Canada **2016**.

[3] D. Libster, A. Aserin, N. Garti, *Polym. Adv. Technol.* **2007**, *18*, 685.

[4] *Plastics Additives Handbook*, (Eds: H. Zweifel, R.-D. Maier, M. Schiller), 6th ed., Hanser, München **2009**.

[5] F. Horváth, J. Molnár, A. Menyhárd, *Polypropylene Handbook. Morphology, Blends and Composites*, (Eds: J. Karger-Kocsis, T. Bárány), Springer, Cham, Switzerland **2019**, pp. 121–184.

[6] M. Gahleitner, C. Grein, S. Kheirandish, J. Wolfschwenger, *Int. Polym. Process.* **2011**, *26*, 2.

[7] K. Bernland, J. G. P. Goossens, P. Smith, T. A. Tervoort, *J. Polym. Sci. B: Polym. Phys.* **2016**, *54*, 865.

[8] K. Bernland, T. Tervoort, P. Smith, *Polymer* **2009**, *50*, 2460.

[9] C. Marco, G. Ellis, M. A. Gómez, J. M. Arribas, *J. Appl. Polym. Sci.* **2002**, *84*, 2440.

[10] J. Lipp, M. Shuster, A. E. Terry, Y. Cohen, *Langmuir* **2006**, *22*, 6398.

[11] Z. Horváth, B. Gyarmati, A. Menyhárd, P. Doshev, M. Gahleitner, J. Varga, B. Pukánszky, *RSC Adv.* **2014**, *4*, 19737.

[12] M. Blomenhofer, S. Ganzleben, D. Hanft, H.-W. Schmidt, M. Kristiansen, P. Smith, K. Stoll, D. Mäder, K. Hoffmann, *Macromolecules* **2005**, *38*, 3688.

[13] F. Abraham, S. Ganzleben, D. Hanft, P. Smith, H.-W. Schmidt, *Macromol. Chem. Phys.* **2010**, *211*, 171.

[14] F. Abraham, R. Kress, P. Smith, H.-W. Schmidt, *Macromol. Chem. Phys.* **2013**, *214*, 17.

[15] M. P. Lightfoot, F. S. Mair, R. G. Pritchard, J. E. Warren, *Chem. Commun.* **1945**, 1999.

[16] M. Kristiansen, P. Smith, H. Chanzy, C. Baerlocher, L. Gramlich, L. McCusker, T. Weber, P. Pattison, M. Blomenhofer, H.-W. Schmidt, *Cryst. Growth Des.* **2009**, *9*, 2556.

[17] T. P. Sathishkumar, S. Satheeshkumar, J. Naveen, *J. Reinf. Plast. Compos.* **2014**, *33*, 1258.

[18] P. K. Mallick, *Fiber-Reinforced Composites. Materials, Manufacturing, and Design*, 3rd ed., CRC Press, Boca Raton, FL **2007**.

[19] M. Etcheverry, S. E. Barbosa, *Materials* **2012**, *5*, 1084.

[20] E. Mäder, H.-J. Jacobasch, K. Grundke, T. Gietzelt, *Compos. A* **1996**, *27*, 907.

[21] J. L. Thomason, G. E. Schoolenberg, *Composites* **1994**, *25*, 197.

[22] W. Liu, Y. Zhu, C. Qian, H. Dai, Y. Fu, Y. Dong, *Compos. B* **2022**, *241*, 110029.

[23] J. F. Feller, Y. Grohens, *Compos. A* **2004**, *35*, 1.

[24] N.-J. Lee, J. Jang, *Compos. Sci. Technol.* **1998**, *57*, 1559.

[25] D. Bikiaris, P. Matzinos, A. Larena, V. Flaris, C. Panayiotou, *J. Appl. Polym. Sci.* **2001**, *81*, 701.

[26] B. Wang, Y. Zheng, C. Yu, P. Pan, *Cryst. Growth Des.* **2023**, *23*, 7535.

[27] H. A. Rijsdijk, M. Contant, A. Peijs, *Compos. Sci. Technol.* **1993**, *48*, 161.

[28] N. Ning, S. Fu, W. Zhang, F. Chen, K. Wang, H. Deng, Q. Zhang, Q. Fu, *Prog. Polym. Sci.* **2012**, *37*, 1425.

[29] N. Ning, W. Zhang, J. Yan, F. Xu, T. Wang, H. Su, C. Tang, Q. Fu, *Polymer* **2013**, *54*, 303.

[30] X.-Y. Xia, L.-Y. Ding, Q. Lv, X.-D. Wang, L.-S. Liao, *Adv. Electron. Mater.* **2022**, *8*, 2200753.

[31] Y. S. Zhao, D. Xiao, W. Yang, A. Peng, J. Yao, *Chem. Mater.* **2006**, *18*, 2302.

[32] Y. S. Zhao, C. Di, W. Yang, G. Yu, Y. Liu, J. Yao, *Adv. Funct. Mater.* **2006**, *16*, 1985.

[33] S.-C. Suen, W.-T. Whang, F.-J. Hou, B.-T. Dai, *Org. Electron.* **2007**, *8*, 505.

[34] J. S. Lee, I. Yoon, J. Kim, H. Ihee, B. Kim, C. B. Park, *Angew. Chem., Int. Ed.* **2011**, *50*, 1164.

[35] L. Adler-Abramovich, D. Aronov, P. Beker, M. Yevnin, S. Stempler, L. Buzhansky, G. Rosenman, E. Gazit, *Nat. Nanotechnol.* **2009**, *4*, 849.

[36] K. Tao, P. Makam, R. Aizen, E. Gazit, *Science* **2017**, *358*, eaam9756.

ADVANCED
SCIENCE NEWS

www.advancedsciencenews.com

Macro-
molecular
Materials and Engineering
Open Access

www.mame-journal.de

[37] S. A. Arabi, J. Dong, M. Mirza, P. Yu, L. Wang, J. He, C. Jiang, *Cryst. Growth Des.* **2016**, *16*, 2624.

[38] Y.-C. Chiu, B.-H. Chen, D.-J. Jan, S.-J. Tang, K.-C. Chiu, *Cryst. Res. Technol.* **2011**, *46*, 295.

[39] D. Schröder, C. Neuber, U. Mansfeld, K. Kreger, H.-W. Schmidt, *Small Sci.* **2024**, *4*, 2300160.

[40] D. Schröder, U. Mansfeld, K. Kreger, H.-W. Schmidt, *Adv. Mater. Interfaces* **2024**, *11*, 2400259.

[41] M. Schmidt, J. J. Wittmann, R. Kress, D. Schneider, S. Steuernagel, H.-W. Schmidt, J. Senker, *Cryst. Growth Des.* **2012**, *12*, 2543.

[42] M. Schmidt, J. J. Wittmann, R. Kress, H.-W. Schmidt, J. Senker, *Chem. Commun.* **2013**, *49*, 267.

[43] M. Bäte, C. Neuber, R. Giesa, H.-W. Schmidt, *Macromol. Rapid Commun.* **2004**, *25*, 371.

[44] C. Neuber, M. Bäte, M. Thelakkat, H.-W. Schmidt, H. Hänsel, H. Zettl, G. Krausch, *Rev. Sci. Instrum.* **2007**, *78*, 72216.

Supporting Information

Hierarchical Glass Fiber Superstructures with Supramolecular Nanofibers for the Nucleation of Isotactic Polypropylene

Dennis Schröder, Jannik Thanner, Klaus Kreger and Hans-Werner Schmidt*

WILEY-VCH

Supporting Information

Hierarchical glass fiber superstructures with supramolecular nanofibers for the nucleation of isotactic polypropylene

*Dennis Schröder,[1] Jannik Thanner,[2] Dr. Klaus Kreger,[1] and Prof. Dr. Hans-Werner Schmidt[1] ***

[1]Macromolecular Chemistry I and Bavarian Polymer Institute, University of Bayreuth, 95447 Bayreuth, Germany

[2]Inorganic Colloids for Electrochemical Energy storage, University of Bayreuth, 95447 Bayreuth, Germany

Table of content

WILEY-VCH

Section 1: Materials and methods

Materials

The synthesis of **BTA 1-6** is described elsewhere.[1] Silicon wafers were obtained from Siegert Consulting. Quartz glass slides were purchased from ThermoFisher Scientific. Glass fiber nonwovens (30 g/m^2) were purchased from HP-Textiles GmbH. Isotactic polypropylene (Profax PH 350, Mn ~6 × 10^4 g mol^{-1}; Mw ~4 × 10^5 g mol^{-1}) were purchased from Montell.[2]

Methods

Thermogravimetric analyses (TGA) were performed in the range from 30 to 700 °C with a heating rate of 10 K min^{-1} under a nitrogen atmosphere with a flow rate of 30 mL min^{-1} using a Mettler Toledo TGA/DSC3+ Star.

High performance liquid chromatography (HPLC) of **BTA 6** was performed on an Agilent series 1100 equipped with a Zorbax, Eclipse, Plus-C18 column and an UV-detector. As eluent acetonitrile/water 60/40 at a flow rate of 0.5 mL min^{-1} was used. The injection volume was 5 µL.

Powder X-Ray Diffraction (XRD): Supramolecular nanofibers of **BTA 6** were prepared via physical vapor deposition on a silicon substrate. These nanofibers were scratched off with a scalpel and used for powder XRD analysis. Powder X-ray diffraction was measured in transmission mode on a STOE Stadi P diffractometer equipped with a Dectris Mython 1 K detector. Diffraction patterns were recorded with Cu-Kα1 radiation (λ = 1.54056 Å, Ge111 monochromator) using a step size of 0.1° and an irradiation time of 60 seconds per step. The sample was sealed in a glass capillary (Hilgenberg GmbH, Germany, 0.7 mm outside diameter).

Polarized light microscopy were performed using a polarized light microscope from Nikon (DIAPHOT 300). Polarized light micrographs were recorded by a Nikon ACT-1 software using a digital camera (Nikon, DMX1200). Temperature profiles were realized using a hot stage (Mettler, model FP82TM).

Glass fiber nonwoven reinforced polypropylene specimen were prepared by sandwiching a neat glass fiber nonwoven or a PVD-structured glass fiber nonwoven with 10 wt% of **BTA 6** nanofibers between two polypropylene films and hot pressing them together with 1.500 kg of force at 210°C for 1 min. After cooling specimen were punched out (Coesfeld Materialtest Inc., electro-hydraulic punching cutter, mold knife for tensile specimen DIN 53 504 S3A)

Tensile tests were performed according ISO 527 on an Instron® 5565 universal tester with pneumatic clamps and a 1 kN load cell. The thickness of the specimens was measured with a digital micrometer (Mitutoyo® 293–831, digimatic MDC Lite). The E-modulus was investigated at a strain rate of 0.2 mm min^{-1} and calculated between 0.1 % and 0.3 % of the strain. After strain of 0.3 %, strain rates of 10.0 mm min^{-1} were applied.

---

[1] Schmidt, H.-W.; Smith, P.; Blomenhofer, M. WO 02/46300 A2.

[2] M. Blomenhofer, S. Ganzleben, D. Hanft, H.-W. Schmidt, M. Kristiansen, P. Smith, K. Stoll, D. Mäder, K. Hoffmann, ""Designer" Nucleating Agents for Polypropylene", *Macromolecules* **2005**, *38*, 3688.

Section 2: Thermal analysis of **BTA 1-6**
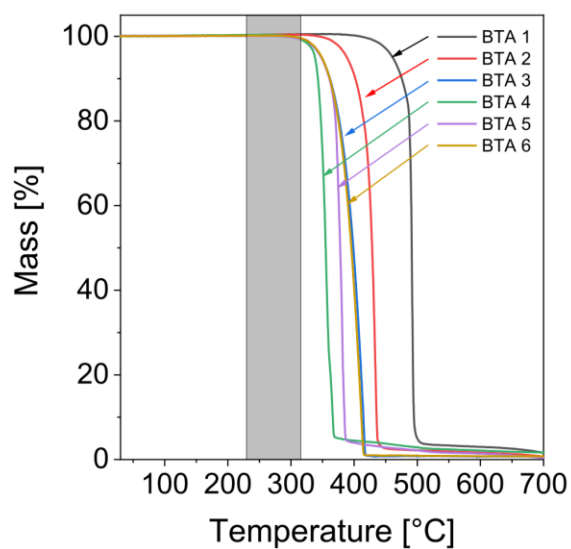
Figure S1. TGA measurement of **BTA 1-6** from 50-700°C at a heating rate of 10 K min^{-1} under N$_2$ with a flow rate of 30 mL min^{-1}. No weight loss occurs until a temperature of 300 °C, indicating a high thermal stability without decomposition into small fragments. The grey area represents the temperature range used for the evaporation of **BTA1-6** during the PVD process.

WILEY-VCH

Section 3: HPLC analysis of **BTA 6** before and after PVD
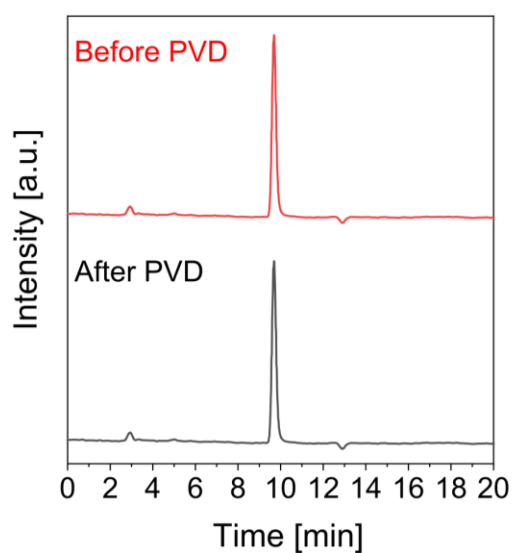
Figure S2: HPLC elugrams of **BTA 6** before PVD (red) and after self-assembly using PVD (black). Both elugrams feature a retention time for **BTA 6** of 9.7 min, demonstrating that the chemical structure is not changed during the PVD process. HPLC conditions: eluent: acetonitrile/water 60/40, flow rate: 0.5 mL min^{-1}, injection volume: 5 µL.

4

WILEY-VCH

Section 4: Supramolecular fiber morphology at different substrate temperatures
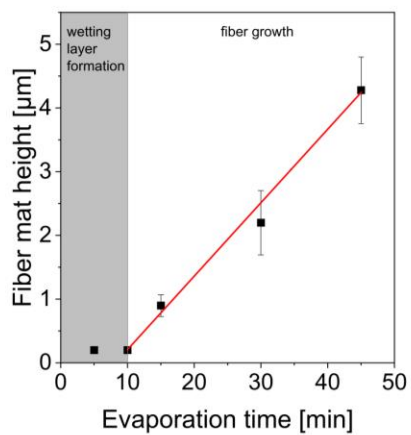
Substrate Temperature
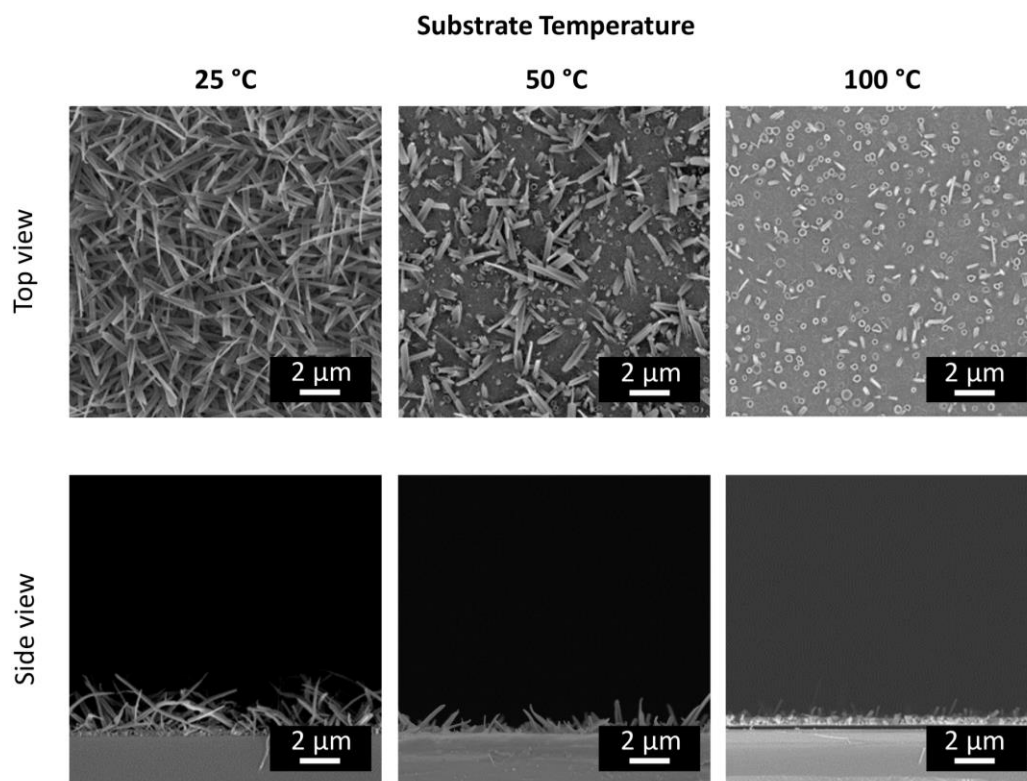
Figure S3. Top and side view SEM images of supramolecular nanofibers of **BTA 6** prepared by PVD on silicon wafers depending on the substrate temperature. The evaporation rate was set to be 1.4 µg s^{-1} resulting from a source temperature of T$_{source}$ = 230°C and an evaporation time of 30 min.

5

WILEY-VCH

Section 5: Supramolecular fiber morphology at different evaporation times
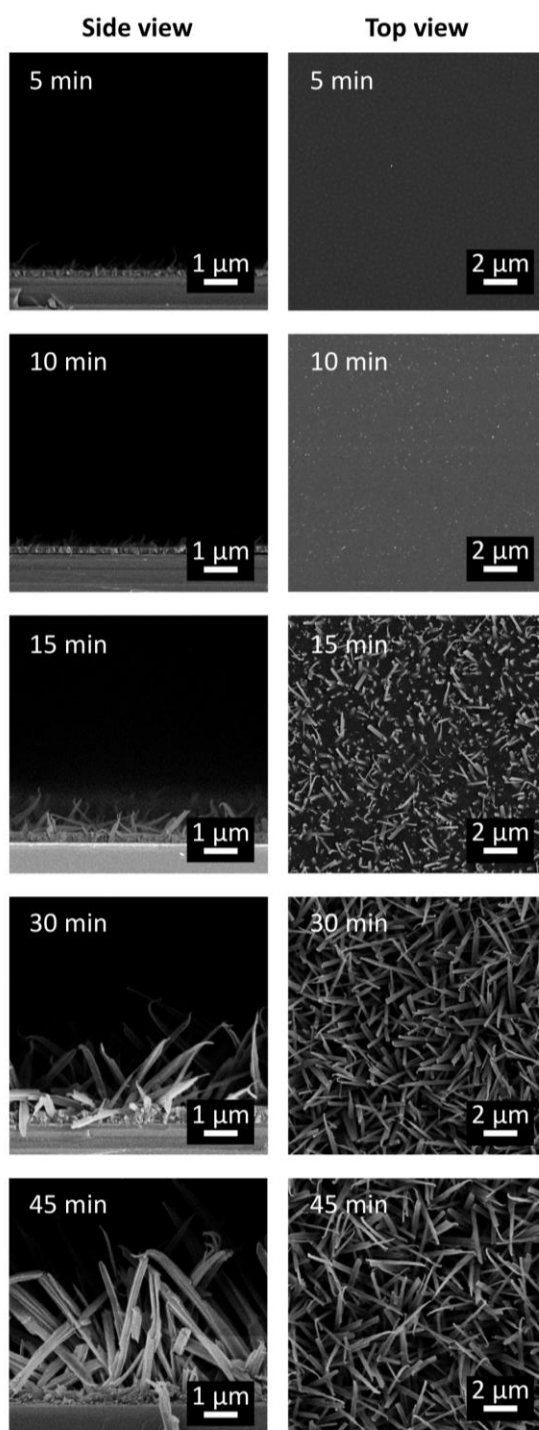
Figure S4. SEM images of vapor deposited **BTA 6** on the same silicon wafer at different evaporation times in a combinatorial approach of the PVD experiment comprising five different sectors (evaporation rate = 1.4 µg s^{-1}, T$_{source}$ = 230°C, T$_{sub}$ =25°C). The five different vapor exposure times, i.e. of 5, 10, 15, 30 and 45 min were realized by successively covering the substrate with a shutter for the given time.

6

WILEY-VCH

Figure S5. Average fiber mat height of vapor deposited **BTA 6** with increasing evaporation time derived. Within the first 10 min only a wetting layer with a thickness of about 0.20 to 0.25 μm is formed. The average fiber mat height was determined 0.90 ± 0.2 μm (15 min), 2.2 ± 0.5 μm (30 min), and 4.3 ± 0.5 μm (45 min). Supramolecular fiber growth proceeds in a linear fashion with a growth rate of 0.1 μm min^{-1}.

7

WILEY-VCH

Section 6: Supramolecular fiber morphology at different evaporation rates
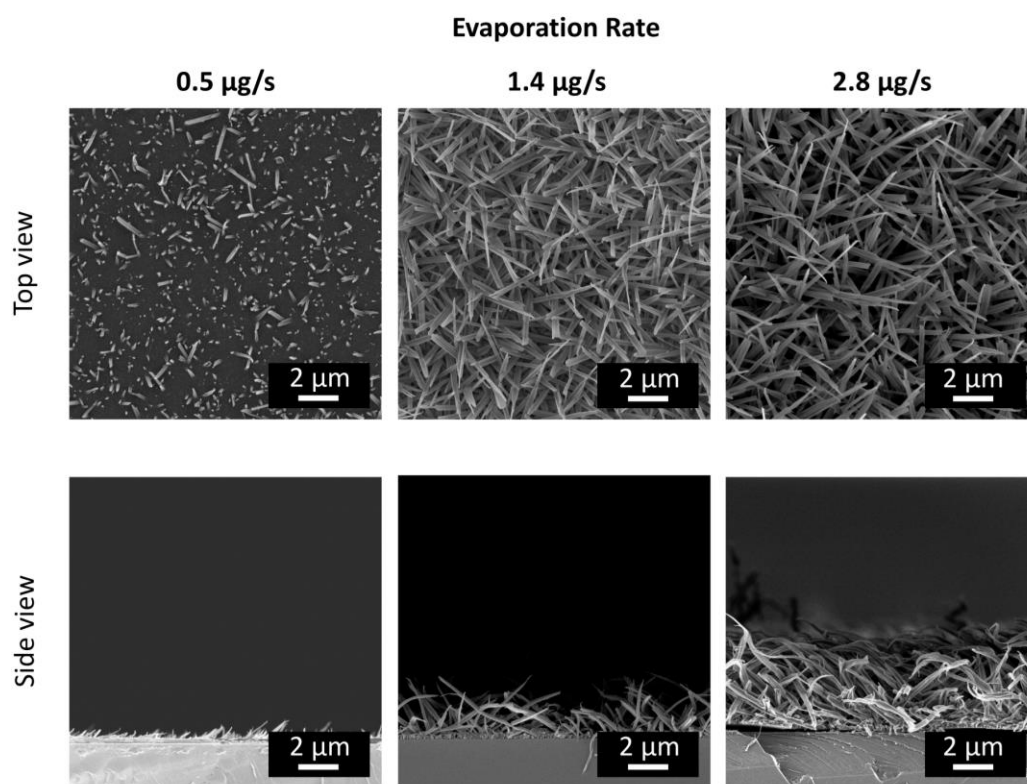
Figure S6. Top and side view SEM images of supramolecular nanofibers of **BTA 6** prepared by PVD on silicon wafers with T_{sub} = 25°C at different evaporation rates and an evaporation time of 30 min for each PVD process. Applying source temperatures of T_{source} = 220°C, 230°C, and 250°C yielded constant evaporation rates of 0.5, 1.4 and 2.8 µg s^{-1}, respectively.

8

Section 7: Supramolecular fiber morphology on different flat substrates

Substrate Material
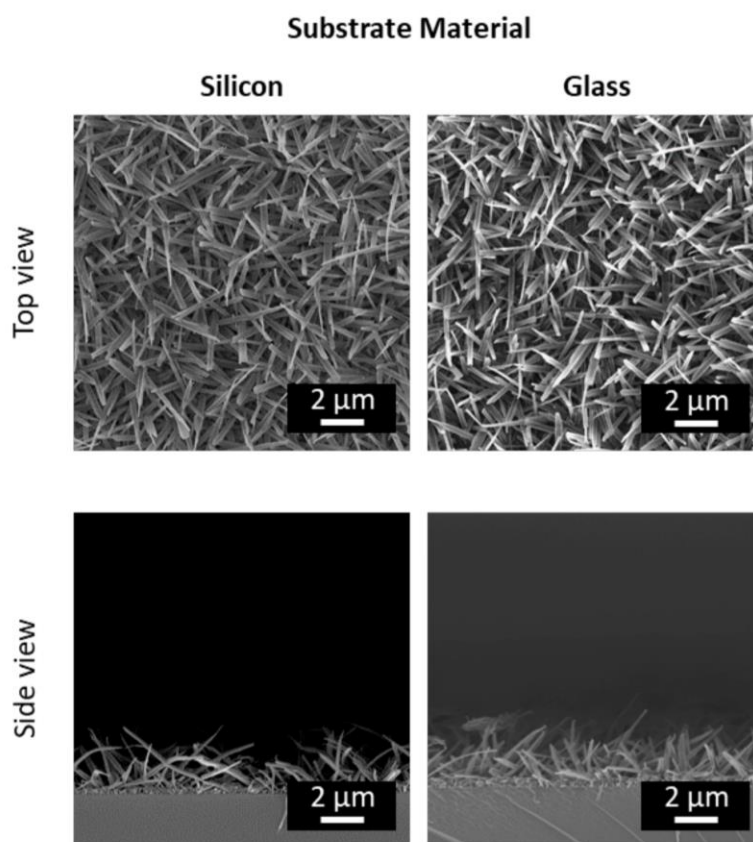
Figure S7. Top and side view SEM images of supramolecular nanofibers of **BTA 6** prepared by PVD on a silicon wafer and a glass slide at a substrate temperature of T_{sub} = 25 °C. The evaporation rate was 1.4 µg s^{-1} using a source temperature of T_{source} = 230°C and an evaporation time of 30 min.

9

WILEY-VCH

Section 8: Characterization of neat glass fiber nonwovens
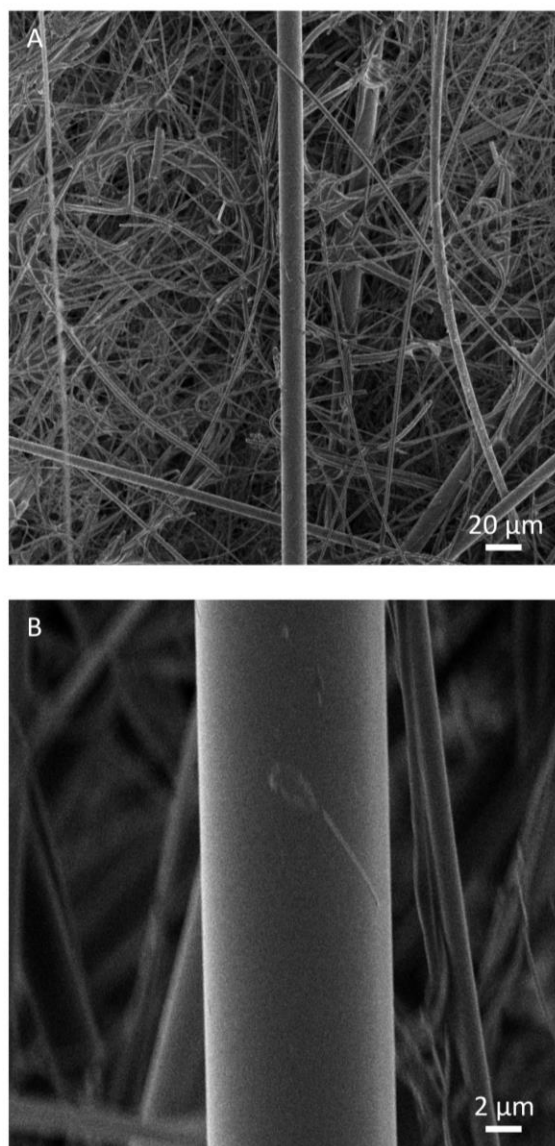
Figure S8. SEM micrographs of an overview (A) and magnification (B) of the used neat glass fiber nonwoven.

10

WILEY-VCH

Section 9: Hierarchical structures of **BTA6** on glass fibers
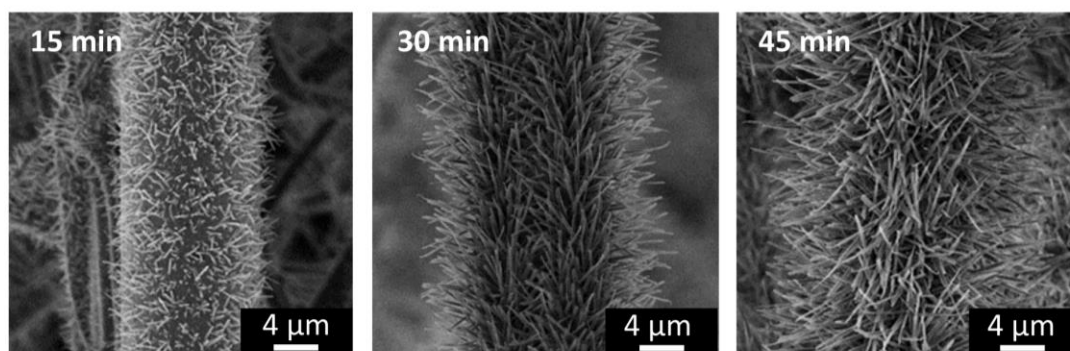
Figure S9. SEM images of hierarchical superstructures prepared via PVD of **BTA 6** on glass fiber nonwovens at T_{sub} = 25°C. The evaporation rate was 1.4 µg s^{-1} using a source temperature of T_{source} = 230°C. Evaporation time was 15, 30 and 45 min for each side.
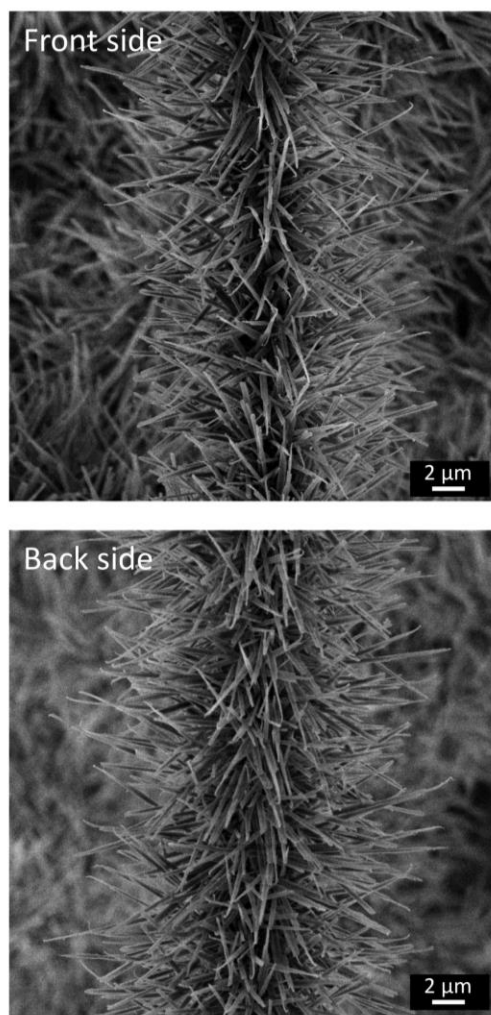

Figure S10. SEM images of the front and back side of hierarchical superstructures prepared via PVD of **BTA 6** on a glass fiber nonwoven at T_{sub} = 25°C. The evaporation rate was 1.4 µg s^{-1} using a source temperature of T_{source} = 230°C. Evaporation time was 45 min for each side.

11

WILEY-VCH

Section 10: XRD of supramolecular nanofibers of **BTA 6** prepared via PVD
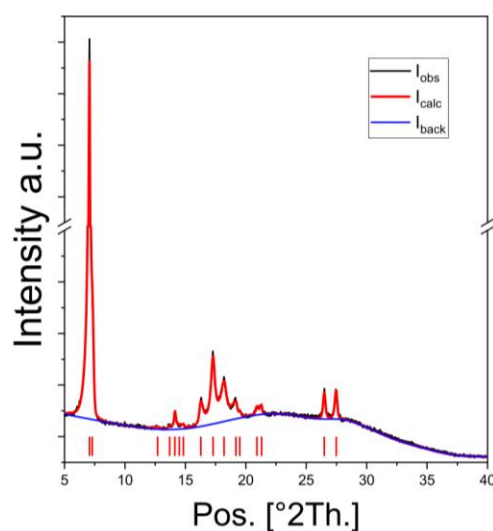
Figure S11. Superposition of powder diffractogram of supramolecular nanofibers of **BTA 6** prepared via PVD (I_{obs}, black), the fitted profile of the diffractogram (I_{calc}, red) and the background (I_{back}, blue). The cell parameters can be deduced as a = 14.80(3) Å, b = 23.8(1) Å, c = 6.74(3) Å, which is in good agreement with previously reported values. All observed reflexes align with predicted ones assuming the $P2_12_12_1$ space group, as previously reported.[3]

---

[3] M. Schmidt, J. J. Wittmann, R. Kress, D. Schneider, S. Steuernagel, H.-W. Schmidt, J. Senker "Crystal Structure of a Highly Efficient Clarifying Agent for Isotactic Polypropylene", *Cryst. Growth Des.* **2012**, *12*, 2543.

WILEY-VCH

Section 11: Crystallization and heterogeneous nucleation of iPP

Reference experiment
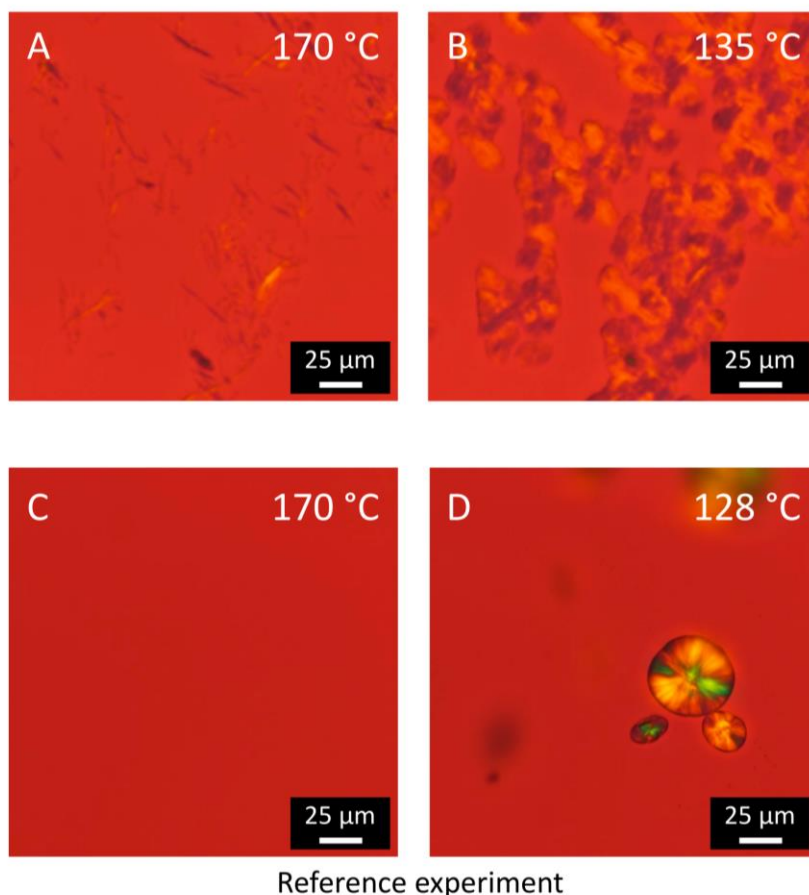
Figure S12. Polarized optical micrographs of supramolecular nanofibers of **BTA 6** prepared by PVD, which was mechanically scratched off the silicon substrate and placed on a melt of iPP at 170°C (A). Transcrystallization of iPP nucleated from supramolecular nanofibers of **BTA 6** at 135°C after cooling it with a cooling rate of 5 K min^{-1} (B). Reference experiment showing only a iPP melt without BTA nanofibers at 170°C (C). Crystallization of large spherulites takes place at 128°C after cooling it down with a cooling rate of 5 K min^{-1} (D). All photographs are taken with λ/4 plate.

13

WILEY-VCH

Section 12: Tensile tests on laminated iPP composites
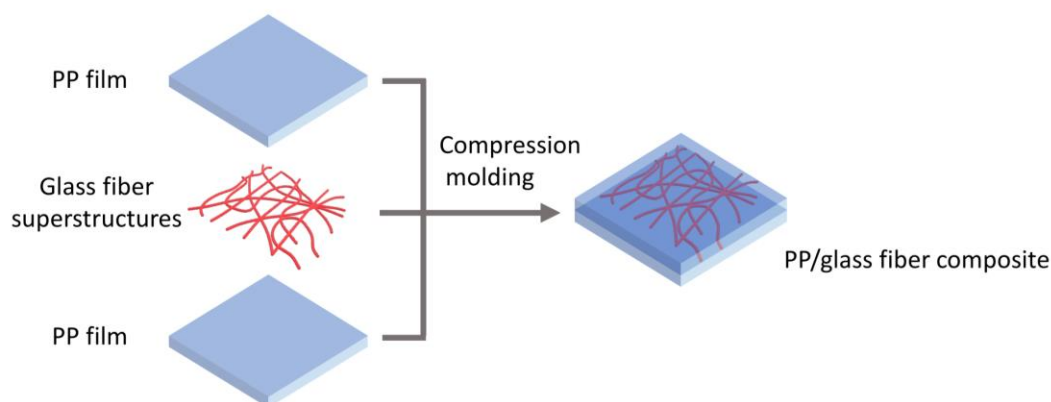
Figure S13. Schematic illustration of the process to prepare laminated structures using PP films and glass fiber nonwoven or glass fiber nonwoven with 10 wt% of **BTA 6**. Compression molding at 210°C with 1.5 metric tons of force for 1 min resulted in homogeneous composites. The typical thickness of all composites was approximately 450 µm.
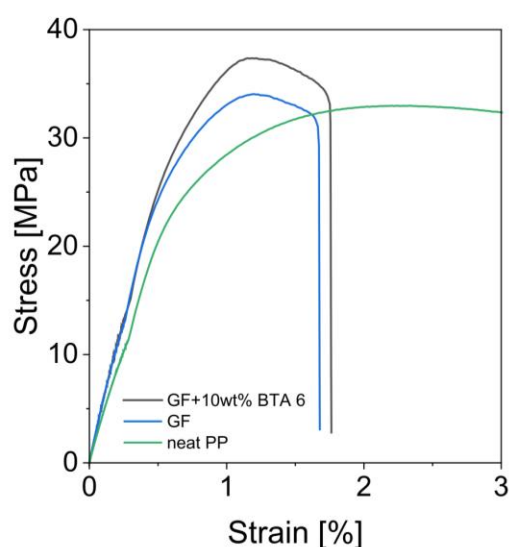
Figure S14. Representative stress-strain curve for PP/PP composite (green), PP/GF/PP composite (blue) and PP/GF+10wt%BTA6/PP (black) composite. Elongation for PP/PP was stopped after 100 % strain (not shown). The E-modulus was calculated to be 1084±113 MPa for PP/PP, 1264±92 MPa for PP/GF/PP and 1609±128 MPa for PP/GF/10wt%BTA/PP.

14

4.3 Publication 2

Mesostructured Polymer and Glass Microfiber Nonwovens with Supramolecular 1,3,5-Benzenetrisamide Nanofibers for Air Filtration

Dennis Schröder, Klaus Kreger, and Hans-Werner Schmidt*

Cite This: *ACS Appl. Mater. Interfaces* 2025, 17, 14569−14577

Read Online

ACCESS | ▥ Metrics & More | ▤ Article Recommendations | ▣ Supporting Information

ABSTRACT: Hierarchically mesostructured nonwovens with complex fiber morphologies are gaining more and more interest for filtration applications as the increased surface area offers improved filtration efficiencies for particulate matter. Several concepts are known to fabricate such complex fiber morphologies; however, the control over the morphology remains challenging. Here, we report on the preparation of mesostructured nonwovens decorated with defined supramolecular nanofibers by physical vapor deposition of a selected commercially available 1,3,5-benzenetrisamide (BTA). Using polymer nonwovens as a support, we show that with this solvent-free process, the supramolecular nanofiber length can be tuned from 5 to 20 μm depending on the evaporation time resembling a bottlebrush-like morphology on the mesoscale. Whereas the model polymer nonwoven is unsuitable to capture particulate matter, the mesostructured nonwovens show an increasingly improved filtration efficiency of up to 87% for 2.0 μm particles at a low pressure drop of 90 Pa. Since the selected BTA has a pronounced thermal stability, this also enables the preparation of more temperature-resistant mesostructured nonwovens using a glass microfiber nonwoven as a support. We show that the morphology as well as the filtration efficiency of the mesostructured glass fiber nonwoven is maintained even after heat treatment at 200 °C for 24 h. This cannot be realized with nonwovens based on commodity polymers and engineering plastics. These results prove the general applicability of vapor-deposited supramolecular nanofibers and broaden the application window for such mesostructured nonwovens in the field of filtration and separation toward more efficient, robust, and also selective filter media.

KEYWORDS: *mesostructured nonwovens, 1,3,5-benzenetrisamide, supramolecular nanofibers, physical vapor deposition, air filtration*
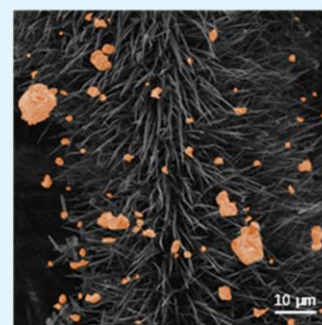
1. INTRODUCTION

Particulate matter (PM) is a serious issue affecting public health, the environment, and the climate.[1−3] Of particular concern are fine particles with diameters below 2.5 μm (PM$_{2.5}$), as they can penetrate deeply into the lungs and cause respiratory diseases, which can also lead to premature death.[4−6] The primary process for removing particulate matter is filtration, whereby conventional filter media are often based on inorganic or polymeric microfibers.[7] The use of microfiber-based filter media, however, faces a trade-off between filtration efficiency and pressure drop, the latter being related to the diameter of the microfiber, which causes the drag.[8,9] This renders the use of nanofibrous materials highly promising because nanofibers feature an advantageously larger surface−volume ratio for particle deposition and do not significantly contribute to the drag as compared to microfibers.[9] In this context, electrospinning is an established and widely used top-down technique for the production of polymer nanofibers from solution in general but also from the melt.[10−12] Recent research focuses on the preparation and use of hierarchically structured systems combining different fiber types, fiber dimensions, or morphologies.[13,14] For example, the simultaneous electrospinning of two different polymer types, i.e., polyacrylonitrile including poly(ethylene oxide) as a binder

and polysulfone, resulted in hierarchically structured composite membranes with high filtration performance.[15,16] Such hierarchically structured fiber membranes, comprising so-called dual-scale fibers, can be also achieved by electrospinning of a single polymer component such as polyamides in the presence of surfactants featuring high filtration efficiencies.[17] Similarly, a fine dual-network structure can be achieved consisting of an electrospun scaffold in which very finely structured two-dimensional (2D) nanonets are embedded, with the latter being mainly responsible for the particle retention.[18−21]

Another approach to hierarchically structured fiber composites combines polymer and supramolecular fibers.[22−24] The formation of supramolecular fibers makes use of spontaneous self-assembly via secondary interactions of molecular building blocks typically processed from solution. Self-assembly is an in situ process that allows for a postmodification process step to create supramolecular fibers within an existing fiber support.

We demonstrated this in situ solution-based approach by using 1,3,5-benzenetricarboxamide derivatives as building blocks to prepare polymer/supramolecular fiber composites.[23,24] Such composites result in improved filtration performance for particulate matter. Similarly, composites can be realized using 1,3:2,4-di(3,4-dimethylbenzylidene) sorbitols as a building block, which yielded a dual-nanonet consisting of polymer and supramolecular nanofibers.[22] Hu et al. showed that such hierarchically structured filter media exhibit a high filtration efficiency at a low pressure drop.[22]

Other recent approaches make use of fibrous structures, which feature more complex morphologies.[13] For example, Xu et al. reported fiber morphologies, which are based on a central para-aramid fiber and off-standing para-aramid nanofiber branches. Proper postmodification initiates surface fibrillation, which subsequently forms the branches. They showed that these fiber morphologies feature very good filtration performance.[25,26] Similar morphologies can be achieved with distinct polymer solutions based on cellulose, poly(vinylpyridine), or poly(vinylidene fluoride), which results in fine branched fibrillation of the electrospun polymer fiber during processing.[27−29] We also demonstrated a similar fiber morphology comprising a central polymer fiber and off-standing branches based on supramolecular nanofibers. For this, we prepared, in a first step, electrospun polymer fibers, which were decorated with nuclei or seeds. In a second processing step, these nuclei or seeds were capable of initiating the self-assembly process, leading to off-standing supramolecular nanofibers.[30,31] We showed that such hierarchical structured morphologies feature high filtration efficiencies at low pressure drops.[32] However, it is challenging to control the seed density, as well as to precisely control the supramolecular fiber length, in these seed-initiated solution-based processes. In this context, nanofiber formation by physical vapor deposition (PVD) differs to some extent from solution-based processes. During vapor deposition of the molecular building blocks, a thin film is formed, depending on the substrate surface. At a critical film height, the growth mode changes from a "layer-by-layer" mode to a "layer-plus-island" mode, referred to as the Stranski−Krastanov growth.[33] The islands, in turn, act as nucleation sites for nanofiber growth. The number of islands can be controlled by conditions such as the substrate and substrate temperature, and nanofiber growth can be controlled by the monomer feed. Thus, the formation of supramolecular nanofibers by PVD does not require prior deposition of nucleation sites, while the length of the supramolecular fibers can be controlled by the evaporation time, as we have recently shown for BTAs and other building blocks.[34−36]

Here, we report on the preparation and use of mesostructured nonwovens for air filtration consisting of polymer or glass microfibers, which are decorated with defined supramolecular nanofibers by physical vapor deposition. As a molecular building block, a 1,3,5-benzenetrisamide (BTA), namely, 1,3,5-tris[2,2-dimethylpropionylamino]benzene, was selected (Figure 1). Upon vapor deposition of the building blocks, the BTAs stack cofacially on top of each other, resulting in supramolecular columns driven by the formation of three helical strands of hydrogen bonds between the amide groups.[37,38] The supramolecular columns are further organized into larger bundles in an antiparallel fashion to compensate for the macrodipoles formed by the directed hydrogen bonds.[39] Using a fibrous support for the deposition of the supramolecular nanofibers, the structure resembles a bottlebrush-
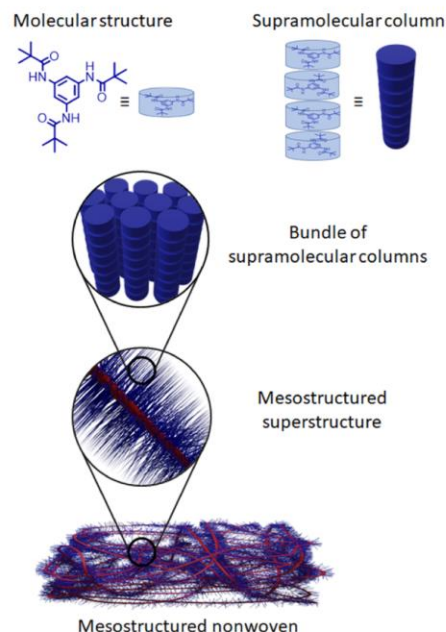
Figure 1. Schematic representation of the hierarchical structure of the mesostructured nonwoven prepared by physical vapor deposition. As a molecular building block, 1,3,5-tris[2,2-dimethylpropionylamino]-benzene (BTA) was selected. This building block assembles into a supramolecular column driven by three strands of hydrogen bonds, which further aggregate into bundles of columns representing a supramolecular nanofiber (blue). Depositing such supramolecular nanofibers on microfibers leads to mesostructured superstructures resembling a bottlebrush-like morphology on the mesoscale. Using either a polymer or glass nonwoven (red), a mesostructured nonwoven with supramolecular BTA nanofiber grafts is realized.

like morphology on the mesoscale, which exhibits similarities to morphologies of the well-known class of bottlebrush polymers typically found on the nanoscale.[40,41] In analogy to the preparation procedures for bottlebrush polymers, the supramolecular nanofiber growth can also be regarded as a "grafting-from" approach. Thus, the nanofibers may also be considered as supramolecular grafts. Since the PVD postmodification step is performed on nonwoven substrates instead of single fibers, the decoration with supramolecular nanofiber grafts leads to mesostructured nonwovens, which can be used for air filtration applications.

In a first set of experiments, we have chosen a viscose/polyester model nonwoven as a support, which is densely covered with supramolecular nanofibers. The length of the supramolecular nanofibers or grafts can be controlled by adjusting the evaporation time. Likewise, the supramolecular fiber length impacts the filtration performance for particulate matter. A well-known characteristic of 1,3,5-benzenetrisamides is their high thermal stability, which enables the preparation of temperature-resistant mesostructured nonwovens. For this, the polymer nonwoven is replaced by a glass microfiber nonwoven as a support and modified with supramolecular BTA fibers. This type of filter composite with supramolecular nanofiber grafts also allowed us to further improve the filtration efficiency, particularly for very fine particles with particle sizes of 0.3 to 2 μm. To demonstrate the capability to be used at elevated temperatures, the mesostructured glass nonwovens

were exposed to a temperature of 200 °C for 24 h. This heat treatment does not change the morphology or the filter performance. Our results show that such mesostructured nonwovens with supramolecular nanofiber grafts broaden the application window in the field of filtration and separation.

2. EXPERIMENTAL SECTION

2.1. Materials. The viscose/polyester microfiber nonwovens with a thickness of 0.15 mm and a basis weight of 32.2 g m^{-2} were commercially available from AMPri. The glass microfiber nonwoven, a commercially available filter medium, with a thickness of 0.5 mm and a basis weight of 100.4 g m^{-2} was purchased from Arteka e.K. 1,3,5-Tris[2,2-dimethylpropionylamino]benzene (BTA) was received from Ciba AG, now BASF SE.

2.2. Thermogravimetric Analyses (TGA) and Simultaneous Differential Thermal Analysis (SDTA). For thermogravimetric analyses, approximately 10 mg of the samples were weighed into crucibles. Dynamic TGA including SDTA was performed in the range from 30 to 700 °C with a heating rate of 10 K min^{-1} under nitrogen or air with a flow rate of 30 mL min^{-1} using a Mettler Toledo TGA/DSC3+ Star. Isothermal TGA was performed by heating the sample to the isothermal temperature with 10 K min^{-1}, which was held at this temperature for 10 min and then measured isothermally for 60 min.

2.3. Infrared Spectroscopy (IR). IR spectra were recorded of the BTA before and after PVD using a PerkinElmer Spectrum 100 FT-IR spectrometer in attenuated total reflection (ATR) mode in the range from 4000 to 650 cm^{-1}.

2.4. Physical Vapor Deposition. For preparation of mesostructured nonwovens, a modified vapor deposition chamber was used as described previously,[34,35] which is based on a PLS 500 from Balzers. Quartz crystal sensors were mounted near the substrate to monitor the evaporation rate. About 500 mg of BTA was weighed into a quartz crucible, which was placed into an effusion cell used as the heating source. The nonwoven was cut into pieces with dimensions of 7.6 cm × 7.6 cm (area of 57.8 cm^2) and fixed in a substrate holder. During the evaporation experiments, the substrate holder was rotated to ensure a uniform deposition. The temperature of the effusion cell was set to 230 °C, leading to an evaporation rate of 1.4 μg s^{-1} at a pressure of 10^{-6} mbar for the PVD experiments. Vapor deposition on the microfiber substrate was initially prevented by a closed shutter until a constant evaporation rate was reached. The shutter was then opened to start deposition. The total deposition times were 60, 120, and 240 min. After half of the deposition time, the substrate was flipped 180° to ensure coverage from both sides of the nonwoven.

2.5. Scanning Electron Microscopy (SEM). For SEM investigations, samples were fixed via double-sided adhesive conductive carbon tape on a SEM sample holder. Subsequently, the samples were sputtered with an about 2.0 nm thick layer of platinum using a Cressington Platinum-Sputter Coater 208HR. SEM micrographs were recorded using a Zeiss 1530 FESEM instrument at an acceleration voltage of 3 kV equipped with an Inlens detector.

2.6. Filter Testing. All measurements were performed using a filter test rig based on the MFP 2000 from PALAS equipped with an RBG 1000 powder dispenser and a Welas digital 2100 white-light-scattering spectrometer Welas digital 2100. As particulate matter, ISO 12103−1, A2 fine test dust, received from Powder Technology Inc., was used. For the filtration tests, the mesostructured fabrics were fixed with a pneumatic sample holder in the filter test rig. The samples had an effective filtration area of 28.3 cm^2. A particle concentration of 30,000 particles cm^{-3} was applied at a flow velocity of 0.25 m s^{-1} for a measuring time of 30 s. Particle sizes were recorded in the range of about 0.3 to 10.0 μm. The filtration efficiency was determined by recording the upstream concentration (particle concentration without filter media) and the downstream concentration (particle concentration after passing filter media). Filter efficiencies for the mesostructured polymer nonwoven were measured at the University of Bayreuth and for the mesostructured glass nonwovens were measured at PALAS GmbH.

2.7. Temperature Resistance Test. For this purpose, mesostructured glass nonwovens were placed in a drying oven, heated to 200 °C, and kept at this temperature in the air for 24 h. The mesostructured glass nonwovens were then cooled to room temperature. The morphology of the samples was analyzed using SEM, and the filter performance was determined as described above.

3. RESULTS AND DISCUSSION

1,3,5-Benzenetrisamides, in particular with short and bulky aliphatic side groups, are known to feature pronounced thermal as well as mechanical stability, which is comparable to semiaromatic polyamides.[42,43] In contrast to polymers build up by covalent bonds, the individual BTA molecules can be evaporated without decomposition due to the reversible nature of the hydrogen bond formation. For the selected BTA with *tert*-butyl side groups, dynamic thermogravimetric analysis (TGA) and simultaneous differential thermal analysis (SDTA) (Figure S1, SI) show that no mass loss and also no phase transition occur up to a temperature of 300 °C applying standard heating rates of 10 K min^{-1}. This finding is also supported by temperature-dependent polarization microscopy, in which no change in the appearance of the BTA powder can be observed up to 300 °C. At a temperature above 360 °C, a rapidly steep and steady decline to 0% was observed, indicating a complete sublimation of BTA without decomposition. To validate that evaporation occurs without decomposition, common analytical techniques, such as HPLC were used. This demonstrates the very good temperature stability of the BTA, which is a crucial requirement for processability by PVD. Initial PVD experiments on substrates, such as silicon wafers or glass substrates, were carried out to explore the morphology of the supramolecular nanofiber formation after deposition. As exemplarily shown in the SEM images of Figure S3, fiber mats with a height of 5 μm consisting of densely packed supramolecular nanofibers with an estimated diameter below 500 nm were found. IR spectroscopy shows that the spectra are almost the same before and after PVD. The amide A, amide I, and amide II vibrations were found at 3302, 1653, and 1529 cm^{-1}, respectively (Figure S4, SI), which were known to be sensitive to a distinct hydrogen pattern[44] and indicate a columnar stacking for the BTA.[36,45] Isothermal TGA measurements on the BTA for 1 h showed that no weight loss is observed at a temperature of 200 °C and only a small weight loss occurs at 300 °C, indicating sublimation of the BTA at these conditions (see Figure S2, SI). This shows that BTA nanofibers can be used for a longer period of time at temperatures of 200 °C. The above-presented findings demonstrate that the supramolecular nanofibers based on the BTA can be prepared by PVD and applied at temperatures beyond the continuous use temperature of common commodity polymers and engineering plastics.

3.1. Supramolecular BTA Nanofibers on Polymer Microfiber Nonwovens. For the preparation of a mesostructured polymer nonwoven with supramolecular nanofibers of the BTA, a model polymer nonwoven with a thickness of 0.15 mm and an average microfiber diameter of 13 μm was selected. PVD of the BTA resembles a solvent-free post-modification process step to decorate the polymer microfibers with supramolecular nanofibers with the controllability of the fiber length. In the following work, experiments with an evaporation rate of the BTA of 1.4 μg s^{-1} for three different evaporation times, i.e., 60, 120, and 240 min, are presented. After half of the respective evaporation time, the nonwovens

were flipped 180° to ensure coverage with BTA on both sides. By weighing the samples, we determined a deposited BTA amount of about 2, 5, and 10 wt %. The increase correlates almost linearly with the evaporation time. Figure 2 displays
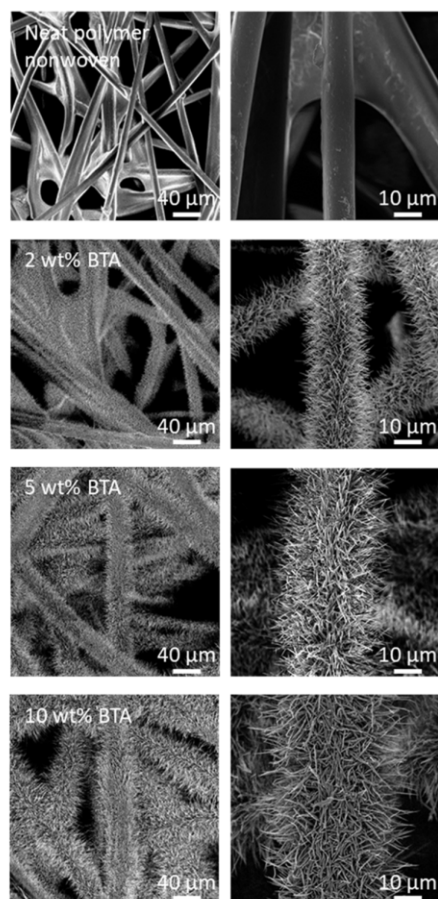
Figure 2. SEM images of an overview (left) and a magnification (right) of the neat polymer nonwoven and the mesostructured polymer nonwoven with different amounts of vapor-deposited BTA nanofibers, i.e., 2, 5, and 10 wt %.

SEM micrographs of the neat polymer nonwoven and the mesostructured nonwoven with an increasing amount of BTA. The overview images show that the polymer nonwoven is completely and homogeneously covered with supramolecular BTA nanofibers already at short evaporation times. The larger magnifications show that the nanofibers have grown in a vertical direction away from the microfibers, resembling a bottlebrush-like morphology on the mesoscale. We estimated the average length of supramolecular fibers based on the diameter of the entire bottlebrush structure to be around 4−5 μm for 60 min, 10−12 μm for 120 min, and 18−20 μm for 240 min evaporation time. The diameter of the supramolecular nanofiber is around 450 nm and is comparable to the nanofiber diameters prepared on silicon wafers described previously.

Figure S5 shows overview SEM images of the front and back sides of a mesostructured nonwoven. Both sides showed a very similar morphology with homogeneously covered BTA fibers,

demonstrating that the PVD process leads to the same result before and after flipping the nonwoven.

An important aspect of these mesostructured polymer nonwovens with supramolecular BTA nanofibers is that the morphology remains intact during air filtration, and no detachment or fragmentation of the nanofiber occurs. To verify the structural integrity, we used a mesostructured polymer nonwoven containing 10 wt % of BTA nanofibers and conducted an airstream test in a filter test rig at a flow velocity of 0.25 m s^{-1} for a period of time of 24 h. For the entire 24 h, no fiber fragments were monitored with the particle analyzer. This result proves that the supramolecular nanofibers are firmly attached to the polymer microfiber and do not detach or break from the superstructure during the airstream test under these conditions. This finding is confirmed by SEM (Figure S6, SI), which shows no significant difference in the morphology of the mesostructured polymer nonwoven before and after the airstream test.

To study how these mesostructured nonwovens influence the filtration performance in contrast to the neat polymer nonwoven, we subjected the samples to air filtration experiments with particulate matter. As particulate matter, we used an iso fine test dust, featuring predominantly a particle size distribution in the range of 0.3 to 10 μm. The particle size distribution of the iso fine test dust is shown in Figure S7. Filtration experiments were conducted using a filter test rig with a constant face velocity of 0.25 m s^{-1} and an aerosol particle concentration (upstream concentration) of about 30,000 particles cm^{-3}. Subsequently, we determined the filtration efficiency, which is defined as the percentage of particles removed by the filter medium. In filtration, the pore size is usually larger than the sizes of particulate matter and filtration is achieved by different mechanisms such as inertial impaction, interception, Brownian diffusion, and possibly electrostatic interaction rendering the deposition of particulate matter size-dependent.[13,46−49] Inertial impaction and interception are very effective for larger microsized particles and Brownian diffusion for nanosized particles. These mechanisms do not entirely overlap, leading to a range of particle sizes that penetrate the filter media. This gap is referred to as the most penetrating particle size (MPPS) and is typically in the range of 0.3 μm, which can be shifted by varying fiber diameter.[49] In Figure 3, the averaged filtration efficiencies of two measurements of individual specimens in the range of 0.3−2 μm are shown for the mesostructured polymer nonwovens with different amounts of BTA nanofibers and the neat polymer nonwoven. The individual measurements are shown in Figure S8.

The neat polymer nonwoven consists of microfibers with large pore sizes (see Figure 2, top), leading to a negligible filtration efficiency for particulate matter below 10%. Likewise, the differential pressure is, on average with 8 Pa, very low under these conditions.

To visualize the particulate matter deposited on the nonwoven material, we performed an SEM study. As can be seen in Figure S9, there were some larger particles with a diameter of more than 2 μm (not shown in Figure 3) as well as smaller removed particles on the microfiber nonwoven.

For mesostructured nonwovens with 2 wt % of supramolecular nanofibers, the filtration efficiency is clearly increased. We found an averaged filtration efficiency of 28% for 0.3 μm particles and of 34% for 2.0 μm particles with a pressure drop of about 24 Pa. For mesostructured nonwovens
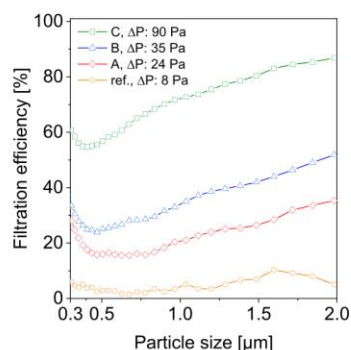
Figure 3. Averaged filtration efficiencies of (A) mesostructured nonwovens with 2 wt % BTA (red diamond) exhibiting an average pressure drop of 24 Pa, (B) mesostructured nonwovens with 5 wt % BTA (blue triangle) with a pressure drop of 35 Pa, and (C) mesostructured nonwovens with 10 wt % BTA (green square) showing a pressure drop of 90 Pa. Neat nonwovens (yellow circle) were used as reference (ref) exhibiting a pressure drop of 8 Pa. Testing conditions: measuring time = 30 s; flow velocity = 0.25 m s^{-1}; filtration area = 28.3 cm^2; test aerosol = ISO fine test dust; upstream aerosol concentration = 30,000 particles cm^{-3}.

with 5 wt % of BTA nanofibers, we found an averaged filtration efficiency of 33% for 0.3 μm particles and 52% 2.0 μm particles at a pressure drop of about 35 Pa and for mesostructured nonwovens with 10 wt % of BTA nanofibers, a filtration efficiency of 61% for 0.3 μm and 87% for 2.0 μm particles at a pressure drop of 90 Pa. The retention capability for all particle sizes of the mesostructured nonwoven with 10 wt % BTA is also visualized by SEM (Figure S9), where various large particles are deposited on the supramolecular nanofibers, while the mesoscale bottlebrush morphology remains intact. These findings show that as the amount of BTA nanofibers increases, the filtration efficiency steadily increases. Figure 3 also shows that the MPPS becomes less permeable as the amount of BTA increases and shifts increasingly toward smaller particle sizes, i.e., to 0.47 μm for the composite with 2 wt % BTA and to 0.40 μm for the composite with 10 wt % BTA, which can also be expected.

Since comparison with other filtration media is challenging due to numerous varying parameters and testing conditions, we compare the results with previous findings using similar supramolecular nanofiber composites comprising the same polymer nonwoven support under the same test setup and conditions.[23,24] These composites were equipped with about 7 wt % of supramolecular nanofibers, which were, however, prepared in situ within the polymer nonwoven using a solution-based process. As a result of the solution processing, the supramolecular BTA nanofibers span over the entire pores, yielding an intertwined nanofiber/microfiber composite. Comparing the filtration results with these composites, which were achieved using identical or similar measurement parameters, we find that the pressure drop for the mesostructured nonwovens is reduced by a factor of 4−5, while the filtration efficiency is comparable. Another figure of merit to assess the filter performance is the quality factor (QF), which is defined as $-\ln(P)/\Delta p$, with P being the penetration of the particles ($P = 1 -$ filtration efficiency) and Δp the pressure drop. For mesostructured nonwovens with 10 wt % of supramolecular nanofibers, we found an average QF of 10 kPa^{-1} at 0.3 μm and of 23 kPa^{-1} at 2.0 μm. These values are

reasonable considering the high face velocity of 0.25 m s^{-1} and are a significant improvement compared to previous results with similar systems with QFs in the range of 3−5 and 2−4 kPa^{-1}.[23,22]

The findings suggest that the morphology with the supramolecular nanofiber grafts results in an improved performance, in contrast to comparable supramolecular nanofiber/polymer microfiber composites. However, Figure 3 also shows a significant penetration, especially for small particles below 1 μm. Since these composites rely on depth filtration instead of surface filtration, a potential way to improve filtration efficiency is to increase the thickness of the medium. For this, we investigated the filtration performance of stacks comprising three layers of mesostructured nonwovens with 2, 5, and 10 wt % BTA and the neat nonwovens as reference. A schematic of a stack is shown in Figure S10. The filter efficiencies of the stacks of the mesostructured nonwovens and the neat polymer reference stack are shown in Figure S11. In general, for all stacks, the filtration efficiencies as well as the pressure drops increase compared to a single mesostructured or neat nonwoven. Also, as shown before, the filtration performance significantly improved with increasing amounts of BTA nanofibers. For example, for a nonwoven stack with 10 wt % BTA, the filtration efficiency is 81% for 0.3 μm particles and 98% for 2.0 μm particles at a pressure drop of 224 Pa. Also, as shown before, the MPPS becomes less permeable and slightly shifts toward smaller particle sizes. For this stack of mesostructured nonwovens, the quality factor is slightly reduced with a QF of 8 kPa^{-1} at 0.3 μm and of 19 kPa^{-1} at 2.0 μm compared to a single mesostructured nonwoven.

To visualize the deposition of the particles, we performed an SEM examination of the individual layers of the mesostructured nonwovens (top, middle, and bottom) after air filtration, as shown in Figure S10. In all stacks, the mesoscale bottlebrush morphology with the supramolecular nanofiber grafts remains intact. In addition, larger particles are mainly deposited in the top and middle layers. Smaller particles are found in all layers, especially in the bottom layer of the stack.

3.2. Supramolecular BTA Nanofibers on Glass Microfiber Nonwovens. Since BTAs, especially with short or bulky aliphatic side groups, have a pronounced thermal stability comparable to that of semiaromatic polyamides, they can be used at elevated temperatures. Typically, this is not the case for most of the polymer fibers based on commodity polymers and engineering plastics. For instance, the selected viscose/polyester nonwoven starts to soften and deform at a temperature above 140 °C, while distinct supramolecular BTA nanofibers remain intact at this temperature.[24] To overcome this issue, polymer nonwovens based on Kapton or aramid fibers as well as inorganic nonwovens based on glass microfibers may be used.[25,26,50−54] Here, we have selected a glass microfiber nonwoven as a porous support to prepare a mesostructured glass fiber nonwoven with BTA nanofibers by the PVD postmodification process. Since we found that the supramolecular nanofiber formation for the BTA during the PVD process is largely substrate-independent, we have used the same parameters as described before. In contrast to the viscose polyester nonwoven, the glass nonwoven has a higher bulk density and a 3 times higher thickness and basis weight. Therefore, by weighing the samples after PVD, we found a relatively lower amount of BTA in the glass microfiber nonwovens with 0.9, 1.8, and 3.3 wt %, although the same

absolute mass of BTA was deposited as in the polymer nonwovens. As shown in Figure 4, the mesoscale bottlebrush
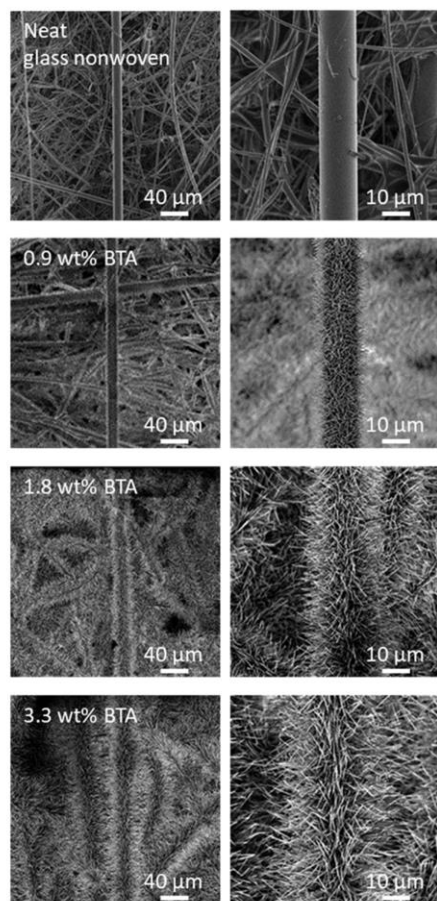

Figure 4. SEM overview (left) and magnification (right) of a neat glass nonwoven and mesostructured glass nonwoven with 0.9, 1.8, and 3.3 wt % BTA.

morphology is highly comparable to that as described before. The supramolecular BTA fibers feature an average fiber length of around 3 μm, 6 μm, and 12 μm for the mesostructured glass fiber nonwoven with 0.9, 1.8, and 3.3 wt % BTA, respectively. The diameter of the supramolecular nanofibers is in the range of about 350 to 550 nm and is comparable to the nanofiber diameters as described before for the polymer nonwovens.

Subsequently, we performed filtration tests with ISO fine dust, as described before. The averaged filtration efficiencies of two measurements of individual specimens in the range of 0.3–2 μm for the mesostructured glass fiber nonwovens with 0.9, 1.8, and 3.3 wt % BTA and the filtration efficiency of a neat glass fiber nonwoven are shown in Figure 5. The individual measurements are shown in Figure S12.

In particular, for fine particles with a size of 0.3 μm, a clear trend can be seen with increasing amount of BTA. The neat glass microfiber nonwoven shows a filtration efficiency for 0.3 μm particles of 87%, which increases to 90% for the mesostructured glass nonwoven with 0.9 wt % BTA, to 92% for the mesostructured glass nonwoven with 1.8 wt % BTA, and to 93% for the mesostructured glass nonwoven with 3.3 wt
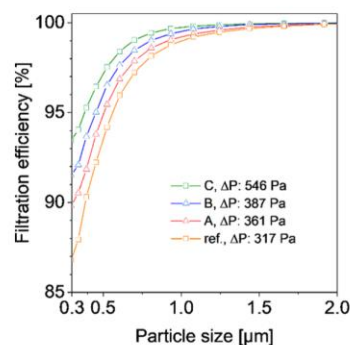
Figure 5. Averaged filtration efficiencies from 0.3 to 2.0 μm of mesostructured glass nonwovens with (A) 0.9 wt % of BTA (red triangle) with a pressure drop of 361 Pa, (B) 1.8 wt % BTA (blue triangle) with a pressure drop of 387 Pa, and (C) 3.3 wt % BTA (green square) with a pressure drop of 546 Pa. A neat glass nonwoven (yellow circle) with a pressure drop of 317 Pa is given as a reference. Testing conditions: measuring time = 30 s; flow velocity = 0.25 m s^{-1}; filtration area = 28.3 cm^2; test aerosol = ISO fine dust; upstream aerosol concentration = 30,000 particles cm^{-3}.

% BTA. Under these conditions, the pressure drops are slightly higher than those for the neat glass fiber nonwoven with 317 Pa and increase with the amount of BTA, on average, to 361, 387, and 546 Pa for mesostructured glass nonwovens with 0.9, 1.8, and 3.3 wt % BTA, respectively. At this particle size, we determined a QF of 6.4 kPa^{-1} for neat glass nonwoven and a QF of 6.4, 6.5, and 5.0 kPa^{-1} for the mesostructured glass fiber nonwovens with 0.9, 1.8, and 3.3 wt % BTA, respectively.

As shown before, we investigated the structural integrity of the BTA nanofibers in a mesostructured glass fiber nonwoven containing 3.3 wt % of BTA nanofibers by conducting an airstream test. Here, we employed a flow velocity of 3.0 m s^{-1}, which is more than 10 times larger than during filtration experiments, and recorded the pressure drop for a period of time of 60 min. The pressure drop rises significantly to 1276 Pa and remains constant over the measuring time of 60 min with a deviation of ±0.25 Pa (see Figure S13, SI). Also, no fiber fragments were monitored with the particle analyzer during the 60 min strongly suggesting that the supramolecular nanofibers are firmly attached to the glass fibers and the sample remains intact.

To study the potential use of the mesostructured glass fiber nonwovens at elevated temperatures, we performed dynamic TGA of the neat and mesostructured glass fiber nonwovens (Figure S14, SI). Interestingly, the neat glass fiber nonwovens exhibit about 6.5 wt % of coating, which starts to decompose in a temperature range of 350–450 °C. Isothermal TGA shows that this is strongly reduced at a temperature of 200 °C (Figure S15, SI). To validate that the morphology of the composites remains intact at elevated temperatures, the mesostructured glass nonwovens with different amounts of BTA nanofibers were heated to 200 °C for 24 h in air. SEM images were taken before heating and after heat treatment from the same samples at different positions. Figure 6 shows that the morphology of mesostructured glass nonwovens remains intact, confirming the findings of the isothermal TGA.

To provide further evidence that the mesostructured nonwovens are suitable to be exposed to elevated temperatures, we conducted further filtration tests. For this, two individual mesostructured nonwovens with 3.3 wt % BTA were

Before heat treatment

After heat treatment for 24h at 200°C
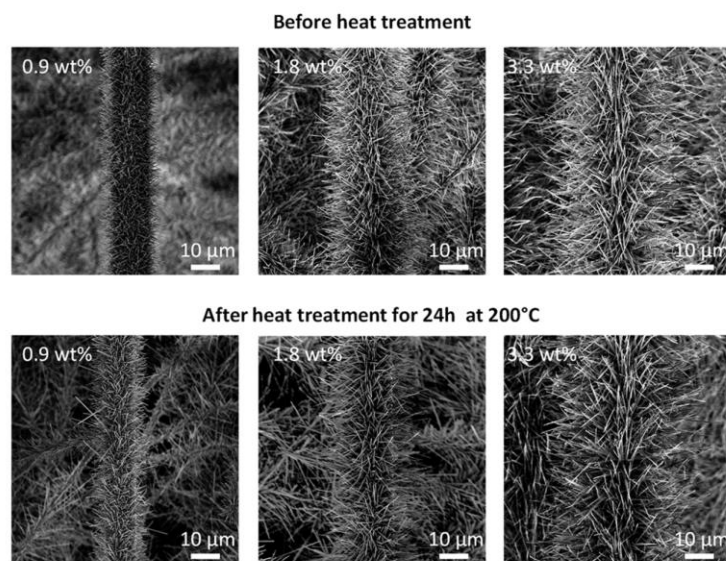
Figure 6. Comparison of SEM micrographs of mesostructured glass nonwovens with 0.9, 1.8, and 3.3 wt % BTA before (top) and after (bottom) a heat treatment of 200 °C for 24 h, showing no observable change in morphology.

prepared and tested without heat treatment, and two individual samples were prepared and tested after heat treatment. In Figure 7, the averaged filtration efficiencies of the mesostruc-
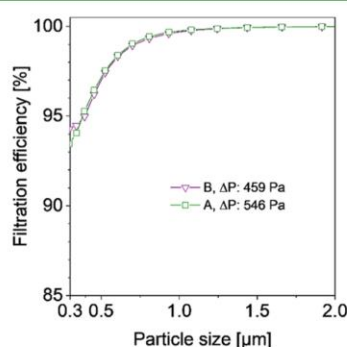
Figure 7. Averaged filtration efficiencies of (A) mesostructured glass fiber nonwovens with 3.3 wt % BTA (green square) with an average pressure drop of 546 Pa and (B) mesostructured glass nonwovens with 3.3 wt % BTA (heat-treated for 24 h at 200 °C) with a pressure drop of 459 PA (purple, triangle). Testing conditions: measuring time = 30 s; flow velocity = 0.25 m s^{-1}; filtration area = 28.3 cm^2; test aerosol = ISO fine test dust; upstream aerosol concentration = 30,000 particles cm^{-3}.

tured glass fiber nonwovens for the particle sizes in the range of 0.3 to 2 μm are shown. The individual measurements are shown in Figure S16. Both the individual measurements as well as the averaged results are highly comparable. These findings demonstrate that the BTA nanofibers on the glass fiber nonwovens withstand thermal exposure, indicating that the composites are suitable for air filtration applications at elevated temperatures.

4. CONCLUSIONS

We demonstrated a solvent-free postmodification process of polymer and glass fiber nonwovens to fabricate mesostructured

nonwovens with a defined bottlebrush-like morphology on the mesoscale by vapor deposition of a selected 1,3,5-benzene-trisamide. The fiber length of the supramolecular nanofiber grafts can be controlled by the evaporation time. For the polymer nonwovens, the length was adjusted between 5 and 20 μm, and for the glass fiber nonwovens, it was adjusted between 3 and 12 μm. In the case of the polymer nonwoven, the filtration performance of the mesostructured nonwovens for particulate matter significantly enhanced up to 87% for 2.0 μm particles at a low pressure drop of 90 Pa, which is in strong contrast to the neat polymer nonwoven. Using a glass microfiber nonwoven as a support allows for the preparation of more temperature-resistant mesostructured nonwovens due to the thermal stability of the BTA nanofibers. This was demonstrated by a 24 h heat treatment of the mesostructured nonwoven at 200 °C, which subsequently exhibited the same morphology and filtration performance as before. This demonstrates that such a postmodification process is a feasible approach to modify the performance of existing nonwoven fibrous media and may pave the way to the fabrication of mesostructured nonwovens, which widen application windows in the field of filtration and separation.

■ ASSOCIATED CONTENT

ⓈⒾ Supporting Information

The Supporting Information is available free of charge at https://pubs.acs.org/doi/10.1021/acsami.4c22310.

Details of thermogravimetric analysis of the BTA; SEM images of BTA nanofibers on solid substrates; IR spectra of BTA; SEM images of mesostructured polymer nonwovens (front and backside) and before and after the airstream test; particle size distribution of ISO fine test dust; filtration efficiencies of individual mesostructured polymer nonwoven; SEM images of the neat polymer nonwoven; mesostructured polymer nonwoven; and a stack of three mesostructured polymer nonwovens; filtration efficiencies of stacks of three mesostructured polymer nonwovens; filtration efficien-

cies of individual mesostructured glass fiber nonwovens; stability test of mesostructured glass fiber nonwovens; thermogravimetric analysis of mesostructured glass fiber nonwovens; filtration efficiencies of individual mesostructured glass fiber nonwovens with and without a heat treatment (PDF)

■ AUTHOR INFORMATION

Corresponding Author

Hans-Werner Schmidt − *Macromolecular Chemistry I and Bavarian Polymer Institute, University of Bayreuth, 95447 Bayreuth, Germany;* ◉ orcid.org/0000-0002-1761-1153; Email: hans-werner.schmidt@uni-bayreuth.de

Authors

Dennis Schröder − *Macromolecular Chemistry I and Bavarian Polymer Institute, University of Bayreuth, 95447 Bayreuth, Germany*

Klaus Kreger − *Macromolecular Chemistry I and Bavarian Polymer Institute, University of Bayreuth, 95447 Bayreuth, Germany;* ◉ orcid.org/0000-0003-3021-1311

Complete contact information is available at:
https://pubs.acs.org/10.1021/acsami.4c22310

Notes

The authors declare no competing financial interest.

■ REFERENCES

(1) Fuzzi, S.; Baltensperger, U.; Carslaw, K.; Decesari, S.; van der Gon, H. D.; Facchini, M. C.; Fowler, D.; Koren, I.; Langford, B.; Lohmann, U.; Nemitz, E.; Pandis, S.; Riipinen, I.; Rudich, Y.; Schaap, M.; Slowik, J. G.; Spracklen, D. V.; Vignati, E.; Wild, M.; Williams, M.; Gilardoni, S. Particulate matter, air quality and climate: lessons learned and future needs. *Atmos. Chem. Phys.* **2015**, *15*, 8217−8299.

(2) Grantz, D.; Garner, J.; Johnson, D. Ecological effects of particulate matter. *Environ. Int.* **2003**, *29*, 213−239.

(3) Kim, K.-H.; Kabir, E.; Kabir, S. A review on the human health impact of airborne particulate matter. *Environ. Int.* **2015**, *74*, 136−143.

(4) Heft-Neal, S.; Burney, J.; Bendavid, E.; Burke, M. Robust relationship between air quality and infant mortality in Africa. *Nature* **2018**, *559*, 254−258.

(5) Lelieveld, J.; Evans, J. S.; Fnais, M.; Giannadaki, D.; Pozzer, A. The contribution of outdoor air pollution sources to premature mortality on a global scale. *Nature* **2015**, *525*, 367−371.

(6) Shen, G.; Ru, M.; Du, W.; Zhu, X.; Zhong, Q.; Chen, Y.; Shen, H.; Yun, X.; Meng, W.; Liu, J.; Cheng, H.; Hu, J.; Guan, D.; Tao, S. Impacts of air pollutants from rural Chinese households under the rapid residential energy transition. *Nat. Commun.* **2019**, *10*, No. 3405.

(7) Henning, L. M.; Abdullayev, A.; Vakifahmetoglu, C.; Simon, U.; Bensalah, H.; Gurlo, A.; Bekheet, M. F. Review on Polymeric, Inorganic, and Composite Materials for Air Filters: From Processing to Properties. *Adv. Energy Sustainability Res.* **2021**, *2*, No. 2100005.

(8) Kiyak, Y.; Mazé, B.; Pourdeyhimi, B. Microfiber nonwovens as potential membranes. *Sep. Purif. Rev.* **2019**, *48*, 282−297.

(9) Liu, H.; Zhu, Y.; Zhang, C.; Zhou, Y.; Yu, D.-G. Electrospun nanofiber as building blocks for high-performance air filter: A review. *Nano Today* **2024**, *55*, No. 102161.

(10) Shen, H.; Han, M.; Shen, Y.; Shuai, D. Electrospun Nanofibrous Membranes for Controlling Airborne Viruses: Present Status, Standardization of Aerosol Filtration Tests, and Future Development. *ACS Environ. Au* **2022**, *2*, 290−309.

(11) Zhu, M.; Han, J.; Wang, F.; Shao, W.; Xiong, R.; Zhang, Q.; Pan, H.; Yang, Y.; Samal, S. K.; Zhang, F.; Huang, C. Electrospun Nanofibers Membranes for Effective Air Filtration. *Macromol. Mater. Eng.* **2017**, *302*, No. 1600353.

(12) Yu, Z.; Fan, T.; Liu, Y.; Li, L.; Liu, J.; Yang, B.; Ramakrishna, S.; Long, Y.-Z. Efficient air filtration through advanced electrospinning techniques in nanofibrous Materials: A review. *Sep. Purif. Technol.* **2024**, *349*, No. 127773.

(13) Lu, T.; Cui, J.; Qu, Q.; Wang, Y.; Zhang, J.; Xiong, R.; Ma, W.; Huang, C. Multistructured Electrospun Nanofibers for Air Filtration: A Review. *ACS Appl. Mater. Interfaces* **2021**, *13*, 23293−23313.

(14) Deng, Y.; Lu, T.; Zhang, X.; Zeng, Z.; Tao, R.; Qu, Q.; Zhang, Y.; Zhu, M.; Xiong, R.; Huang, C. Multi-hierarchical nanofiber membrane with typical curved-ribbon structure fabricated by green electrospinning for efficient, breathable and sustainable air filtration. *J. Membr. Sci.* **2022**, *660*, No. 120857.

(15) Zhang, S.; Liu, H.; Yin, X.; Yu, J.; Ding, B. Anti-deformed Polyacrylonitrile/Polysulfone Composite Membrane with Binary Structures for Effective Air Filtration. *ACS Appl. Mater. Interfaces* **2016**, *8*, 8086−8095.

(16) Shao, Z.; Kang, G.; Chen, H.; Jiang, J.; Wang, X.; Li, W.; Liu, Y.; Zheng, G. Preparation, characterization, and air filtration property of electrospun bimodal fibrous membrane based on low conductivity blended polymers solution. *Mater. Today Commun.* **2023**, *34*, No. 105014.

(17) Yang, Y.; Li, X.; Zhou, Z.; Qiu, Q.; Chen, W.; Huang, J.; Cai, W.; Qin, X.; Lai, Y. Ultrathin, ultralight dual-scale fibrous networks with high-infrared transmittance for high-performance, comfortable and sustainable PM0.3 filter. *Nat. Commun.* **2024**, *15*, No. 1586.

(18) Xu, X.; Liu, S.; Liu, X.; Yu, J.; Ding, B. Engineering self-assembled 2D nano-network membranes through hierarchical phase separation for efficient air filtration. *J. Colloid Interface Sci.* **2024**, *657*, 463−471.

(19) Zhang, S.; Liu, H.; Tang, N.; Zhou, S.; Yu, J.; Li, B.; Ding, B. Spider-web-inspired PM0. 3 filters based on self-sustained electrostatic nanostructured networks. *Adv. Mater.* **2020**, *32*, No. 2002361.

(20) Liu, H.; Zhang, S.; Liu, L.; Yu, J.; Ding, B. A fluffy dual-network structured nanofiber/net filter enables high-efficiency air filtration. *Adv. Funct. Mater.* **2019**, *29*, No. 1904108.

(21) Chen, J.; Yu, B.; Zhu, J.; Gao, Y.; Deng, W.; Chen, R.; Wang, H.-L. Electrospinning of Biodegradable, Monolithic Membrane with Distinct Bimodal Micron-Sized Fibers and Nanofibers for High Efficiency PMs Removal. *ACS Appl. Mater. Interfaces* **2023**, *15*, 35507−35515.

(22) Hu, M.; Wang, Y.; Yan, Z.; Zhao, G.; Zhao, Y.; Xia, L.; Cheng, B.; Di, Y.; Zhuang, X. Hierarchical dual-nanonet of polymer nanofibers and supramolecular nanofibrils for air filtration with a high filtration efficiency, low air resistance and high moisture permeation. *J. Mater. Chem. A* **2021**, *9*, 14093−14100.

(23) Misslitz, H.; Kreger, K.; Schmidt, H.-W. Supramolecular Nanofiber Webs in Nonwoven Scaffolds as Potential Filter Media. *Small* **2013**, *9*, 2053−2058.

(24) Weiss, D.; Skrybeck, D.; Misslitz, H.; Nardini, D.; Kern, A.; Kreger, K.; Schmidt, H.-W. Tailoring Supramolecular Nanofibers for Air Filtration Applications. *ACS Appl. Mater. Interfaces* **2016**, *8*, 14885−14892.

(25) Xu, K.; Deng, J.; Tian, G.; Zhan, L.; Ma, J.; Wang, L.; Ke, Q.; Huang, C. Downy feather-like para-aramid fibers and nonwovens with enhanced absorbency, air filtration and thermal insulation performances. *Nano Res.* **2022**, *15*, 5695−5704.

(26) Xu, K.; Deng, J.; Lin, R.; Zhang, H.; Ke, Q.; Huang, C. Surface fibrillation of para -aramid nonwoven as a multi-functional air filter with ultralow pressure drop. *J. Mater. Chem. A* **2020**, *8*, 22269−22279.

(27) Zhang, K.; Li, Z.; Kang, W.; Deng, N.; Yan, J.; Ju, J.; Liu, Y.; Cheng, B. Preparation and characterization of tree-like cellulose nanofiber membranes via the electrospinning method. *Carbohydr. Polym.* **2018**, *183*, 62−69.

(28) Shao, Z.; Chen, Y.; Jiang, J.; Xiao, Y.; Kang, G.; Wang, X.; Li, W.; Zheng, G. Multistage-Split Ultrafine Fluffy Nanofibrous Membrane for High-Efficiency Antibacterial Air Filtration. *ACS Appl. Mater. Interfaces* **2022**, *14*, 18989−19001.

(29) Li, Z.; Xu, Y.; Fan, L.; Kang, W.; Cheng, B. Fabrication of polyvinylidene fluoride tree-like nanofiber via one-step electro-spinning. *Mater. Des.* **2016**, *92*, 95−101.

(30) Frank, A.; Weber, M.; Hils, C.; Mansfeld, U.; Kreger, K.; Schmalz, H.; Schmidt, H.-W. Functional Mesostructured Electrospun Polymer Nonwovens with Supramolecular Nanofibers. *Macromol. Rapid Commun.* **2022**, *43*, No. e2200052.

(31) Frank, A.; Hils, C.; Weber, M.; Kreger, K.; Schmalz, H.; Schmidt, H.-W. Hierarchical Superstructures by Combining Crystal-lization-Driven and Molecular Self-Assembly. *Angew. Chem., Int. Ed.* **2021**, *60*, 21767−21771.

(32) Burgard, M.; Weiss, D.; Kreger, K.; Schmalz, H.; Agarwal, S.; Schmidt, H.-W.; Greiner, A. Mesostructured Nonwovens with Penguin Downy Feather-Like Morphology—Top-Down Combined with Bottom-Up. *Adv. Funct. Mater.* **2019**, *29*, No. 1903166.

(33) Stranski, I. N.; Krastanow, L. Zur Theorie der orientierten Ausscheidung von Ionenkristallen aufeinander. *Monatsh. Chem.* **1937**, *71*, 351−364.

(34) Schröder, D.; Kreger, K.; Mansfeld, U.; Schmidt, H.-W. Controlled Surface Decoration with Functional Supramolecular Nanofibers by Physical Vapor Deposition. *Adv. Mater. Interfaces* **2024**, *11*, No. 2400259.

(35) Schröder, D.; Neuber, C.; Mansfeld, U.; Kreger, K.; Schmidt, H.-W. Mesostructured Nonwovens with Supramolecular Tricycloqui-nazoline Nanofibers as Heterogenous Photocatalyst. *Small Sci.* **2024**, *4*, No. 2300160.

(36) Schröder, D.; Thanner, J.; Kreger, K.; Schmidt, H.-W. Hierarchical Glass Fiber Superstructures with Supramolecular Nano-fibers for the Nucleation of Isotactic Polypropylene. *Macromol. Mater. Eng.* **2024**, No. 2400389.

(37) Lightfoot, M. P.; Mair, F. S.; Pritchard, R. G.; Warren, J. E. New supramolecular packing motifs: π-stacked rods encased in triply-helical hydrogen bonded amide strands. *Chem. Commun.* **1999**, 1945−1946.

(38) Cantekin, S.; de Greef, T. F. A.; Palmans, A. R. A. Benzene-1,3,5-tricarboxamide: a versatile ordering moiety for supramolecular chemistry. *Chem. Soc. Rev.* **2012**, *41*, 6125−6137.

(39) Zehe, C. S.; Hill, J. A.; Funnell, N. P.; Kreger, K.; van der Zwan, K. P.; Goodwin, A. L.; Schmidt, H.-W.; Senker, J. Mesoscale Polarization by Geometric Frustration in Columnar Supramolecular Crystals. *Angew. Chem., Int. Ed.* **2017**, *56*, 4432−4437.

(40) Sheiko, S. S.; Sumerlin, B. S.; Matyjaszewski, K. Cylindrical molecular brushes: Synthesis, characterization, and properties. *Prog. Polym. Sci.* **2008**, *33*, 759−785.

(41) Li, Z.; Tang, M.; Liang, S.; Zhang, M.; Biesold, G. M.; He, Y.; Hao, S.-M.; Choi, W.; Liu, Y.; Peng, J.; Lin, Z. Bottlebrush polymers: From controlled synthesis, self-assembly, properties to applications. *Prog. Polym. Sci.* **2021**, *116*, No. 101387.

(42) Rulkens, R.; Koning, C. Chemistry and Technology of Polyamides. In *Polymer Science: A Comprehensive Reference*, 2nd ed.; Moeller, M., Ed.; Elsevier Science & Technology: San Diego, 2012; pp 431−467.

(43) Kluge, D.; Singer, J. C.; Neubauer, J. W.; Abraham, F.; Schmidt, H.-W.; Fery, A. Influence of the molecular structure and morphology of self-assembled 1,3,5-benzenetrisamide nanofibers on their mechan-ical properties. *Small* **2012**, *8*, 2563−2570.

(44) Stals, P. J. M.; Smulders, M. M. J.; Martín-Rapún, R.; Palmans, A. R. A.; Meijer, E. W. Asymmetrically substituted benzene-1,3,5-tricarboxamides: self-assembly and odd-even effects in the solid state and in dilute solution. *Chem. - Eur. J.* **2009**, *15*, 2071−2080.

(45) Schmidt, M.; Wittmann, J. J.; Kress, R.; Schneider, D.; Steuernagel, S.; Schmidt, H.-W.; Senker, J. Crystal Structure of a Highly Efficient Clarifying Agent for Isotactic Polypropylene. *Cryst. Growth Des.* **2012**, *12*, 2543−2551.

(46) Kang, Y.; Low, Z.-X.; Zou, D.; Zhong, Z.; Xing, W. Multifunctional Nanofibrous Membranes for Integrated Air Purifica-tion. *Adv. Fiber Mater.* **2024**, *6*, 1306−1342.

(47) Yang, C. Aerosol Filtration Application Using Fibrous Media-An Industrial Perspective. *Chin. J. Chem. Eng.* **2012**, *20*, 1−9.

(48) *Handbook of Nonwoven Filter Media*, 1st ed.; Butterworth-Heinemann: Oxford, Burlington, MA, 2007.

(49) Li, P.; Wang, C.; Zhang, Y.; Wei, F. Air Filtration in the Free Molecular Flow Regime: A Review of High-Efficiency Particulate Air Filters Based on Carbon Nanotubes. *Small* **2014**, *10*, 4543−4561.

(50) Zhang, R.; Liu, C.; Hsu, P.-C.; Zhang, C.; Liu, N.; Zhang, J.; Lee, H. R.; Lu, Y.; Qiu, Y.; Chu, S.; Cui, Y. Nanofiber Air Filters with High-Temperature Stability for Efficient PM2.5 Removal from the Pollution Sources. *Nano Lett.* **2016**, *16*, 3642−3649.

(51) Li, J.; Zhao, J.; Xu, Z.; Zhai, Y.; Su, X.; Luo, D.; Jia, C.; Zhu, M. High-Temperature-Resistant Dual-Scale Ceramic Nanofiber Films toward Improved Air Filtration. *ACS Appl. Mater. Interfaces* **2024**, *16*, 60608−60615.

(52) Li, Z.; Song, J.; Long, Y.; Jia, C.; Liu, Z.; Li, L.; Yang, C.; Liu, J.; Lin, S.; Wang, H.; et al. Large-scale blow spinning of heat-resistant nanofibrous air filters. *Nano Res.* **2020**, *13*, 861−867.

(53) Marzocchi, A.; Lachut, F.; Willis JR, W. H. Glass Fibers and Their Use as Filter Media. *J. Air Pollut. Control Assoc.* **1962**, *12*, 38−42.

(54) Spaite, P. W.; Stephan, D. G.; Rose, A. H., Jr High temperature fabric filtration of industrial gases. *J. Air Pollut. Control Assoc.* **1961**, *11*, 243−258.

Supporting Information

Mesostructured polymer and glass microfiber nonwovens with supramolecular 1,3,5-benzenetrisamide nanofibers for air filtration

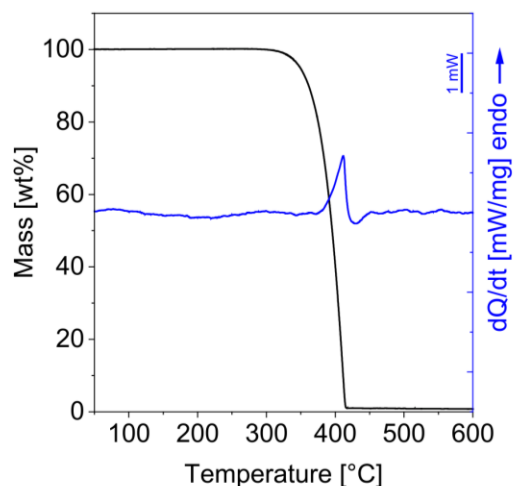*Dennis Schröder, Klaus Kreger, and Hans-Werner Schmidt**

Macromolecular Chemistry I and Bavarian Polymer Institute, University of Bayreuth, Universitätsstraße 30, 95447 Bayreuth, Germany.

*Corresponding author: hans-werner.schmidt@uni-bayreuth.de

Table of contents

Section S1: Thermal properties of the BTA


Figure S1. Dynamic TGA of the BTA shown from 50-600°C (black) and the corresponding SDTA (blue) at a heating rate of 10 K min^{-1} under N_2 with a flow rate of 30 mL min^{-1}. No weight loss occurs up to a temperature of 300 °C. SDTA reveals only a phase transition with a maximum at approximately 410 °C.
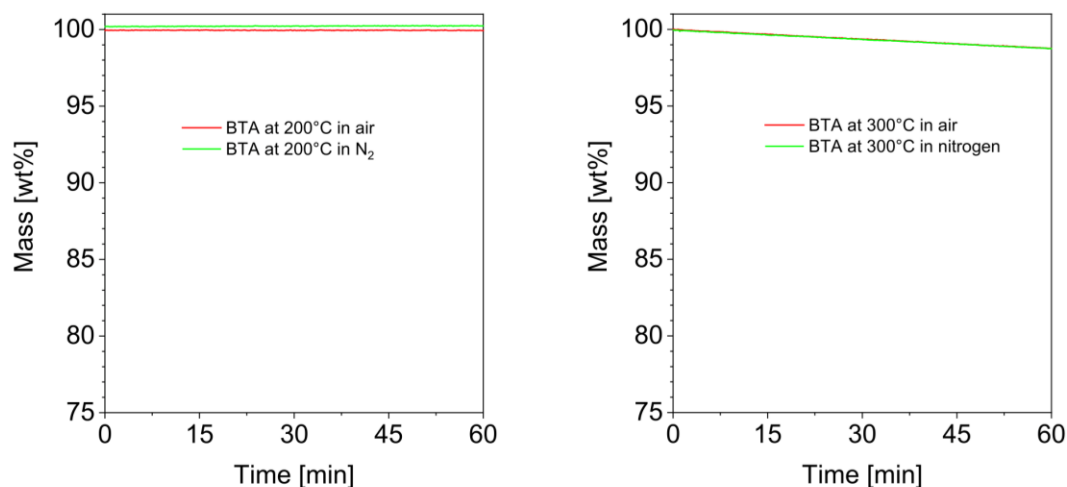
Figure S2. Isothermal TGA of the BTA under N_2 (green) or in air (red) at 200 °C (left) and at 300 °C (right). At 200 °C, no weight loss can be observed regardless of the atmosphere. At 300 °C, a slight weight loss of about 1.25 wt% is observed after 1 hour, indicating sublimation of the BTA. After all isothermal experiments, the remaining BTA in the crucibles keeps its white appearance.
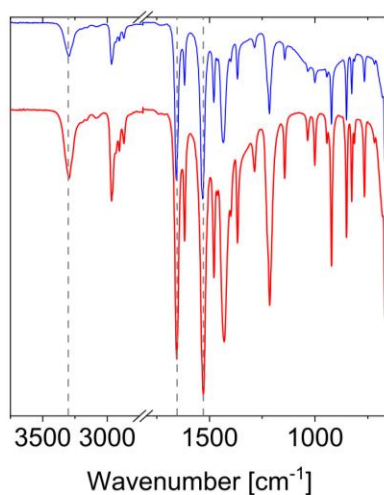
1

Section S2: Morphology of supramolecular nanofibers on silicon wafers
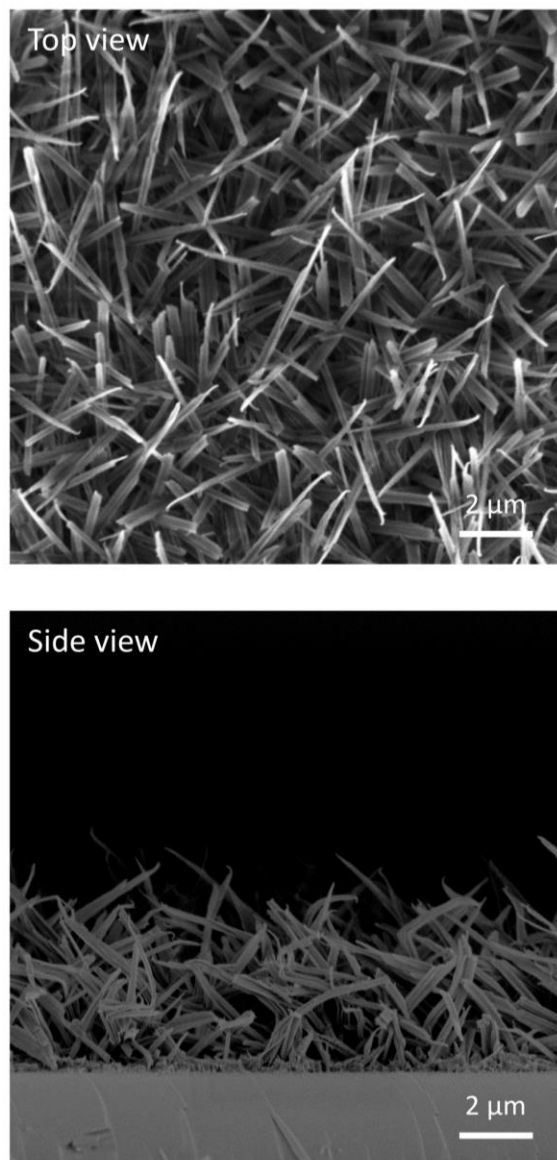
Figure S3. SEM top view images (top) and side view images (bottom) of vapor deposited **BTA** on a silicon wafer after an evaporation time of 45 min. PVD conditions: Evaporation rate = 1.4 μg s^{-1}, T_{source} = 230°C, T_{sub} =25°C.

2

Section S3: IR spectra of the BTA before and after PVD

Figure S4. FT-IR spectra of the BTA before PVD (red) and after PVD (blue). Both spectra are almost identical. The relevant region for amide vibrations (amide A, amide I and II) are indicated by grey dashed lines. For both spectra, the amide A (N-H stretch vibrations) is found at 3302 cm^{-1}, the amide I (C=O stretch vibration) at 1653 cm^{-1} and at the amide II (superposition of N-H bend and C-N stretch vibrations) at 1529 cm^{-1}. The location of these vibrations is indicative for a columnar stacking for this BTA.

3

Section S4: Morphology of a mesostructured polymer nonwoven
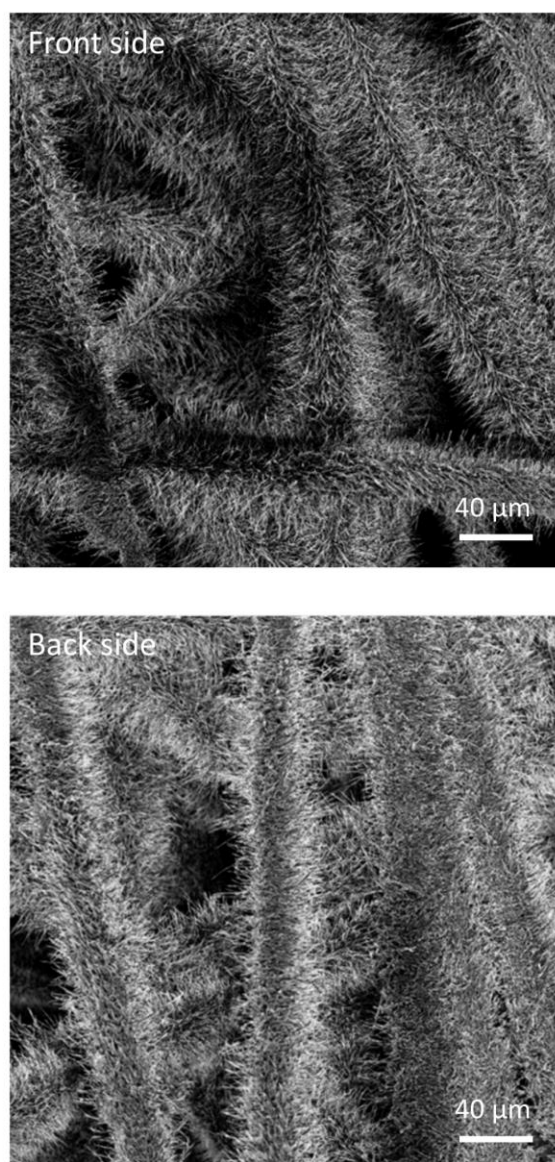
Figure S5. SEM images of front side (top) and back side (bottom) of the mesostructured polymer nonwoven with 10 wt% of BTA nanofibers. No significant difference in morphology can be observed.

4

Section S5: Morphology of mesostructured polymer nonwoven before and after airstream test
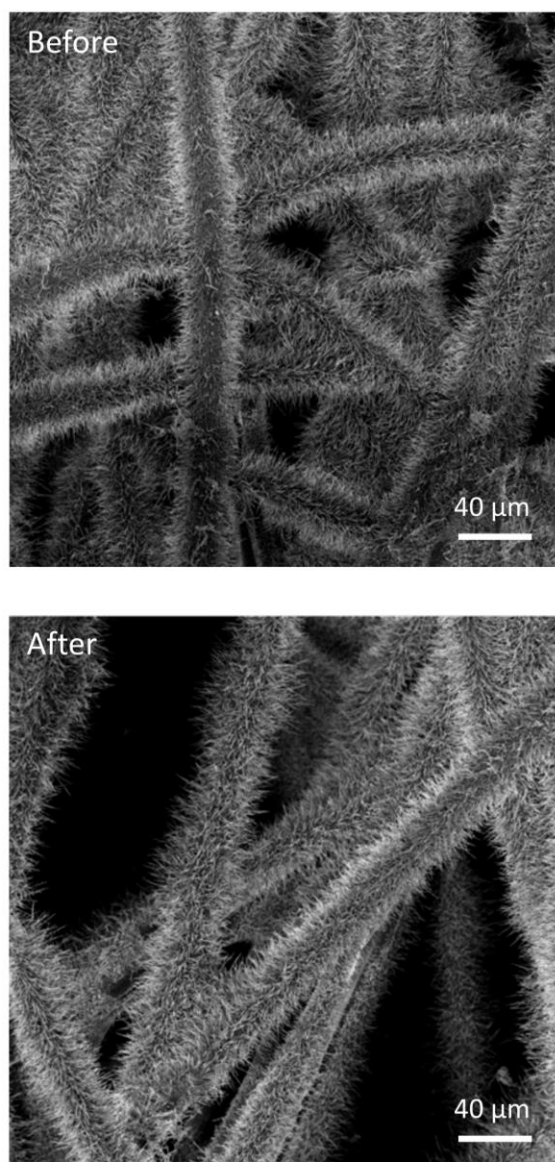
Figure S6. SEM overview images of a mesostructured polymer nonwoven with 10 wt% of BTA nanofibers before (top) and after (bottom) conducting an airstream test. Conditions: Face velocity of 0.25 m s^{-1} for 24 h. No significant difference in morphology can be observed.

5

Section S6: Particle size distribution of the fine test dust
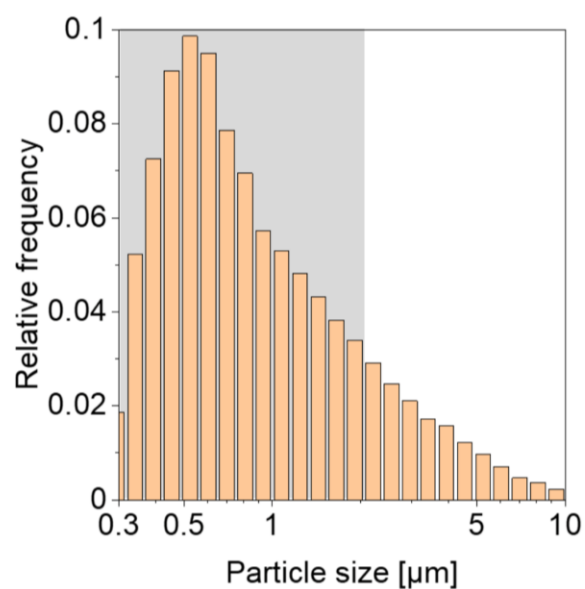
Figure S7. Particle size distribution of the ISO 12103-1, A2 fine test dust monitored in the particle size range from 0.3 to 10.0 μm. The area highlighted in grey is the range of particle sizes displayed in the filtration efficiency plots.

6

Section S7: Filtration efficiencies of individual neat and mesostructured polymer nonwovens
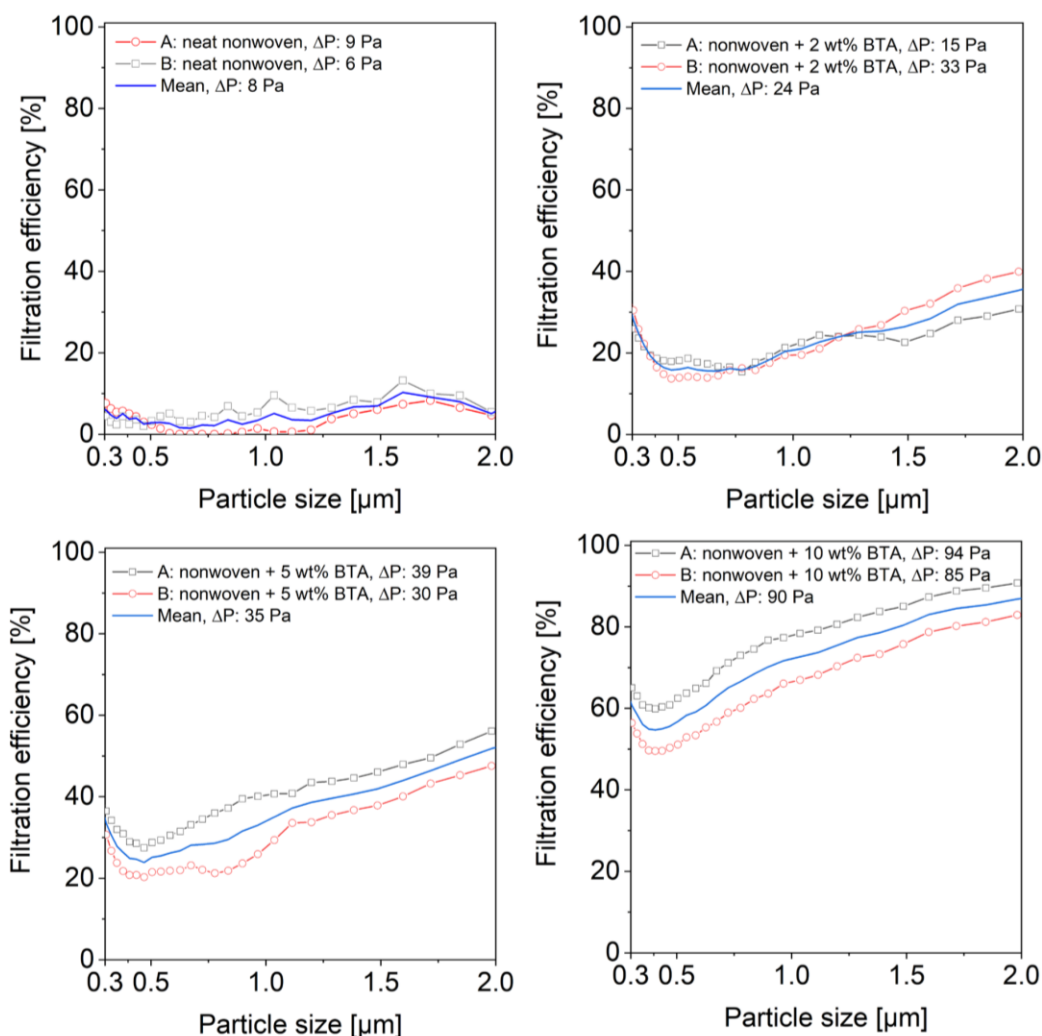
Figure S8. Filtration efficiencies in the range of 0.3 to 2.0 µm of two individual neat polymer nonwovens (top, left), of two individual mesostructured polymer nonwovens with 2 wt% BTA (top, right), of two individual mesostructured polymer nonwovens with 5 wt% BTA (bottom, left) and of two individual mesostructured polymer nonwovens with 10 wt% (bottom, right). The mean values for each graph are shown in blue. Testing conditions: measuring time = 30 s; flow velocity = 0.25 m s^{-1}; filtration area = 28.3 cm^2, test aerosol = ISO fine test dust, upstream aerosol concentration = 30,000 particles cm^{-3}.

7

Section S8: Morphology of a neat and a mesostructured polymer nonwoven after air filtration
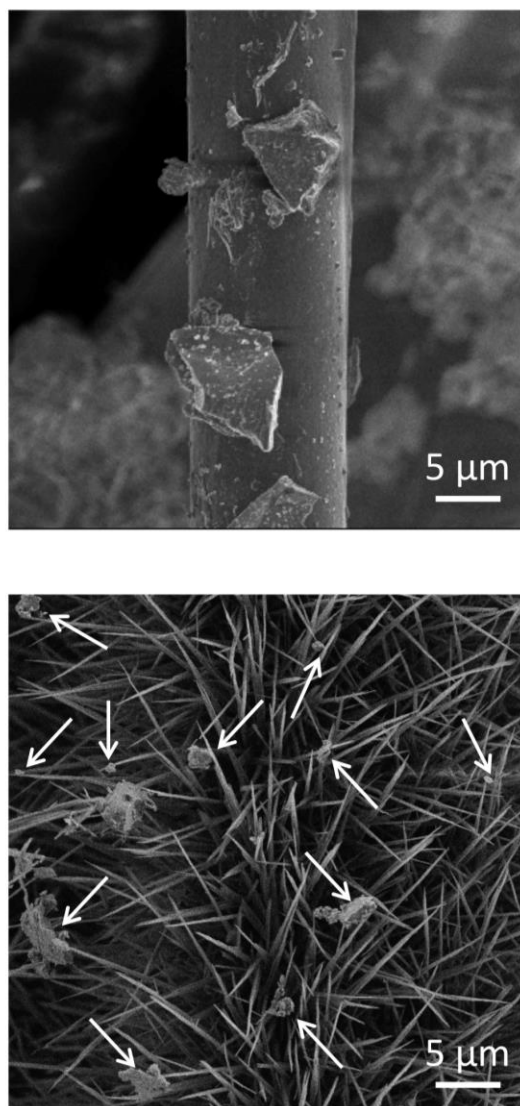
Figure S9. SEM images of a neat polymer nonwoven (top) and of a mesostructured polymer nonwoven with 10 wt% BTA nanofibers (bottom) after air filtration with fine test dust. The supramolecular nanofibers remain intact after exposure to fine test dust and are capable of capturing the particulate matter more efficiently. (Arrows pointing to the particles are guide to the eye). Filtration test conditions: Measuring time = 30 s; face velocity = 0.25 m s^{-1}; filtration area = 28.3 cm^2, test aerosol = ISO fine test dust, upstream aerosol concentration = 30,000 particles cm^{-3}.

8

Section S9: Schematic and morphology of a filter stack after air filtration

Figure S10. Schematic of a filter stack comprising three mesostructured nonwovens (left). Overview SEM images (middle) and magnification SEM images (right) of the top, middle, and the bottom mesostructured polymer nonwovens with 10 wt% BTA of the filter stack after air filtration. Filtration test conditions: Measuring time = 30 s; face velocity = 0.25 m s^{-1}; filtration area = 28.3 cm^2, test aerosol = ISO fine test dust, upstream aerosol concentration = 30,000 particles cm^{-3}.
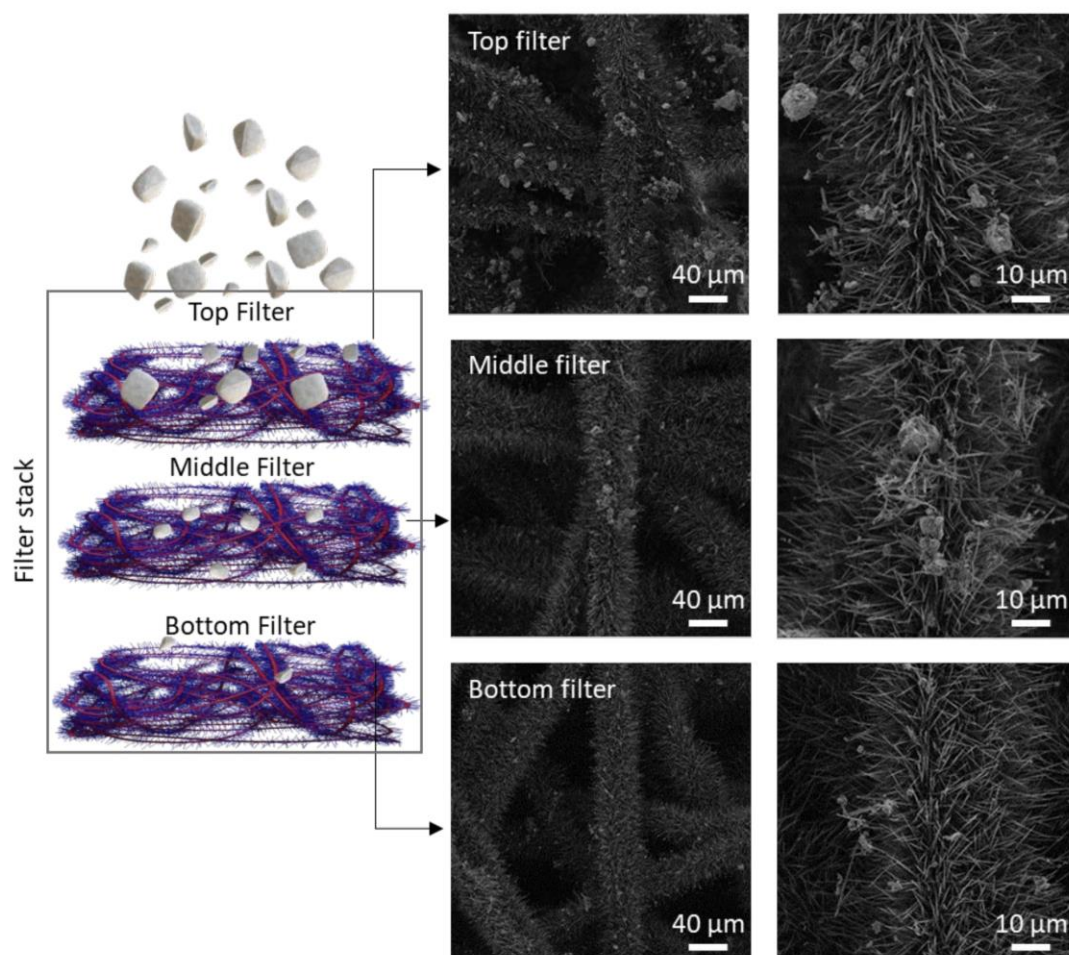
9

Section S10: Average filtration efficiencies of filter stacks of neat and mesostructured polymer nonwovens
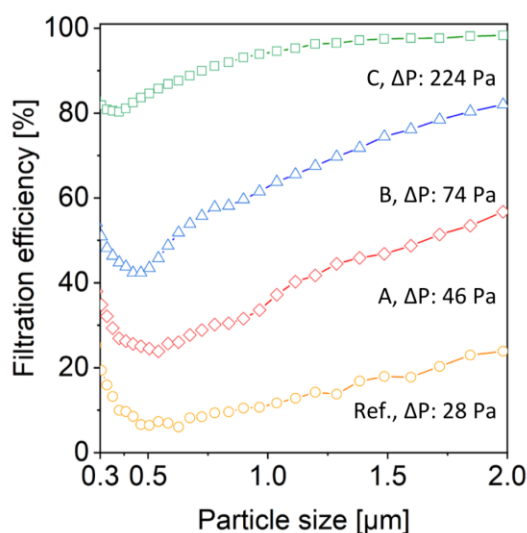
Figure S11. Filtration efficiencies of A) a stack of three mesostructured nonwovens with 2 wt% BTA content (red diamond) exhibiting a pressure drop of 46 Pa, B) a stack of three mesostructured nonwovens with 5 wt% (blue triangle) exhibiting a pressure drop of 74 Pa, C) a stack of three mesostructured nonwovens with 10 wt% BTA content (green square) exhibiting a pressure drop of 224 Pa, and Ref.) a stack of three of neat nonwovens (yellow circle) exhibiting a pressure drop of 28 Pa as reference. Testing conditions: measuring time = 30 s; flow velocity = 0.25 m s^{-1}; filtration area = 28.3 cm^2, test aerosol = ISO fine test dust, upstream aerosol concentration = 30,000 particles cm^{-3}.

10

Section S11: Filtration efficiencies of individual mesostructured glass fiber nonwovens
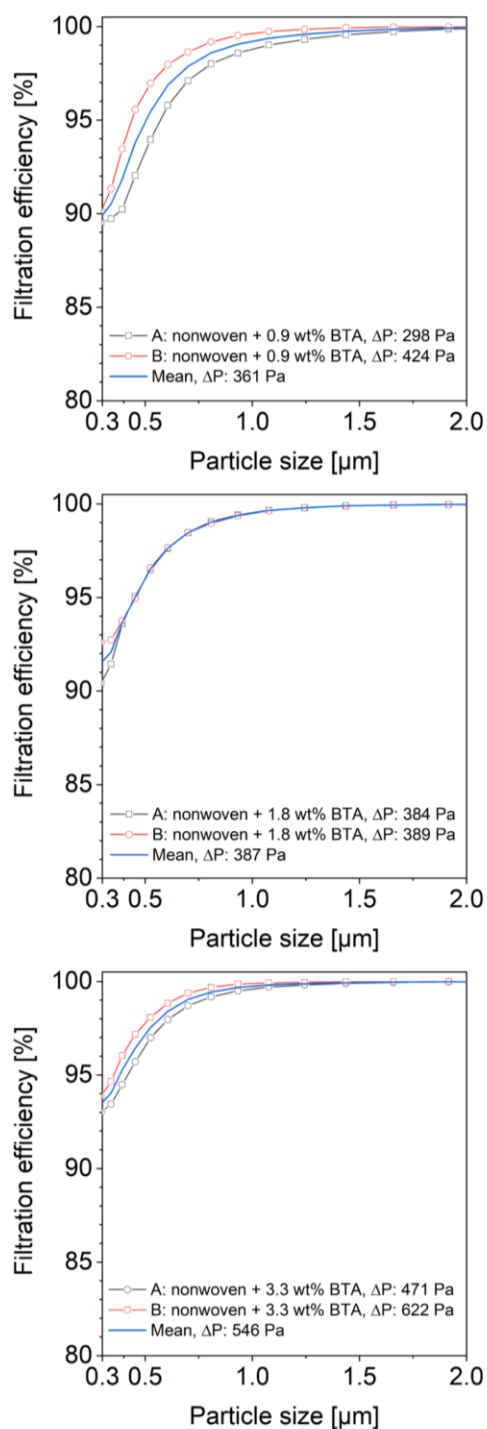
Figure S12. Filtration efficiencies in the range of 0.3 to 2.0 µm of two individual mesostructured glass fiber nonwovens with 0.9 wt% BTA (top), 1.8 wt% (middle) and 3.3 wt% BTA (bottom). The mean values for each graph are shown in blue. Testing conditions: measuring time = 30 s; flow velocity = 0.25 m s^{-1}; filtration area = 28.3 cm^2, test aerosol = ISO fine test dust, upstream aerosol concentration = 30,000 particles cm^{-3}.

11

Section S12: Airstream stability test at high flow velocity
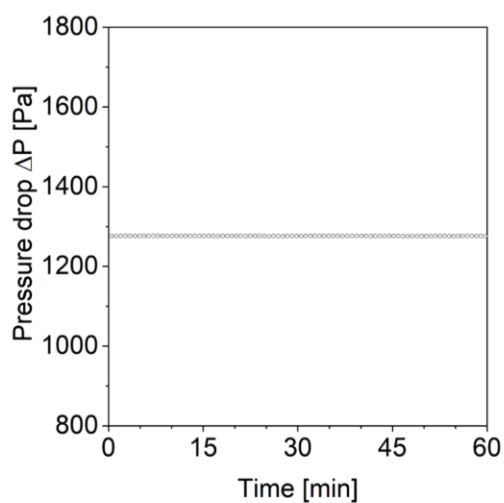
Figure S13. Airstream stability test at a flow velocity of 3 m s^{-1} using a mesostructured glass fiber nonwoven with 3.3 wt% of BTA. The pressure drop is 1276 Pa $\pm$ 0.25 Pa and remains constant over the measuring time of 60 minutes strongly suggesting that the sample remains intact.

12

Section S13: Thermogravimetric analysis of the neat and mesostructured glass fiber nonwovens
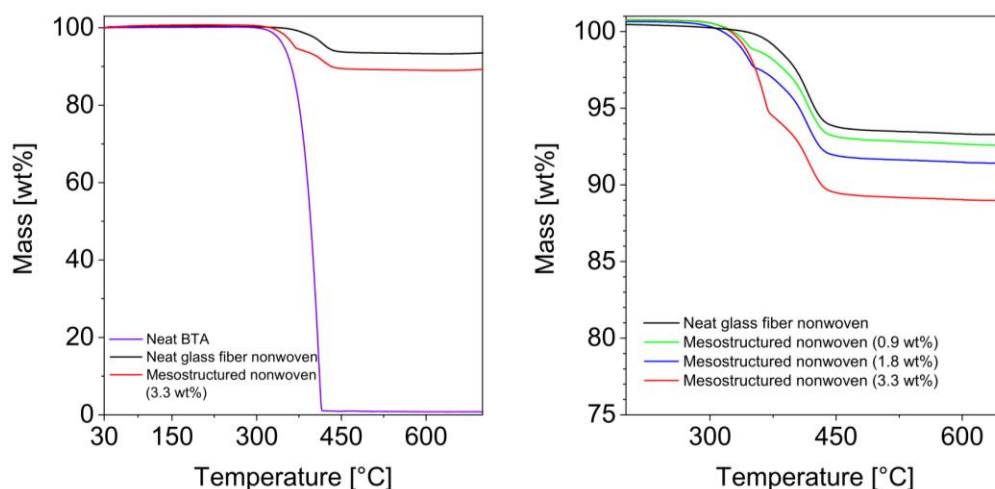
Figure S14. Dynamic TGA of the neat BTA (purple), neat glass fiber nonwoven (black) and mesostructured nonwoven with 3.3 wt% BTA (red) at a heating rate of 10 K min^{-1} under N_2 with a flow rate of 30 mL min^{-1} (left). The BTA fully sublimes, whereas a step of about 6.5 wt% is overserved in the neat glass fiber nonwoven. This is attributed to the decomposition of a coating in the commercial filter media. The difference between the neat nonwoven and the mesostructured nonwoven present above 450°C is attributed to the sublimed amount of the BTA, which is about 4.3 wt%. By comparing the dynamic TGAs of the neat glass fiber nonwoven (black) and the various mesostructured nonwoven with 0.9 wt% (green), 1.8 wt% (blue), and 3.3 wt% (red) of BTA, it can be observed that the relative amount of BTA within the nonwovens follows the same trend and exhibits with 0.7, 1.9, and 4.3 wt% of BTA very similar values as found by weighing the samples.
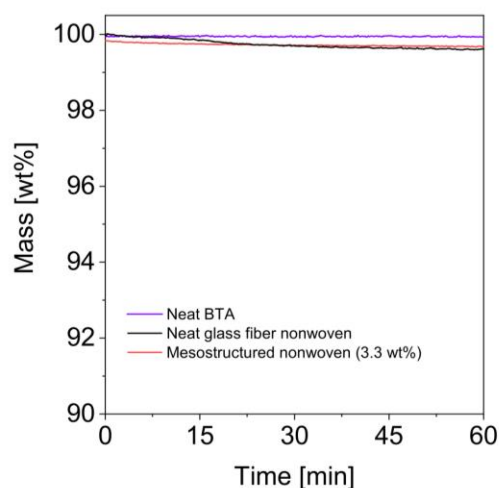
Figure S15. Isothermal TGA of the neat glass fiber nonwoven (black), the neat BTA (purple) and the mesostructured nonwoven with the 3.3 wt% of BTA (red) under nitrogen at 200 °C for 1 h. For the BTA, no weight loss is overserved. The neat glass fiber nonwoven features a weight loss of 0.4 wt%. The same value is found for the mesostructured nonwoven, which is in both cases attributed to the coating of the glass fiber nonwoven.

13

Section S14: Filtration efficiencies of individual mesostructured glass fiber nonwovens before and after heat treatment
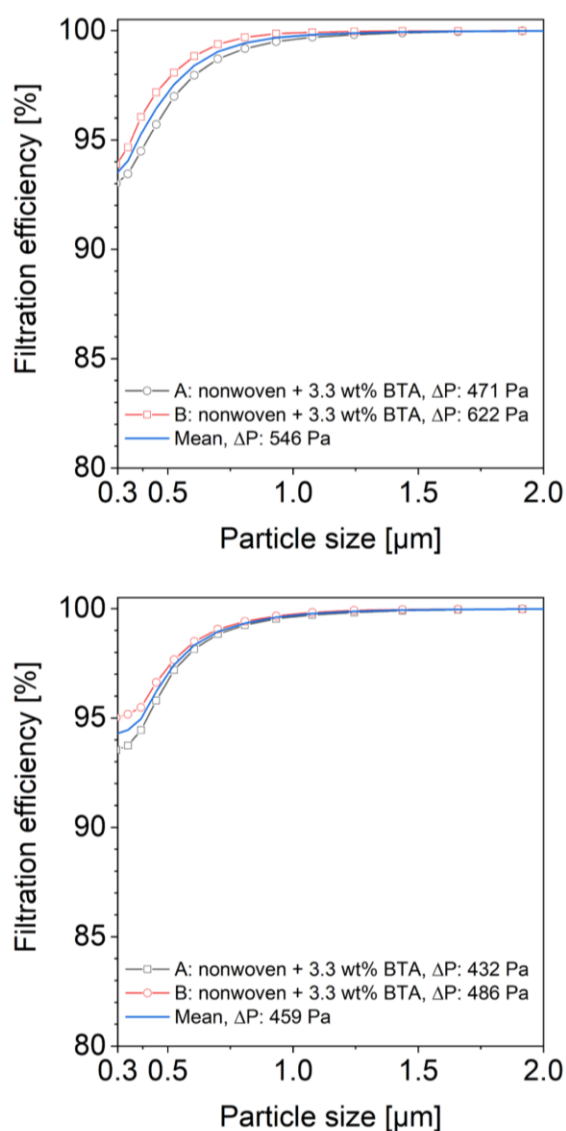
Figure S16. Filtration efficiencies in the range of 0.3 to 2.0 μm of two individual mesostructured glass fiber nonwovens with 3.3 wt% BTA before heat treatment (top) and of two further individual mesostructured glass fiber nonwovens with 3.3 wt% BTA after heat treatment (bottom). The mean values are given in blue. Testing conditions: measuring time = 30 s; flow velocity = 0.25 m s^{-1}; filtration area = 28.3 cm^2, test aerosol = ISO fine test dust, upstream aerosol concentration = 30,000 particles cm^{-3}.

14

4.4 Publication 3

RESEARCH ARTICLE

Controlled Surface Decoration with Functional Supramolecular Nanofibers by Physical Vapor Deposition

Dennis Schröder, Klaus Kreger, Ulrich Mansfeld, and Hans-Werner Schmidt*

Surface decoration of support structures by physical vapor deposition (PVD) of small molecular building blocks offers a versatile platform to realize functional supramolecular nanofibers in a controlled manner and with tailored properties. Here, details on the preparation of surface-decorated polyamide fabrics by PVD using N^1,N^3,N^5-tris[2-(diisopropylamino)-ethyl]-1,3,5-benzenetricarboxamide (1) as a molecular building block are reported. It is shown that a defined morphology with uniform nanofiber length can be achieved, which is controlled by the PVD conditions. The functional periphery of supramolecular nanofibers of 1 allows the immobilization of gold nanoparticles (AuNPs). This results in AuNP-loaded nanostructures with a high surface area, which can be used as a heterogenous catalyst for the reduction of 4-nitrophenol in aqueous media. The surface-decorated support structures with firmly deposited AuNPs also provide the opportunity to conveniently reuse these structures without compromising the catalytic performance. This approach provides fabrication strategies for the controlled surface decoration of macroscopic support structures with small molecular building blocks by PVD with the potential to realize functional robust supramolecular nanofibers for various catalytic or filtration applications.

1. Introduction

Fibrous materials with increased complexity gain growing interest due to their expanded property profile including flexibility and stiffness, controlled porosity, and high surface-to-volume ratio. Introducing different functionalities broadens the field of application including for example filter media with improved moisture permeability, and antiviral and antibacterial properties or

paves the way to novel applications including fibrous membranes for wearable electronics, energy generation, and energy storage as well as heterogeneous catalysis.[1–4]

The production of conventional and functional fibers based on polymer materials are performed by established top-down techniques from solution or melt.[5–7] In this context, electrospinning is one of the most extensively used techniques.[8–10] A way to improve or widen the characteristics toward multi-structured fibrous media is to combine different fiber types often based on different materials.[11] This includes for example the simultaneous electrospinning of two different polymer types resulting in a hierarchically structured fiber morphology.[12] Another example is based on one or two different polymers, consisting of an electrospun polymer fiber scaffold in which finely structured 2D nanofiber networks are embedded.[13–15]

Another approach is based on the combination of polymer fibers and supramolecular fibers. In contrast to top-down approaches, supramolecular fiber formation is based on a bottom-up strategy, namely the spontaneous self-assembly of dissolved small molecular building blocks from solution into fibrillar objects via secondary interactions. As a result, supramolecular fibers form in situ between an existing polymer fiber support. For example, we demonstrated the preparation of polymer/supramolecular fiber composites by immersing a polymer nonwoven in a solution of a 1,3,5-benzenetricarboxamide derivative (BTA) as a molecular building block and subsequent drying of the nonwoven.[16,17] These composites feature a significantly improved performance for the filtration of particulate matter. Hu et al. demonstrated the formation of a dual-nanonet of polymer nanofibers and supramolecular nanofibrils based on 1,3:2,4-di(3,4-dimethylbenzylidene) sorbitol.[18] These dual-nanonet filter media feature, besides a high moisture permeability, remarkable filtration efficiencies at low-pressure drops. In another approach, we prepared compact and shape-persistent sheets based on a network of functional supramolecular BTA nanofibers and polyacrylonitrile short fibers by a wet-laid technique.[19] The functional supramolecular nanofibers within the polymer fibers allow efficient immobilization of gold nanoparticles (AuNPs), which enables the use of the sheet as a reusable heterogeneous catalyst.

D. Schröder, K. Kreger, H.-W. Schmidt
Macromolecular Chemistry I and Bavarian Polymer Institute
University of Bayreuth
95440 Bayreuth, Germany
E-mail: hans-werner.schmidt@uni-bayreuth.de

U. Mansfeld
Bavarian Polymer Institute
University of Bayreuth
95440 Bayreuth, Germany

Publications

**ADVANCED
SCIENCE NEWS**

www.advancedsciencenews.com

**ADVANCED
MATERIALS
INTERFACES**
Open Access

www.advmatinterfaces.de

Apart from the combination of different fiber types, recent approaches make use of fibers with complex morphologies. For example, complex fiber morphologies based on central para-aramid fibers with off-standing nanofiber branches were demonstrated by Xu et al. They used chemical hydrolysis and physical shearing, which resulted in surface fibrillation of the central para-aramid fibers. These multiscale fiber morphologies feature outstanding filtration performance as well as good thermal insulation characteristics.[20,21] We demonstrated another approach to complex fiber morphologies based on a central polymer fiber with off-standing branches of supramolecular fibers. This morphology was realized by decorating the electrospun polymer fibers with seeds capable of initiating supramolecular fiber growth.[22] Similar polymer fiber/supramolecular branch – morphologies were realized by depositing suitable patches on the polymer fiber surface.[23,24] In particular for hierarchical structures based on such supramolecular and polymer fiber types, a distinct two-step procedure is required. In the first step, the seeds or patches were deposited on supporting polymer fibers. Subsequently, supramolecular fibers were grown from these seeds and patches, which acted as nucleation sites in a guided solution-based self-assembly process. Furthermore, in seed-initiated solution-based processes, it is challenging to achieve precise control over the supramolecular fiber length.

However, a fundamental aspect is how to precisely control the formation and morphology of polymer or supramolecular nanofibers at the interface on substrates. A promising approach that allows the defined surface decoration with tailored short fibers on substrates is based on chemical or physical vapor deposition (PVD), which has recently been demonstrated for various polymer and supramolecular materials.[25–29] In contrast to solution-based self-assembly processes, the use of additional tailored seeds is not required. In addition, the fiber length can be precisely controlled by the evaporation time.[29]

Another appealing aspect in this context is the introduction of functionality into the periphery of such fibers, which can ultimately be used for metal particle immobilization by attractive secondary interactions.

Here, we demonstrate the controlled surface decoration of a woven fabric with short and uniform functional supramolecular fibers by PVD (**Figure 1**). A polyamide fabric with defined fiber diameter and porosity was selected as model support. N^1,N^3,N^5-tris[2-(diisopropylamino)-ethyl]−1,3,5-benzenetricarboxamide (**1**) was selected as molecular building block, which is capable of forming supramolecular columns via three strands of hydrogen bonds. The supramolecular fibers feature an amino-functionalized surface suitable to efficiently immobilize gold nanoparticles (AuNPs) from the solution. We demonstrate that the AuNP-loaded mesostructured fabric can be beneficially used and reused as a heterogeneous catalyst in the model reaction, i.e., the reduction of 4-nitrophenol to 4-aminophenol.

2. Results and Discussion

2.1. Preparation of Supramolecular Nanofibers by PVD

1,3,5-Benzenetrisamides are a well-investigated class of supramolecular materials, which is characterized by the formation of three helical hydrogen bonds resulting in fiber-like
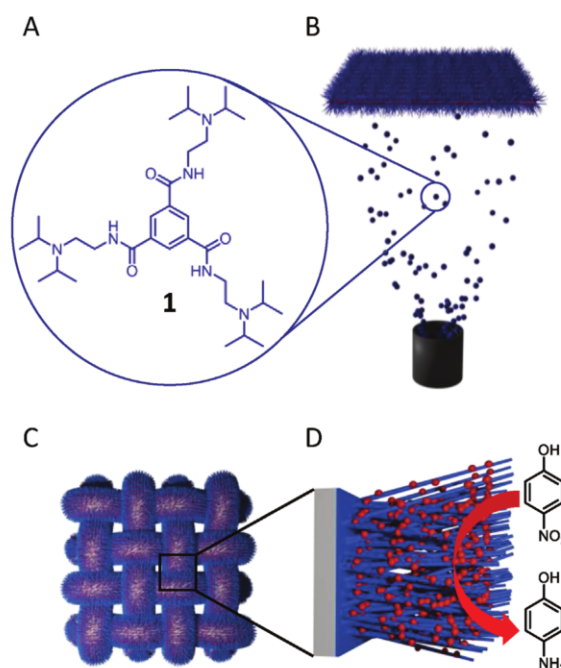
Figure 1. A) Chemical structure of the molecular building block, N^1,N^3,N^5-tris[2-(diisopropylamino)-ethyl]−1,3,5-benzenetricarboxamide 1. B) Schematic illustration of the PVD process. C) Corresponding woven fabrics decorated with supramolecular nanofibers of 1 prepared using PVD. D) The functional surface of the supramolecular nanofibers (in blue) on the woven fabric (in grey) allows the immobilization of AuNPs (in red) which can be used as heterogeneous catalysts for the reduction of 4-nitrophenol to 4-aminophenol in the presence of $NaBH_4$.

columnar assemblies.[30,31] Attaching short or bulky side aliphatic or aromatic groups to the amide groups typically leads to materials with high melting points and also high decomposition temperatures.[32] In particular, the latter is a prerequisite to be used in PVD processes. Recently, we have studied a 1,3,5-benzenetricarboxamide with peripheral functional side groups, i.e., N,N-diisopropylaminoethyl substituents (**1**, for details, see, Section S1, Supporting Information), those supramolecular fibers were capable of immobilizing metal nanoparticles.[24] The thermal properties, of this BTA derivative were determined by thermogravimetric analysis (TGA) and differential scanning calorimetry (DSC, see, Section S2, Supporting Information). TGA reveals no weight loss up to a temperature of ≈300 °C indicating a high thermal stability without decomposition into fragments. The DSC experiments yield a melting point of 275 °C and an isotropization temperature of 298 °C indicating the usability of **1** at evaporation temperatures below 300 °C. In the first set of PVD experiments, we found that **1** starts to evaporate at a temperature of 230 °C under a pressure of 10^{-6} mbar. Thus, the compound sublimes under these conditions. High performance liquid chromatography (HPLC) analysis of **1** after PVD compared to a sample before PVD shows only a single peak confirming that no decomposition takes place (see, Section S3, Supporting Information). In addition, we performed fourier transform infrared (FT-IR) spectroscopy before and after PVD (see, Section

S4, Supporting Information). The spectra are almost identical, which is in agreement with the findings of the HPLC analysis. Importantly, both FT-IR spectra feature amide A (N—H stretch vibration) at 3244 cm^{-1}, amide I (C=O stretch vibration) at 1638 cm^{-1}, and amide II (superposition of N—H bend and C—N stretch vibrations) at ≈1553 cm^{-1}. These vibrations indicate that hydrogen bonds are formed between the amide groups of BTA molecules ultimately resulting in a columnar arrangement of the BTAs.[33] Thus, vapor deposited **1** are present in an ordered fashion on the substrate. To investigate the morphology of the vapor-deposited BTAs, we performed a combinatorial PVD experiment on the same silicon substrate. For this, we applied the same conditions as used before; however, a shutter initially covering the substrate was moved by 1/5 at a given time resulting in a stepwise gradient. As a result, we received five individual sectors with a total vapor exposure time of 5, 10, 15, 30, and 45 min. For each sector, the morphology was analyzed using scanning electron microscopy (SEM) as depicted in **Figure 2**. During the first 5 min under these conditions, **1** appears to be deposited on the silicon substrate in a non-homogeneous droplet-like manner, which becomes a fully covered layer after 10 min. This initial formed layer, which is also referred to as a wetting layer, is often found as a deposit of small molecules prior to subsequent object formation. Consequently, this wetting layer acts as a nucleation sites for the supramolecular fiber growth. With increasing evaporation time, the supramolecular nanofiber growth proceeds largely perpendicular to the substrate in a roughly linear fashion resulting in a densely packed fiber mat. The fiber mat thickness ranges from ≈0.2 to 2.3 µm after evaporation time of 10 to 45 min. Both aspects, the initially formed layer of nucleation sites and the adjustable evaporation time at a constant building block feed allow precise control of the supramolecular fiber length, in contrast to solution-based self-assembly processes.

2.2. Surface Decoration of Woven Fabrics with Defined Supramolecular Nanofibers

Woven or nonwoven fabrics are mechanically stable fibrous porous structures. Thus, these fabrics can be regarded as macroscopic support materials with a high surface-to-volume ratio, which are readily accessible by liquid media. In contrast to nonwovens, woven fabrics are characterized by their defined geometry including the fiber diameter and the pore size and shape, which we use as a model support structure. Here, we have selected a mono-layered interwoven polyamide fabric with a fiber diameter of 35 µm and mesh width of 50 µm (see, Section S5, Supporting Information). To prepare a fully surface-decorated woven fabric with BTA nanofibers, square pieces of 7.6 cm × 7.6 cm were placed in the vapor deposition chamber. PVD was performed at a pressure of 10^{-6} mbar and a source temperature of 230 °C for 120 min. To ensure complete coverage of both sides of the fabric, the support was flipped by 180° and the PVD process was repeated. The morphology of the vapor-deposited supramolecular nanofiber on the woven fabric was investigated by scanning electron microscopy and is depicted in **Figure 3**. The overview image reveals that the entire polyamide fabric is densely and homogeneously covered with supramolecular BTA nanofibers
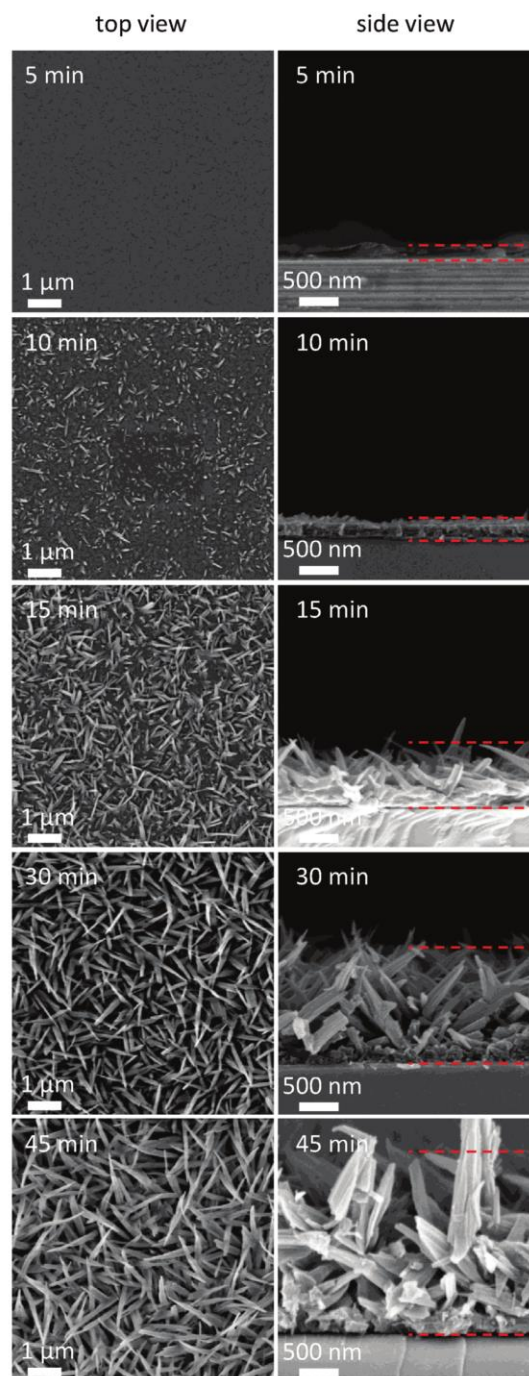
Figure 2. SEM images of vapor deposited **1** on the same silicon wafer at different evaporation times in a combinatorial approach of the PVD experiment comprising five different sectors (evaporation rate = 1.4 µg s^{-1}, T_{source} = 230, $T_{substrate}$ = 25 °C). The five different vapor exposure times, i.e., 5, 10, 15, 30, and 45 min, were realized by successively covering the substrate with a shutter for the given time. The left column shows top view images and the right column side views images. Dashed red lines in the side view images are a guide to the eye indicating the height of deposited fiber mat of **1** ranging from 0.2 µm (for 5 min) to 2.3 µm (for 45 min).

2400259 (3 of 8)
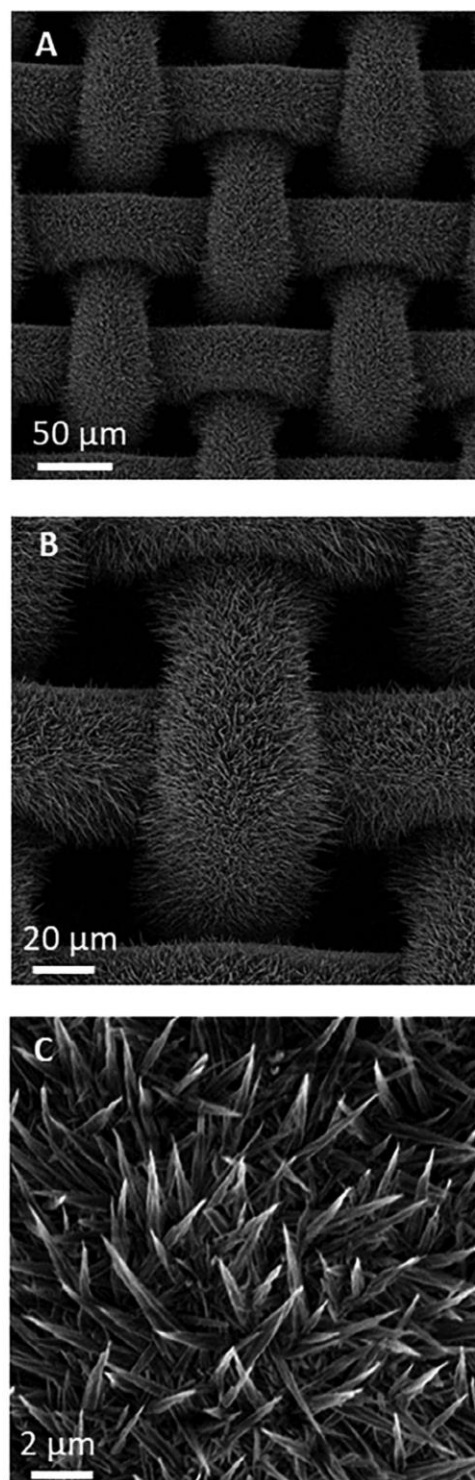
**Figure 3.** SEM micrographs of surface-decorated woven fabrics with defined supramolecular nanofibers. A) Overview image and B, C) different magnifications of the polyamide woven fabric with fibers of 1. PVD conditions: T_{source} = 230, $T_{substrate}$ = 25 °C. p = 10^{-6} mbar, deposition time 120 min.

(Figure 3A). At larger magnifications it can be seen (Figure 3B,C), that the supramolecular nanofibers of the vapor-deposited building blocks were grown perpendicularly from the surface of the support structure, in a similar manner as observed before for the solid silicon substrate. Additionally, the nanofiber morphology of **1** was found to be almost identical when viewed from either the front or back side of the woven fabric (see, Section S6, Supporting Information). This indicates that the nanofiber formation via PVD is a robust and reproducible process. This was also demonstrated by several repetitions of the PVD experiment with other neat woven fabrics of the same kind. From these images, we were able to estimate a supramolecular fiber diameter of ≈350 nm. Yet, the nanofiber length after 120 min of evaporation cannot be clearly recognized. Owing to the defined structure of the woven fabric, we were able to superimpose a neat woven fabric with a surface-decorated fabric with a high degree of accuracy. This allows us to identify the starting point of the nanofiber growth as well as the ending of the supramolecular nanofibers. Applying these processing conditions, we determine a uniform length of the supramolecular BTA fibers to be 8 μm (see, Section S7, Supporting Information).

2.3. Immobilization of AuNPs on the Supramolecular Nanofibers

To demonstrate the use of the functional periphery of the supramolecular nanofibers decorated on the fabric, we investigate the immobilization of AuNPs. For this purpose, we synthesized AuNPs according to the well-established procedure of Gittins and Caruso.[34] This involves the reduction of tetrachloroauric(III) acid in toluene and subsequent stabilization and transfer to aqueous media using dimethylaminopyridine (DMAP) as a non-acidic ligand. UV/vis spectroscopy of the dark red solution in water shows an absorption maximum at 520 nm attributed to plasmon resonance of the AuNPs (see, Section S8, Supporting Information). Using dynamic light scattering (DLS) we found a uniform particle size distribution and no indication for agglomerates. The average diameter of the AuNPs was found to be ≈10 nm. We used this aqueous solution to immobilize the DMAP-stabilized AuNPs on the functional surface of the short supramolecular nanofibers on the woven fabric by dipping the mesostructured fabric into the AuNPs dispersion. To remove non-immobilized AuNPs, the fabric was washed with water and then dried. SEM investigations of the AuNP-loaded surface-decorated woven fabrics reveal that the overall morphology of mesostructured woven fabric remains largely unchanged (**Figure 4A,B**). The first evidence for successful deposition of the AuNPs on the supramolecular nanofibers was obtained by using a back-scatter detector during SEM. This results in bright features on top of the supramolecular nanofibers in the micrographs, which is indicative of the presence of metal particles. Since the mesostructured woven is very densely packed with supramolecular nanofibers, no statement can be made on the AuNPs immobilization capability of the polyamide woven support (Figure 4C,D). Thus, we used a neat polyamide woven fabric as a reference and immersed it in the AuNPs dispersion followed by a washing step; however, no AuNPs were found on the fabric demonstrating the importance of the functional periphery of the supramolecular nanofibers for the AuNPs
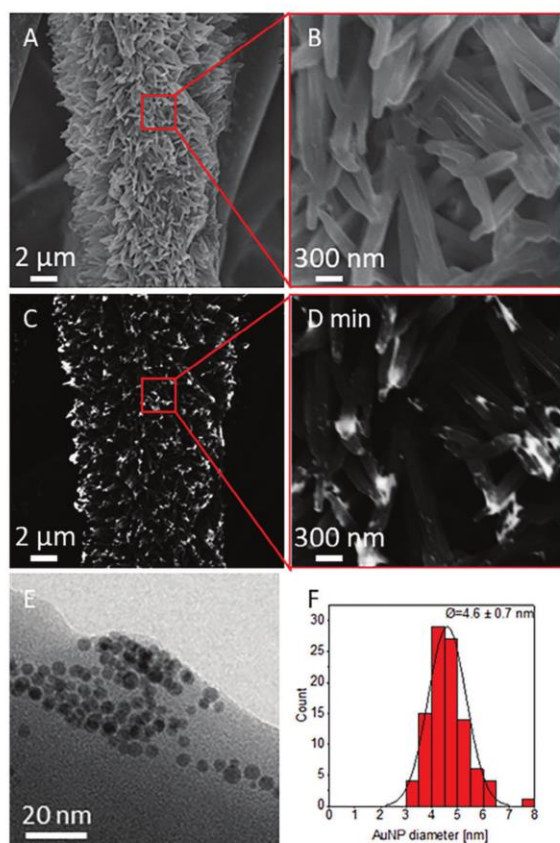
Figure 4. A,B) SEM images at different magnifications of AuNP decorated mesostructured woven using an Inlens detector. C,D) SEM images at different magnifications using the same woven and a backscatter electron detector reveal bright areas on top of the supramolecular fibers indicating the presence of gold particles. E) Distinct individual AuNPs on mechanically detached supramolecular nanofibers as revealed by TEM featuring a uniform particle size distribution. F) Corresponding histogram of the diameter of the immobilized AuNPs determined by evaluating 100 particles showing an average particle diameter of 4.6 ± 0.7 nm.

immobilization. After detaching and transferring small fragments of supramolecular nanofibers with immobilized AuNPs onto substrates, we investigated several nanofibers by transmission electron microscopy (TEM, Section S9, Supporting Information). TEM micrographs of different fibers reveal that distinct AuNPs on the supramolecular fibers are present, which appear to be arranged in a thread-like manner. At higher magnifications, small non-agglomerated AuNPs with uniform particle size distribution were identified (Figure 4E; Section S9, Supporting Information). The average diameter of the immobilized AuNPs was determined to be 4.7 nm (Figure 4F). Compared to the diameter of the as-prepared AuNPs determined by DLS, this value is smaller by a factor of about two, which is attributed to an overestimation of DLS values.[35] To determine the amount of AuNPs that is loaded onto the surface-decorated woven fabric, we performed inductively coupled plasma-optical emission spectrometry (ICP-OES). Three individual samples each for the

mesostructured woven were analyzed yielding a gold content of 21 µg.

2.4. Immobilized AuNPs on Mesostructured Woven Support for Heterogeneous Catalysis

Ultimately, we investigated the surface-decorated woven fabrics loaded with AuNPs as heterogeneous catalysts for the reduction of 4-nitrophenol to 4-aminophenol in the presence of $NaBH_4$. The AuNP-catalyzed reduction of 4-nitrophenol is a frequently studied model reaction in which the degree of conversion can be readily investigated by UV–vis spectroscopy. In this case, the reaction kinetics are monitored by following the progression of the absorption at 400 nm. This absorption is attributed to the sodium 4-nitrophenolate, which is immediately formed by the addition of a large excess of $NaBH_4$. In the presence of the AuNP catalyst, the absorption of 4-nitrophenolate is steadily decreasing and simultaneously a new absorption at ≈ 300 nm is increasingly established due to the formation of 4-aminophenolate (**Figure 5A**). The decrease in the reactant, i.e., sodium 4-nitrophenolate, (c_t/c_0) over time with and without the immobilized AuNP catalyst is plotted in Figure 5B. As anticipated, the absence of AuNPs precludes any discernible conversion. In contrast, the immobilized AuNP catalyst on the woven support facilitates a rapid reaction, resulting in a conversion of up to 95% within 4 min. The progression of the conversion, as illustrated in Figure 5B, also indicates that the reaction rate of the 4-nitrophenol reduction to 4-aminophenol follows pseudo-first-order kinetics, which is related to the substantial excess of $NaBH_4$. Consequently, plotting $-\ln(c_t/c_0)$ over time revealed a linear relationship (Figure 5C). The apparent kinetic reaction rate constants (k_{app}) were derived from the slope of the linear regression and found to be $k_{app} = 1.16$ min^{-1}. Compared to previously reported k_{app} values on reusable fiber-based systems in literature,[36–40] and in particular to our recent findings,[19] this k_{app} seems to be relatively high. With respect to the latter AuNP-loaded supramolecular/polymer fiber composite, this finding may be attributed to easier accessibility to reactive catalytic sites.

An important feature of deposited AuNPs on macroscopic supports is the potential to remove and reuse the heterogeneous catalysts while the catalytic activity is maintained. To verify the reusability, we performed three consecutive cycles of the catalysis experiments. For each cycle, the same round-shaped AuNP-loaded mesostructured woven fabric was immersed in a freshly prepared reaction mixture containing 4-nitrophenol and removed after completion of the reduction to 4-aminophenol as confirmed by absorption measurements. Figure 5D depicts the progress of the reaction by absorption measurements over time for three consecutive runs. In all three cycles, the time to complete the reaction as well as the k_{app} remains the same. Consequently, a reduction in the catalytic activity of the supramolecular nanofiber carrying the AuNPs cannot be observed. This indicates that the morphology of the supramolecular nanofiber remains intact. This also indicates that the AuNPs on the supramolecular nanofiber maintain their reactivity and do not leach to the solution.

To verify these findings, we conducted SEM, TEM, and ICP-OES measurements on dried samples (see, Section S10,

132
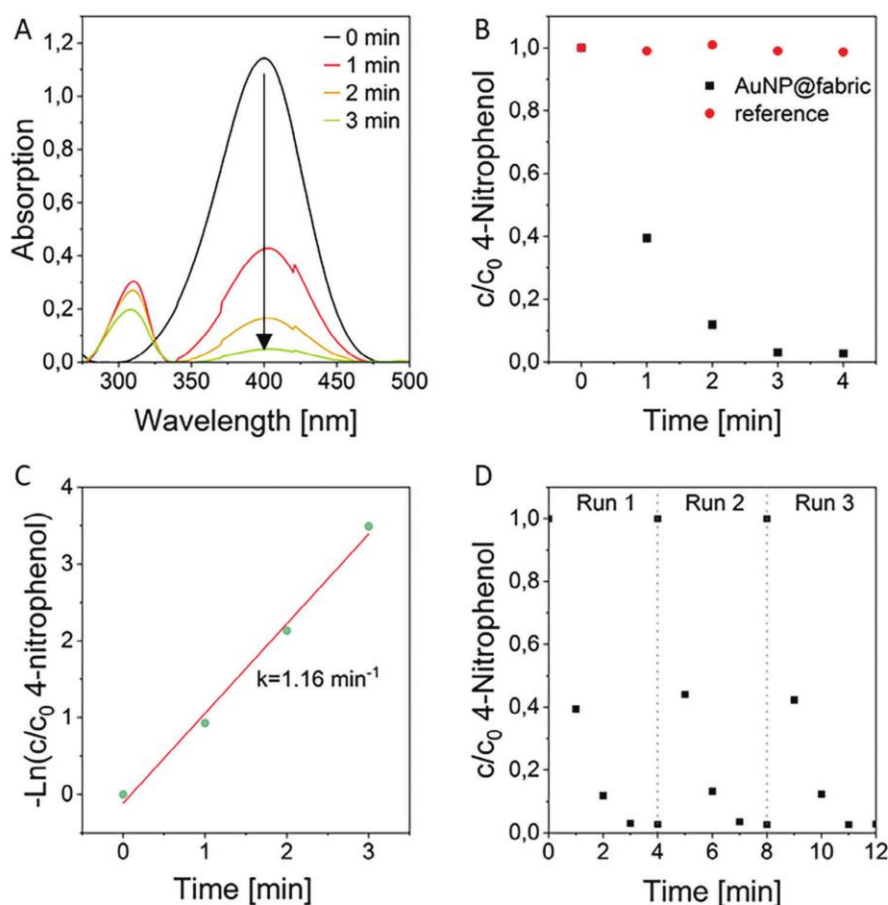
Figure 5. A) Temporal evolution of UV/vis spectra recorded from 250 to 500 nm during the reduction of 4-nitrophenolate to 4-aminopenolate using NaBH$_4$ and AuNP decorated mesostructured woven as heterogenous catalyst. B) Decrease of the 4-nitrophenolate concentration (c_t/c_0) over time with and without AuNP-deposited catalyst on mesostructured woven fabric. C) Determination of k$_{app}$ from the slope of the linear regression. D) Reusability experiments of the AuNP decorated mesostructured woven in three consecutive catalytic cycles. Reaction conditions for (A–D): 1.5 mL of 0.1 mm aqueous 4-nitrophenol solution, 1.5 mL of 100 mm aqueous NaBH$_4$, and 21 µg of immobilized AuNPs on mesostructured woven fabrics. The reaction is performed at 25 °C with stirring at 600 rpm.

Supporting Information). The SEM micrographs demonstrate that the surface-decorated morphology remains intact, with no significant change observable. This indicates a strong adhesion of supramolecular nanofibers to the woven fabric. Similarly, TEM of fragments of supramolecular nanofibers revealed a similar picture of deposited AuNPs with an average size of 4.7 nm, indicating that the AuNPs are firmly immobilized. This finding is consistent with ICP-OES analysis of the reaction solution after catalysis, which showed no gold within the detection limit of the method.

3. Conclusion

Here, we presented a feasible approach to realize tailored surface-decorated support structures by PVD comprising uniform supramolecular nanofibers based on N^1,N^3,N^5-tris[2-(diisopropylamino)-ethyl]−1,3,5-benzenetricarboxamide (1) and a polyamide woven fabric. Unlike solution-based self-assembly processes, the PVD process enables precise control of the supramolecular fiber length on different substrates without the use of pre-deposited seeds. The functional periphery of supramolecular nanofibers of **1** facilitates a robust immobilization of AuNPs, which can be used as a heterogeneous catalyst for the reduction of 4-nitrophenol. The catalytic reaction proceeds with an k$_{app}$ of 1.16 min^{-1}, which we attribute to ready accessibility to the reactive catalytic sites on the surface-decorated support. Beneficially, such surface-decorated fabrics with immobilized AuNPs, be easily removed and reused without compromising the catalytic performance due to the robust mechanical stability of and between the integral components. We anticipate that the tailored preparation of surface-decorated support structures by PVD can be conveniently transferred to other functional uniform supramolecular BTA nanofibers. The rational design of the functional BTA could pave the way to the development of mesostructured surfaces for various applications in (photo)catalysis, filtration, or antibacterial coatings.

4. Experimental Section

Preparation of Supramolecular Nanofibers of 1 on Substrates by PVD: For PVD of **1**, a modified vapor deposition chamber PLS 500 from Balzers was used. Quartz crystal sensors were mounted near the substrate holder and used to monitor the evaporation rate. About 500 mg of **1** was weighed into a quartz crucible, which was placed into an effusion cell used as a heating source. As substrate a silicon wafer was used. At 230 °C temperature of the effusion cell and 10^{-6} mbar, a constant apparent evaporation rate was monitored by the quartz crystal sensors and found to be 1.4 µg s^{-1}. For the preparation of step thickness gradients, a combinatorial set-up was used to obtain five different sectors by moving a shutter at a distinct distance in a similar manner as described previously.[29] At the end of each experiment, the vacuum chamber was ventilated with air.

Surface Decoration of Woven Fabrics with Defined Supramolecular Nanofibers of 1: For the preparation of a fully surface-decorated woven fabric with BTA nanofibers, the same PVD setup as outlined above was used. As support material, a polyamide woven fabric with a uniform fiber diameter of 35 µm and a mesh width of 50 µm was used and cut into a square piece of 7.6 cm × 7.6 cm having a mass of ≈200 mg. The cut piece of the fabric was clamped into a custom-made 3D-printed holder and fixated in a substrate holder, which was located ≈35 cm above the effusion cells in the vapor deposition chamber. A closed shutter covers the substrate holder prior to the evaporation process. PVD was initiated at a pressure of 10^{-6} mbar and a source temperature of 230 °C of the effusion cell. A constant evaporation rate was monitored by quartz crystal sensors and determined to be 1.4 µg s^{-1}. The shutter was fully opened and after an evaporation time of 240 min, the chamber was ventilated with air, opened and the custom-made holder was flipped by 180°. Subsequently, the process was repeated to ensure complete coverage of both sides of the mono-layered woven fabric with supramolecular nanofibers.

Gold Nanoparticle Loading: AuNP immobilization on the supramolecular nanofibers was done by dipping a round-shaped piece of mesostructured woven with a diameter of 12 mm (m = 720 µg) into an aqueous dispersion of the freshly prepared DMAP-stabilized AuNPs for 1 h. After deposition of the AuNPs, the woven fabric was removed from the immersion solution and washed with ultrapure water until an excess of non-immobilized AuNPs was removed. The AuNP-loaded woven fabric was subsequently dried in a vacuum (<5 mbar) at 40 °C for 15 h.

UV/vis Spectroscopy: Absorption measurements were performed on a Jasco Spectrometer V-670 with a scan speed of 400 nm min^{-1} at 25 °C using a quartz glass cuvette (D = 10 mm). Baseline correction was carried out by measuring a blank sample with Milli-Q water before measurements.

SEM: Scanning electron microscopy was performed with a Zeiss 1530 FESEM at 3 kV using an Inlens detector. Samples were fixed via a double-sided adhesive conductive carbon tape on an SEM sample holder and subsequently sputtered with platinum (2 nm) prior to SEM investigation. For visualization of AuNP a back-scatter detector was used at 10 kV.

TEM: Transmission electron microscopy was performed on a JEOL JEM-2200FS. For the investigation of the AuNPs distribution on the supramolecular fibers, a lacey carbon-coated copper grid (LC400, EMS, USA) was wiped over the surface of the mesostructured woven to transfer supramolecular fiber fragments on the TEM grid. The same procedure was applied for the analysis of the AuNP size distribution on a mesostructured woven after that was used three times in the catalytic reduction of 4-nitrophenol. All samples were investigated at room temperature using the bright-field mode with energy filtering at an acceleration voltage of 200 kV.

ICP-OES: Inductively coupled plasma-optical emission spectrometry measurements were carried out using a PerkinElmer Avio 200 equipped with an S10 autosampler, Echelle polychromator, Argon humidifier, and a DBI-CCD detector. The samples were calibrated against a single gold standard (PerkinElmer Pure, Gold 1000 mg L^{-1} in 10% HCl) with concentrations of 0.05, 0.1, 0.5, 1, and 10 mg L^{-1}, respectively. For sample preparation, the AuNP solution before and after immersion of the mesostructured woven fabrics as well as the reaction solutions after catalysis was evaporated completely at 70 °C, dissolved in 0.5 mL of aqua regia, and diluted with 9.5 mL of deionized water (18.2 MΩ cm).

Reduction of 4-Nitrophenol by AuNP-Loaded Mesostructured Woven Fabrics as Heterogeneous Catalyst: The catalytic activity of the AuNP-loaded mesostructured woven fabrics was examined by the reduction of 4-nitrophenol to 4 aminophenol. For this, 1.5 mL of a 0.1 mм 4-nitrophenol solution and 1.5 mL of a 100 mм NaBH$_4$ solution were put in a quartz cuvette. Subsequently, a round-shaped Au-loaded woven fabric with a diameter of 13 mm was completely immersed in the reaction solution using a tweezer. Then the reaction was stirred at 25 °C and 600 rpm for 15 min. The progress of the reaction was monitored by absorption measurements taken every minute in the range of 250–500 nm with a scan speed of 400 nm min^{-1}.

Supporting Information

Supporting Information is available from the Wiley Online Library or from the author.

Acknowledgements

Conflict of Interest

The authors declare no conflict of interest.

Data Availability Statement

The data that support the findings of this study are available from the corresponding author upon reasonable request.

Keywords

[1] E. Loccufier, D. P. Debecker, D. R. D'hooge, K. de Buysser, K. de Clerck, *ChemCatChem* **2024**, 202301563, https://doi.org/10.1002/cctc.202301563.

[2] C. Chen, J. Feng, J. Li, Y. Guo, X. Shi, H. Peng, *Chem. Rev.* **2023**, *123*, 613.

[3] J.-W. Jung, C.-L. Lee, S. Yu, I.-D. Kim, *J. Mater. Chem. A* **2016**, *4*, 703.

[4] X. Li, Z.-H. Lin, G. Cheng, X. Wen, Y. Liu, S. Niu, Z. L. Wang, *ACS Nano* **2014**, *8*, 10674.

2400259 (7 of 8)

**ADVANCED
SCIENCE NEWS**

www.advancedsciencenews.com

**ADVANCED
MATERIALS
INTERFACES**
Open Access

www.advmatinterfaces.de

[5] C. J. Ellison, A. Phatak, D. W. Giles, C. W. Macosko, F. S. Bates, *Polymer* **2007**, *48*, 3306.

[6] E. S. Medeiros, G. M. Glenn, A. P. Klamczynski, W. J. Orts, L. H. C. Mattoso, *J. Appl. Polym. Sci.* **2009**, *113*, 2322.

[7] J. G. McCulloch, *Int. Nonwovens J.* **1999**, *os-8*, 139.

[8] A. Greiner, J. H. Wendorff, *Angew. Chem., Int. Ed.* **2007**, *46*, 5670.

[9] M. Bognitzki, W. Czado, T. Frese, A. Schaper, M. Hellwig, M. Steinhart, A. Greiner, J. H. Wendorff, *Adv. Mater.* **2001**, *13*, 70.

[10] J. Xue, T. Wu, Y. Dai, Y. Xia, *Chem. Rev.* **2019**, *119*, 5298.

[11] T. Lu, J. Cui, Q. Qu, Y. Wang, J. Zhang, R. Xiong, W. Ma, C. Huang, *ACS Appl. Mater. Interfaces* **2021**, *13*, 23293.

[12] S. Zhang, H. Liu, X. Yin, J. Yu, B. Ding, *ACS Appl. Mater. Interfaces* **2016**, *8*, 8086.

[13] H. Liu, S. Zhang, L. Liu, J. Yu, B. Ding, *Adv. Funct. Mater.* **2019**, *29*, 1904108.

[14] S. Zhang, H. Liu, N. Tang, S. Zhou, J. Yu, B. Ding, *Adv. Mater.* **2020**, *32*, 2002361.

[15] X. Xu, S. Liu, X. Liu, J. Yu, B. Ding, *J. Colloid Interface Sci.* **2024**, *657*, 463.

[16] H. Misslitz, K. Kreger, H.-W. Schmidt, *Small* **2013**, *9*, 2053.

[17] D. Weiss, D. Skrybeck, H. Misslitz, D. Nardini, A. Kern, K. Kreger, H.-W. Schmidt, *ACS Appl. Mater. Interfaces* **2016**, *8*, 14885.

[18] M. Hu, Y. Wang, Z. Yan, G. Zhao, Y. Zhao, L. Xia, B. Cheng, Y. Di, X. Zhuang, *J. Mater. Chem. A* **2021**, *9*, 14093.

[19] M. Drummer, C. Liang, K. Kreger, S. Rosenfeldt, A. Greiner, H.-W. Schmidt, *ACS Appl. Mater. Interfaces* **2021**, *13*, 34818.

[20] K. Xu, J. Deng, R. Lin, H. Zhang, Q. Ke, C. Huang, *J. Mater. Chem. A* **2020**, *8*, 22269.

[21] K. Xu, J. Deng, G. Tian, L. Zhan, J. Ma, L. Wang, Q. Ke, C. Huang, *Nano Res.* **2022**, *15*, 5695.

[22] M. Burgard, D. Weiss, K. Kreger, H. Schmalz, S. Agarwal, H.-W. Schmidt, A. Greiner, *Adv. Funct. Mater.* **2019**, *29*, 1903166.

[23] A. Frank, C. Hils, M. Weber, K. Kreger, H. Schmalz, H.-W. Schmidt, *Angew. Chem., Int. Ed.* **2021**, *60*, 21767.

[24] A. Frank, M. Weber, C. Hils, U. Mansfeld, K. Kreger, H. Schmalz, H.-W. Schmidt, *Macromol. Rapid Commun.* **2022**, *43*, 2200052.

[25] D. Varadharajan, K. Nayani, C. Zippel, E. Spuling, K. C. Cheng, S. Sarangarajan, S. Roh, J. Kim, V. Trouillet, S. Bräse, N. L. Abbott, J. Lahann, *Adv. Mater.* **2022**, *34*, 2108386.

[26] K. C. K. Cheng, M. A. Bedolla-Pantoja, Y.-K. Kim, J. V. Gregory, F. Xie, A. de France, C. Hussal, K. Sun, N. L. Abbott, J. Lahann, *Science* **2018**, *362*, 804.

[27] L. Adler-Abramovich, D. Aronov, P. Beker, M. Yevnin, S. Stempler, L. Buzhansky, G. Rosenman, E. Gazit, *Nat. Nanotechnol.* **2009**, *4*, 849.

[28] N. Amdursky, M. Molotskii, D. Aronov, L. Adler-Abramovich, E. Gazit, G. Rosenman, *Nano Lett.* **2009**, *9*, 3111.

[29] D. Schröder, C. Neuber, U. Mansfeld, K. Kreger, H.-W. Schmidt, *Small Sci* **2023**, *4*, 2300160.

[30] M. P. Lightfoot, F. S. Mair, R. G. Pritchard, J. E. Warren, *Chem. Commun.* **1999**, *19*, 1945.

[31] S. Cantekin, T. F. A. de Greef, A. R. A. Palmans, *Chem. Soc. Rev.* **2012**, *41*, 6125.

[32] M. Blomenhofer, S. Ganzleben, D. Hanft, H.-W. Schmidt, M. Kristiansen, P. Smith, K. Stoll, D. Mäder, K. Hoffmann, *Macromolecules* **2005**, *38*, 3688.

[33] P. J. M. Stals, M. M. J. Smulders, R. Martín-Rapún, A. R. A. Palmans, E. W. Meijer, *Chem. − A Eur. J.* **2009**, *15*, 2071.

[34] D. I. Gittins, F. Caruso, *Angew. Chem., Int. Ed.* **2001**, *40*, 3001.

[35] H. Hinterwirth, S. K. Wiedmer, M. Moilanen, A. Lehner, G. Allmaier, T. Waitz, W. Lindner, M. Lämmerhofer, *J. Sep. Science* **2013**, *36*, 2952.

[36] M. Abbas, H. H. Susapto, C. A. E. Hauser, *ACS Omega* **2022**, *7*, 2082.

[37] X. Cao, S. Yan, F. Hu, J. Wang, Y. Wan, B. Sun, Z. Xiao, *RSC Adv.* **2016**, *6*, 64028.

[38] N. Guarrotxena, L. Garrido, I. Quijada-Garrido, *Adv. Mater. Interfaces* **2018**, *5*, 1801374.

[39] J. Li, C. Liu, Y. Liu, *J. Mater. Chem.* **2012**, *22*, 8426.

[40] K. Sawada, S. Sakai, M. Taya, *J. Mater. Sci.* **2014**, *49*, 4595.

2400259 (8 of 8)

Supporting Information

Controlled surface decoration with functional supramolecular nanofibers by physical vapor deposition

Dennis Schröder[1], Klaus Kreger[1], Ulrich Mansfeld[2], Hans-Werner Schmidt[1] *

[1]Macromolecular Chemistry I and Bavarian Polymer Institute, University of Bayreuth, 95440 Bayreuth, Germany
[2]Bavarian Polymer Institute, University of Bayreuth, 95440 Bayreuth, Germany

Table of content:

WILEY-VCH

Section 1: Materials and methods

Materials

The polyamide woven fabric with a mesh size of 50 μm and a fiber diameter of 35 μm was purchased from Klein und Wieler oHG and cut to square pieces of 7.6 x 7.6 cm that were used during the physical vapor deposition process.

Tetrachloroauric(III) acid trihydrate ($HAuCl_4 \cdot 3H_2O$, 99.99%) and sodium borohydride ($NaBH_4$, 98%) were purchased from abcr GmbH. 4-Nitrophenol (≥99%), 4-dimethylaminopyridine (DMAP, ReagentPlus, ≥99%), sulfuric acid (97%), sodium hydroxide, and tetraoctylammonium bromide (99.99%) were purchased from Sigma-Aldrich. Deionized water was demineralized and purified with a Millipore-Q Plus purification system (column, QPAK2; electrical conductivity, 18.2 MΩ cm).

1 was synthesized as described previously.[1] For this, we dispersed 21.5 g of trimesic acid trimethyl ester in 75.0 mL of *N,N*-diisopropyl-ethylenediamine. The mixture stirred for 12 h at 125 °C. After cooling to room temperature, the crude product was refluxed in approx. 700 mL of ethyl acetate and filtered off. After repeating this procedure twice and finally drying in high vacuum, we obtained 37.3 g (74%) of **1** as a white powder. ^{1}H NMR (300 MHz, $CDCL_3$, δ): 1.06 (d, 36H), 2.72 (t, 6H), 3.08 (hept, 6H), 3.46 (q, 6H) 7.30 (s$_{br}$, 3H) 8.43 (s, 3H) ppm; ^{13}C NMR (75 MHz, $CDCl_3$, δ): 20.9, 38.6, 43.2, 48.2, 128.1, 135.5, 165.5 ppm.

4-Dimethylaminopyridine (DMAP) stabilized gold nanoparticles (AuNP) were prepared according to established literature procedures.[2] First, a solution of 354 mg (0.9 mmol) tetrachloroauric(III) acid trihydrate ($HAuCl_4 \cdot 3 H_2O$) dissolved in 30 mL deionized water was added to a solution of 1.09 g (2 mmol) tetraoctylammonium bromide dissolved in 80 mL toluene. To this solution 378 mg (10 mmol) $NaBH_4$ dissolved in 25 mL deionized water was added to the mixture as stirred 30 min. Afterwards the two phases were separated and the organic phase was subsequently washed with 0.1 M H_2SO_4, 0.1 M NaOH, and H_2O (three times), and then dried over anhydrous Na_2SO_4. For stabilization of the AuNP a solution of 122 mg (1 mmol) DMAP dissolved in 10 mL deionized water was added to aliquots (10 mL) of the as-prepared nanoparticle mixture. Direct phase transfer across the organic/aqueous boundary was completed within 1 h.

[1] Frank, A.; Weber, M.; Hils, C.; Mansfeld, U.; Kreger, K.; Schmalz, H.; Schmidt, H.-W. *Macromol. Rapid Commun.* **2022**, *43*, e2200052.
[2] Gittins, D. I.; Caruso, F. *Angew. Chem. Int. Ed.* **2001**, *40*, 3001–3004.

WILEY-VCH

Methods

^{1}H NMR and ^{13}C NMR spectra in solution were recorded on a Bruker Avance Ultrashield 300 at room temperature. For the preparation of the NMR samples, approx. 5 mg of **1** was dissolved in 0.6 mL of CDCl$_3$.

Thermogravimetric analyses (TGA) were performed in the range from 30 to 700 °C with a heating rate of 10 K min^{-1} under a nitrogen atmosphere with a flow rate of 30 mL min^{-1} using a Mettler Toledo TGA/DSC3+ Star.

Melting points and recrystallisation were investigated by differential scanning calorimetry (DSC) using a Mettler Toledo DSC2. Approx. 10 mg of the solid were filled in sealable crucibles. Spectra were recorded with a heating/cooling rate of 10 K·min^{-1} in a temperature range from 50 °C to 320 °C.

Infrared spectroscopy (IR) spectra were recorded of an as-synthesized powder of **1** and of a physical vapor deposited **1** fiber mat on a silicon wafer using a PerkinElmer Spectrum 100 FT-IR spectrometer in attenuated total reflection (ATR) mode in the range from 4000 cm^{-1} to 650 cm^{-1}.

High performance liquid chromatography (HPLC) of **1** was performed on an Agilent series 1100 equipped with a Zorbax, Eclipse, Plus-C18 column and an UV-detector. As eluent acetonitrile/water 30/70 at a flow rate of 1mL min^{-1} was used. The injection volume was 10 μL. Retention time of **1** was determined to be 1.46 min.

Dynamic light scattering (DLS) was conducted on a Zetasizer Nano S (Malvern Panalytical, UK) instrument equipped with a red He-Ne laser (λ = 632.8 nm) and a detector placed at θ = 173° to the incident radiation. The AuNP dispersion was measured without further dilution at 25 °C in quartz glass cuvettes (10.0 mm path length), which were sealed with Teflon tape to prevent solvent evaporation. Data analyses were carried out using the Malvern Zetasizer software (version 7.13).

Section 2: Thermal characterization of **1**
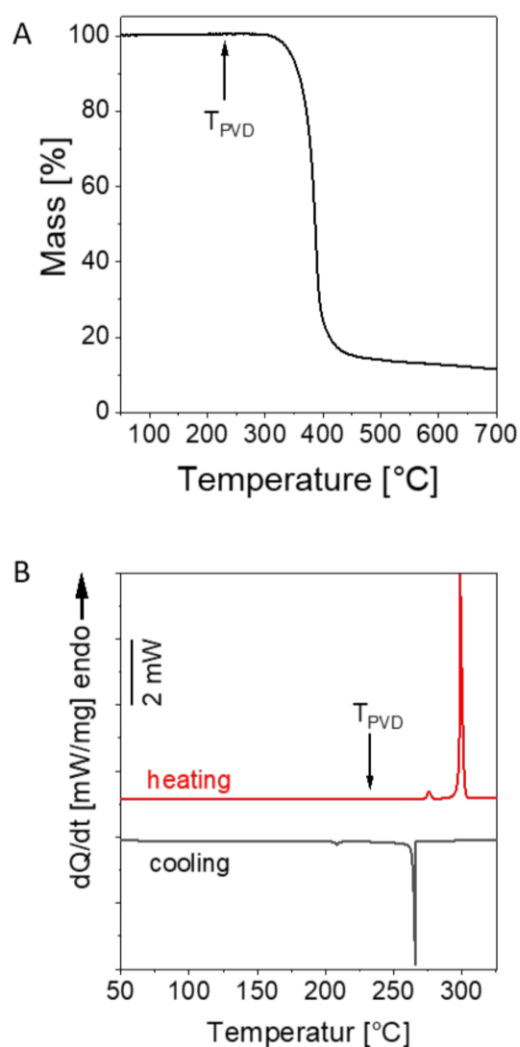
Figure S1. A) TGA measurement of **1** from 50-700°C at a heating rate of 10 K min^{-1} under N$_2$ with a flow rate of 30 mL min^{-1}. B) DSC measurements of **1** from 50-320 °C at a rate of 10 K min^{-1}; shown are the 1st heating curve (red) and cooling curve (blue). The black arrows indicate the temperature at which PVD was performed (230°C).

4

WILEY-VCH

Section 3: HPLC analysis of **1** before and after PVD
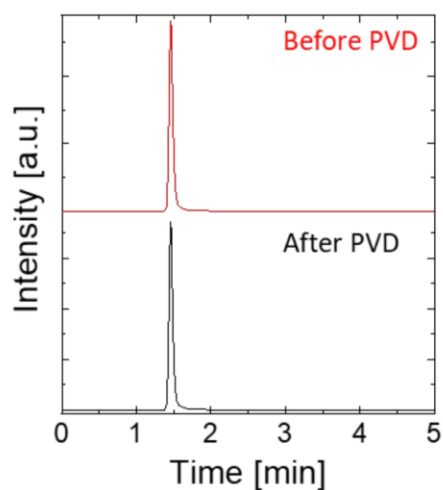
Figure S2: HPLC elugrams of **1** before PVD (red) and after self-assembly using PVD (black). Both elugrams feature a retention time for **1** of 1.46 min, demonstrating, that the chemical composition is not changed during the PVD process. HPLC conditions: eluent: acetonitrile/water 30/70, flow rate: 1mL min^{-1}, injection volume: 10 μL.

5

WILEY-VCH

Section 4: IR analysis of **1** before and after PVD
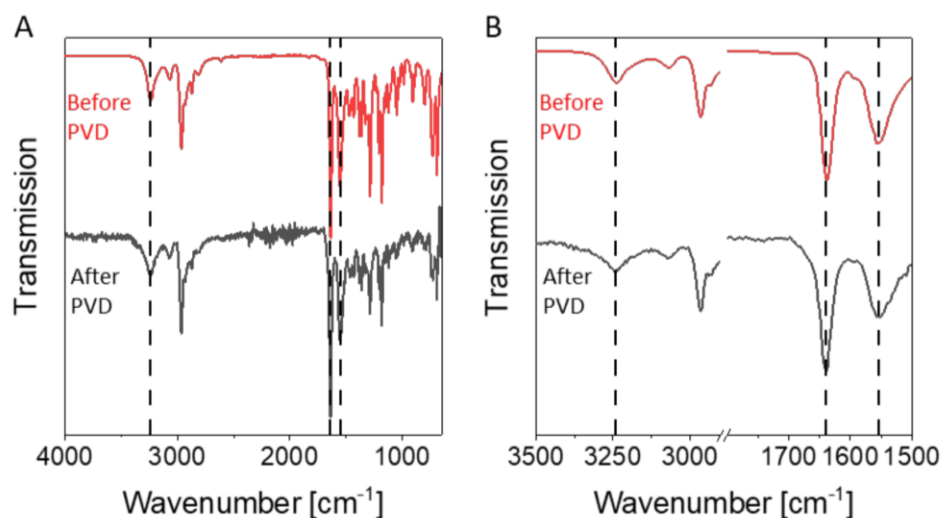
Figure S3. A) FT-IR spectra of **1** before (red) and after (black) PVD. Both spectra are almost identical. B) Sections of the relevant region for amide vibrations (amide A, amide I and II) indicated by grey dashed lines. For both spectra, the amide A (N-H stretch vibrations) is found at 3244 cm^{-1}, the amide I (C=O stretch vibration) at 1638 cm^{-1} and at the amide II (superposition of N-H bend and C-N stretch vibrations) at 1553 cm^{-1}. The location of these vibrations is indicative for a columnar stacking of the BTA molecules.[3]

---

[3] P. J. M. Stals, M. M. J. Smulders, R. Martín-Rapún, A. R. A. Palmans, E. W. Meijer, "Asymmetrically Substituted Benzene-1,3,5-tricarboxamides: Self-Assembly and Odd–Even Effects in the Solid State and in Dilute Solution", *Chemistry – A European Journal* **2009**, *15*, 2071.

WILEY-VCH

Section 5: SEM images of the neat woven fabric
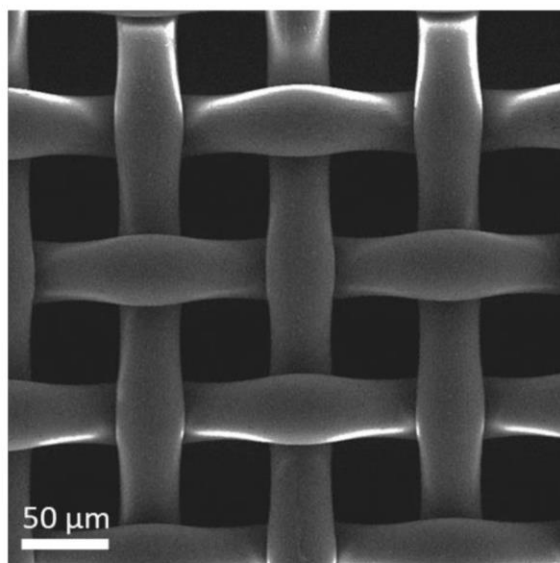
Figure S4. SEM images of the as received polyamide woven fabric featuring a mesh size of 50 μm and a fiber diameter of 35 μm.

WILEY-VCH

Section 6: Nanofiber morphology of the front and back side of the woven fabric
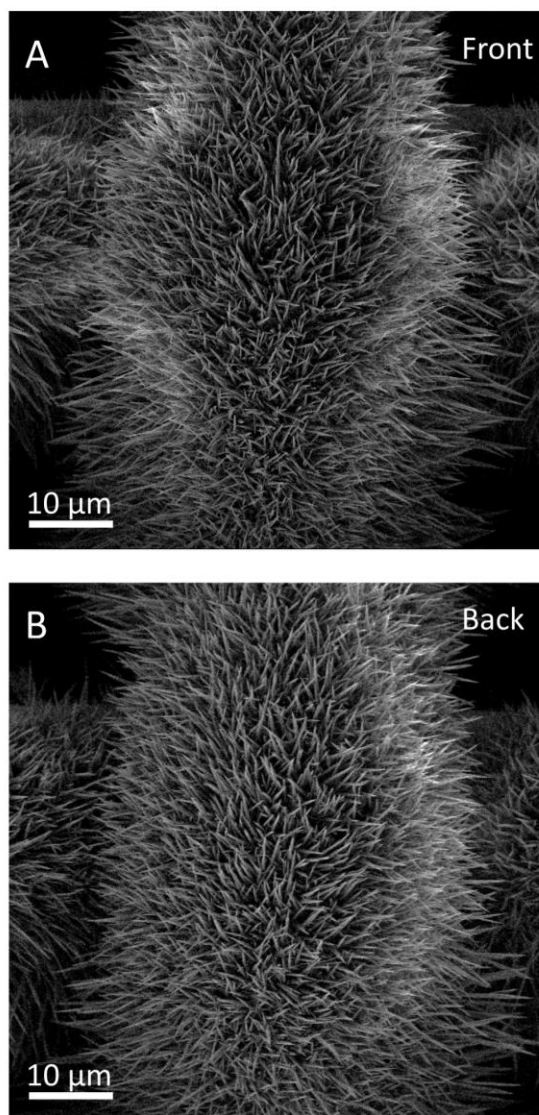
Figure S5. SEM images of a woven fabric with vapor deposited supramolecular nanofibers of **1** showing nearly the same morphology on A) the front and B) back side of woven fabric. PVD conditions: $T_{source} = 230\ °C$, $T_{substrate} = 25\ °C$. $p = 10^{-6}$ mbar, deposition time 120 min per side.

WILEY-VCH

Section 7: Supramolecular nanofiber length determination on woven fabrics
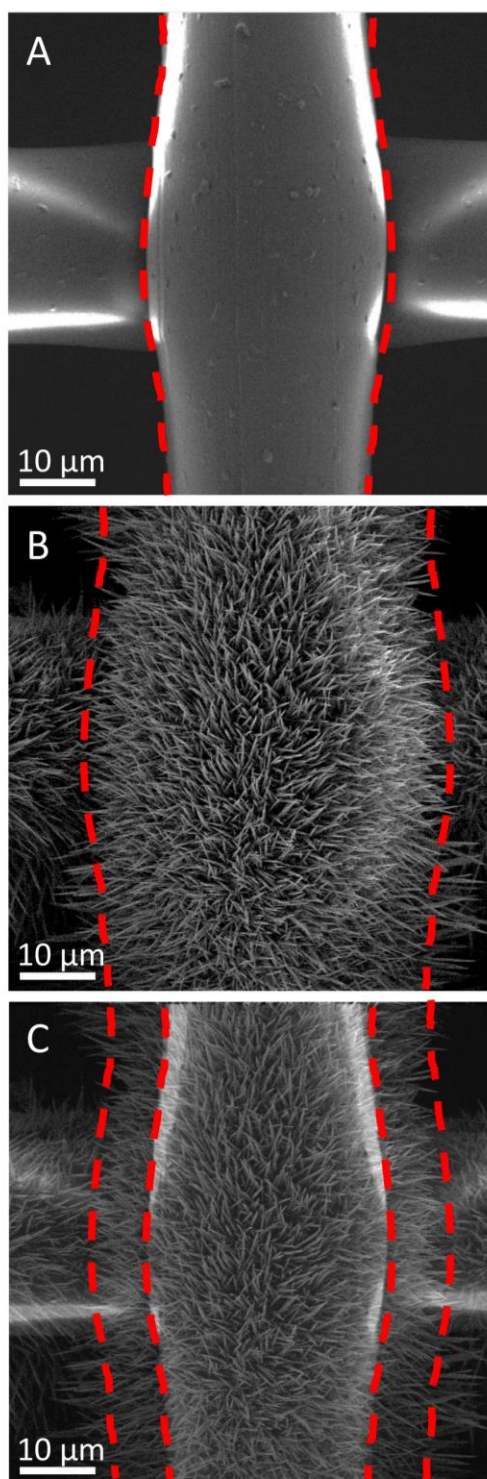
Figure S6. SEM micrographs of A) a neat woven fabric, B) a surface-decorated fabric and C) the corresponding superimposed image of A) and B). The red dashed lines indicate the outer border of the neat woven fabric and the surface-decorated fabric. The difference between the lines indicates the supramolecular fiber length of about 8 µm.

9

WILEY-VCH

Section 8: Characterization of as-prepared AuNP
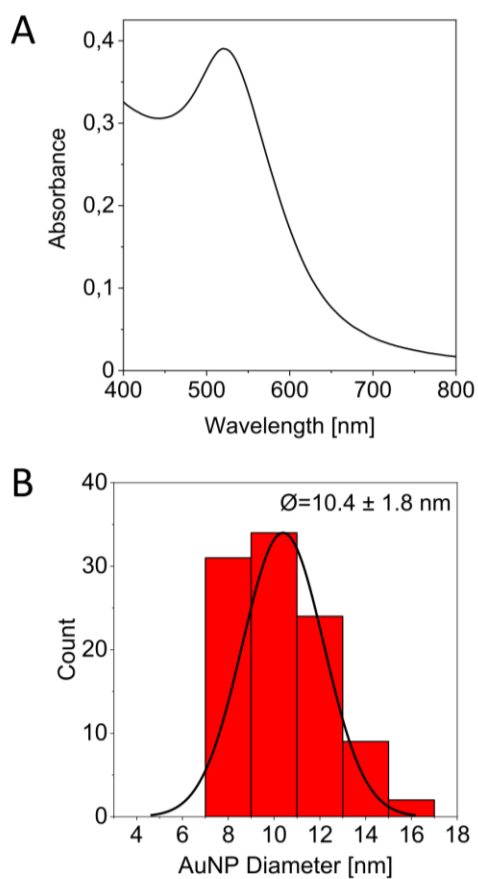
Figure S7. A) UV/vis spectra of DMAP stabilized AuNPs in water. B) Distribution of the particle size of as-prepared DMAP stabilized AuNP as determined by DLS in water.

10

WILEY-VCH

Section 9: TEM micrographs of AuNP-loaded supramolecular nanofibers
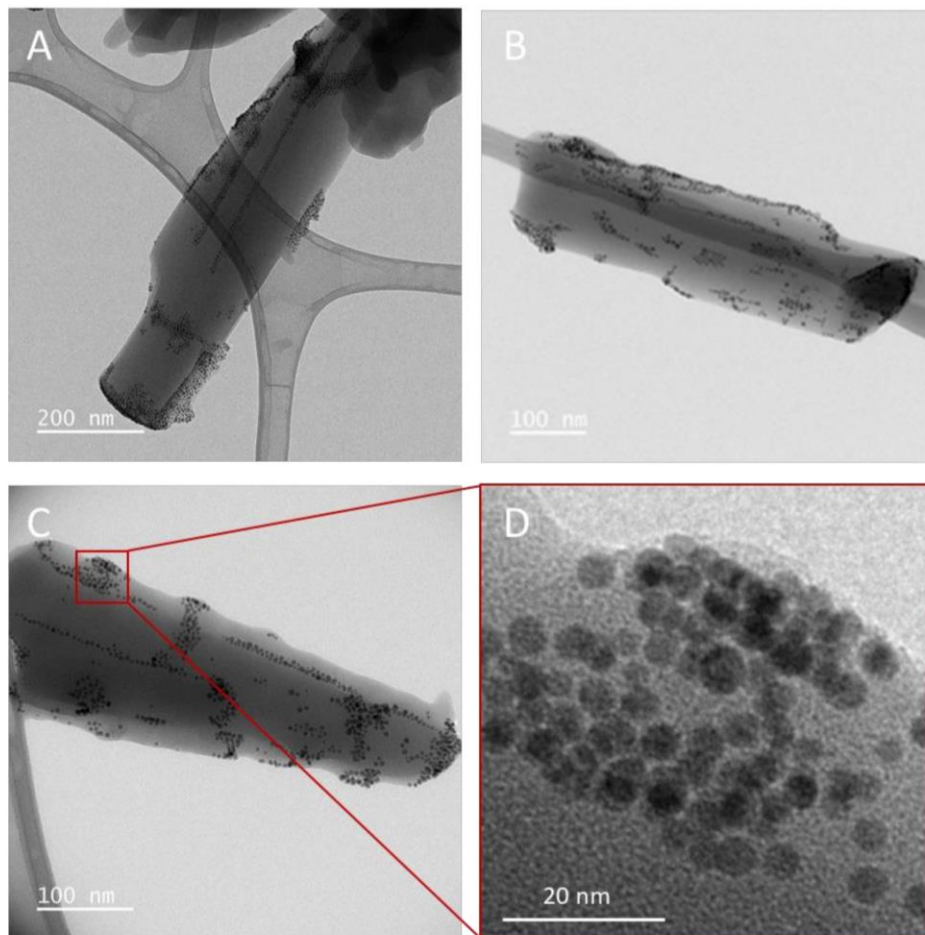
Figure S8. TEM micrographs of detached supramolecular nanofibers with immobilized AuNPs A, B) TEM micrographs of different detached supramolecular nanofibers. The AuNPs are arranged in thread-like manner. C, D) TEM-micrographs of a detached supramolecular nanofiber with AuNPs at different magnifications. At higher magnifications individual AuNPs are visible.

11

Section 10: Morphology and nanoparticle analysis of AuNP-loaded supramolecular nanofibers after three consecutive runs of 4-nitrophenol reduction
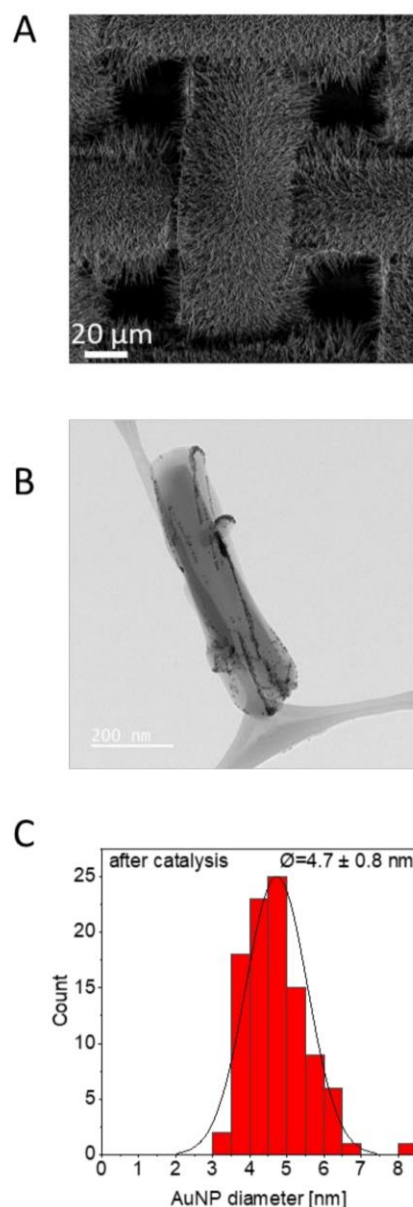
Figure S9. A) SEM images of a mesostructured woven after three consecutive runs of 4-nitrophenol reduction shows that the morphology is maintained. B) TEM image of a mechanical detached supramolecular nanofiber of a mesostructured woven after three consecutive runs of catalysis. The dark spots are immobilized AuNPs. C) Histogram of the diameter of the immobilized AuNP size determined by evaluating 100 particles in the TEM images. The mean diameter was found to be 4.7±0.8 nm.

12

4.5 Publication 4

RESEARCH ARTICLE

Mesostructured Nonwovens with Supramolecular Tricycloquinazoline Nanofibers as Heterogenous Photocatalyst

Dennis Schröder, Christian Neuber, Ulrich Mansfeld, Klaus Kreger, and Hans-Werner Schmidt*

Functional supramolecular nanostructures are a promising class of materials, which can be used as potential heterogeneous photocatalysts in water. Self-assembly to nanoobjects in solution typically requires large solubilizing groups linked to the photoactive building block, and possibly hampers access to the photocatalytic active sites. Herein, a straightforward method to fabricate supramolecular nanofibers based on the disclike tricycloquinazoline (TCQ) by physical vapor deposition (PVD) is reported. It is demonstrated that TCQ can be assembled on different substrates into supramolecular nanofibers with diameters of about 70 nm resulting in densely packed fiber layers. With optimized conditions, the evaporation time allows full control over the fiber length and the absorbance of the TCQ fiber layer. A bottlebrush-like morphology with TCQ nanofibers is realized using glass-microfiber nonwovens as porous support. These mesostructured nonwovens can be used as photocatalysts for the degradation of rhodamine B in a batch process in water where the morphology remains intact after the reaction. After photocatalytic degradation of rhodamine B or tetracycline under continuous flow conditions, the supramolecular TCQ nanofibers still remain on the support. These findings demonstrate that PVD is a feasible approach to achieve functional mesostructured nonwovens with controlled morphology for use and reuse in catalytic applications.

1. Introduction

Functional supramolecular architectures via self-assembly of defined molecular building blocks have attracted significant attention in the field of materials science, because of their tailored and unique property profile.[1] As a result, the development of functional supramolecular materials holds great potential in various fields, including biomedical applications,[2] drug delivery,[3] photovoltaics,[4] energy storage,[5] and (photo)catalysis.[6,7] In particular, photocatalysis has emerged as a rapidly evolving research area for solar fuels,[6–10] chemical transformations,[11] and environmental remediation.[8,12,13] In this context, functional supramolecular materials offer intriguing prospects for enhancing the performance of photocatalytic systems due to their defined morphology on the nanoscale. The potential of photocatalytic supramolecular materials has already been demonstrated for various systems based on chromophoric cores such as perylene bisimides,[12–14] porphyrins,[10,15] quinacridones,[16] ullazines,[17] and heptazines.[9] Through precise control of non-covalent interactions, these materials can exhibit a high surface-to-volume ratio, tunable light absorption, efficient charge separation, and enhanced catalytic activity.

Self-assembly of molecular building blocks via directed secondary interactions into supramolecular nanoobjects, in particular nanofibers, requires typically a solution-based process. Several parameters are decisive for the preparation of specific aggregates with defined morphology including the molecular structure, solvent, concentration, and processing window. The interplay between these parameters to realize defined nanoobjects often demands large solubilizing groups linked to the periphery of the molecular building blocks. These photo-inactive solubilizing groups may hamper access to the π-conjugated core, which is necessary to form the photocatalytic active species.

Apart from these considerations, self-assembled objects on the nanoscale after the photocatalytic process in solution cannot be easily removed, redispersed, and reused, which is due to their small size and their potential to form larger agglomerates during the photocatalytic process and the removal step. Unsupported nanofibers may also hamper their use in continuous flow processes, because the release of the nanoobjects into the environment is difficult to control. In contrast, fixated supramolecular nanofibers on a macroscopic support are beneficial because the nanoscopic heterogeneous photocatalyst can be conveniently removed, reused, and recycled in this way, while its morphology

D. Schröder, C. Neuber, U. Mansfeld, K. Kreger, H.-W. Schmidt
Macromolecular Chemistry I and Bavarian Polymer Institute
University of Bayreuth
95440 Bayreuth, Germany
E-mail: hans-werner.schmidt@uni-bayreuth.de

(ID) The ORCID identification number(s) for the author(s) of this article can be found under https://doi.org/10.1002/smsc.202300160.

is maintained. Moreover, the use of porous supports allows to apply continuous flow processes through the support.

A potentially promising method for nucleation, fixation, and formation of supramolecular objects on a substrate is physical vapor deposition (PVD), in which the molecular building blocks are deposited from the gas phase. Since PVD is a solvent-free process, no solubilizing groups on the molecular building blocks are required. Under a proper set of conditions, similarly as described earlier, this process allows for the formation of nano-structures such as nanofibers or nanobelts.[18] Several research groups have demonstrated the potential of PVD-processed nano-materials in optoelectronic applications[19] including sensors[20] and transistors[21] as well as in biomedical and health care applications.[22] Molecular building blocks, which were used for this purpose, are among others pentacene, perylene, and porphyrin derivatives. These aromatic compounds were selected for the preparation of nanomaterials by PVD because of their high thermal stability and evaporability as well as their ability to form aggregates via π–π-interactions. In this context, a less investigated molecular building block is tricycloquinazoline (TCQ). TCQ is a nitrogen-containing heteroaromatic compound with high chemical and thermal stability, which feature light absorption in the visible range up to about 500 nm.[23,24] TCQ derivatives has been investigated as discotic liquid crystals[25] and more recently as covalent organic frameworks. The latter have gained attention due to their conductivity[26] and gas sorption properties,[27] which enabled the use as cathode materials in batteries[28] and as electrocatalysts in CO_2 reduction.[29] However, the use of TCQ as a heterogeneous photocatalyst has not yet been demonstrated.

Here, we report on mesostructured nonwovens with supramolecular TCQ nanofibers, suitable as a heterogeneous photocatalyst for the photocatalytic degradation of organic pollutants such as rhodamine B and tetracycline. Such mesostructured nonwovens were realized by using PVD as a straightforward method to well-defined supramolecular nanofibers of TCQ on a glass-microfiber support (**Figure 1**). To demonstrate control over the morphology of TCQ nanofiber layers by PVD on various compact substrates, we investigated several process parameters, including deposition time, substrate material, and substrate geometry. By using glass-microfiber nonwovens as porous support, mesostructured nonwovens with a bottlebrush-like morphology comprising supramolecular TCQ nanofibers were obtained. The morphology remains intact when used in a batch-type photodegradation process of rhodamine B in aqueous media. Applying continuous flow conditions, the supramolecular TCQ nanofibers still remain attached on the glass-fiber support without leaching into the reaction solution. Due to the fixation of TCQ nanofibers on the support, these functional mesostructured nonwovens can be used, removed, and reused demonstrating the potential of supported TCQ nanofibers as photocatalysts for the degradation of organic pollutants.

2. Results and Discussion

2.1. Preparation of Supramolecular Nanofibers via PVD

TCQ is a C_3-symmetric heteroaromatic disclike compound, which can be obtained in a tricyclization reaction of three
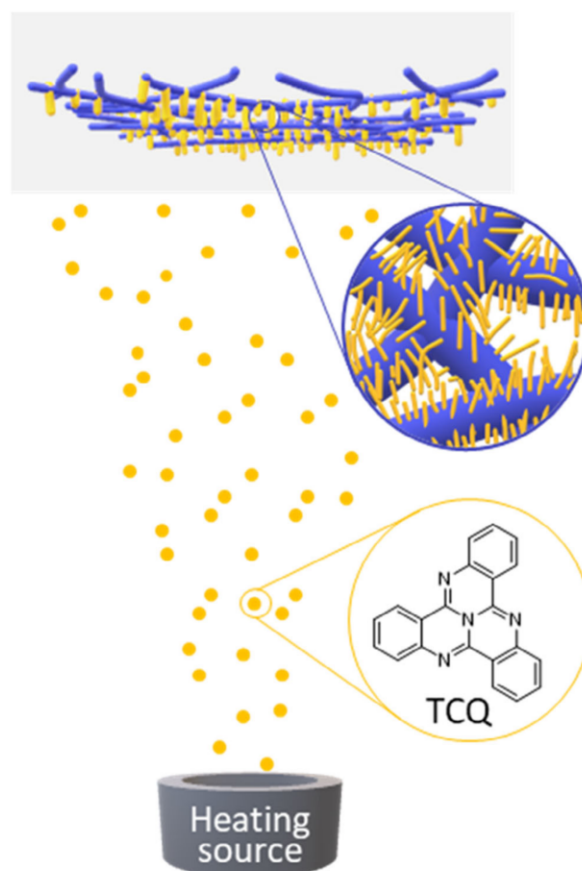
Figure 1. Schematic illustration of the physical vapor deposition (PVD) of tricycloquinazoline (TCQ, orange) forming supramolecular nanofibers on a microglass-fiber support (blue) yielding mesostructured nonwovens with a bottlebrush-like morphology for photocatalytic applications.

o-aminobenzonitriles using catalytic amounts of $ZnCl_2$ as described by Ponomarev et al.[24] Complete conversion to the product can be monitored by Fourier-transform infrared (FTIR) spectroscopy due to the absence of nitrile (CN) stretching vibrations at 2207 cm^{-1} and two amine (NH)-stretching vibrations at 3366 and 3458 cm^{-1} (Section S2, Supporting Information). The molecular structure of the TCQ was clearly identified by analytical methods such as proton nuclear magnetic resonance (^{1}H NMR) spectroscopy and mass spectrometry (MS). Differential scanning calorimetry (DSC) reveals a melting point T_{melt} for TCQ at 317 °C and a crystallization temperature of T_{cryst} at 293 °C (Section S3, Supporting Information). Thermogravimetric analysis (TGA) shows that TCQ starts to evaporate at 325 °C. This process is completed without residue at ≈420 °C. Thus, high purification can be easily performed by sublimation in high vacuum at about 300 °C resulting in fine yellow needles in a good yield. These findings already provide evidence that TCQ can be processed to fiber-like structures, which is schematically depicted in **Figure 2**A for the deposition on substrates in a controlled manner by PVD techniques. For this, we have used a custom-made PVD chamber with an
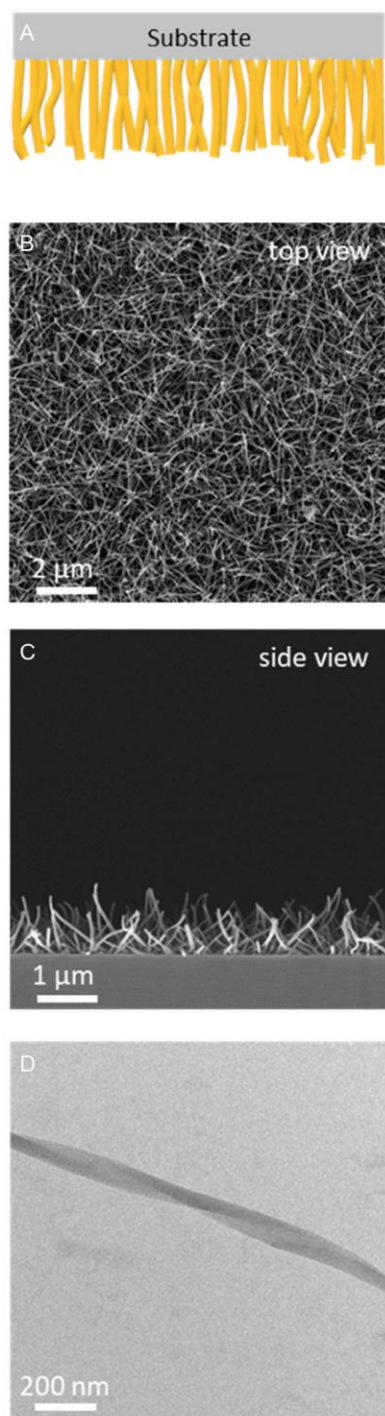
Figure 2. A) Schematic view of supramolecular TCQ nanofibers physical vapor deposited onto a silicon wafer as substrate. B,C) SEM images of the TCQ nanofibers: top view and side view. D) TEM image of an isolated TCQ nanofiber. PVD conditions: $T_{source} = 200\,°C$, $p = 10^{-6}\,mbar$, deposition time: 300 s, and $T_{substrate} = 25\,°C$.

effusion cell source loaded with TCQ. As processing conditions, a reduced pressure of 10^{-6} mbar, 200 °C of source temperature, and a substrate temperature of 25 °C were selected. At these conditions, a constant evaporation rate was monitored by a quartz crystal microbalance during the entire processing time. For initial morphology investigations, TCQ was deposited for 300 s on a silica wafer. Scanning electron microscopy (SEM) investigations (Figure 2B,C) reveal that TCQ forms a homogeneously and densely packed layer of supramolecular nanofibers. In particular, the side-view microscopy image indicates a grasslike morphology across the whole substrate with the supramolecular nanofibers growing in a perpendicular manner away from the substrate. Although we cannot clearly visualize the first deposited layers of TCQ, we attribute this dense fiber growth behavior to a large number of small TCQ nuclei initially formed on the substrate. At these conditions, the nanofiber diameter was determined to be 66 ± 11 nm featuring a nanofiber-layer thickness of about 1.0 μm. Transmission electron microscopy (TEM) analysis of scratched off supramolecular TCQ nanoobjects indicate a ribbon-like and partially twisted structure with a typical width of about 70 nm (Figure 2D), which we refer in the following section as nanofibers. Selected-area electron diffraction (SAED) on these nanofibers demonstrates that TCQ is highly oriented along the fiber's long axis (Section S4, Supporting Information). Although the SAED cannot rule out some degree of disorder, DSC measurements using these nanofibers shows only a single melting point upon first heating indicating one polymorph. From these data, a TCQ inter-disc distance of 3.9 Å (d-spacing in the longitudinal direction) and TCQ intercolumnar distance of 9.7 Å (d-spacing in the perpendicular direction) can be determined. These findings are in good agreement with the inter-disc and intercolumnar stacking as found in the crystal structure of TCQ.[30]

To investigate how the fiber density and fiber length can be controlled by the evaporation time, we performed a combinatorial experiment with three sectors I–III as schematically depicted in **Figure 3**A. By moving a shutter by one third of the substrate width every 300 s during vapor deposition, we established a stepwise gradient of the fiber-layer height on the same substrate. A silicon wafer substrate was used for SEM investigations and a quartz glass substrate for absorption measurements. TCQ was continuously deposited on both substrates at 10^{-6} mbar and 200 °C source temperature with sectors I–III being exposed to the vapor for 300, 600, and 900 s.

Prior to the optical properties of the nanofibers, we determined the absorption spectra of TCQ in CHCl₃ solution (Section S5, Supporting Information). Molecularly dissolved TCQ features a structured absorption with the maximum of the 0–0 transition being at 450 nm. The absorption spectra on nanofibers show similar features, yet the absorption is slightly broadened and the 0–0 transition is redshifted by about 15 nm, which is attributed to aggregation. Very similar spectra were found when performing UV–vis spectroscopy on the different sectors of the quartz glass slide (Figure 3B). With increasing deposition time of TCQ, the absorbance is increasing. Figure 3C indicates a linear correlation of the deposition time and the absorbance in the sectors I–III. From the glass slides, we determined the optical gap of the TCQ nanofibers derived
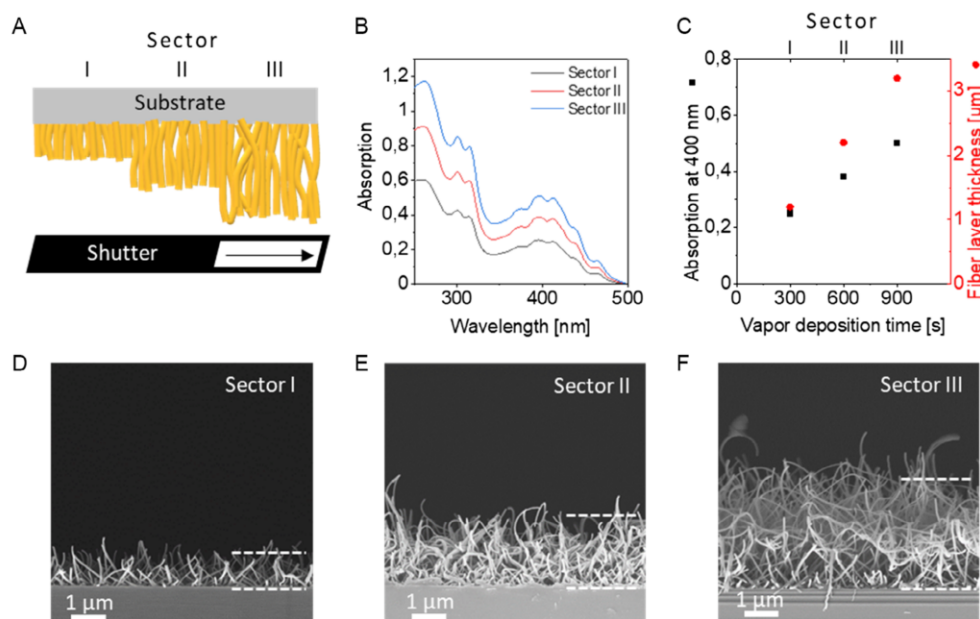
Figure 3. A) Schematic illustration of supramolecular TCQ nanofibers with increasing fiber-layer thicknesses by combinatorial vapor deposition with a shutter being moved stepwise from left to right. The vapor deposition time for sector I is 300 s, for sector II 600 s, and for sector III 900 s. B) Absorption spectra of sector I (black), II (red), and III (blue) on a quartz glass substrate. C) Absorption at 400 nm (in black) and the TCQ fiber-layer thickness (in red) as function of the vapor deposition time revealing an average fiber growth rate of 3.3 nm s^{-1}. D–F) Side-view SEM images of TCQ nanofibers for sectors I, II, and III on a silicon wafer with a fiber-layer thickness of about 1.0, 2.1, and 3.1 μm. The dotted lines are a guide to the eye to indicate the thickness. PVD conditions: $T_{source} = 200\,°C$, $p = 10^{-6}$ mbar, and $T_{substrate} = 25\,°C$.

from a Tauc plot of the UV–vis spectrum to be 2.57 eV (Figure S6, Supporting Information).

SEM side-view images of TCQ supramolecular nanofibers on the silicon substrate show a similar trend, namely an increase in the fiber-layer thickness (Figure 3D–F). Notably, the homogeneity and density of the nanofibers within each section are highly comparable and the TCQ nanofiber diameter of about 70 nm remains constant. We found that the nanofiber-layer thickness for the sectors I–III increases steadily from 1.0 to 2.1 to 3.1 μm demonstrating a high control over the resulting supramolecular nanofiber morphology. To validate that the morphology of the TCQ nanofibers is comparable on different substrate types, we investigated by SEM the nanofiber morphology on glass, quartz glass, and plasma-etched glass slides as well as on poly(lactic acid) films. For all tested types of substrates, the morphology of the TCQ nanofibers is highly identical (Section S7, Supporting Information). This finding suggests that a very comparable kind and number of nuclei are present on the different substrates at a substrate temperature of 25 °C initiating the nanofiber growth.

2.2. Preparation of Supramolecular TCQ Nanofiber/ Glass-Microfiber Nonwovens

To make use of the supramolecular TCQ nanofibers as photoactive material in aqueous media, we deposited the nanofibers on a porous support to achieve a supramolecular TCQ nanofiber/

glass-microfiber nonwoven. Such mesostructured nonwovens are beneficial, because they can be used under batch and continuous flow conditions, where the immobilized supramolecular TCQ nanofibers can be easily placed into water, removed, and reused again. Since the morphology of the deposited supramolecular TCQ nanofibers is highly independent on the substrate material, we have selected a commercial glass-microfiber nonwoven as porous support. The round-shaped glass-fiber nonwoven has a diameter of 37 mm and a thickness of 0.4 mm. It features a distribution of submicron and microfibers with an average fiber diameter of 2.2 ± 1.7 μm (Section S8, Supporting Information) indicating that the nonwoven consists of some hundred layers of glass microfibers. Ultimately, supramolecular TCQ nanofiber/glass-microfiber nonwoven were prepared as schematically depicted in **Figure 4**A by PVD employing the same conditions as described before. Figure 4B,C shows SEM images of the supramolecular TCQ nanofiber/glass-microfiber nonwoven obtained after 1500 s of deposition time at different magnifications. The top view images reveal that the glass-fiber nonwoven is entirely and homogenously covered with supramolecular TCQ nanofibers. They also show that several layers of the glass microfibers are covered indicating a larger accessible area for the TCQ vapor stream. At larger magnifications (Figure 4D,E), it can be observed that supramolecular TCQ nanofibers have been grown away from the support microfibers in a similar manner as found after deposition of TCQ on glass slides. The nanofiber lengths and diameter are well defined indicating a high control over these parameters during processing. The average TCQ nanofiber
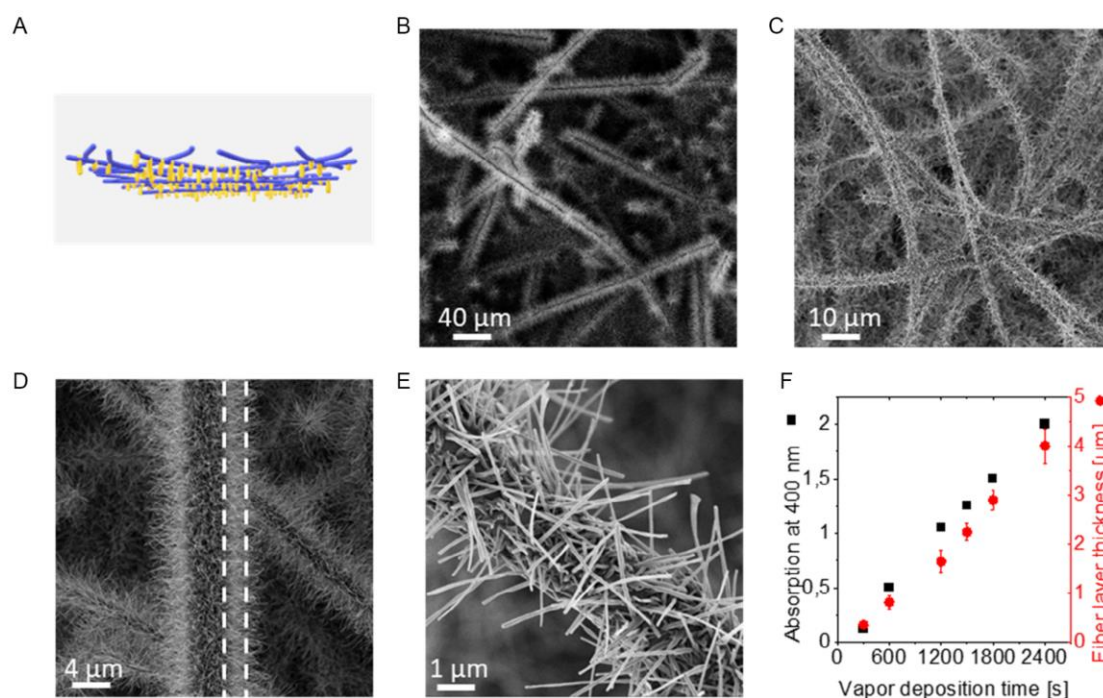
Figure 4. A) Schematic illustration of the supramolecular TCQ nanofiber/glass-microfiber nonwovens prepared by PVD. B,C) SEM overview image of a mesostructured nonwoven after a vapor deposition time of 1500 s. D,E) SEM images of the same nonwoven at different magnifications showing a bottlebrush-like morphology. The dashed lines in (C) indicate the fiber-layer thickness of about 2 μm surrounding the glass microfiber. F) Absorption at 400 nm of TCQ nanofibers on glass slides (in black) as function of the vapor deposition time and TCQ fiber-layer thickness (in red) at identical conditions. The calculated TCQ nanofiber growth rate was found to be 1.7 nm s^{-1}. PVD conditions: $T_{source} = 200\,°C$, $T_{substrate} = 25\,°C$, $p = 10^{-6}$ mbar, and deposition time = 1500 s.

diameter is 75 nm, being in good agreement as found in the previous PVD experiments with the glass slides. Interestingly, the magnification also indicates that TCQ deposits not only on top of the glass microfibers, but also around the glass microfibers resulting in a bottlebrush-like morphology. The TCQ fiber-layer thickness after 1500 s of evaporation is about 2 μm, which is significantly thinner compared to glass slides and attributed to the larger accessible surface area. To get a clearer picture with respect to the TCQ nanofiber growth rate in the glass-fiber nonwovens, we have prepared a series of mesostructured nonwovens by varying the deposition time of 300, 600, 1200, 1500, 1800, and 2400 s and investigated the specimens by SEM (Section S9, Supporting Information). The microscopy images show that nanofiber growth is initiated simultaneously and homogeneously at the entire accessible surface area of the glass-fiber nonwoven. We also found that the nanofiber diameter in all mesostructured nonwovens is almost the same indicating that only the nanofiber length is varied with increasing evaporation time. The insets in Figure S9, Supporting Information (Section S9, Supporting Information), also show that the yellowish color on top of the mesostructured nonwovens is increasing with evaporation, whereas the backside of specimen is unchanged. Since UV–vis spectroscopy on the TCQ on the glass-fiber nonwovens is not unambiguously possible due to strong scattering of the nonwoven, we have additionally placed a quartz glass slide next

to the glass-fiber nonwoven in the same substrate holder during the PVD experiment. This reference was used to determine the absorbance of the TCQ by UV–vis spectroscopy. Figure 4F shows the progress of the absorbance at 400 nm with increasing evaporation times determined from the quartz glass slides. The linear increase of the absorbance goes very well in line as found before indicating that the same amount of TCQ is deposited on the support. Similarly, the fiber-layer thicknesses was found to increase linearly with evaporation time, however, with a significantly smaller fiber-layer thickness as found before due to the large accessible surface area. As a result, the determined fiber growth rate of the TCQ nanofibers on the microfiber-glass nonwoven was found to be of 1.7 nm s^{-1}, which is approximately half the value.

2.3. Photocatalytic Degradation of Organic Pollutants

The potential of the TCQ nanofiber/glass-microfiber nonwovens as heterogenous photocatalyst was studied for the degradation of organic pollutants in water. As organic pollutants, we focused on two compounds, namely rhodamine B and tetracycline. Rhodamine B is a widely used dye, which was selected, since the degradation process can be conveniently investigated by UV–vis. Moreover, the degradation pathways are literature-known.[31] The second compound, tetracycline, is a widely used

broad-spectrum antibiotic.[32] Tetracycline is difficult to metabolize in the human and animal digestive systems and therefore has the potential to accumulate in wastewater.[32,33] A prerequisite for the use of phototactically active organic materials is a high photochemical stability against the applied conditions during operation. To validate the suitability of the TCQ nanofiber/glass-microfiber nonwovens, we have conducted UV light exposure tests under harsh conditions. For this, a mesostructured nonwoven was immersed in deionized water and the upper side with the TCQ nanofibers was exposed to 5 suns of UV radiation for 48 h. After removing and drying, the TCQ were fully dissolved and analyzed by high-pressure liquid chromatography (HPLC). HPLC elugrams of solutions before and after UV light exposure reveal only signals of TCQ (Section S10, Supporting Information). Moreover, HPLC analysis of the residual water shows that no further organic compounds can be found demonstrating the high photochemical stability of TCQ under these conditions. Further evidence is provided by SEM investigations before and after the UV exposure test showing that the bottlebrush-like morphology remains intact (Section S11, Supporting Information).

In a first set of experiments, we investigated the potential of the TCQ nanofiber/glass-microfiber nonwovens as a photocatalyst in a batch-type process. The setup is shown in Section S12, Supporting Information. As a light source, we used a 6200 K light-emitting diode (LED) with an irradiance of 29 mW cm^{-2} in the visible-light regime ranging from 400–700 nm, which fits to the TCQ absorption (Section S12, Supporting Information). The prepared and used mesostructured glass-fiber nonwoven with a diameter of 37 mm and a TCQ nanofiber length of 4 μm as described earlier. These nonwovens contain in total 0.4 mg of TCQ nanofibers resulting in a loading capacity of TCQ nanofibers of 0.05 mg cm^{-2}. The mesostructured nonwoven is placed in the reactor setup in a manner, where TCQ nanofibers are facing to the light source. A 10^{-5} mol L^{-1} rhodamine B solution in water was used since this concentration can be conveniently monitored via UV–vis spectroscopy. The progress of the decomposition was recorded in 15 min intervals for 4 h. The UV–vis spectra show that during degradation the absorption maximum shifts from 554 to 500 nm (Section S13, Supporting Information). This behavior is attributed to a degradation pathway via N-deethylation of rhodamine B.[31] The UV–vis spectra also reveal a rapid decomposition of rhodamine B (Section S13, Supporting Information) with 92% of the rhodamine B being decomposed within 4 h. This type of reaction requires a permanent illumination forming the reactive species for degradation, which quickly stops when the illumination is turned off. This is demonstrated by applying successive 30 min light-on and light-off cycles for the degradation of rhodamine B in the presence of a mesostructured nonwoven for 7.5 h in total (see Section S14, Supporting Information). In the "dark," the reaction largely comes on halt, yielding eventually almost the same result as obtained for the permanent illumination. Assuming a pseudo first-order kinetic for the reaction using permanent illumination, the apparent rate constant k' can be calculated by $\ln(c/c_0) = k't$ and was determined to 1.0×10^{-2} min^{-1}. SEM investigations on mesostructured nonwovens after photocatalysis shows that the bottlebrush-like morphology is maintained (Section S15, Supporting Information).

To investigate how the immobilization of TCQ nanofibers on the nonwoven fabric affects the photocatalytic activity, a reference experiment was conducted using only unsupported TCQ nanofibers as photocatalyst. For this, the same amount, namely 0.4 mg of TCQ nanofibers, was added to the reaction chamber. The photocatalytic degradation of rhodamine B using immobilized TCQ and unsupported TCQ is shown in Section S16, Supporting Information. Interestingly, the photocatalytic degradation progresses faster with the mesostructured nonwoven. The corresponding rate constant k' for the experiment with the unsupported TCQ nanofibers is 7.8×10^{-3} min^{-1}, which corresponds to a 22% decrease compared to the immobilized TCQ nanofibers. This lower activity can be attributed to agglomeration of the TCQ nanofibers and thus a decrease in the active surface area.

To elucidate the mechanism of photocatalytic degradation of organic pollutants by TCQ, we studied the photodegradation of rhodamine B in the presence of various scavengers capable of scavenging specific reactive oxygen species during the reaction. As radical scavengers, we used isopropanol (^{i}PrOH), p-benzoquinone (p-BQ), and triethanolamine (TEOA) for hydroxyl and superoxide radicals, as well as holes, respectively.[34] The influence of the different scavenger molecules on the photocatalytic degradation of an aqueous rhodamine B solution using a mesostructured nonwoven in a batch-type setup is depicted in Section S17, Supporting Information. The use of ^{i}PrOH as a scavenger shows no negative effect on photocatalysis, suggesting that hydroxy radicals are not involved in the degradation of rhodamine B. The degradation rate k' in the presence of TEOA was found to be 25% slower than compared to the reaction where no scavenger is present. This indicates that photogenerated holes may play a role as reactive species in the degradation. The strongest influence on the reaction rate, however, was observed with p-BQ as scavenger. Here, the rate constant decreased 85% of the original value, indicating the superoxide radicals generated via reduction of O$_2$ by photogenerated electrons are the main reactive species for the degradation of rhodamine B.

In contrast to batch-type processes, processes under continuous flow conditions have the advantage that larger quantities can be converted and a lower treatment time may be required.[35] Thus, we investigated the suitability of TCQ nanofiber/glass-microfiber nonwovens as photocatalyst for degradation of the dye rhodamine B and the common antibiotic tetracycline in water under continuous flow conditions.

A schematic illustration of the circulating continuous flow photoreactor is shown in **Figure 5**A and a photograph in Section S12, Supporting Information. For all experiments, mesostructured nonwovens as described earlier for the batch-type photodegradation were prepared. Similarly, the mesostructured nonwoven was clamped in the photoreactor chamber with the TCQ nanofibers facing the light source. The tenfold volume of an aqueous solution of the dye rhodamine B with the same initial concentration of 10^{-5} mol L^{-1} was circulated with a peristaltic pump through the photoreactor. The degradation pathway of rhodamine B using a TCQ nanofiber/glass-microfiber nonwoven under these conditions proceeds as shown before (see Section S18, Supporting Information) and 95% of the initial concentration was degraded within 4 h as shown in Figure 5B. This value is very close to that found for the batch-type reaction.
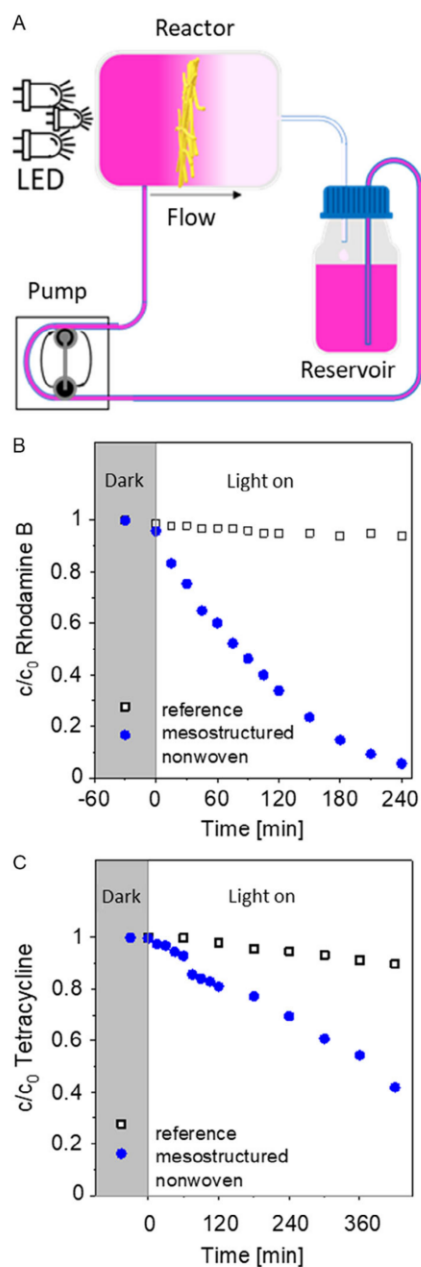
Figure 5. A) Schematic illustration of photocatalytic degradation of organic pollutants using a continuous flow reactor: Organic pollutants are circulated from a reservoir solution with a flow rate of $1.5\,L\,h^{-1}$. The nanofiber/microfiber nonwoven is fixated as a heterogenous photocatalyst upon visible-light LED irradiation. B) Progress of photodegradation of rhodamine B as a function of time without (dark) and with irradiation (light on) using mesostructured nonwovens (closed circle) and neat glass microfibers as reference (open squared). C) Progress of photodegradation of tetracycline as a function of time without (dark) and with irradiation (light on) using nanofiber/microfiber nonwovens and neat glass microfibers as reference.

The apparent rate constant k' with the mesostructured nonwoven was calculated to be $1.1 \times 10^{-2}\,min^{-1}$. As reference, a photolysis experiment, that is illumination without photocatalyst, was performed. Using a rhodamine B solution with the same concentration, we found that only minor portion of 5% was degraded within 4 h. The apparent rate constant k' of the photolysis was found to be $9.05 \times 10^{-4}\,min^{-1}$, which is a reduction by a factor of 12 demonstrating only a minor degradation without the mesostructured nonwoven.

To evaluate how much of the degraded rhodamine B was mineralized to CO_2, we performed total organic carbon (TOC) measurements after the photocatalysis using the TCQ nanofiber/glass-microfiber nonwoven. The TOC value for the initial rhodamine B solution is $4.26\,mg\,L^{-1}$ and drops after photocatalysis to $2.8\,mg\,L^{-1}$, which means that 35% are decomposed to CO_2, while the remaining 65% are decomposed to other products.

After photodegradation experiments, we investigated the remaining water solution toward traces of TCQ by HPLC applying appropriate conditions (Section S19, Supporting Information) and found that no TCQ leaches from the mesostructured nonwoven after 4 h of circulation. This encouraged us to investigate the reusability of the same mesostructured nonwovens as photocatalysts by performing three successive runs using freshly prepared rhodamine B solutions for each run. For all runs, no significant loss in the photocatalytic activity was observed (Section S20, Supporting Information) indicating that the TCQ nanofibers remains on the glass-fiber nonwoven. SEM investigations of these mesostructured nonwovens after the third run reveal that although the initial bottlebrush-like structure is not clearly maintained, indeed the supramolecular TCQ nanofibers are still on top of the glass-microfiber nonwoven (Section S21, Supporting Information) and contribute in the same manner to the photocatalytic degradation without detaching and leaching from the glass-microfiber nonwoven. We also analyzed the photocatalyst after the reusability test by HPLC measurements to investigate if changes in the molecular structure of the TCQ occur after use. The HPLC elugrams of the photocatalyst dissolved from the mesostructured nonwoven and TCQ as reference, both elugrams show only one peak, demonstrating the high chemical stability of TCQ (see Section S22, Supporting Information).

Finally, we have investigated the supramolecular TCQ nanofiber/glass-microfiber nonwovens for the photocatalytic degradation of tetracycline, an antibiotic that often can be found in waste water. Here, we have used an aqueous solution of tetracycline with an initial concentration of $10^{-4}\,mol\,L^{-1}$. All other parameters with respect to setup of the continuous flow photoreactor, illumination procedure, and the composition and size of the mesostructured nonwoven were used as described earlier. In contrast to the experiments with rhodamine B, the progress of the tetracycline degradation is conducted by HPLC (Section S23, Supporting Information). As shown in Figure 5C, circulation in the dark in the presence of the mesostructured nonwoven shows no change. Similarly, photolysis, without the photocatalysts, shows only a minor decomposition of tetracycline. Under illumination of the TCQ-mesostructured nonwoven with $0.05\,mg\,cm^{-2}$ loading, the tetracycline is degraded by 60% within 7 h. Determination of the amount of TOC in the

remaining solution revealed that 40% of the degraded tetracycline concentration was mineralized to CO_2.

3. Conclusion

We have demonstrated a straightforward method to fabricate supramolecular nanofibers based on TCQ by PVD into dense and homogeneous fiber layers with full control over the fiber length by adjusting the deposition time. At these conditions, we found a uniform nanofiber diameter of about 70 nm, which can also be realized on different substrates. Utilizing glass-microfiber nonwoven as porous support material allowed us to obtain TCQ nanofiber/glass-microfiber nonwovens with a bottlebrush-like morphology. We showed that these mesostructured nonwovens act as photocatalysts in the visible light for the degradation of the dye rhodamine B and the antibiotic tetracycline under continuous flow conditions in aqueous solutions. These findings may pave the way to realize novel and robust functional supramolecular nanostructures with controlled morphology via an elegant PVD-processing method, which can be used and reused in catalytic applications.

4. Experimental Section

Materials: For the synthesis and characterization of TCQ, see Section S1, Supporting Information. Glass-microfiber filter (37 mm, MN85/90BF) was purchased by Macherey-Nagel GmbH & Co. KG. Rhodamine B was purchased by Kremer Pigmente GmbH & Co. KG and tetracycline Hydrochloride from Carl Roth GmbH & Co. KG. Isopropyl alcohol and benzoquinone were purchased from Merck KGaA. TEOAs were purchased from abcr GmbH.

Methods: UV–vis absorbance spectra were recorded on a Jasco V-670 spectrophotometer. SEM was performed with a Zeiss 1530 field-emission SEM (FESEM) at 3 kV using Inlens detector. Samples were fixed via a double-sided adhesive conductive carbon tape on an SEM sample holder and subsequently sputtered with platinum (2 nm) prior SEM investigation.

TEM was performed on a JEOL JEM-2200FS at 200 kV. Samples were prepared by drop-casting a suspension of the powder onto a carbon-coated copper grid (S160, Plano EM, Germany) and the supernatant solution was removed by a filter paper. The specimens were imaged at room temperature in bright-field and SAED mode using a Gatan OneView camera. TOC measurements were performed on a TOC-L analyzer (Shimadzu, Kyoto, Japan) by using the 680 °C combustion catalytic oxidation method. Carbon content could be measured in concentrations from $4 \, \mu g \, L^{-1}$ to $30.000 \, mg \, L^{-1}$. Total sample combustion was achieved by heating to 680 °C in an oxygen-rich environment inside combustion tubes filled with a platinum catalyst. The generated CO_2 was detected by an infrared gas analyzer.

Physical Vapor Deposition of TCQ: For preparation of nanofiber layer of TCQ, a modified vapor deposition chamber PLS 500 from Balzers was used. Quartz crystal sensors were mounted near the substrate and used to monitor the evaporation rate. About 300 mg of TCQ was weighed into a quartz crucible, which was placed into an effusion cell (heating source). At 10^{-6} mbar and 200 °C temperature of the effusion cell, a constant apparent evaporation rate was monitored by the quartz crystal sensors and found to be $3.3 \, nm \, s^{-1}$. The shutter was fully opened to start the deposition onto the substrate. At the end of the experiment, the vacuum chamber was ventilated with air. For the preparation of step thickness gradients, a combinatorial setup was used to obtain different sectors.[36] The substrate holder was a custom-made 3D-printed holder with cavities either for three quartz slides ($76.2 \times 25.4 \times 1.0$ mm) or for 2×1 glass-fiber filters with a diameter of 37 mm and a cavity for a glass slide for reference measurements.

Photocatalytical Degradation Experiments: For initial photocatalytical experiments, the degradation of rhodamine B in a batch setup was conducted. For this, a mesostructured nonwoven (TCQ loading of 0.4 mg or $0.05 \, mg \, cm^{-2}$) was placed in a batch reactor and aqueous rhodamine B solution (0.02 L, $10^{-5} \, mol \, L^{-1}$) were added. After every 15 min of irradiation with 6200 K LED ($29 \, mW \, cm^{-2}$), the rhodamine B concentration was determined photometrically by UV–vis. As reference experiment, 0.4 mg TCQ nanofibers were dispersed in aqueous rhodamine B solution (0.02 L, $10^{-5} \, mol \, L^{-1}$) in a batch reactor. Evaluation of the photocatalytic activity was conducted as described earlier. To investigate which reactive oxygen species is involved during the photodegradation to a solution of rhodamine B (0.02 L, $10^{-5} \, mol \, L^{-1}$), a mesostructured nonwoven (TCQ loading of 0.4 mg or $0.05 \, mg \, cm^{-2}$) and a scavenging agent (0.1 mL of TEOA or 0.1 mL of ^{i}PrOH or 1.0 mg of *p*-BQ) were mixed into the batch reactor. The photocatalytic reactions were subsequently performed as described earlier.

For the light on/off reference experiments, a solution of rhodamine B (0.02 L, $10^{-5} \, mol \, L^{-1}$) and a mesostructured nonwoven (TCQ loading of 0.4 mg or $0.05 \, mg \, cm^{-2}$) were brought together into the batch reactor. Light on/off cycles were performed in successive 30 min intervals turning the light on and off for a total time of 7.5 h.

In addition, a continuous flow reactor was used to study the photocatalytic activity under flow conditions. For this, an aqueous rhodamine B solution (0.25 L, $10^{-5} \, mol \, L^{-1}$) or an aqueous solution of tetracycline (0.25 L, $10^{-4} \, mol \, L^{-1}$) was circulated through the reactor with a volume of 0.1 L and a flow rate of $1.5 \, L \, h^{-1}$. The remaining volume ensured a constant continuous circulation of the solution. After every 15 min of irradiation with 6200 K LED ($29 \, mW \, cm^{-2}$), the rhodamine B concentration was determined photometrically by UV–vis and the tetracycline concentration was determined using HPLC.

Supporting Information

Supporting Information is available from the Wiley Online Library or from the author.

Conflict of Interest

The authors declare no conflict of interest.

Data Availability Statement

The data that support the findings of this study are available from the corresponding author upon reasonable request.

155

Publications

[1] a) T. Aida, E. W. Meijer, S. I. Stupp, *Science* **2012**, *335*, 813; b) S. I. Stupp, V. LeBonheur, K. Walker, L.-S. Li, K. E. Huggins, M. Keser, A. Amstutz, *Science* **1997**, *276*, 384.

[2] R. Dong, Y. Zhou, X. Huang, X. Zhu, Y. Lu, J. Shen, *Adv. Mater.* **2015**, *27*, 498.

[3] a) S. C. Larnaudie, J. C. Brendel, I. Romero-Canelón, C. Sanchez-Cano, S. Catrouillet, J. Sanchis, J. P. C. Coverdale, J.-I. Song, A. Habtemariam, P. J. Sadler, K. A. Jolliffe, *Biomacromolecules* **2018**, *19*, 239; b) S. C. Larnaudie, J. Sanchis, T.-H. Nguyen, R. Peltier, S. Catrouillet, J. C. Brendel, C. J. Porter, K. A. Jolliffe, S. Perrier, *Biomaterials* **2018**, *178*, 570; c) S. Eskandari, T. Guerin, I. Toth, R. J. Stephenson, *Adv. Drug Delivery Rev.* **2017**, *110–111*, 169.

[4] a) T. Aytun, P. J. Santos, C. J. Bruns, D. Huang, A. R. Koltonow, M. Olvera de la Cruz, S. I. Stupp, *J. Phys. Chem. C* **2016**, *120*, 3602; b) Y. Lin, J. A. Lim, Q. Wei, S. C. B. Mannsfeld, A. L. Briseno, J. J. Watkins, *Chem. Mater.* **2012**, *24*, 622; c) X. Feng, M. Liu, W. Pisula, M. Takase, J. Li, K. Müllen, *Adv. Mater.* **2008**, *20*, 2684.

[5] a) Y. Chen, J. Li, Q. Zhu, K. Fan, Y. Cao, G. Zhang, C. Zhang, Y. Gao, J. Zou, T. Zhai, C. Wang, *Angew. Chem., Int. Ed.* **2022**, *61*, e202116289; b) C. Gu, X.-Q. Xie, Y. Liang, J. Li, H. Wang, K. Wang, J. Liu, M. Wang, Y. Zhang, M. Li, H. Kong, *Energy Environ. Sci.* **2021**, *14*, 4451.

[6] O. Zozulia, M. A. Dolan, I. V. Korendovych, *Chem. Soc. Rev.* **2018**, *47*, 3621.

[7] K. S. Lee, J. R. Parquette, *Chem. Commun.* **2015**, *51*, 15653.

[8] K. Nath, M. Chandra, D. Pradhan, K. Biradha, *ACS Appl. Mater. Interfaces* **2018**, *10*, 29417.

[9] T. Li, B.-T. Liu, Z.-B. Fang, Q. Yin, R. Wang, T.-F. Liu, *J. Mater. Chem. A* **2021**, *9*, 4687.

[10] L. Liu, X. Chen, Y. Chai, W. Zhang, X. Liu, F. Zhao, Z. Wang, Y. Weng, B. Wu, H. Geng, Y. Zhu, *Chem. Eng. J.* **2022**, *444*, 136621.

[11] M. Hao, G. Sun, M. Zuo, Z. Xu, Y. Chen, X.-Y. Hu, L. Wang, *Angew. Chem., Int. Ed.* **2020**, *59*, 10095.

[12] Y. Sun, D. Wang, Y. Zhu, *Chem. Eng. J.* **2022**, *438*, 135667.

[13] P. Chen, L. Blaney, G. Cagnetta, J. Huang, B. Wang, Y. Wang, S. Deng, G. Yu, *Environ. Sci. Technol.* **2019**, *53*, 1564.

[14] a) Y. Sheng, W. Li, L. Xu, Y. Zhu, *Adv. Mater.* **2022**, *34*, 2102354; b) D. Liu, J. Wang, X. Bai, R. Zong, Y. Zhu, *Adv. Mater.* **2016**, *28*, 7284; c) A. S. Weingarten, R. V. Kazantsev, L. C. Palmer, M. McClendon, A. R. Koltonow, A. P. S. Samuel, D. J. Kiebala, M. R. Wasielewski, S. I. Stupp, *Nat. Chem.* **2014**, *6*, 964.

[15] a) J. Yang, J. Jing, Y. Zhu, *Adv. Mater.* **2021**, *33*, 2101026; b) Z. Zhang, Y. Zhu, X. Chen, H. Zhang, J. Wang, *Adv. Mater.* **2019**, *31*, 1806626.

[16] M. Xu, K. Kong, H. Ding, Y. Chu, S. Zhang, F. Yu, H. Ye, Y. Hu, J. Hua, *J. Mater. Chem. C* **2020**, *8*, 930.

[17] O. Dumele, L. Đorđević, H. Sai, T. J. Cotey, M. H. Sangji, K. Sato, A. J. Dannenhoffer, S. I. Stupp, *J. Am. Chem. Soc.* **2022**, *144*, 3127.

[18] X.-Y. Xia, L.-Y. Ding, Q. Lv, X.-D. Wang, L.-S. Liao, *Adv. Electron. Mater.* **2022**, *8*, 2200753.

[19] a) Y. S. Zhao, D. Xiao, W. Yang, A. Peng, J. Yao, *Chem. Mater.* **2006**, *18*, 2302; b) Y. S. Zhao, C. Di, W. Yang, G. Yu, Y. Liu, J. Yao, *Adv. Funct. Mater.* **2006**, *16*, 1985; c) S.-C. Suen, W.-T. Whang, F.-J. Hou, B.-T. Dai, *Org. Electron.* **2007**, *8*, 505; d) N. Amdursky, M. Molotskii, D. Aronov, L. Adler-Abramovich, E. Gazit, G. Rosenman, *Nano Lett.* **2009**, *9*, 3111; e) J. S. Lee, I. Yoon, J. Kim, H. Ihee, B. Kim, C. B. Park, *Angew. Chem., Int. Ed.* **2011**, *50*, 1164.

[20] a) Y. Khopkar, A. Kojtari, D. Swearer, S. Zivanovic, H.-F. Ji, *J. Nanosci. Nanotechnol.* **2014**, *14*, 6786; b) V. Sahibbeyli, D. B. Yildiz, G. Papir, Y. Dede, G. Demirel, *ACS Appl. Nano Mater.* **2020**, *3*, 4305.

[21] a) Q. Guo, X. Ye, Q. Lin, Q. Han, C. Ge, X. Zheng, L. Zhang, S. Cui, Y. Wu, C. Li, Y. Liu, *Chem. Mater.* **2020**, *32*, 7618; b) V. Podzorov, *MRS Bull.* **2013**, *38*, 15; c) Q. Lin, X. Ye, Q. Guo, X. Zheng, Q. Han, L. Zhang, S. Cui, C. Li, J. Jiang, Y. Liu, X. Tao, *Chem. Mater.* **2022**, *34*, 1030; d) S. A. Arabi, J. Dong, M. Mirza, P. Yu, L. Wang, J. He, C. Jiang, *Cryst. Growth Des.* **2016**, *16*, 2624.

[22] a) K. Tao, P. Makam, R. Aizen, E. Gazit, *Science* **2017**, *358*, eaam9756; b) L. Adler-Abramovich, D. Aronov, P. Beker, M. Yevnin, S. Stempler, L. Buzhansky, G. Rosenman, E. Gazit, *Nat. Nanotechnol.* **2009**, *4*, 849.

[23] F. Yoneda, K. Mera, *Chem. Pharm. Bull.* **1973**, *21*, 1610.

[24] I. I. Ponomarev, S. V. Vinogradova, *Bull. Acad. Sci. USSR, Div. Chem. Sci.* **1990**, *39*, 2229.

[25] a) E. Keinan, S. Kumar, S. P. Singh, R. Ghirlando, E. J. Wachtel, *Liq. Cryst.* **1992**, *11*, 157; b) S. Kumar, E. J. Wachtel, E. Keinan, *J. Org. Chem.* **1993**, *58*, 3821; c) S. Kumar, D. S. Rao, S. K. Prasad, *J. Mater. Chem.* **1999**, *9*, 2751; d) R. K. Gupta, V. Manjuladevi, C. Karthik, S. Kumar, K. A. Suresh, *Colloids Surf., A* **2012**, *410*, 91; e) R. K. Gupta, V. Manjuladevi, C. Karthik, S. Kumar, *J. Phys.: Conf. Ser.* **2013**, *417*, 12068.

[26] W. B. Wang, Y. T. Zhang, L. F. Chen, H. Chen, S. Z. Hu, Q. Li, H. N. Liu, S. L. Qiao, *Polym. Chem.* **2021**, *12*, 650.

[27] O. Buyukcakir, R. Yuksel, Y. Jiang, S. H. Lee, W. K. Seong, X. Chen, R. S. Ruoff, *Angew. Chem., Int. Ed.* **2019**, *58*, 872.

[28] Z. Z. Yang, T. Wang, H. Chen, X. Suo, P. Halstenberg, H. Lyu, W. Jiang, S. M. Mahurin, I. Popovs, S. Dai, *ACS Energy Lett.* **2021**, *6*, 41.

[29] J. J. Liu, D. Yang, Y. Zhou, G. Zhang, G. L. Xing, Y. P. Liu, Y. H. Ma, O. Terasaki, S. B. Yang, L. Chen, *Angew. Chem., Int. Ed.* **2021**, *60*, 14473.

[30] J. Iball, W. D. Motherwe, *Acta Crystallogr., Sect. B: Struct. Sci., Cryst. Eng. Mater.* **1969**, *25*, 882.

[31] K. Yu, S. Yang, H. He, C. Sun, C. Gu, Y. Ju, *J. Phys. Chem. A* **2009**, *113*, 10024.

[32] F. Ahmad, D. Zhu, J. Sun, *Environ. Sci. Eur.* **2021**, *33*, 64.

[33] P. Mahamallik, S. Saha, A. Pal, *Chem. Eng. J.* **2015**, *276*, 155.

[34] a) Z. Chen, A. Savateev, S. Pronkin, V. Papaefthimiou, C. Wolff, M. G. Willinger, E. Willinger, D. Neher, M. Antonietti, D. Dontsova, *Adv. Mater.* **2017**, *29*, 1700555; b) Q. Liu, Y. Guo, Z. Chen, Z. Zhang, X. Fang, *Appl. Catal., B* **2016**, *183*, 231.

[35] C. Sahoo, B. B. Panda, A. K. Gupta, *ChemistrySelect* **2022**, *7*, e202201179.

[36] a) M. Thelakkat, C. Schmitz, H.-W. Schmidt, *Adv. Mater.* **2002**, *14*, 577; b) M. Bäte, C. Neuber, R. Giesa, H.-W. Schmidt, *Macromol. Rapid Commun.* **2004**, *25*, 371.

156

Supporting Information

Mesostructured Nonwovens with Supramolecular Tricycloquinazoline Nanofibers as Heterogenous Photocatalyst

Dennis Schröder, Christian Neuber, Ulrich Mansfeld, Klaus Kreger, and Hans-Werner Schmidt*

Table of content

WILEY-VCH

WILEY-VCH

S1: Materials and Methods

Materials:

o-Aminobenzonitrile (98%) was purchased by Fluka Analytical. Anhydrous zinc chloride (98%) was purchased from Grüssing GmbH. α-Chloronaphthalene and diethyl ether was received by Sigma Aldrich and were used as received.

Methods:

^{1}H NMR and ^{13}C NMR spectra in solution were recorded on a Bruker Avance Ultrashield 300 (300 MHz and 75 MHz, respectively) at room temperature. For the preparation of the NMR samples, approx. 5 mg of the compounds were dissolved in 0.6 mL of CDCl$_3$.

High resolution mass spectra (HRMS) were carried out on a FINNIGAN MAT 8500 spectrometer from Thermo-Fisher Scientific using electron spray ionization (ESI).

Infrared (IR) spectra were recorded using a small amount of the solid powder on a PerkinElmer Spectrum 100 FT-IR spectrometer in attenuated total reflection (ATR) mode in the range from 4000 cm^{-1} to 650 cm^{-1}.

Thermogravimetric analyses (TGA) were performed in the range from 30 to 700 °C with a heating rate of 10 K min^{-1} under a nitrogen atmosphere with a flow rate of 30 mL min^{-1} using a Mettler Toledo TGA/DSC3+ Star.

Melting points and recrystallisation were investigated by differential scanning calorimetry using a Mettler Toledo DSC2. Approximately 10 mg of the solid were filled in sealable crucibles. Spectra were recorded with a heating/cooling rate of 10 K·min^{-1} in a temperature range from 30 °C to 330 °C.

Elemental analysis was measured with a Vario El III instrument from Elementar Analysen-Systeme.

2

WILEY-VCH

To test the photochemical resistance and reveal potential degradation of tricycloquinazoline (TCQ) nanofibers against strong light irradiation, we have performed a UV/light exposure test. For this, supramolecular TCQ nanofiber/glass microfiber nonwovens were irradiated under controlled accelerated weathering conditions using a Q-SUN XE-3 test chamber (Q-LAB Corporation, Westlake, OH). Three xenon arc lamps equipped with a Daylight-Q filter system were used as irradiation source. The irradiance was set to 60 W/m^2 at 300–400 nm and performed at a relative humidity of 50%. The total irradiance was 594 W/m^2 resembling approximately the 5-fold of standard outdoor irradiation.

High performance liquid chromatography of TCQ was performed on an Agilent 1100 with a C_{18} reversed phase stationary phase with an eluent of acetonitrile/water 70/30 with of low rate of 1mL min^{-1} and an UV-detector. The injection volume was 10 µL. Retention time of TCQ was determined to be 20.1 min.

High performance liquid chromatography of tetracycline was performed on an Agilent 1260 Infinity II with a Zorbax SB-C18 stationary phase with an eluent of water (1% formic acid) /MeOH 85/15 with a flow rate of 1mL min^{-1} and an UV-detector. The injection volume was 5 µL. Retention time of tetracycline was determined to be 5.85 min.

3

S2: Synthetic scheme, procedure, and molecular characterization of TCQ

o-Aminobenzonitrile   Tricycloquinazoline (TCQ)

Figure S1. Synthetic scheme to TCQ as described by Ponomarev *et al.*.[1]

5.9 g (50 mmol, 1 eq.) of *o*-aminobenzonitrile and 68 mg (0.5 mmol, 0.01 eq.) of anhydrous zinc chloride was heated in 30 mL of α-chloronaphthalene in argon atmosphere at 290 °C for 8 h. Upon cooling to room temperature, a precipitate was obtained and filtered off. The solid was washed three times with 50 mL of diethyl ether and subsequently dried in vacuo. The crude product was purified by sublimation at 10^{-6} mbar and 300 °C to give 4.5 g (14 mmol, 84 % yield) of TCQ as fine yellow needles.

^{1}H NMR (300 MHz, CDCl$_3$, δ): 8.47 (dd, J = 8.1, 1.2 Hz, 3H), 7.61 (ddd, J = 8.1 7.1, 1.5 Hz, 3H), 7.52 (dd, J = 8.1, 1.3 Hz, 3H), 7.35 (ddd, J = 8.1, 7.1, 1.3 Hz, 3H)) ppm.

^{13}C NMR (75 MHz, CDCl$_3$, δ): 145.73, 144.78, 134.00, 127.07, 126.96, 126.26, 121.03 ppm.

HRMS (ESI) *m/z*: [M + H]$^+$ calcd for C$_{21}$H$_{12}$N$_4$, 321.1135; found, 321.1135.

Anal. calcd for C$_{21}$H$_{12}$N$_4$: C 78.73, H 3.78, N 17.49; found: C 77.29, H 4.01, N 16.98.

FT–IR: v = 3061 (w), 1619 (s), 1590 (s), 1565 (s), 1476 (s), 1459 (m), 1335 (m), 1297 (m), 1234 (m), 1160 (m), 1136 (s), 1026 (m), 923 (m), 754 (s), 694 (s), 676 (s), 594 cm^{-1} (m).

Mp (DSC,second heating): 317 °C

UV–vis (*chloroform*): λ_{max} (ε) = 296 (22000), 309 nm (18000), 380 (17700), 401 (16800), 426 (6300), 453 (2340).

---

[1] Ponomarev, II; Vinogradova, S. V. An Efficient Method for the Synthesis of Tricycloquinazoline. *Bull. Acad. Sci. USSR, Div. Chem. Sci. (Engl. Transl.)* **1990**, *39*, 2229.

WILEY-VCH

A

B

Figure S2. A: ^{1}H NMR of TCQ. The inset shows the aromatic region with the relevant protons. B: IR-Spectra of o-aminobenzonitrile (red) and TCQ (black). The grey areas indicate the regions of the nitrile (CN) stretching vibration at 2207 cm^{-1} and both amine (NH) stretching vibrations at 3366 cm^{-1} and 3458cm^{-1}, which can be clearly seen for the o-aminobenzonitrile and are not present in the TCQ spectra.

5

WILEY-VCH

S3: Thermal characterization of TCQ

A

B
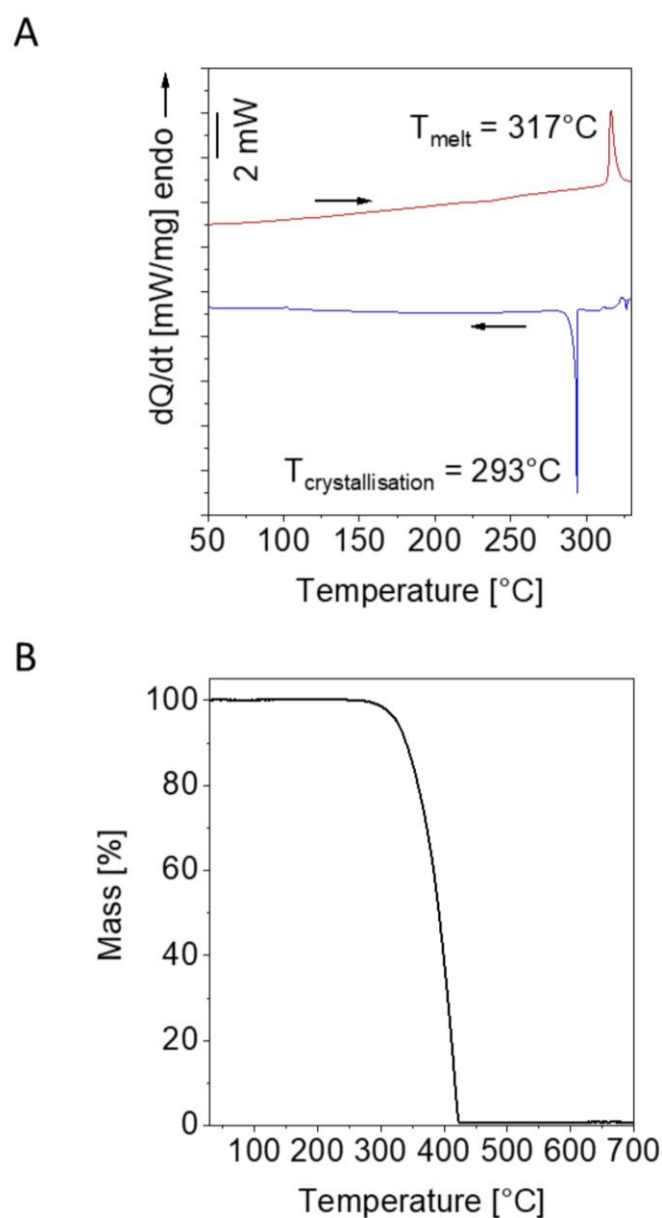
Figure S3. A: DSC measurements of TCQ from 30-330°C at a rate of 10 K min^{-1}; shown are the 2nd heating curve (red) and cooling curve (blue). B: TGA measurements of TCQ from 30-700°C at a heating rate of 10 K min^{-1} under N_2 with a flow rate of 30 mL min^{-1}.

WILEY-VCH

S4: TEM micrograph and SAED of supramolecular TCQ nanofibers via PVD
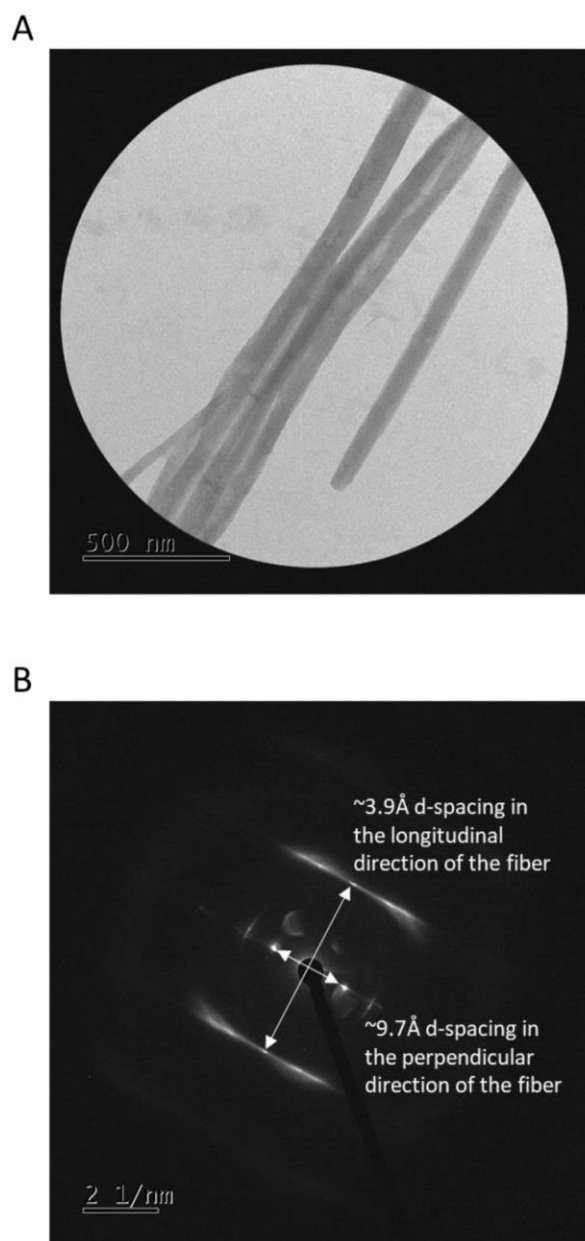
Figure S4. A: TEM image of TCQ nanofibers by PVD with a fiber diameter of 70 nm. Prior to TEM, TCQ nanofibers were scratched from a glass substrate and placed onto the TEM grid. B: Corresponding selected area electron diffraction (SAED) measurement of the nanofibers. In the SAED an inter disc distance of around 3.9 Å in the longitudinal direction of the fiber and a inter columnar distance of around 9.7 Å in perpendicular direction of the fiber can be observed.

7

WILEY-VCH

S5: UV-vis characterization of TCQ in solution and TCQ nanofibers prepared via physical vapor deposition
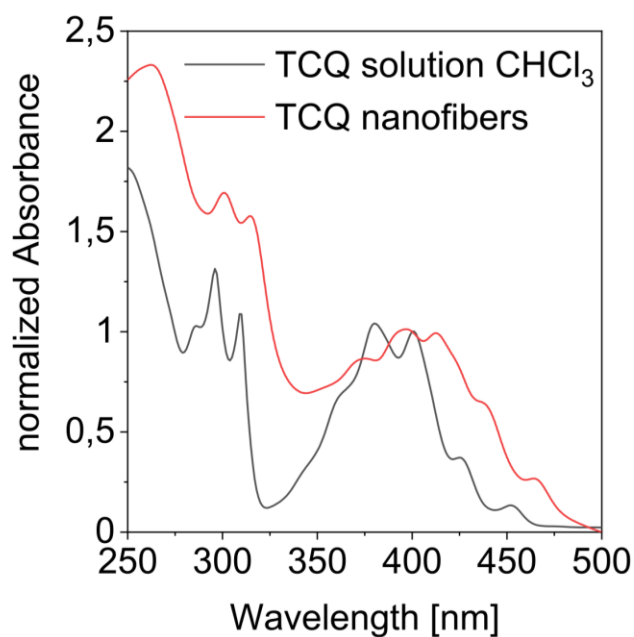
Figure S5. UV-vis absorption spectra of a 10^{-4} M TCQ solution in CHCl$_3$ (black) and a 1 μm thick supramolecular TCQ nanofiber mat on a quartz glass substrate prepared by PVD (red). For comparison, both spectra are normalized at 400 nm.

S6: Optical gap of supramolecular TCQ nanofibers
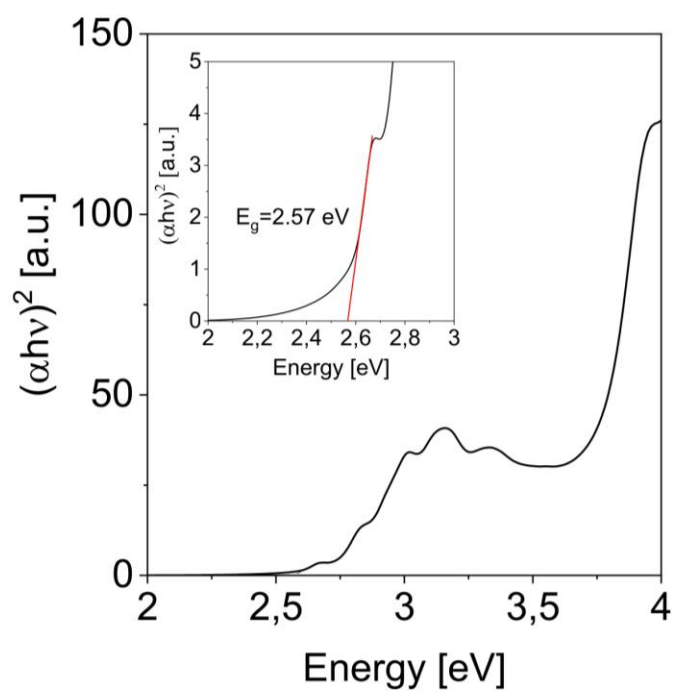
Figure S6. Tauc Plot of the supramolecular TCQ nanofibers physical vapor deposited on a quarz slide. The Inlet shows the onset of the optical gap which was determined to be 2.57 eV.

WILEY-VCH

S7: Morphology investigations of physically vapor deposited TCQ nanofibers on different substrates
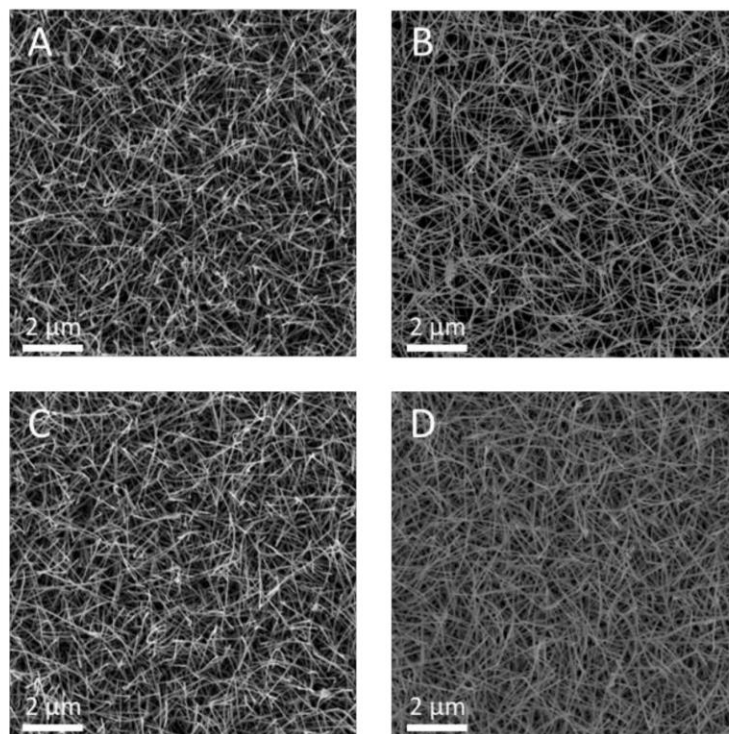
Figure S7. SEM images of TCQ supramolecular nanofibers prepared by PVD on different substrates. A) glass slide, B) quartz glass slide, C) plasma-etched glass slide and D) poly(lactic acid) substrate. For all substrates, a off-standing homogeneous fiber mat of TCQ nanofibers with a TCQ fiber diameter of 70 nm and a very similar densely packed morphology can be found. PVD conditions: T_{source} = 200°C, $T_{substrate}$ = 25°C, p = 10^{-6} mbar, deposition time = 300 s, evaporation rate = 3.3 nm/s.

WILEY-VCH

S8: Photo- and micrograph characterization of the used glass microfiber nonwoven
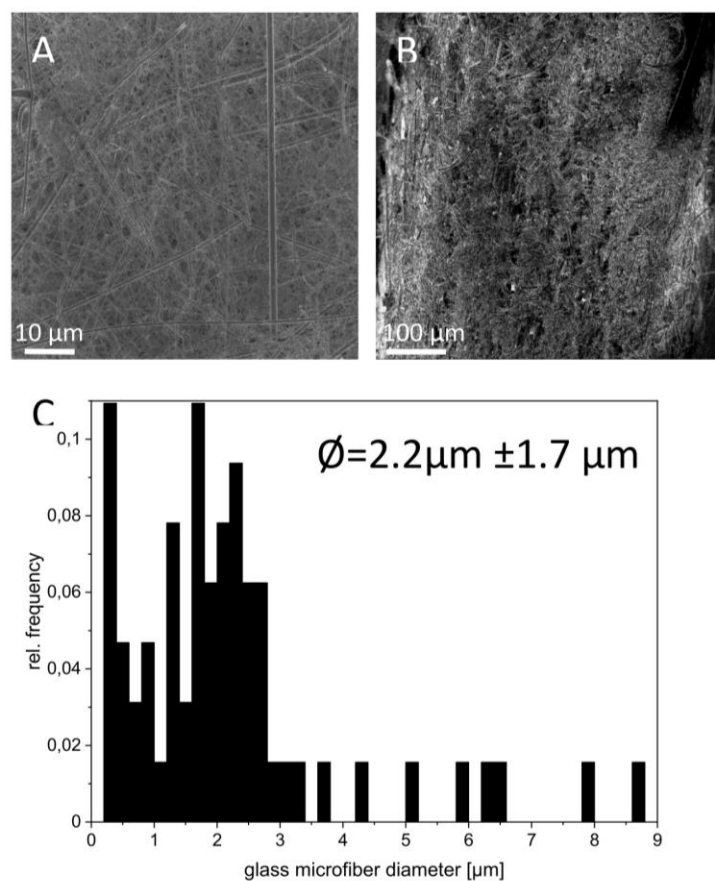
Figure S8. A and B: SEM images of a neat glass fiber nonwoven with a diameter of 37 mm and a thickness of 0.5 mm. C: Histogram of the glass microfiber diameters calculated by evaluating 100 fibers.

11

WILEY-VCH

S9: Morphology investigations of supramolecular TCQ nanofiber/glass microfiber nonwovens
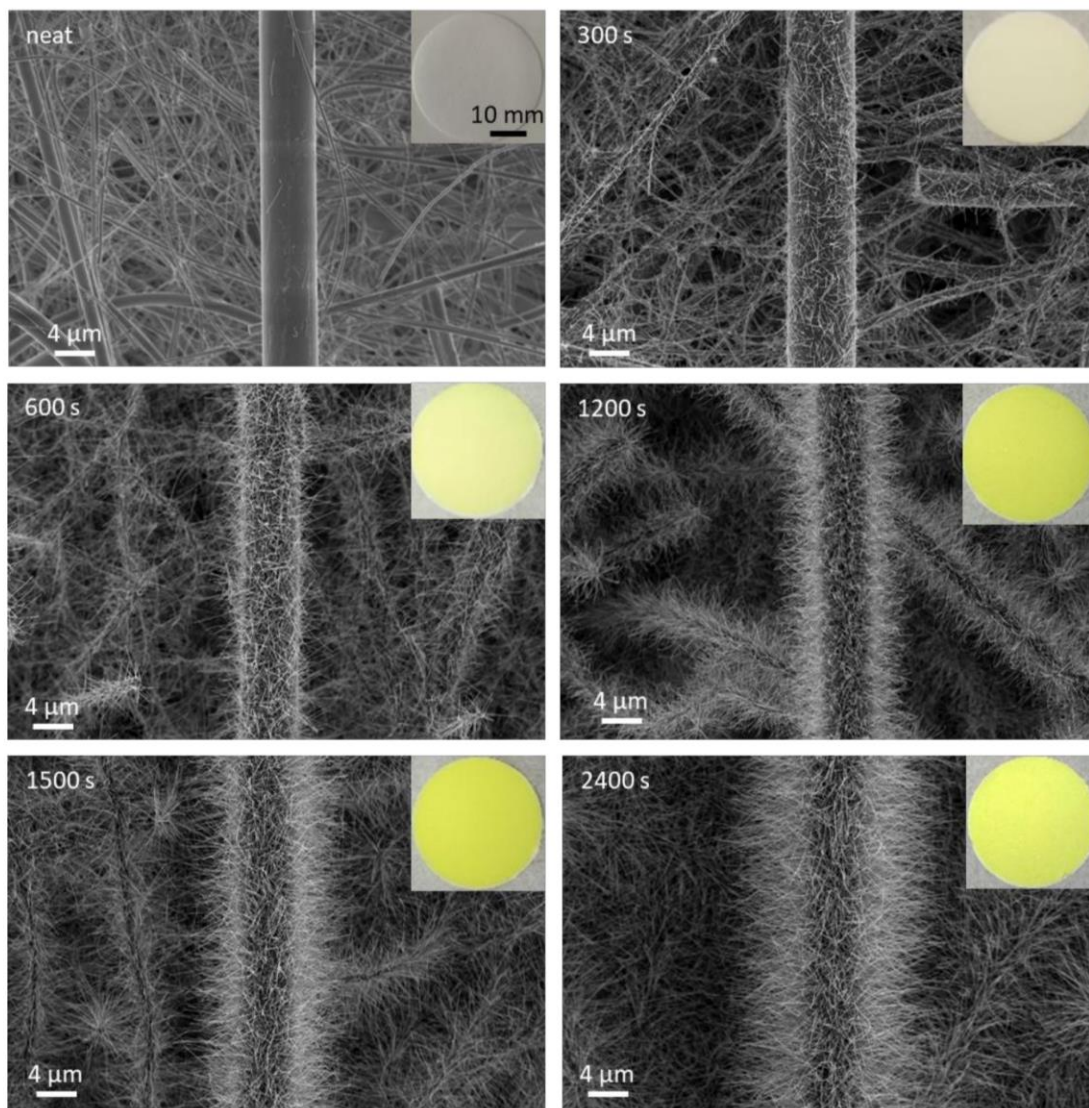
Figure S9. SEM images of neat glass fiber nonwoven and supramolecular TCQ nanofiber/ glass microfiber nonwovens by PVD with increasing deposition time from 300, 600, 1200, 1500 to 2400 seconds. The average diameter of the TCQ nanofibers for all mesostructured nonwovens were determined to be around 70 nm. The inlets show photographs of the mesostructured nonwovens with a macroscopic diameter of the specimen of 37 mm. PVD conditions: T_{source} = 200°C, $T_{substrate}$ = 25°C, p = 10^{-6} mbar, deposition time see figure, evaporation rate = 1.7 nm/s.

12

S10: HPLC Spectra before and after UV/light exposure tests of the supramolecular TCQ nanofiber/glass microfiber nonwoven
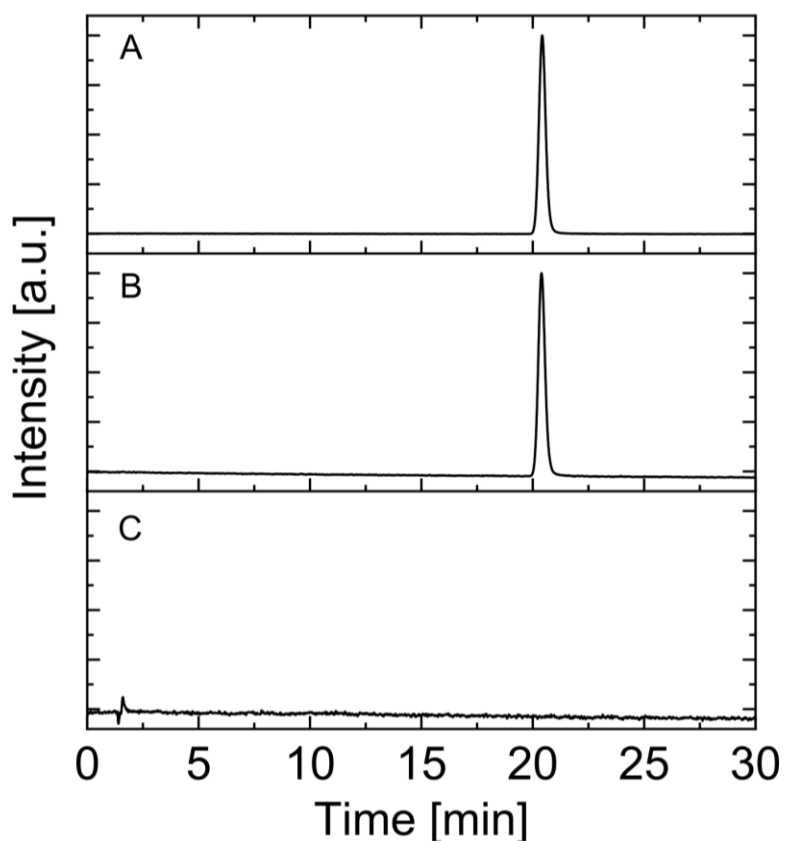
Figure S10. HPLC elugram of the supramolecular TCQ nanofiber/glass microfiber nonwoven immersed in water before (A) and after (B) UV/light exposure test. HPLC samples were prepared by immersing small pieces of the nanofiber/glass microfiber nonwoven in acetonitrile till the TCQ was completely dissolved. The water where the mesostructured nonwoven was immersed during the UV/light exposure test, was also analyzed (C) and did not show any TCQ in it. HPLC conditions: eluent: acetonitrile/water 70/30, flow rate: 1mL min^{-1}, injection volume: 10 μL.

13

WILEY-VCH

S11: SEM images before and after UV/light exposure tests of the supramolecular TCQ nanofiber/glass microfiber nonwoven
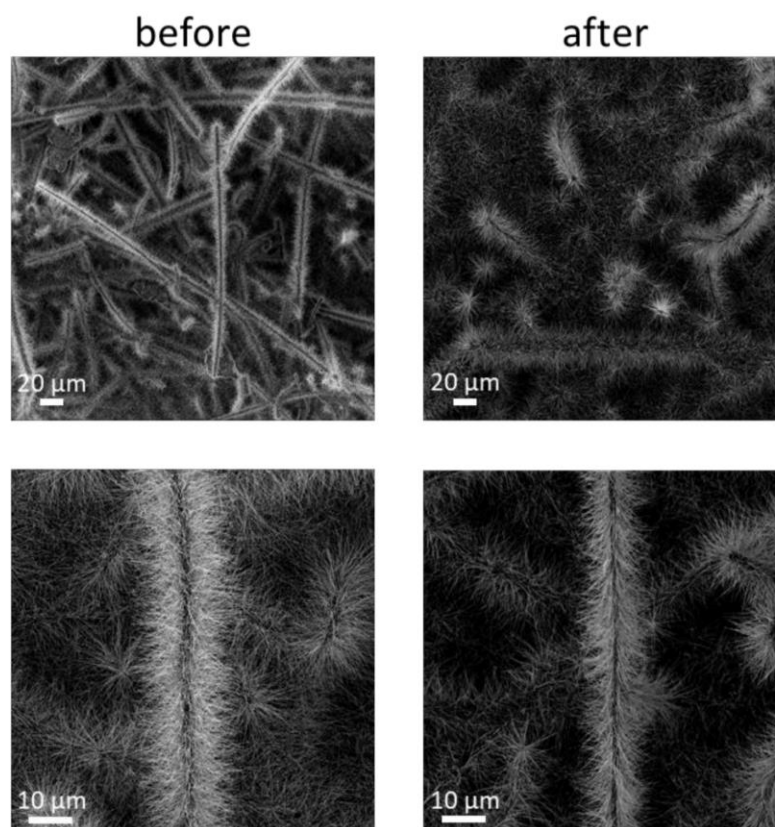
Figure S11. SEM images overview (top) and magnification (bottom) of supramolecular TCQ nanofiber/glass microfiber nonwovens before (left) and after (right) UV/light exposure tests. The illumination of the mesostructured nonwoven in water do not lead to a significant change of the morphology.

14

WILEY-VCH

S12: Setups for photocatalytic degradation of Rhodamine B using mesostructured nonwoven

A

B

C

D
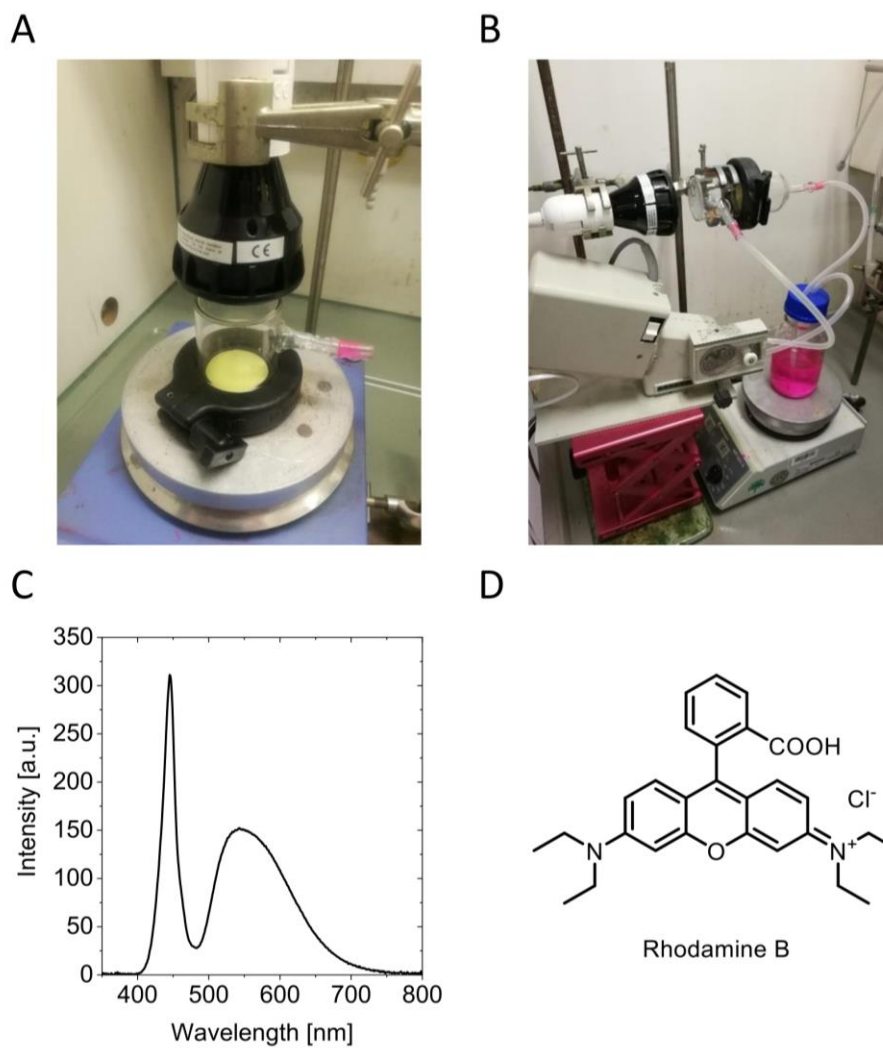
Figure S12. A: Batch setup for the degradation of Rhodamine B, B: Continuous flow setup for the degradation of Rhodamine B and Tetracycline. C: Emission spectra of the used LED light source. D: Molecular structure of Rhodamine B.

15

WILEY-VCH

S13: Photocatalytic degradation of Rhodamine B using mesostructured nonwoven in a batch setup
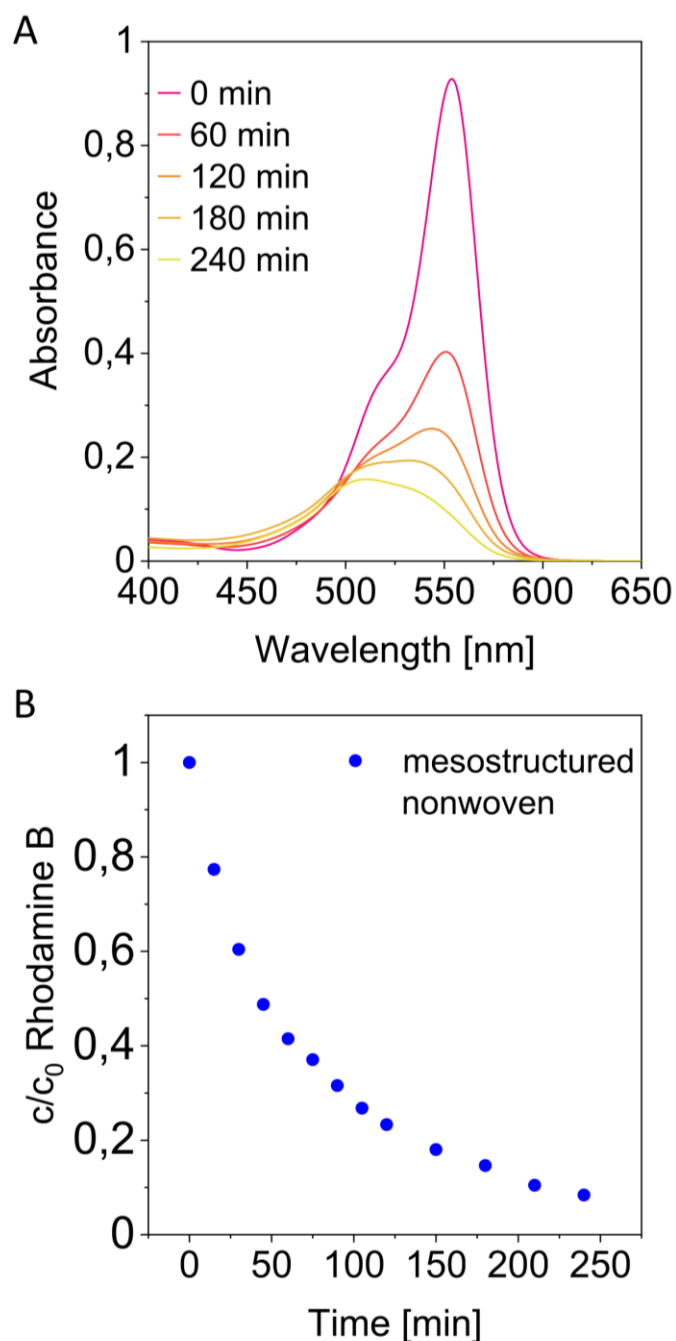
Figure S13. A: Progress of the UV-vis absorption of aqueous Rhodamine B solution during photocatalysis using a mesostructured nonwoven and a batch setup, B: Progress of photodegradation of Rhodamine B as a function of time using mesostructured nonwovens.

16

WILEY-VCH

S14: Light on/off experiment during the photocatalytic degradation of Rhodamine B using mesostructured nonwoven in a batch setup
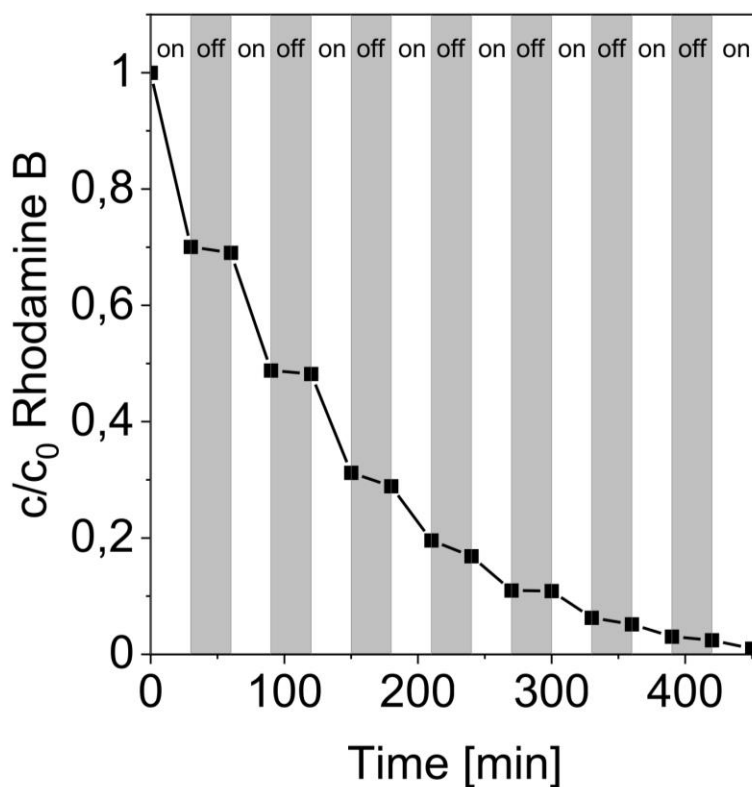
Figure S14. Progress of photodegradation of Rhodamine B as a function of time treating mesostructured nonwovens with successive 30 min periods of turning the light on and off for a total of 7.5 h.

17

WILEY-VCH

S15: Morphology investigations of supramolecular nanofiber/glass microfiber nonwoven after photocatalysis in a batch setup
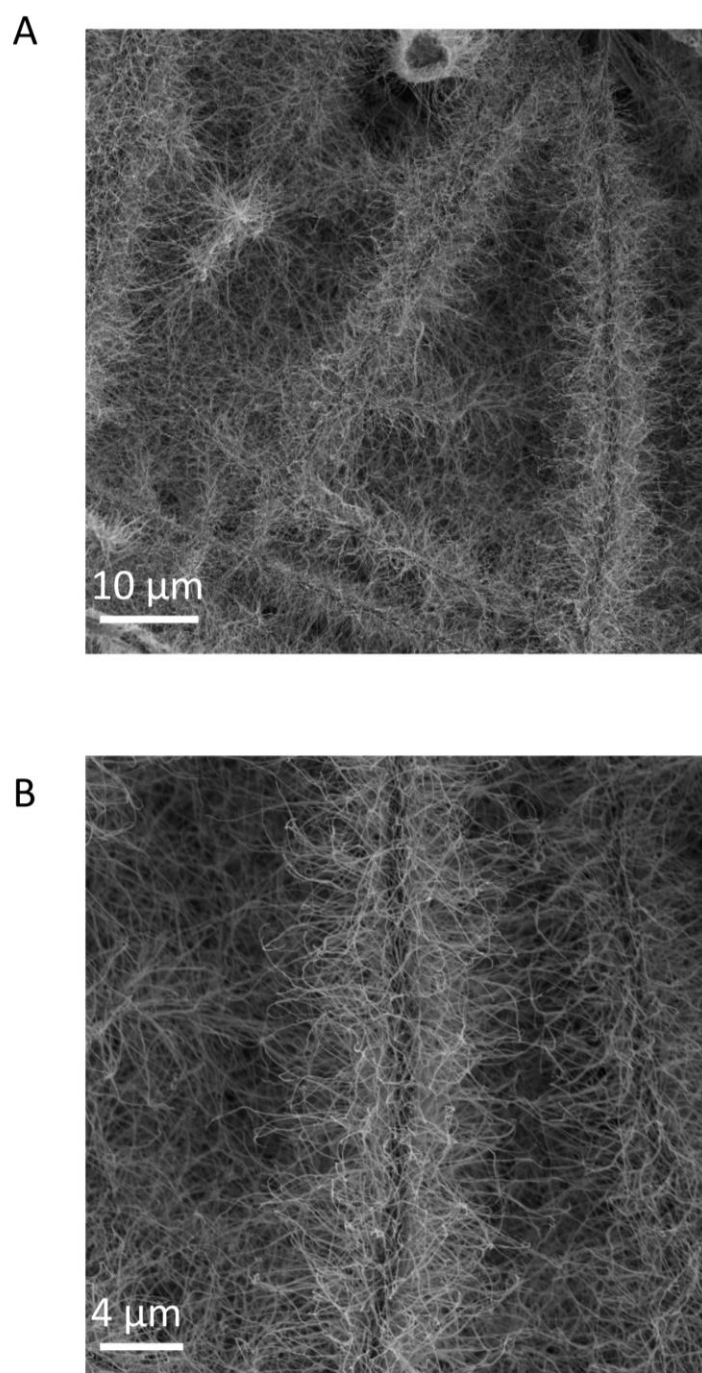
Figure S15. SEM image overview (A) and magnification (B) of TCQ nanofiber/glass microfiber nonwoven after 4 hours of photocatalysis in a batch reactor.

WILEY-VCH

S16: Photocatalytic degradation of Rhodamine B using unsupported TCQ nanofibers in a batch setup
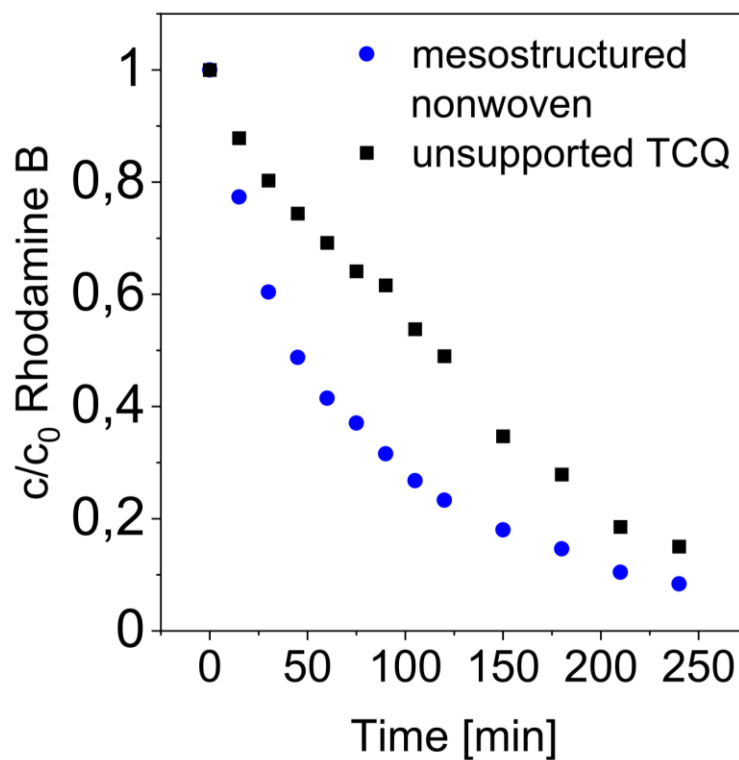
Figure S16. Progress of photodegradation of Rhodamine B as a function of time using unsupported TCQ nanofibers and a mesostructured nonwoven with the same amount of TCQ nanofibers for comparison.

19

S17: Reaction mechanism studies on the photocatalytic degradation of Rhodamine B using mesostructured nonwoven in a batch setup
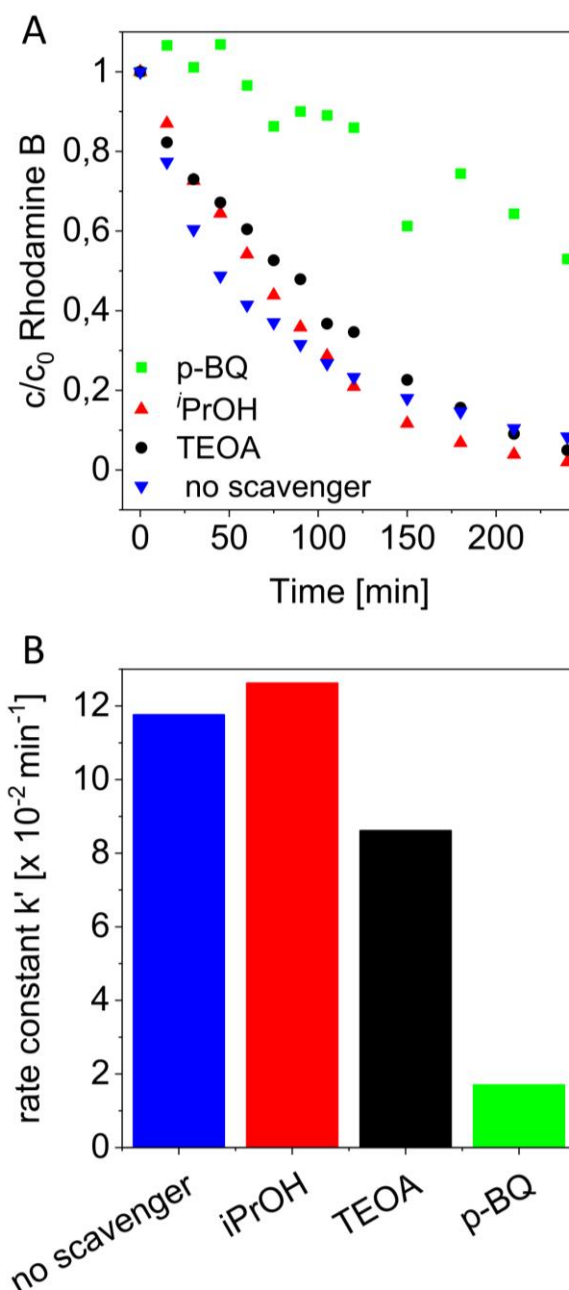
Figure S17. A: Progress of photodegradation of Rhodamine B as a function of time using mesostructured nonwovens in the presence of isopropanol (*i*PrOH), triethanolamine (TEOA) and *p*-benzoquinone (*p*-BQ) that were used as radical scavengers for hydroxyl, hole and superoxide radicals, respectively. B: corresponding apparent rate constants k' assuming first order kinetics.

20

S18: Photocatalytic degradation of Rhodamine B using mesostructured nonwoven in a continuous flow setup
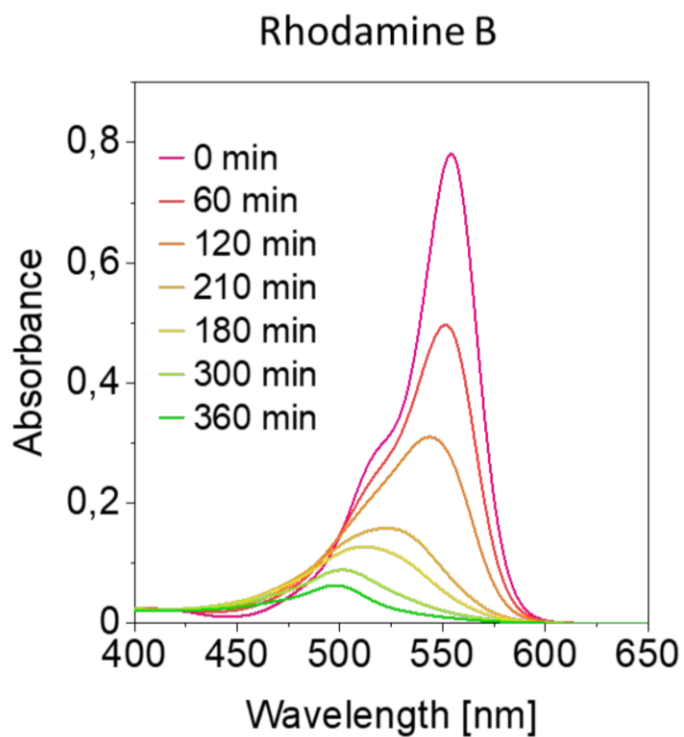
Figure S18. Progress of the UV-vis absorption of aqueous Rhodamine B solution during photocatalysis using a continuous flow setup.

21

S19: Leaching test of TCQ from the mesostructured nonwoven
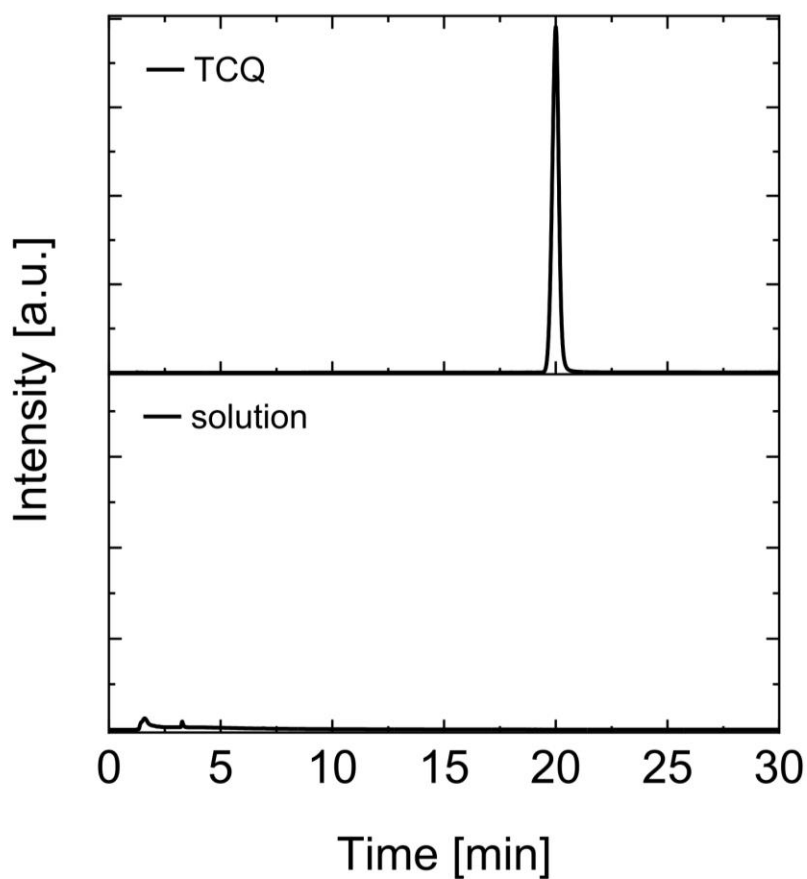
Figure S19. HPLC Chromatograms of TCQ (top) and the solution (bottom) after photodegradation of tetracycline that was circulated for 6h in the continuous-flow setup with a flow rate of 1.50 L/h, showing that no TCQ was leached or dissolved from the mesostructured nonwoven.

22

S20: Reusability test of supramolecular nanofiber/glass microfiber nonwoven
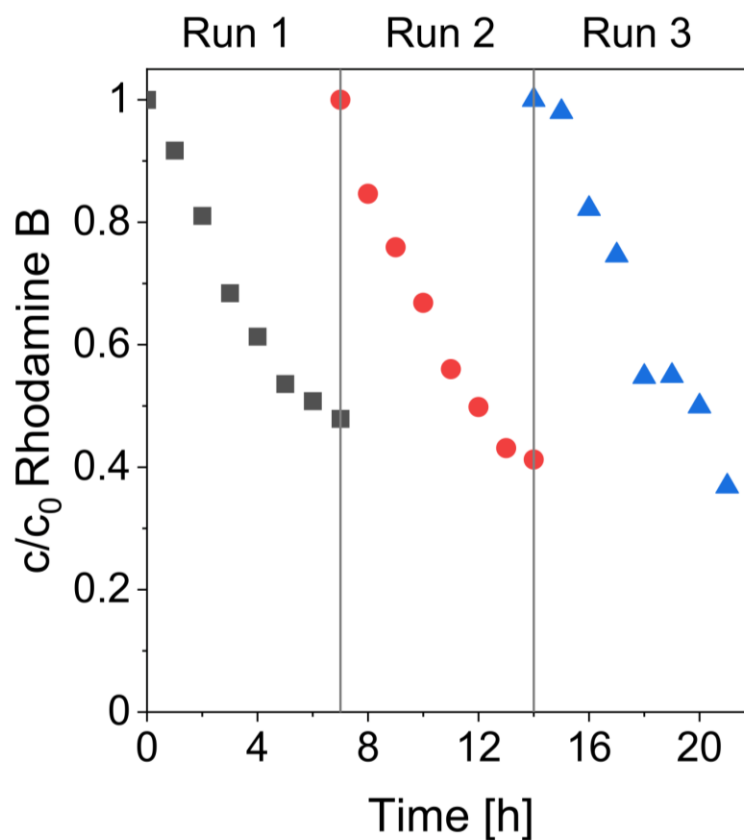
Figure S20. Reusability tests of TCQ mesostructured nonwoven in photocatalytic degradation of Rhodamine B. After each run, the mesostructured nonwoven was dried and reused in the continuous-flow setup, employing a fresh solution of Rhodamine B with the same concentration. Comparing the three runs, no significant loss in activity can be observed. Note that a mesostructured nonwoven with a TCQ loading of 0.015 mg cm^{-2} was used.

23

WILEY-VCH

S21: Morphology investigations of supramolecular nanofiber/glass microfiber nonwoven after photocatalysis
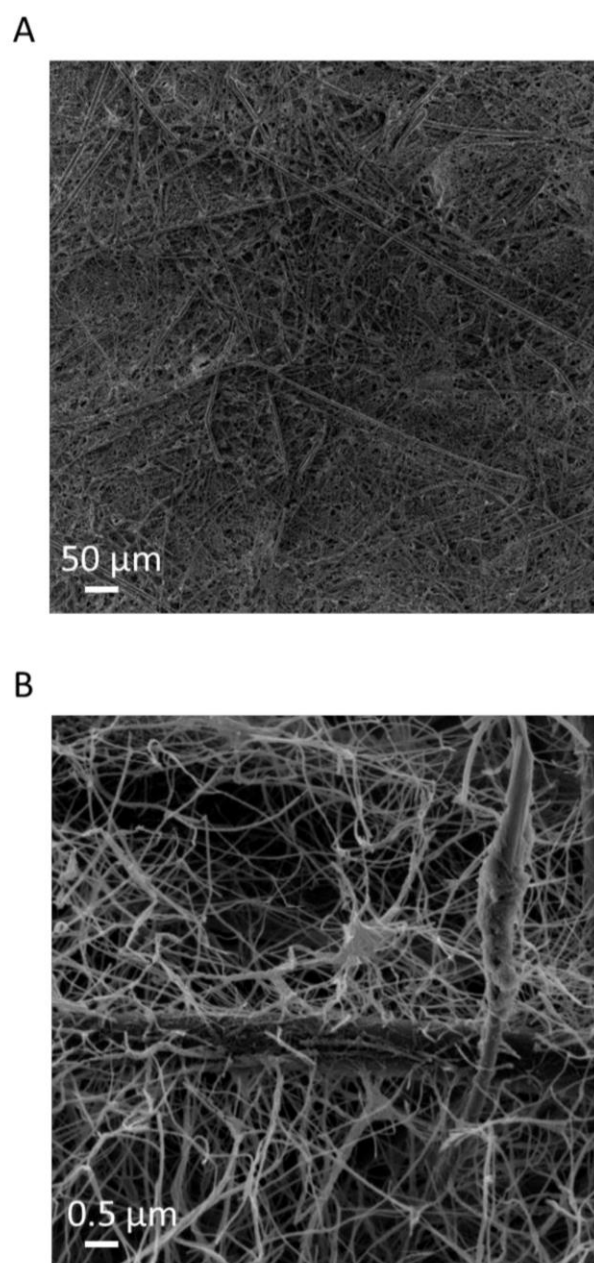
Figure S21. SEM image overview (A) and magnification (B) of TCQ nanofiber/glass microfiber nonwoven after three cycles (3x6 hours) of photocatalysis in a continuous-flow reactor with a flow rate of 1.50 L/h.

WILEY-VCH

S22: HPLC investigations of supramolecular nanofiber/glass microfiber nonwoven after photocatalysis
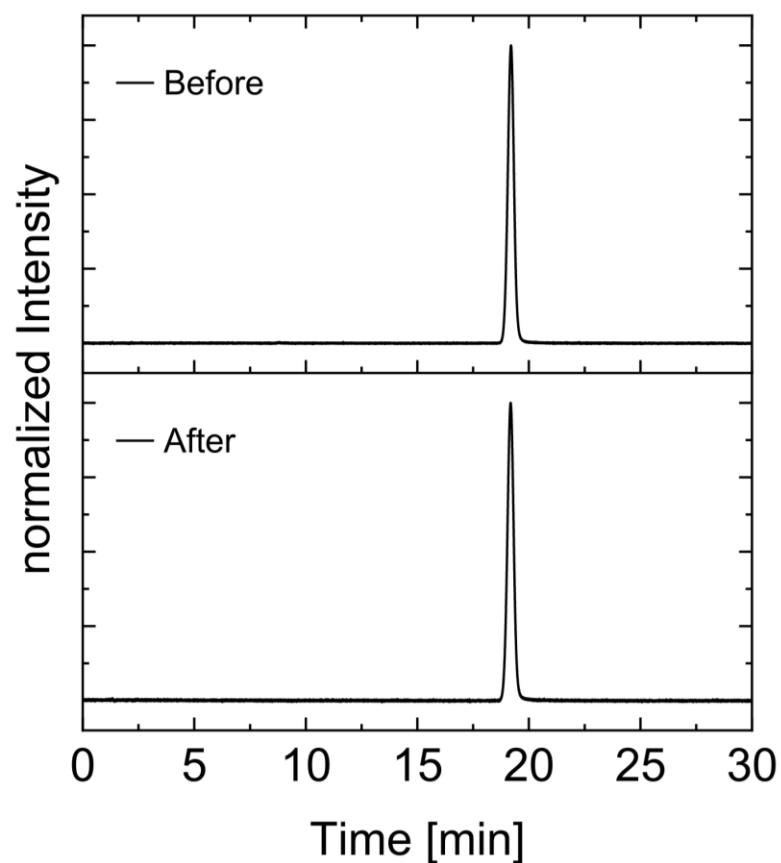
Figure S22. HPLC elugram of the supramolecular TCQ nanofiber/glass microfiber nonwoven before (top) and after (bottom) three runs of photocatalysis. HPLC samples were prepared by immersing small pieces of the nanofiber/glass microfiber nonwoven in acetonitrile till the TCQ was completely dissolved. HPLC conditions: eluent: acetonitrile/water 70/30, flow rate: 1mL min^{-1}, injection volume: 10 μL

25

WILEY-VCH

S23: Photocatalytic degradation of Tetracycline using a continuous flow reactor

A

Tetracycline

B
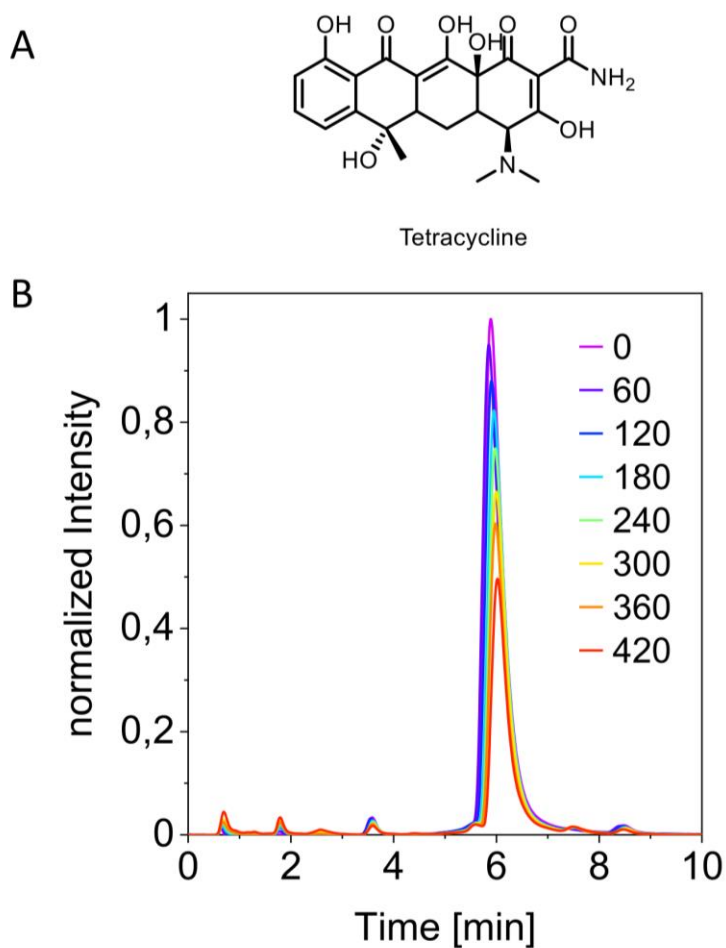
Figure S23.A: Molecular structure of tetracycline, B: HPLC elugram of aqueous solution of tetracycline during photocatalysis using a continuous flow setup at different irradiation times. HPLC conditions: eluent: water (1% formic acid)/MeOH 85/15, flow rate: 1mL min^{-1}, injection volume: 5 μL.

5 Literature

[1] C. Neuber, M. Bäte, M. Thelakkat, H.-W. Schmidt, H. Hänsel, H. Zettl, G. Krausch "Combinatorial preparation and characterization of thin-film multilayer electro-optical devices", *Rev. Sci. Instrum.* **2007**, *78*, 72216.

[2] C. Schmitz, M. Thelakkat, H.-W. Schmidt "A Combinatorial Study of the Dependence of Organic LED Characteristics on Layer Thickness", *Adv. Mater.* **1999**, *11*, 821.

[3] S. Lobe, A. Bauer, S. Uhlenbruck, D. Fattakhova-Rohlfing "Physical Vapor Deposition in Solid-State Battery Development: From Materials to Devices", *Adv. Sci.* **2021**, *8*, 2002044.

[4] B. Uzakbaiuly, A. Mukanova, Y. Zhang, Z. Bakenov "Physical Vapor Deposition of Cathode Materials for All Solid-State Li Ion Batteries: A Review", *Front. Energy Res.* **2021**, *9*.

[5] L. Geyao, D. Yang, C. Wanglin, W. Chengyong "Development and application of physical vapor deposited coatings for medical devices: A review", *Procedia CIRP* **2020**, *89*, 250.

[6] A. Perrotta, O. Werzer, A. M. Coclite "Strategies for Drug Encapsulation and Controlled Delivery Based on Vapor-Phase Deposited Thin Films", *Adv. Eng. Mater.* **2018**, *20*, 1700639.

[7] D. M. Mattox, *Handbook of Physical Vapor Deposition (PVD) Processing*, William Andrew, Norwich **2010**.

[8] E. Vetrivendan, S. Ningshen, J. Philip "Microstructural and phase characterisation of pyrolytic graphite coating by CVD using propane and methane as precursor", *Mater. High Temp.* **2019**, *36*, 540.

[9] M. Hu, H. Wu, G.-J. Zhang "High-performance silicon/graphite anode prepared by CVD using SiCl4 as precursor for Li-ion batteries", *Chem. Phys. Lett.* **2023**, *833*, 140917.

[10] Y. Avigal, I. Beinglass, M. Schieber "A New Method for Chemical Vapor Deposition of Silicon Dioxide", *J. Electrochem. Soc.* **1974**, *121*, 1103.

[11] Q. Guo, X. Ye, L. L. Zhang, Q. L. Lin, C. C. Li, Q. X. Han, X. X. Zheng, J. K. Jiang, H. M. Zhang, Y. Liu, X. T. Tao "Microspacing In-Air Sublimation Growth of Thickness-Controllable Lead Halide Crystal and the Morphology Evolution in Conversion to Perovskite", *ACS Appl. Energy Mater.* **2022**, *5*, 1618.

[12] Q. Guo, X. Ye, Q. Lin, Q. Han, C. Ge, X. Zheng, L. Zhang, S. Cui, Y. Wu, C. Li, Y. Liu, X. Tao "Microspacing In-Air Sublimation Growth of Ultrathin Organic Single Crystals", *Chem. Mater.* **2020**, *32*, 7618.

[13] T. Hai, Z. Feng, Y. Sun, W.-Y. Wong, Y. Liang, Q. Zhang, Y. Lei "Vapor-Phase Living Assembly of π-Conjugated Organic Semiconductors", *ACS Nano* **2022**, *16*, 3290.

[14] Q. Lin, X. Ye, Q. Guo, X. Zheng, Q. Han, L. Zhang, S. Cui, C. Li, J. Jiang, Y. Liu, X. Tao "Fabrication of Wafer-Scale Organic Single-Crystal Films with Uniform In-Plane Orientation via Wetting-Assisted In-Air Sublimation for High-Performance Transistor Arrays", *Chem. Mater.* **2022**, *34*, 1030.

[15] X. Ye, Y. Liu, Q. Guo, Q. X. Han, C. Ge, S. Y. Cui, L. L. Zhang, X. T. Tao "1D versus 2D cocrystals growth via microspacing in-air sublimation", *Nat. Commun.* **2019**, *10*.

[16] X. Ye, Y. Liu, Q. X. Han, C. Ge, S. Y. Cui, L. L. Zhang, X. X. Zheng, G. F. Liu, J. Liu, D. Liu, X. T. Tao "Microspacing In-Air Sublimation Growth of Organic Crystals", *Chem. Mater.* **2018**, *30*, 412.

[17] M. Thelakkat, C. Schmitz, C. Neuber, H.-W. Schmidt "Materials Screening and Combinatorial Development of Thin Film Multilayer Electro-Optical Devices", *Macromol. Rapid Commun.* **2004**, *25*, 204.

[18] M. Thelakkat, C. Schmitz, H.-W. Schmidt "Fully Vapor-Deposited Thin-Layer Titanium Dioxide Solar Cells", *Adv. Mater.* **2002**, *14*, 577.

[19] C. Schmitz, H.-W. Schmidt, M. Thelakkat, in *Organic Light-Emitting Materials and Devices IV* (Ed.: Z. H. Kafafi), SPIE **2000**, p. 183.

[20] C. Schmitz, H.-W. Schmidt, M. Thelakkat "Lithium–Quinolate Complexes as Emitter and Interface Materials in Organic Light-Emitting Diodes", *Chem. Mater.* **2000**, *12*, 3012.

[21] C. Schmitz, P. Pösch, M. Thelakkat, H.-W. Schmidt "Efficient screening of materials and fast optimization of vapor deposited OLED characteristics", *Macromol. Symp.* **2000**, *154*, 209.

[22] C. Schmitz, P. Pösch, M. Thelakkat, H.-W. Schmidt "Efficient screening of electron transport material in multi-layer organic light emitting diodes by combinatorial methods", *Phys. Chem. Chem. Phys.* **1999**, *1*, 1777.

[23] H.-W. Schmidt, C. Schmitz, P. Poesch, M. Thelakkat, in *Organic Light-Emitting Materials and Devices III* (Ed.: Z. H. Kafafi), SPIE **1999**, p. 58.

[24] K. Kreger, M. Bäte, C. Neuber, H.-W. Schmidt, P. Strohriegl "Combinatorial Development of Blue OLEDs Based on Star Shaped Molecules", *Adv. Funct. Mater.* **2007**, *17*, 3456.

[25] C. Neuber, A. Ringk, T. Kolb, F. Wieberger, P. Strohriegl, H.-W. Schmidt, V. Fokkema, M. Cooke, C. Rawlings, U. Dürig, A. W. Knoll, J.-F. de Marneffe, P. de Schepper, M. Kaestner, Y. Krivoshapkina, M. Budden, I. W. Rangelow, in *Alternative Lithographic Technologies VI* (Eds.: D. J. Resnick, C. Bencher), SPIE **2014**, 90491V.

[26] F. Pfeiffer, N. M. Felix, C. Neuber, C. K. Ober, H.-W. Schmidt "Towards environmentally friendly, dry deposited, water developable molecular glass photoresists", *Phys. Chem. Chem. Phys.* **2008**, *10*, 1257.

[27] T. Kolb, C. Neuber, M. Krysak, C. K. Ober, H.-W. Schmidt "Multicomponent Physical Vapor Deposited Films with Homogeneous Molecular Material Distribution Featuring Improved Resist Sensitivity", *Adv. Funct. Mater.* **2012**, *22*, 3865.

[28] F. Pfeiffer, C. Neuber, H.-W. Schmidt, in *Advances in Resist Materials and Processing Technology XXV* (Ed.: C. L. Henderson), SPIE **2008**, 69231F.

[29] F. Wieberger, T. Kolb, C. Neuber, C. K. Ober, H.-W. Schmidt, in *Advances in Patterning Materials and Processes XXXI* (Eds.: T. I. Wallow, C. K. Hohle), SPIE **2014**, 90510G.

[30] F. Wieberger, C. Neuber, C. K. Ober, H.-W. Schmidt "Tailored Star Block Copolymer Architecture for High Performance Chemically Amplified Resists", *Adv. Mater.* **2012**, *24*, 5939.

[31] M. Bäte, C. Neuber, R. Giesa, H.-W. Schmidt "Combinatorial Investigation of the Vapor Deposition Polymerization of Aromatic Polyimides", *Macromol. Rapid Commun.* **2004**, *25*, 371.

[32] C. Neuber, M. Bäte, R. Giesa, H.-W. Schmidt "Combinatorial methods for the optimization of the vapor deposition of polyimide monomers and their polymerization", *J. Mater. Chem.* **2006**, *16*, 3466.

[33] H. Brune "Epitaxial growth of thin films", *Surf. Interface Sci.* **2014**, *4*, 421.

[34] F. C. Frank, J. H. van der Merwe "One-dimensional dislocations. II. Misfitting monolayers and oriented overgrowth", *Proc. R. Soc. London, Ser. A* **1949**, *198*, 216.

[35] J. H. van der Merwe "Misfitting monolayers and oriented overgrowth", *Discuss. Faraday Soc.* **1949**, *5*, 201.

[36] M. Volmer, A. Weber "Keimbildung in übersättigten Gebilden", *Z. Phys. Chem.* **1926**, *119*, 277.

[37] Iwan N. Stranski, L. Krastanow "Zur Theorie der orientierten Ausscheidung von Ionenkristallen aufeinander", *Monatshefte für Chemie* **1937**, *71*, 351.

[38] J. W. Lee, K. Kim, D. H. Park, M. Y. Cho, Y. B. Lee, J. S. Jung, D.-C. Kim, J. Kim, J. Joo "Light-Emitting Rubrene Nanowire Arrays: A Comparison with Rubrene Single Crystals", *Adv. Funct. Mater.* **2009**, *19*, 704.

[39] S. Karan, B. Mallik "Templating Effects and Optical Characterization of Copper (II) Phthalocyanine Nanocrystallites Thin Film: Nanoparticles, Nanoflowers, Nanocabbages, and Nanoribbons", *J. Phys. Chem. C* **2007**, *111*, 7352.

[40] Y. Han, W. Ning, H. Du, J. Yang, N. Wang, L. Cao, F. Li, F. Zhang, F. XU, M. Tian "Preparation, optical and electrical properties of PTCDA nanostructures", *Nanoscale* **2015**, *7*, 17116.

[41] J. M. Obrero, A. N. Filippin, M. Alcaire, J. R. Sanchez-Valencia, M. Jacob, C. Matei, F. J. Aparicio, M. Macias-Montero, T. C. Rojas, J. P. Espinos, Z. Saghi, A. Barranco, A. Borras "Supported Porous Nanostructures Developed by Plasma Processing of Metal Phthalocyanines and Porphyrins", *Front. Chem.* **2020**, *8*, 520.

[42] H. Pan, X. Zhang, Y. Yang, Z. Shao, W. Deng, K. Ding, Y. Zhang, J. Jie "Patterned growth of single-crystal 3, 4, 9, 10-perylenetetracarboxylic dianhydride nanowire arrays for field-emission and optoelectronic devices", *Nanotechnology* **2015**, *26*, 295302.

[43] H. Yuan, Y. Chen, R. Lin, D. Tan, J. Zhang, Y. Wang, E. Gazit, W. Ji, R. Yang "Modified Stranski–Krastanov Growth of Amino Acid Arrays toward Piezoelectric Energy Harvesting", *ACS Appl. Mater. Interfaces* **2022**, *14*, 46304.

[44] Y.-C. Chiu, B.-H. Chen, D.-J. Jan, S.-J. Tang, K.-C. Chiu "Growth behavior of CuPc films by physical vapor deposition", *Cryst. Res. Technol.* **2011**, *46*, 295.

[45] V. Sahibbeyli, D. B. Yildiz, G. Papir, Y. Dede, G. Demirel "The Role of Molecular Structure of Phenylalanine Peptides on the Formation of Vertically Aligned Ordered Bionanostructures: Implications for Sensing Application", *ACS Appl. Nano Mater.* **2020**, *3*, 4305.

[46] P. Guo, Y. Han, W. ZHANG, L. LIU, K. A. WANG, F. XU "Modulation of PTCDA Nanostructures and Optical Property: Dependence on growth Temperature", *Nano* **2014**, *09*, 1450068.

[47] Y. Huang, R. Yuan, S. Zhou "Gas phase-based growth of highly sensitive single-crystal rectangular micro- and nanotubes", *J. Mater. Chem.* **2012**, *22*, 883.

[48] H.-F. Ji, R. Majithia, X. Yang, X. Xu, K. More "Self-Assembly of Perylenediimide and Naph-thalenediimide Nanostructures on Glass Substrates through Deposition from the Gas Phase", *J. Am. Ceram. Soc.* **2008**, *130*, 10056.

[49] Y. Khopkar, A. Kojtari, D. Swearer, S. Zivanovic, H.-F. Ji "Perylenetetracarboxylic diimide (PTCDI) nanowires for sensing ethyl acetate in wine", *J. Nanosci. Nanotechnol.* **2014**, *14*, 6786.

[50] W. Luo, Y. Liu, F. Li, Z. Zhang, Z. Chao, J. Fan "Low-Dimensional and High-Crystallinity Car-bonyl Cathodes Prepared by Physical Vapor Deposition for Green Aluminum Organic Bat-teries", *ACS Appl. Mater. Interfaces* **2023**, *15*, 37433.

[51] S.-C. Suen, W.-T. Whang, F.-J. Hou, B.-T. Dai "Growth enhancement and field emission char-acteristics of one-dimensional 3,4,9,10-perylenetetracarboxylic dianhydride nanostruc-tures on pillared titanium substrate", *Org. Electron.* **2007**, *8*, 505.

[52] K. Vasseur, C. Rolin, S. Vandezande, K. Temst, L. Froyen, P. Heremans "A Growth and Mor-phology Study of Organic Vapor Phase Deposited Perylene Diimide Thin Films for Transistor Applications", *J. Phys. Chem. C* **2010**, *114*, 2730.

[53] A. Borras, M. Aguirre, O. Groening, C. Lopez-Cartes, P. Groening "Synthesis of Supported Single-Crystalline Organic Nanowires by Physical Vapor Deposition", *Chem. Mater.* **2008**, *20*, 7371.

[54] A. Borras, O. Gröning, M. Aguirre, F. Gramm, P. Gröning "One-Step Dry Method for the Synthesis of Supported Single-Crystalline Organic Nanowires Formed by π-Conjugated Mol-ecules", *Langmuir* **2010**, *26*, 5763.

[55] J.-S. Hu, H.-X. Ji, L.-J. Wan "Metal Octaethylporphyrin Nanowire Array and Network toward Electric/Photoelectric Devices", *J. Phys. Chem. C* **2009**, *113*, 16259.

[56] T. Mirabito, B. Huet, J. M. Redwing, D. W. Snyder "Influence of the Underlying Substrate on the Physical Vapor Deposition of Zn-Phthalocyanine on Graphene", *ACS Omega* **2021**, *6*, 20598.

[57] K. Sayo, S. Deki, T. Noguchi, K. Goto "Composite films produced by successive vapor-depo-sitions of nylon-11 and porphyrin compounds", *Thin Solid Films* **1999**, *349*, 276.

[58] Y. Ueda, T. Hari, T. Thumori, M. Yano, J. Ni "Crystal growth and molecular orientation of tetraphenylmetalporphyrin vapor-deposited on poly(tetrafluoroethylene) friction-trans-ferred layers", *Appl. Surf. Sci.* **1997**, *113-114*, 304.

[59] S. M. Yoon, I.-C. Hwang, K. S. Kim, H. C. Choi "Synthesis of Single-Crystal Tetra(4-pyridyl)por-phyrin Rectangular Nanotubes in the Vapor Phase", *Angew. Chem., Int. Ed.* **2009**, *48*, 2506.

[60] A. N. Filippin, V. López-Flores, T. C. Rojas, Z. Saghi, V. J. Rico, J. R. Sanchez-Valencia, J. P. Espinós, A. Zitolo, M. Viret, P. A. Midgley, A. Barranco, A. Borras "Self-Assembly of the Non-planar Fe(III) Phthalocyanine Small-Molecule: Unraveling the Impact on the Magnetic Prop-erties of Organic Nanowires", *Chem. Mater.* **2018**, *30*, 879.

[61] S. Karan, B. Mallik "Nanoflowers Grown from Phthalocyanine Seeds: Organic Nanorectifi-ers", *J. Phys. Chem. C* **2008**, *112*, 2436.

[62] F. Liu, J. Sun, S. Xiao, W. Huang, S. Tao, Y. Zhang, Y. Gao, J. Yang "Controllable fabrication of copper phthalocyanine nanostructure crystals", *Nanotechnology* **2015**, *26*, 225601.

[63] Q. Min, X. Zhao, B. Cai, Y. Liu, Q. Tang, Y. Tong, W. Hu, Y. Liu "An ordered array based on vapor-processed phthalocyanine nanoribbons", *J. Mater. Chem. C* **2014**, *2*, 5667.

[64] T. Mirabito, B. Huet, A. L. Briseno, D. W. Snyder "Physical vapor deposition of zinc phthalocyanine nanostructures on oxidized silicon and graphene substrates", *J. Cryst. Growth* **2020**, *533*, 125484.

[65] W. Y. Tong, A. B. Djurisić, M. H. Xie, A. C. M. Ng, K. Y. Cheung, W. K. Chan, Y. H. Leung, H. W. Lin, S. Gwo "Metal phthalocyanine nanoribbons and nanowires", *J. Phys. Chem. B* **2006**, *110*, 17406.

[66] W. Y. Tong, Z. X. Li, A. B. Djurišić, W. K. Chan, S. F. Yu "Field emission from copper phthalocyanine and copper hexadecafluorophthalocyanine nanowires", *Mater. Lett.* **2007**, *61*, 3842.

[67] H. Wang, S. Mauthoor, S. Din, J. A. Gardener, R. Chang, M. Warner, G. Aeppli, D. W. McComb, M. P. Ryan, W. Wu, A. J. Fisher, M. Stoneham, S. Heutz "Ultralong copper phthalocyanine nanowires with new crystal structure and broad optical absorption", *ACS Nano* **2010**, *4*, 3921.

[68] Y. S. Zhao, D. Xiao, W. Yang, A. Peng, J. Yao "2,4,5-Triphenylimidazole Nanowires with Fluorescence Narrowing Spectra Prepared through the Adsorbent-Assisted Physical Vapor Deposition Method", *Chem. Mater.* **2006**, *18*, 2302.

[69] Y. S. Zhao, C. Di, W. Yang, G. Yu, Y. Liu, J. Yao "Photoluminescence and Electroluminescence from Tris(8- hydroxyquinoline)aluminum Nanowires Prepared by Adsorbent-Assisted Physical Vapor Deposition", *Adv. Funct. Mater.* **2006**, *16*, 1985.

[70] K.-J. Huang, Y.-S. Hsiao, W.-T. Whang "Low-temperature formation of self-assembled 1,5-diaminoanthraquinone nanofibers: Substrate effects and field emission characteristics", *Org. Electron.* **2011**, *12*, 686.

[71] S. A. Arabi, J. Dong, M. Mirza, P. Yu, L. Wang, J. He, C. Jiang "Nanoseed Assisted PVT Growth of Ultrathin 2D Pentacene Molecular Crystal Directly onto SiO2 Substrate", *Cryst. Growth Des.* **2016**, *16*, 2624.

[72] S.-C. Suen, W.-T. Whang, B.-W. Wu, Y.-F. Lai "Low-temperature fabrication of carbon nanofibers by self-assembling of polycyclic aromatic hydrocarbon molecules", *Appl. Phys. Lett.* **2004**, *84*, 3157.

[73] L. Adler-Abramovich, D. Aronov, P. Beker, M. Yevnin, S. Stempler, L. Buzhansky, G. Rosenman, E. Gazit "Self-assembled arrays of peptide nanotubes by vapour deposition", *Nat. Nanotechnol.* **2009**, *4*, 849.

[74] N. Amdursky, I. Koren, E. Gazit, G. Rosenman "Adjustable photoluminescence of peptide nanotubes coatings", *J. Nanosci. Nanotechnol.* **2011**, *11*, 9282.

[75] N. Amdursky, M. Molotskii, D. Aronov, L. Adler-Abramovich, E. Gazit, G. Rosenman "Blue Luminescence Based on Quantum Confinement at Peptide Nanotubes", *Nano Lett.* **2009**, *9*, 3111.

[76] B. Bank-Srour, P. Becker, L. Krasovitsky, A. Gladkikh, Y. Rosenberg, Z. Barkay, G. Rosenman "Physical vapor deposition of peptide nanostructures", *Polym. J.* **2013**, *45*, 494.

[77] P. Beker, G. Rosenman "Bioinspired nanostructural peptide materials for supercapacitor electrodes", *J. Mater. Res.* **2010**, *25*, 1661.

[78] J. S. Lee, I. Yoon, J. Kim, H. Ihee, B. Kim, C. B. Park "Self-Assembly of Semiconducting Photoluminescent Peptide Nanowires in the Vapor Phase", *Angew. Chem., Int. Ed.* **2011**, *50*, 1164.

[79] G. Rosenman, P. Beker, I. Koren, M. Yevnin, B. Bank-Srour, E. Mishina, S. Semin "Bioinspired peptide nanotubes: deposition technology, basic physics and nanotechnology applications", *J. Pept. Sci.* **2011**, *17*, 75.

[80] J. Ryu, C. B. Park "High-Temperature Self-Assembly of Peptides into Vertically Well-Aligned Nanowires by Aniline Vapor", *Adv. Mater.* **2008**, *20*, 3754.

[81] K. Tao, P. Makam, R. Aizen, E. Gazit "Self-assembling peptide semiconductors", *Science* **2017**, *358*, eaam9756.

[82] X. Fang, X. Yang, D. Yan "Vapor-phase π–π molecular recognition: a fast and solvent-free strategy towards the formation of co-crystalline hollow microtube with 1D optical waveguide and up-conversion emission", *J. Mater. Chem. C* **2017**, *5*, 1632.

[83] Q. Tang, Y. Tong, Y. Zheng, Y. He, Y. Zhang, H. Dong, W. Hu, T. Hassenkam, T. Bjørnholm "Organic nanowire crystals combine excellent device performance and mechanical flexibility", *Small* **2011**, *7*, 189.

[84] L. R. Fleet, J. Stott, B. Villis, S. Din, M. Serri, G. Aeppli, S. Heutz, A. Nathan "Self-Assembled Molecular Nanowires for High-Performance Organic Transistors", *ACS Appl. Mater. Interfaces* **2017**, *9*, 20686.

[85] R. Q. Albuquerque, A. Timme, R. Kress, J. Senker, H.-W. Schmidt "Theoretical Investigation of Macrodipoles in Supramolecular Columnar Stackings", *Chem. - Eur. J.* **2013**, *19*, 1647.

[86] K. Hanabusa, A. Kawakami, M. Kimura, H. Shirai "Small Molecular Gelling Agents to Harden Organic Liquids: Trialkyl cis-1,3,5-Cyclohexanetricarboxamides", *Chem. Lett.* **1997**, *26*, 191.

[87] A. T. Haedler, K. Kreger, A. Issac, B. Wittmann, M. Kivala, N. Hammer, J. Köhler, H.-W. Schmidt, R. Hildner "Long-range energy transport in single supramolecular nanofibres at room temperature", *Nature* **2015**, *523*, 196.

[88] B. Wittmann, F. A. Wenzel, S. Wiesneth, A. T. Haedler, M. Drechsler, K. Kreger, J. Köhler, E. W. Meijer, H.-W. Schmidt, R. Hildner "Enhancing Long-Range Energy Transport in Supramolecular Architectures by Tailoring Coherence Properties", *J. Am. Ceram. Soc.* **2020**, *142*, 8323.

[89] F. Xu, H. Su, J. J. B. van der Tol, S. A. H. Jansen, Y. Fu, G. Lavarda, G. Vantomme, S. Meskers, E. W. Meijer "Supramolecular Polymerization as a Tool to Reveal the Magnetic Transition Dipole Moment of Heptazines", *J. Am. Ceram. Soc.* **2024**, *146*, 15843.

[90] N. Mohmeyer, B. Müller, N. Behrendt, J. Hillenbrand, M. Klaiber, X. Zhang, P. Smith, V. Altstädt, G. M. Sessler, H.-W. Schmidt "Nucleation of isotactic polypropylene by triphenylamine-based trisamide derivatives and their influence on charge-storage properties", *Polymer* **2004**, *45*, 6655.

[91] M. L. Ślęczkowski, M. F. J. Mabesoone, M. D. Preuss, Y. Post, A. R. A. Palmans, E. W. Meijer "Helical bias in supramolecular polymers accounts for different stabilities of kinetically trapped states", *J. Polym. Sci.* **2022**, *60*, 1871.

[92] Y.-R. Luo, *Comprehensive handbook of chemical bond energies*, CRC press **2007**.

[93] P. A. Gale, J. W. Steed (Eds.), *Supramolecular chemistry: From molecules to nanomaterials*, Wiley, Chichester **2012**.

[94] M. P. Lightfoot, F. S. Mair, R. G. Pritchard, J. E. Warren "New supramolecular packing motifs: π-stacked rods encased in triply-helical hydrogen bonded amide strands", *Chem. Commun.* **1999**, 1945.

[95] S. Cantekin, T. F. A. de Greef, A. R. A. Palmans "Benzene-1,3,5-tricarboxamide: a versatile ordering moiety for supramolecular chemistry", *Chem. Soc. Rev.* **2012**, *41*, 6125.

[96] M. Wegner, D. Dudenko, D. Sebastiani, A. R. A. Palmans, T. F. A. de Greef, R. Graf, H. W. Spiess "The impact of the amide connectivity on the assembly and dynamics of benzene-1, 3, 5-tricarboxamides in the solid state", *Chem. Sci.* **2011**, *2*, 2040.

[97] C. S. Zehe, J. A. Hill, N. P. Funnell, K. Kreger, K. P. van der Zwan, A. L. Goodwin, H.-W. Schmidt, J. Senker "Mesoscale polarization by geometric frustration in columnar supramolecular crystals", *Angew. Chem., Int. Ed.* **2017**, *56*, 4432.

[98] A. Timme, R. Kress, R. Q. Albuquerque, H.-W. Schmidt "Phase Behavior and Mesophase Structures of 1,3,5-Benzene- and 1,3,5-Cyclohexanetricarboxamides: Towards an Understanding of the Losing Order at the Transition into the Isotropic Phase", *Chem. - Eur. J.* **2012**, *18*, 8329.

[99] T. Akutagawa, K. Iuchi, Y. Matsunaga "Mesomorphic behaviour of N,N-dialkanoyl-3,4,5,6-tetramethylbenzene-1,2-diamines and related compounds", *Liq. Cryst* **2000**, *27*, 1399.

[100] Y. Matsunaga, N. Miyajima, Y. Nakayasu, S. Sakai, M. Yonenaga "Design of novel mesomorphic compounds: N, N', N"-trialkyl-1, 3, 5-benzenetricarboxamides", *Bull. Chem. Soc. Jpn.* **1988**, *61*, 207.

[101] D. Weiss, K. Kreger, H.-W. Schmidt "Self-Assembly of Alkoxy-Substituted 1,3,5-Benzenetrisamides Under Controlled Conditions", *Macromol. Mater. Eng.* **2017**, *302*, 1600390.

[102] Markus Drummer, *Functional supramolecular nanofibers and their applications in nanoparticle immobilization and catalysis*, Dissertation, University of Bayreuth **2022**.

[103]   A. Frank, A. Bernet, K. Kreger, H.-W. Schmidt "Supramolecular microtubes based on 1,3,5-benzenetricarboxamides prepared by self-assembly upon heating", *Soft Matter* **2020**, *16*, 4564.

[104]   A. Bernet, R. Q. Albuquerque, M. Behr, S. T. Hoffmann, H.-W. Schmidt "Formation of a supramolecular chromophore: a spectroscopic and theoretical study", *Soft Matter* **2012**, *8*, 66.

[105]   Marina Cornelia Behr, *Supramolecular hydrogels based on 1,3,5-benzene tricarbox-amides*, Dissertation, University of Bayreuth **2014**.

[106]   N. Raßmann, M. Weber, R. E. J. Glaß, K. Kreger, N. Helfricht, H.-W. Schmidt, G. Papas-tavrou "Electrogelation: Controlled Fast Formation of Micrometer-Thick Films from Low-Molecular Weight Hydrogelators", *Langmuir* **2023**, *39*, 17190.

[107]   N. Helfricht, A. Mark, M. Behr, A. Bernet, H.-W. Schmidt, G. Papastavrou "Writing with Fluid: Structuring Hydrogels with Micrometer Precision by AFM in Combination with Nanofluidics", *Small* **2017**, *13*, 1700962.

[108]   F. Abraham, S. Ganzleben, D. Hanft, P. Smith, H.-W. Schmidt "Synthesis and Structure–Efficiency Relations of 1,3,5-Benzenetrisamides as Nucleating Agents and Clarifiers for Iso-tactic Poly(propylene)", *Macromol. Chem. Phys.* **2010**, *211*, 171.

[109]   F. Abraham, R. Kress, P. Smith, H.-W. Schmidt "A New Class of Ultra-Efficient Supramo-lecular Nucleating Agents for Isotactic Polypropylene", *Macromol. Chem. Phys.* **2013**, *214*, 17.

[110]   N. Behrendt, N. Mohmeyer, J. Hillenbrand, M. Klaiber, X. Zhang, G. M. Sessler, H.-W. Schmidt, V. Altstädt "Charge storage behavior of isotropic and biaxially-oriented polypro-pylene films containing α- and β-nucleating agents", *J. Appl. Polym. Sci.* **2006**, *99*, 650.

[111]   M. Blomenhofer, S. Ganzleben, D. Hanft, H.-W. Schmidt, M. Kristiansen, P. Smith, K. Stoll, D. Mäder, K. Hoffmann ""Designer" Nucleating Agents for Polypropylene", *Macromole-cules* **2005**, *38*, 3688.

[112]   M. Kristiansen, P. Smith, H. Chanzy, C. Baerlocher, V. Gramlich, L. McCusker, T. Weber, P. Pattison, M. Blomenhofer, H.-W. Schmidt "Structural Aspects of 1,3,5-Benzenetrisam-ides–A New Family of Nucleating Agents", *Cryst. Growth Des.* **2009**, *9*, 2556.

[113]   P. M. Kristiansen, A. Gress, P. Smith, D. Hanft, H.-W. Schmidt "Phase behavior, nuclea-tion and optical properties of the binary system isotactic polypropylene/N,N′,N″-tris-iso-pentyl-1,3,5-benzene-tricarboxamide", *Polymer* **2006**, *47*, 249.

[114]   F. Richter, H.-W. Schmidt "Supramolecular Nucleating Agents for Poly(butylene tereph-thalate) Based on 1,3,5-Benzenetrisamides", *Macromol. Mater. Eng.* **2013**, *298*, 190.

[115]   M. Aksit, B. Klose, C. Zhao, K. Kreger, H.-W. Schmidt, V. Altstädt "Morphology control of extruded polystyrene foams with benzene-trisamide-based nucleating agents", *J. Cell. Plast.* **2019**, *55*, 249.

Literature

[116]   M. Aksit, C. Zhao, B. Klose, K. Kreger, H.-W. Schmidt, V. Altstädt "Extruded Polystyrene Foams with Enhanced Insulation and Mechanical Properties by a Benzene-Trisamide-Based Additive", *Polymers* **2019**, *11*.

[117]   H. Misslitz, K. Kreger, H.-W. Schmidt "Supramolecular Nanofiber Webs in Nonwoven Scaffolds as Potential Filter Media", *Small* **2013**, *9*, 2053.

[118]   D. Weiss, D. Skrybeck, H. Misslitz, D. Nardini, A. Kern, K. Kreger, H.-W. Schmidt "Tailoring Supramolecular Nanofibers for Air Filtration Applications", *ACS Appl. Mater. Interfaces* **2016**, *8*, 14885.

[119]   Helga Thomas, Xiomin Zhu, Martin Möller, Klaus Kreger, David Nardini, Hans-Werner Schmidt "Supramolecular nanofiber composites for highly efficient and selective removal of gold(III) from aqueous media", *Technische Textilien* **2019**, 80 E.

[120]   David Nardini, *Sulfur-Containing Functional Supramolecular Fibers for Filtration Applications*, Dissertation, University of Bayreuth **2021**.

[121]   M. Drummer, C. Liang, K. Kreger, S. Rosenfeldt, A. Greiner, H.-W. Schmidt "Stable Mesoscale Nonwovens of Electrospun Polyacrylonitrile and Interpenetrating Supramolecular 1,3,5-Benzenetrisamide Fibers as Efficient Carriers for Gold Nanoparticles", *ACS Appl. Mater. Interfaces* **2021**, *13*, 34818.

[122]   M. Burgard, D. Weiss, K. Kreger, H. Schmalz, S. Agarwal, H.-W. Schmidt, A. Greiner "Mesostructured Nonwovens with Penguin Downy Feather-Like Morphology—Top-Down Combined with Bottom-Up", *Adv. Funct. Mater.* **2019**, *29*, 1903166.

[123]   A. Frank, C. Hils, M. Weber, K. Kreger, H. Schmalz, H.-W. Schmidt "Hierarchical Superstructures by Combining Crystallization-Driven and Molecular Self-Assembly", *Angew. Chem., Int. Ed.* **2021**, *60*, 21767.

[124]   A. Frank, C. Hils, M. Weber, K. Kreger, H. Schmalz, H.-W. Schmidt "Hierarchische Überstrukturen durch Kombination von kristallisationsinduzierter und molekularer Selbstassemblierung", *Angew. Chem.* **2021**, *133*, 21935.

[125]   A. Frank, M. Weber, C. Hils, U. Mansfeld, K. Kreger, H. Schmalz, H.-W. Schmidt "Functional Mesostructured Electrospun Polymer Nonwovens with Supramolecular Nanofibers", *Macromol. Rapid Commun.* **2022**, *43*, e2200052.

[126]   M. Weber, F. Bretschneider, K. Kreger, A. Greiner, H.-W. Schmidt "Mimicking Cacti Spines via Hierarchical Self-Assembly for Water Collection and Unidirectional Transport", *Adv. Mater. Interfaces* **2024**, *n/a*, 2400101.

[127]   P. Jacobson, L. Huber "Über Bildung von Indazolkörpern aus orthomethylierten Anilinbasen", *Ber. Dtsch. Chem. Ges.* **1908**, *41*, 660.

[128]   J. Kozak, Kalmus A. "Über Tricyklochinazolin", *Bull. Int. Acad. Pol. Sci. Lett., Cl. Sci. Math. Nat., Ser. A* **1933**, 532.

[129]   J. Iball, W. D. Motherwe "Crystal and Molecular Structure of Tricycloquinazoline", *Acta Crystallogr., Sect. B:Struct. Sci., Cryst. Eng. Mater.* **1969**, *B 25*, 882-888.

[130]   J. Iball, S. M. Motherwe "CRYSTAL STRUCTURES OF TRICYCLOQUINAZOLINE AND OF ITS COMPLEX WITH CUPRIC CHLORIDE", *Acta Crystallogr., Sect. A:Found. Crystallogr.* **1966**, *S 21*, A143-&.

[131]   F. C. Cooper, M. W. Partridge "Cyclic amidines. Part I. Derivatives of phenhomazine (dibenzo[b, f]-1 5-diazocine)", *J. Chem. Soc.* **1954**, 3429.

[132]   F. Yoneda, K. Mera "A Novel One-step Synthesis of Tricycloquinazolines", *Chem. Pharm. Bull.* **1973**, *21*, 1610.

[133]   Ponomarev, II, S. V. Vinogradova "An Efficient Method fot the Synthesis of Tricyclo-quinazoline", *Bull. Acad. Sci. USSR, Div. Chem. Sci. (Engl. Transl.)* **1990**, *39*, 2229.

[134]   O. Buyukcakir, R. Yuksel, Y. Jiang, S. H. Lee, W. K. Seong, X. Chen, R. S. Ruoff "Synthesis of Porous Covalent Quinazoline Networks (CQNs) and Their Gas Sorption Properties", *Angew. Chem., Int. Ed.* **2019**, *58*, 872.

[135]   K. Butler, M. W. Partridge "293. Cyclic amidines. Part VIII. Derivatives of 12H-6 7 12a-triazabenz[a]anthracene and 5aH-5 6 11a-triazanaphthacene", *J. Chem. Soc.* **1959**, 1512.

[136]   K. Butler, M. W. Partridge "Cyclic Amidines. Part IX. Tricycloquinazoline", *J. Chem. Soc.* **1959**, 2396.

[137]   H. G. Dean, R. J. Grout, M. W. Partridge, H. J. Vipond "Cyclic Amidines. Part XXI. [14C]Tri-cycloquinazoline and Hydroxytricycloquinazolines", *J. Chem. Soc. C* **1968**, 142-&.

[138]   E. Keinan, S. Kumar, S. P. Singh, R. Ghirlando, E. J. Wachtel "New Discotic Liquid-Crystals having a Tricycloquinazoline Core", *Liq. Cryst* **1992**, *11*, 157.

[139]   P. Uznanski, M. Kryszewski (Eds.: J. Rutkowska, S. J. Klosowicz, J. Zielinski, J. Zmija) **1998**, p. 398.

[140]   R. Hiesgen, H. Schonherr, S. Kumar, H. Ringsdorf, D. Meissner "Scanning tunneling microscopy investigation of tricycloquinazoline liquid crystals on gold", *Thin Solid Films* **2000**, *358*, 241.

[141]   H. Schönherr, F. J. B. Kremer, S. Kumar, J. A. Rego, H. Wolf, H. Ringsdorf, M. Jaschke, H.-J. Butt, E. Bamberg "Self-Assembled Monolayers of Discotic Liquid Crystalline Thioethers, Discoid Disulfides, and Thiols on Gold: Molecular Engineering of Ordered Surfaces", *J. Am. Ceram. Soc.* **1996**, *118*, 13051.

[142]   S. Kumar, E. J. Wachtel, E. Keinan "Hexaalkoxytricycloquinazolines - New Discotic Liquid-crystals", *J. Org. Chem.* **1993**, *58*, 3821.

[143]   S. Kumar "A simple, rapid, one-step synthesis of aryl poly ethers from aryl acetates: Improved synthesis of hexaalkoxytricycloquinazoline derivatives", *Mol. Cryst. Liq. Cryst. Sci. Technol., Sect. A* **1996**, *289*, 247.

[144]   S. Kumar, D. S. Rao, S. K. Prasad "New branched chain tricycloquinazoline derivatives: a room temperature electron deficient discotic system", *J. Mater. Chem.* **1999**, *9*, 2751.

[145]   J. Kadam, C. F. Faul, U. Scherf "Induced liquid crystallinity in switchable side-chain discotic molecules", *Chem. Mater.* **2004**, *16*, 3867.

[146] H. K. Bisoyi, V. A. Raghunathan, S. Kumar "A nanophase segregated mesophase mor-phology in self-organized novel disc-rod oligomesogens", *Chem. Commun.* **2009**, 7003.

[147] R. K. Gupta, V. Manjuladevi, C. Karthik, S. Kumar, IOP **2013**.

[148] N. Boden, R. J. Bushby, K. Donovan, Q. Y. Liu, Z. B. Lu, T. Kreouzis, A. Wood "2,3,7,8,12,13-Hexakis[2-(2-methoxyethoxy)ethoxy]-tricycloquinazoline: a discogen which allows enhanced levels of n-doping", *Liq. Cryst* **2001**, *28*, 1739.

[149] C. Karthik, V. Manjuladevi, R. K. Gupta, S. Kumar "Solvatochromism of a tricycloquinazo-line based disk-shaped liquid crystal: a potential molecular probe for fluorescence imag-ing", *RSC Adv.* **2015**, *5*, 84592.

[150] N. Boden, R. C. Borner, R. J. Bushby, J. Clements "First Observation of a n-Doped Quasi-One-Dimensional Electronically-Conducting Discotic Liquid Crystal", *J. Am. Ceram. Soc.* **1994**, *116*, 10807.

[151] R. K. Gupta, V. Manjuladevi, C. Karthik, S. Kumar, K. A. Suresh "Studies on Langmuir mon-olayer of tricycloquinazoline based disk-shaped liquid crystal molecules", *Colloids Surf., A* **2012**, *410*, 91.

[152] C. Karthik, V. Manjuladevi, R. K. Gupta, S. Kumar "Pattern formation in Langmuir-Blodgett films of tricycloquinazoline based discotic liquid crystal molecules", *J. Mol. Struct.* **2014**, *1070*, 52.

[153] W. B. Wang, Y. T. Zhang, L. F. Chen, H. Chen, S. Z. Hu, Q. Li, H. N. Liu, S. L. Qiao "Tricyclo-quinazoline-containing 3D conjugated microporous polymers and 2D covalent quinazoline networks: microstructure and conductivity", *Polym. Chem.* **2021**, *12*, 650.

[154] X. Suo, F. Zhang, Z. Yang, L. Wang, M. Lei, J. A. Gaugler, M. Li, J. Fan, B. P. Thapaliya, I. Popovs, A. S. Ivanov, L. C. Gallington, D. Jiang, Z. Liu, S. Dai "Electrochemical CO2-to-eth-ylene conversion on metal-free covalent quinazoline network-derived electrodes", *Chem Catal.* **2023**, *3*, 100506.

[155] Z. Z. Yang, T. Wang, H. Chen, X. Suo, P. Halstenberg, H. Lyu, W. Jiang, S. M. Mahurin, I. Popovs, S. Dai "Surpassing the Organic Cathode Performance for Lithium-Ion Batteries with Robust Fluorinated Covalent Quinazoline Networks", *ACS Energy Lett.* **2021**, *6*, 41.

[156] C. Lu, B. Clayville, J. Y. Choi, J. Park "2D metal-organic frameworks as an emerging plat-form with tunable electronic structures", *Chem* **2023**, *9*, 2757.

[157] J.-H. Dou, M. Q. Arguilla, Y. Luo, J. Li, W. Zhang, L. Sun, J. L. Mancuso, L. Yang, T. Chen, L. R. Parent, G. Skorupskii, N. J. Libretto, C. Sun, M. C. Yang, P. V. Dip, E. J. Brignole, J. T. Miller, J. Kong, C. H. Hendon, J. Sun, M. Dincă "Atomically precise single-crystal structures of elec-trically conducting 2D metal-organic frameworks", *Nat. Mater.* **2021**, *20*, 222.

[158] R. Dong, X. Feng "Making large single crystals of 2D MOFs", *Nat. Mater.* **2021**, *20*, 122.

[159] G. Skorupskii, B. A. Trump, T. W. Kasel, C. M. Brown, C. H. Hendon, M. Dincă "Efficient and tunable one-dimensional charge transport in layered lanthanide metal–organic frame-works", *Nat. Chem.* **2020**, *12*, 131.

[160]   L. S. Xie, G. Skorupskii, M. Dincă "Electrically Conductive Metal–Organic Frameworks", *Chem. Rev.* **2020**, *120*, 8536.

[161]   J. J. Liu, D. Yang, Y. Zhou, G. Zhang, G. L. Xing, Y. P. Liu, Y. H. Ma, O. Terasaki, S. B. Yang, L. Chen "Tricycloquinazoline-Based 2D Conductive Metal-Organic Frameworks as Promising Electrocatalysts for CO2 Reduction", *Angew. Chem., Int. Ed.* **2021**, *60*, 14473.

[162]   J. Yan, Y. Cui, M. Xie, G.-Z. Yang, D.-S. Bin, D. Li "Immobilizing Redox-Active Tricycloquinazoline into a 2D Conductive Metal-Organic Framework for Lithium Storage", *Angew. Chem., Int. Ed.* **2021**, *60*, 24467.

[163]   C.-K. Liu, V. Piradi, J. Song, Z. Wang, L.-W. Wong, E.-H.-L. Tan, J. Zhao, X. Zhu, F. Yan "2D Metal-Organic Framework Cu3 (HHTT)2 Films for Broadband Photodetectors from Ultraviolet to Mid-Infrared", *Adv. Mater.* **2022**, *34*, e2204140.

[164]   J. Cao, C.-K. Liu, V. Piradi, H.-L. Loi, T. Wang, H. Cheng, X. Zhu, F. Yan "Ultrathin Self-Assembly Two-Dimensional Metal–Organic Framework Films as Hole Transport Layers in Ideal-Bandgap Perovskite Solar Cells", *ACS Energy Lett.* **2022**, *7*, 3362.

[165]   N. Pasquini, A. Addeo, *Polypropylene handbook*, Hanser Munich **2005**.

[166]   B. Tieke, *Makromolekulare Chemie: Eine Einführung*, Wiley-VCH Verlag GmbH & Co. KGaA, Weinheim **2014**.

[167]   G. Natta, P. Pino, P. Corradini, F. Danusso, E. Mantica, G. Mazzanti, G. Moraglio "CRYSTALLINE HIGH POLYMERS OF α-OLEFINS", *J. Am. Ceram. Soc.* **1955**, *77*, 1708.

[168]   A. D. Jenkins, P. Kratochvíl, R. F. T. Stepto, U. W. Suter "Glossary of basic terms in polymer science (IUPAC Recommendations 1996) **1996**, *68*, 2287.

[169]   B. Lotz, J. C. Wittmann, A. J. Lovinger "Structure and morphology of poly(propylenes): a molecular analysis", *Polymer* **1996**, *37*, 4979.

[170]   P. H. Geil, *Polymer single crystals*, Interscience Publisher **1963**.

[171]   J. W. Mullin, *Crystallization*, Elsevier **2001**.

[172]   Felix A. Wenzel, *Supramolecular and Polymer Systems for Exciton Energy Transport* **2024**.

[173]   Daniel Kremer, *Developing a next generation of trisamide clarifiers for isotactic polypropylene* **2019**.

[174]   E. Piorkowska, G. C. Rutledge, *Handbook of polymer crystallization*, John Wiley & Sons **2013**.

[175]   Florian Richter, *Supramolecular polymer additives to improve the crystallization behavior and optical properties of polybutylene terephthalate and polyamides* **2012**.

[176]   Michaela Mörl, *Steigerung der Zähigkeit von isotaktischem Polypropylen durch Kontrolle der Morphologie mittels 1,3,5-Benzoltrisamiden* **2017**.

[177]   J. Lipp, M. Shuster, A. E. Terry, Y. Cohen "Fibril formation of 1,3:2,4-di(3, 4-dimethylbenzylidene) sorbitol in a polypropylene melt", *Langmuir* **2006**, *22*, 6398.

[178]   T. Wang, Y. Yang, C. Zhang, Z. Tang, H. Na, J. Zhu "Effect of 1,3,5-trialkyl-benzenetricarboxylamide on the crystallization of poly (lactic acid)", *J. Appl. Polym. Sci.* **2013**, *130*, 1328.

Literature

[179] M. Schmidt, J. J. Wittmann, R. Kress, D. Schneider, S. Steuernagel, H.-W. Schmidt, J. Senker "Crystal structure of a highly efficient clarifying agent for isotactic polypropylene", *Cryst. Growth Des.* **2012**, *12*, 2543.

[180] Y. Cheng, N. Ma, C. Witt, S. Rapp, P. S. Wild, M. O. Andreae, U. Pöschl, H. Su "Face masks effectively limit the probability of SARS-CoV-2 transmission", *Science* **2021**, *372*, 1439.

[181] Jeremy Howard, Austin Huang, Zhiyuan Li, Zeynep Tufekci, Vladimir Zdimal, Helene-Mari van der Westhuizen, Arne von Delft, Amy Price, Lex Fridman, Lei-Han Tang, Viola Tang, Gregory L. Watson, Christina E. Bax, Reshama Shaikh, Frederik Questier, Danny Hernandez, Larry F. Chu, Christina M. Ramirez, Anne W. Rimoin "An evidence review of face masks against COVID-19", *Proc. Natl. Acad. Sci. U. S. A.* **2021**, *118*, e2014564118.

[182] J. Schwartz, C. Spix, H. E. Wichmann, E. Malin "Air pollution and acute respiratory illness in five German communities", *Environ. Res.* **1991**, *56*, 1.

[183] J. L. Temte, S. Barlow, E. Temte, M. Goss, A. Bateman, K. Florek, A. Uzicanin "Severe acute respiratory syndrome coronavirus 2 (SARS-CoV-2) codetection with influenza A and other respiratory viruses among school-aged children and their household members—12 March 2020 to 22 February 2022, Dane County, Wisconsin", *Clin. Infect. Dis.* **2022**, *75*, S205-S215.

[184] I. M. Hutten, *Handbook of nonwoven filter media*, Elsevier **2007**.

[185] S. Han, J. Kim, S. H. Ko "Advances in air filtration technologies: structure-based and interaction-based approaches", *Mater. Today Adv.* **2021**, *9*, 100134.

[186] W. C. Hinds, Y. Zhu, *Aerosol technology: properties, behavior, and measurement of airborne particles*, John Wiley & Sons **2022**.

[187] K. W. Lee, B. Y. Liu "Theoretical study of aerosol filtration by fibrous filters", *Aerosol Sci. Technol.* **1982**, *1*, 147.

[188] P. Li, C. Wang, Y. Zhang, F. Wei "Air filtration in the free molecular flow regime: a review of high-efficiency particulate air filters based on carbon nanotubes", *Small* **2014**, *10*, 4543.

[189] C.-S. Wang "Electrostatic forces in fibrous filters—a review", *Powder Technol.* **2001**, *118*, 166.

[190] F. Zabihi, J. Reissner, A. Friese, M. Schulze, C. Nie, P. Nickl, L. Lehmann, P. Siller, C. Melcher, T. Schneiders, T. Gries, U. Rösler, R. Haag "Development of Functional Filter Materials for Virus Protective Face Masks", *Adv. Mater. Technol.* **2023**, *8*, 2300141.

[191] C. Brochot, A. Bahloul, P. Abdolghader, F. Haghighat "Performance of mechanical filters used in general ventilation against nanoparticles", *IOP Conf. Ser.: Mater. Sci. Eng.* **2019**, *609*, 32044.

[192] Holger Misslitz, *Supramolecular Nanofibers - Preparation, Structure-Property Relations, and Applications*, Dissertation, University of Bayreuth **2013**.

[193] H. Darcy "Les Fontaines Publiques de la Ville de Dijon; Paris: Dalmont, 1856 **1856**.

[194] A. Patanaik, V. Jacobs, R. D. Anandjiwala "Performance evaluation of electrospun nanofibrous membrane", *J. Membr. Sci.* **2010**, *352*, 136.

[195]   R. Givehchi, Q. Li, Z. Tan "Quality factors of PVA nanofibrous filters for airborne particles in the size range of 10–125 nm", *Fuel* **2016**, *181*, 1273.

[196]   X.-H. Qin, S.-Y. Wang "Filtration properties of electrospinning nanofibers", *J. Appl. Polym. Sci.* **2006**, *102*, 1285.

[197]   T. Lu, J. Cui, Q. Qu, Y. Wang, J. Zhang, R. Xiong, W. Ma, C. Huang "Multistructured Electrospun Nanofibers for Air Filtration: A Review", *ACS Appl. Mater. Interfaces* **2021**, *13*, 23293.

[198]   J. Li, D. Zhang, T. Yang, S. Yang, X. Yang, H. Zhu "Nanofibrous membrane of graphene oxide-in-polyacrylonitrile composite with low filtration resistance for the effective capture of PM2.5", *J. Membr. Sci.* **2018**, *551*, 85.

[199]   A. J.-P. Bauer, Z. B. Grim, B. Li "Hierarchical Polymer Blend Fibers of High Structural Regularity Prepared by Facile Solvent Vapor Annealing Treatment", *Macromol. Mater. Eng.* **2018**, *303*, 1700489.

[200]   X. Huang, T. Jiao, Q. Liu, L. Zhang, J. Zhou, B. Li, Q. Peng "Hierarchical electrospun nanofibers treated by solvent vapor annealing as air filtration mat for high-efficiency PM2.5 capture", *Sci. China Mater.* **2019**, *62*, 423.

[201]   X. Dai, X. Li, X. Wang "Morphology controlled porous poly(lactic acid)/zeolitic imidazolate framework-8 fibrous membranes with superior PM2.5 capture capacity", *Chem. Eng. J.* **2018**, *338*, 82.

[202]   K. Xu, J. Deng, G. Tian, L. Zhan, J. Ma, L. Wang, Q. Ke, C. Huang "Downy feather-like para-aramid fibers and nonwovens with enhanced absorbency, air filtration and thermal insulation performances", *Nano Res.* **2022**, *15*, 5695.

[203]   K. Xu, J. Deng, R. Lin, H. Zhang, Q. Ke, C. Huang "Surface fibrillation of para-aramid nonwoven as a multi-functional air filter with ultralow pressure drop", *J. Mater. Chem. A* **2020**, *8*, 22269.

[204]   M. Hu, Y. Wang, Z. Yan, G. Zhao, Y. Zhao, L. Xia, B. Cheng, Y. Di, X. Zhuang "Hierarchical dual-nanonet of polymer nanofibers and supramolecular nanofibrils for air filtration with a high filtration efficiency, low air resistance and high moisture permeation", *J. Mater. Chem. A* **2021**, *9*, 14093.

[205]   M. Faraday "The Bakerian Lecture. —Experimental relations of gold (and other metals) to light", *Philos. Trans. R. Soc. London* **1857**, *147*, 145.

[206]   R. A. Zsigmondy, J. Alexander, *Colloids and the ultramicroscope: a manual of colloid chemistry and ultramicroscopy*, J. Wiley & sons **1909**.

[207]   P. Scherrer "Bestimmung der Grosse und inneren Struktur von Kolloidteilchen mittels Rontgenstrahlen", *Nach Ges Wiss Gottingen* **1918**, *2*, 8.

[208]   J. Turkevich, J. Hillier "Electron Microscopy of Colloidal Systems", *Anal. Chem.* **1949**, *21*, 475.

[209]   J. Turkevich, P. C. Stevenson, J. Hillier "A study of the nucleation and growth processes in the synthesis of colloidal gold", *Discuss. Faraday Soc.* **1951**, *11*, 55.

[210]   J. A. Creighton, C. G. Blatchford, M. G. Albrecht "Plasma resonance enhancement of Raman scattering by pyridine adsorbed on silver or gold sol particles of size comparable to the excitation wavelength", *J. Chem. Soc., Faraday Trans. 2* **1979**, *75*, 790.

[211]   J. Turkevich "Colloidal gold. Part I", *Gold Bull.* **1985**, *18*, 86.

[212]   S. Wilhelm, A. J. Tavares, Q. Dai, S. Ohta, J. Audet, H. F. Dvorak, W. C. W. Chan "Analysis of nanoparticle delivery to tumours", *Nat. Rev. Mater.* **2016**, *1*, 16014.

[213]   J. K. Patra, G. Das, L. F. Fraceto, E. V. R. Campos, M. P. Del Rodriguez-Torres, L. S. Acosta-Torres, L. A. Diaz-Torres, R. Grillo, M. K. Swamy, S. Sharma, S. Habtemariam, H.-S. Shin "Nano based drug delivery systems: recent developments and future prospects", *J. Nanobiotechnol.* **2018**, *16*, 71.

[214]   Y. Liu, P. Bhattarai, Z. Dai, X. Chen "Photothermal therapy and photoacoustic imaging via nanotheranostics in fighting cancer", *Chem. Soc. Rev.* **2019**, *48*, 2053.

[215]   X. Lang, X. Chen, J. Zhao "Heterogeneous visible light photocatalysis for selective organic transformations", *Chem. Soc. Rev.* **2014**, *43*, 473.

[216]   L. Liu, A. Corma "Metal Catalysts for Heterogeneous Catalysis: From Single Atoms to Nanoclusters and Nanoparticles", *Chem. Rev.* **2018**, *118*, 4981.

[217]   T. W. van Deelen, C. Hernández Mejía, K. P. de Jong "Control of metal-support interactions in heterogeneous catalysts to enhance activity and selectivity", *Nat. Catal.* **2019**, *2*, 955.

[218]   Neus G. Bastus, Eudald Casals, Isaac Ojea, Miriam Varon, Victor Puntes, in *Abbass A. Hashim – The Delivery of Nanoparticles*, Vol. 2012, 377-400.

[219]   X. Li, L. Jiang, Q. Zhan, J. Qian, S. He "Localized surface plasmon resonance (LSPR) of polyelectrolyte-functionalized gold-nanoparticles for bio-sensing", *Colloids Surf., A* **2009**, *332*, 172.

[220]   R. Jin, C. Zeng, M. Zhou, Y. Chen "Atomically Precise Colloidal Metal Nanoclusters and Nanoparticles: Fundamentals and Opportunities", *Chem. Rev.* **2016**, *116*, 10346.

[221]   P. Zhao, N. Li, D. Astruc "State of the art in gold nanoparticle synthesis", *Coord. Chem. Rev.* **2013**, *257*, 638.

[222]   S. Kumar, K. S. Gandhi, R. Kumar "Modeling of Formation of Gold Nanoparticles by Citrate Method", *Ind. Eng. Chem. Res.* **2007**, *46*, 3128.

[223]   G. FRENS "Controlled Nucleation for the Regulation of the Particle Size in Monodisperse Gold Suspensions", *Nature, Phys. Sci.* **1973**, *241*, 20.

[224]   X. Ji, X. Song, J. Li, Y. Bai, W. Yang, X. Peng "Size Control of Gold Nanocrystals in Citrate Reduction: The Third Role of Citrate", *J. Am. Ceram. Soc.* **2007**, *129*, 13939.

[225]   K. R. Brown, A. P. Fox, M. J. Natan "Morphology-Dependent Electrochemistry of Cytochrome c at Au Colloid-Modified SnO2 Electrodes", *J. Am. Ceram. Soc.* **1996**, *118*, 1154.

[226]   M. Giersig, P. Mulvaney "Preparation of ordered colloid monolayers by electrophoretic deposition", *Langmuir* **1993**, *9*, 3408.

[227]   M. Brust, M. Walker, D. Bethell, D. J. Schiffrin, R. Whyman "Synthesis of thiol-derivatised gold nanoparticles in a two-phase Liquid–Liquid system", *J. Chem. Soc., Chem. Commun.* **1994**, 801.

[228]   D. Zhang, O. Neumann, H. Wang, V. M. Yuwono, A. Barhoumi, M. Perham, J. D. Hartgerink, P. Wittung-Stafshede, N. J. Halas "Gold Nanoparticles Can Induce the Formation of Protein-based Aggregates at Physiological pH", *Nano Lett.* **2009**, *9*, 666.

[229]   S. Sistach, M. Beija, V. Rahal, A. Brûlet, J.-D. Marty, M. Destarac, C. Mingotaud "Thermoresponsive Amphiphilic Diblock Copolymers Synthesized by MADIX/RAFT: Properties in Aqueous Solutions and Use for the Preparation and Stabilization of Gold Nanoparticles", *Chem. Mater.* **2010**, *22*, 3712.

[230]   S. Zhang, G. Leem, T. R. Lee "Monolayer-Protected Gold Nanoparticles Prepared Using Long-Chain Alkanethioacetates", *Langmuir* **2009**, *25*, 13855.

[231]   B. K. Jena, C. R. Raj "Synthesis of Flower-like Gold Nanoparticles and Their Electrocatalytic Activity Towards the Oxidation of Methanol and the Reduction of Oxygen", *Langmuir* **2007**, *23*, 4064.

[232]   G. Li, D. Li, L. Zhang, J. Zhai, E. Wang "One-Step Synthesis of Folic Acid Protected Gold Nanoparticles and Their Receptor-Mediated Intracellular Uptake", *Chem. - Eur. J.* **2009**, *15*, 9868.

[233]   M. S. Yavuz, W. Li, Y. Xia "Facile Synthesis of Gold Icosahedra in an Aqueous Solution by Reacting HAuCl4 with N-Vinyl Pyrrolidone", *Chem. - Eur. J.* **2009**, *15*, 13181.

[234]   M. A. Raj, S. B. Revin, S. A. John "Selective determination of 3,4-dihydroxyphenylacetic acid in the presence of ascorbic acid using 4-(dimethylamino)pyridine capped gold nanoparticles immobilized on gold electrode", *Colloids Surf., B* **2011**, *87*, 353.

[235]   A. Yu, Z. Liang, J. Cho, F. Caruso "Nanostructured Electrochemical Sensor Based on Dense Gold Nanoparticle Films", *Nano Lett.* **2003**, *3*, 1203.

[236]   D. I. Gittins, F. Caruso "Spontaneous Phase Transfer of Nanoparticulate Metals from Organic to Aqueous Media", *Angew. Chem., Int. Ed.* **2001**, *40*, 3001.

[237]   P. M. Shem, R. Sardar, J. S. Shumaker-Parry "One-Step Synthesis of Phosphine-Stabilized Gold Nanoparticles Using the Mild Reducing Agent 9-BBN", *Langmuir* **2009**, *25*, 13279.

[238]   J. Ramírez, M. Sanaú, E. Fernández "Gold(0) Nanoparticles for Selective Catalytic Diboration", *Angew. Chem., Int. Ed.* **2008**, *47*, 5194.

[239]   J. Shan, H. Tenhu "Recent advances in polymer protected gold nanoparticles: synthesis, properties and applications", *Chem. Commun.* **2007**, 4580.

[240]   J. Shan, M. Nuopponen, H. Jiang, T. Viitala, E. Kauppinen, K. Kontturi, H. Tenhu "Amphiphilic Gold Nanoparticles Grafted with Poly(N-isopropylacrylamide) and Polystyrene", *Macromolecules* **2005**, *38*, 2918.

[241]   K. Gries, M. El Helou, G. Witte, S. Agarwal, A. Greiner "Vinyl-functionalized gold nanoparticles as artificial monomers for the free radical copolymerization with methyl methacrylate", *Polymer* **2012**, *53*, 1632.

[242] C. Krüger, S. Agarwal, A. Greiner "Stoichiometric Functionalization of Gold Nanoparticles in Solution through a Free Radical Polymerization Approach", *J. Am. Ceram. Soc.* **2008**, *130*, 2710.

[243] J. Kronawitt, Z. Fan, M. Schöttle, S. Agarwal, A. Greiner "Redispersible Gold Nanoparticle/Polymer Composite Powders Ready for Ligand Exchange Reactions", *ChemNanoMat* **2019**, *5*, 181.

[244] C. Liang, J. Y. Cheong, G. Sitaru, S. Rosenfeldt, A. S. Schenk, S. Gekle, I.-D. Kim, A. Greiner "Size-Dependent Catalytic Behavior of Gold Nanoparticles", *Adv. Mater. Interfaces* **2022**, *9*, 2100867.

[245] M. K. Corbierre, N. S. Cameron, R. B. Lennox "Polymer-Stabilized Gold Nanoparticles with High Grafting Densities", *Langmuir* **2004**, *20*, 2867.

[246] C. Gentilini, F. Evangelista, P. Rudolf, P. Franchi, M. Lucarini, L. Pasquato "Water-Soluble Gold Nanoparticles Protected by Fluorinated Amphiphilic Thiolates", *J. Am. Ceram. Soc.* **2008**, *130*, 15678.

[247] M. A. Gordillo, P. A. Benavides, K. Ma, S. Saha "Transforming an Insulating Metal–Organic Framework (MOF) into Semiconducting MOF/Gold Nanoparticle (AuNP) and MOF/Polymer/AuNP Composites to Gain Electrical Conductivity", *ACS Appl. Nano Mater.* **2022**, *5*, 13912.

[248] W. Shi, W. Lu, L. Jiang "The fabrication of photosensitive self-assembly Au nanoparticles embedded in silica nanofibers by electrospinning", *J. Colloid Interface Sci.* **2009**, *340*, 291.

[249] H.-L. Wang, F.-C. Lee, T.-Y. Tang, C. Zhou, D.-H. Tsai "Assembly of functional gold nanoparticle on silica microsphere", *J. Colloid Interface Sci.* **2016**, *469*, 99.

[250] J. Wang, A.-H. Lu, M. Li, W. Zhang, Y.-S. Chen, D.-X. Tian, W.-C. Li "Thin porous alumina sheets as supports for stabilizing gold nanoparticles", *ACS Nano* **2013**, *7*, 4902.

[251] J. Yuan, X. Chen, H. Duan, X. Cai, Y. Li, L. Guo, X. Huang, Y. Xiong "Gold nanoparticle–decorated metal organic frameworks on immunochromatographic assay for human chorionic gonadotropin detection", *Microchim. Acta* **2020**, *187*, 640.

[252] F. Schüth "Colloidal deposition as method to study the influence of the support on the activity of gold catalysts in CO-oxidation", *Phys. Status Solidi B* **2013**, *250*, 1142.

[253] A. Dodero, M. Castellano, P. Lova, M. Ottonelli, E. Brunengo, S. Vicini, M. Alloisio "Composite Poly(vinyl alcohol)-Based Nanofibers Embedding Differently-Shaped Gold Nanoparticles: Preparation and Characterization", *Polymers* **2021**, *13*.

[254] A. Kurniawan, M.-J. Wang "Gold nanoparticles-decorated electrospun poly(N-vinyl-2-pyrrolidone) nanofibers with tunable size and coverage density for nanomolar detection of single and binary component dyes by surface-enhanced raman spectroscopy", *Nanotechnology* **2017**, *28*, 355703.

[255] S. Montolio, G. Abarca, R. Porcar, J. Dupont, M. I. Burguete, E. García-Verdugo, S. V. Luis "Hierarchically structured polymeric ionic liquids and polyvinylpyrrolidone mat-fibers fabricated by electrospinning", *J. Mater. Chem. A* **2017**, *5*, 9733.

[256] Y. Liu, G. Jiang, L. Li, H. Chen, Q. Huang, T. Jiang, X. Du "Silver nanoparticles supported on electrospun polyacrylonitrile nanofibrous mats for catalytic applications", *MRS Commun.* **2016**, *6*, 31.

[257] Q.-L. Zhu, Q. Xu "Immobilization of Ultrafine Metal Nanoparticles to High-Surface-Area Materials and Their Catalytic Applications", *Chem* **2016**, *1*, 220.

[258] C.-L. Zhang, S.-H. Yu "Nanoparticles meet electrospinning: recent advances and future prospects", *Chem. Soc. Rev.* **2014**, *43*, 4423.

[259] C. Hils, M. Dulle, G. Sitaru, S. Gekle, J. Schöbel, A. Frank, M. Drechsler, A. Greiner, H. Schmalz "Influence of patch size and chemistry on the catalytic activity of patchy hybrid nonwovens", *Nanoscale Adv.* **2020**, *2*, 438.

[260] J. Schöbel, M. Burgard, C. Hils, R. Dersch, M. Dulle, K. Volk, M. Karg, A. Greiner, H. Schmalz "Bottom-Up Meets Top-Down: Patchy Hybrid Nonwovens as an Efficient Catalysis Platform", *Angew. Chem., Int. Ed.* **2017**, *56*, 405.

[261] M. Drummer, *Functional supramolecular nanofibers and their applications in nanoparticle immobilization and catalysis* **2023**.

[262] D. Nardini, *Sulfur-Containing Functional Supramolecular Fibers for Filtration Applications* **2022**.

[263] H. Thomas, X. Zhu, M. Möller, K. Kreger, D. Nardini, H.-W. Schmidt "Supramolecular nanofiber composites for highly efficient and selective removal of gold(III) from aqueous media", *Technische Textilien* **2019**, 80.

[264] T. Mitsudome, K. Kaneda "Gold nanoparticle catalysts for selective hydrogenations", *Green Chem.* **2013**, *15*, 2636.

[265] P. Hervés, M. Pérez-Lorenzo, L. M. Liz-Marzán, J. Dzubiella, Y. Lu, M. Ballauff "Catalysis by metallic nanoparticles in aqueous solution: model reactions", *Chem. Soc. Rev.* **2012**, *41*, 5577.

[266] A. Corma, H. Garcia "Supported gold nanoparticles as catalysts for organic reactions", *Chem. Soc. Rev.* **2008**, *37*, 2096.

[267] P. Zhao, X. Feng, D. Huang, G. Yang, D. Astruc "Basic concepts and recent advances in nitrophenol reduction by gold- and other transition metal nanoparticles", *Coord. Chem. Rev.* **2015**, *287*, 114.

[268] W. H. Glaze, J.-W. Kang, D. H. Chapin "The Chemistry of Water Treatment Processes Involving Ozone, Hydrogen Peroxide and Ultraviolet Radiation", *Ozone: Sci. Eng.* **1987**, *9*, 335.

[269] M. A. Oturan, J.-J. Aaron "Advanced Oxidation Processes in Water/Wastewater Treatment: Principles and Applications. A Review", *Crit. Rev. Environ. Sci. Technol.* **2014**, *44*, 2577.

[270] P. Kumari, A. Kumar "ADVANCED OXIDATION PROCESS: A remediation technique for organic and non-biodegradable pollutant", *Results in Surfaces and Interfaces* **2023**, *11*, 100122.

[271]   A. Kujawska, U. Kiełkowska, A. Atisha, E. Yanful, W. Kujawski "Comparative analysis of separation methods used for the elimination of pharmaceuticals and personal care products (PPCPs) from water – A critical review", *Sep. Purif. Technol.* **2022**, *290*, 120797.

[272]   H. J. H. Fenton "Oxidation of tartaric acid in presence of iron", *J. Chem. Soc., Trans.* **1894**, *65*, 899.

[273]   F. Haber, J. Weiss "The catalytic decomposition of hydrogen peroxide by iron salts", *Proc. R. Soc. London, Ser. A* **1934**, *147*, 332.

[274]   F. Haber, J. Weiss "On the catalysis of hydroperoxide", *Naturwissenschaften (1913-2014)* **1932**, *20*, 948.

[275]   Evonik Industries AG, *Anspruchsvolles Industrieabwasser nachhaltig klären* **2022**.

[276]   F. Zaviska, P. Drogui, G. Mercier, J.-F. Blais "Procédés d'oxydation avancée dans le traitement des eaux et des effluents industriels: Application à la dégradation des polluants réfractaires", *Rev. Sci. Eau* **2009**, *22*, 535.

[277]   H. Paillard, R. Brunet, M. Dore "Optimal conditions for applying an ozone-hydrogen peroxide oxidizing system", *Water Res.* **1988**, *22*, 91.

[278]   R. Hernandez, M. Zappi, J. Colucci, R. Jones "Comparing the performance of various advanced oxidation processes for treatment of acetone contaminated water", *J. Hazard. Mater.* **2002**, *92*, 33.

[279]   K. van Craeynest, H. van Langenhove, R. Stuetz, in *Advanced Oxidation Processes*, IWA Publishing **2004**, p. 275.

[280]   R. G. Zepp, B. C. Faust, J. Hoigne "Hydroxyl radical formation in aqueous reactions (pH 3-8) of iron (II) with hydrogen peroxide: the photo-Fenton reaction", *Environ. Sci. Technol.* **1992**, *26*, 313.

[281]   B. C. Faust, J. Hoigné "Photolysis of Fe (III)-hydroxy complexes as sources of OH radicals in clouds, fog and rain", *Atmos. Environ., Part A* **1990**, *24*, 79.

[282]   J. J. Pignatello "Dark and photoassisted iron (3+)-catalyzed degradation of chlorophenoxy herbicides by hydrogen peroxide", *Environ. Sci. Technol.* **1992**, *26*, 944.

[283]   S. E. Braslavsky, K. N. Houk, J. W. Verhoeven "Glossary of terms used in photochemistry", *Pure Appl. Chem.* **1988**, *60*, 1055.

[284]   E. H. Khader, S. A. Muslim, N. M. C. Saady, N. S. Ali, I. K. Salih, T. J. Mohammed, T. M. Albayati, S. Zendehboudi "Recent advances in photocatalytic advanced oxidation processes for organic compound degradation: A review", *Desalin. Water Treat.* **2024**, *318*, 100384.

[285]   J. Li, M. Jiang, H. Zhou, P. Jin, K. M. C. Cheung, P. K. Chu, K. W. K. Yeung "Vanadium Dioxide Nanocoating Induces Tumor Cell Death through Mitochondrial Electron Transport Chain Interruption", *Glob Chall* **2019**, *3*, 1800058.

[286]   W. He, H.-K. Kim, W. G. Wamer, D. Melka, J. H. Callahan, J.-J. Yin "Photogenerated Charge Carriers and Reactive Oxygen Species in ZnO/Au Hybrid Nanostructures with Enhanced Photocatalytic and Antibacterial Activity", *J. Am. Ceram. Soc.* **2014**, *136*, 750.

[287]   M. M. Khan, S. F. Adil, A. Al-Mayouf "Metal oxides as photocatalysts", *J. Saudi Chem. Soc.* **2015**, *19*, 462.

[288]   Q. Zhu, Q. Xu, M. Du, X. Zeng, G. Zhong, B. Qiu, J. Zhang "Recent Progress of Metal Sulfide Photocatalysts for Solar Energy Conversion", *Adv. Mater.* **2022**, *34*, 2202929.

[289]   Q. Wang, H. Zhou, X. Liu, T. Li, C. Jiang, W. Song, W. Chen "Facet-dependent generation of superoxide radical anions by ZnO nanomaterials under simulated solar light", *Environ. Sci.: Nano* **2018**, *5*, 2864.

[290]   F. Parrino, S. Livraghi, E. Giamello, R. Ceccato, L. Palmisano "Role of Hydroxyl, Superoxide, and Nitrate Radicals on the Fate of Bromide Ions in Photocatalytic TiO2 Suspensions", *ACS Catal.* **2020**, *10*, 7922.

[291]   C. A. Gueymard "The sun's total and spectral irradiance for solar energy applications and solar radiation models", *Sol. Energy* **2004**, *76*, 423.

[292]   H. G. Brittain, G. Barbera, J. DeVincentis, A. W. Newman, in *Analytical Profiles of Drug Substances and Excipients*, Vol. 21 (Ed.: H. G. Brittain), Academic Press **1992**, p. 659.

[293]   S. Heinonen, J.-P. Nikkanen, E. Huttunen-Saarivirta, E. Levänen "Investigation of long-term chemical stability of structured ZnO films in aqueous solutions of varying conditions", *Thin Solid Films* **2017**, *638*, 410.

[294]   K. Kočí, L. Obalová, L. Matějová, D. Plachá, Z. Lacný, J. Jirkovský, O. Šolcová "Effect of TiO2 particle size on the photocatalytic reduction of CO2", *Appl. Catal., B* **2009**, *89*, 494.

[295]   C. Karunakaran, V. Rajeswari, P. Gomathisankar "Enhanced photocatalytic and antibacterial activities of sol–gel synthesized ZnO and Ag-ZnO", *Mater. Sci. Semicond. Process.* **2011**, *14*, 133.

[296]   S. Heinonen, J.-P. Nikkanen, H. Hakola, E. Huttunen-Saarivirta, M. Kannisto, L. Hyvärinen, M. Järveläinen, E. Levänen "Effect of temperature and concentration of precursors on morphology and photocatalytic activity of zinc oxide thin films prepared by hydrothermal route", *IOP Conf. Ser.: Mater. Sci. Eng.* **2016**, *123*, 12030.

[297]   A. I. Kontos, Im Arabatzis, D. S. Tsoukleris, Kontos, AG, M. C. Bernard, de Petrakis, P. Falaras "Efficient photocatalysts by hydrothermal treatment of TiO2", *Catal. Today* **2005**, *101*, 275.

[298]   M. Bizarro "High photocatalytic activity of ZnO and ZnO: Al nanostructured films deposited by spray pyrolysis", *Appl. Catal., B* **2010**, *97*, 198.

[299]   L. Liu, C. Zhao, D. Pitts, H. Zhao, Y. Li "CO 2 photoreduction with H 2 O vapor by porous MgO–TiO 2 microspheres: effects of surface MgO dispersion and CO 2 adsorption–desorption dynamics", *Catal. Sci. Technol.* **2014**, *4*, 1539.

[300]   T. Li, B.-T. Liu, Z.-B. Fang, Q. Yin, R. Wang, T.-F. Liu "Integrating active C 3 N 4 moieties in hydrogen-bonded organic frameworks for efficient photocatalysis", *J. Mater. Chem. A* **2021**, *9*, 4687.

[301]   D. Cecconet, M. Sturini, L. Malavasi, A. G. Capodaglio "Graphitic Carbon Nitride as a Sustainable Photocatalyst Material for Pollutants Removal. State-of-the Art, Preliminary Tests and Application Perspectives", *Materials* **2021**, *14*.

[302]   Y. Cui, Z. Ding, P. Liu, M. Antonietti, X. Fu, X. Wang "Metal-free activation of H2O2 by g-C3N4 under visible light irradiation for the degradation of organic pollutants", *Phys. Chem. Chem. Phys.* **2012**, *14*, 1455.

[303]   X. Wang, K. Maeda, A. Thomas, K. Takanabe, G. Xin, J. M. Carlsson, K. Domen, M. Antonietti "A metal-free polymeric photocatalyst for hydrogen production from water under visible light", *Nat. Mater.* **2009**, *8*, 76.

[304]   Y. Wang, X. Wang, M. Antonietti "Polymeric Graphitic Carbon Nitride as a Heterogeneous Organocatalyst: From Photochemistry to Multipurpose Catalysis to Sustainable Chemistry", *Angew. Chem., Int. Ed.* **2012**, *51*, 68.

[305]   L. Liu, X. Chen, Y. Chai, W. Zhang, X. Liu, F. Zhao, Z. Wang, Y. Weng, B. Wu, H. Geng, Y. Zhu, C. Wang "Highly efficient photocatalytic hydrogen production via porphyrin-fullerene supramolecular photocatalyst with donor-acceptor structure", *Chem. Eng. J.* **2022**, *444*, 136621.

[306]   J. Yang, J. Jing, Y. Zhu "A Full-Spectrum Porphyrin-Fullerene D-A Supramolecular Photocatalyst with Giant Built-In Electric Field for Efficient Hydrogen Production", *Adv. Mater.* **2021**, *33*, e2101026.

[307]   Z. Zhang, Y. Zhu, X. Chen, H. Zhang, J. Wang "A Full-Spectrum Metal-Free Porphyrin Supramolecular Photocatalyst for Dual Functions of Highly Efficient Hydrogen and Oxygen Evolution", *Adv. Mater.* **2019**, *31*, e1806626.

[308]   P. Chen, L. Blaney, G. Cagnetta, J. Huang, B. Wang, Y. Wang, S. Deng, G. Yu "Degradation of Ofloxacin by Perylene Diimide Supramolecular Nanofiber Sunlight-Driven Photocatalysis", *Environ. Sci. Technol.* **2019**, *53*, 1564.

[309]   Di Liu, J. Wang, X. Bai, R. Zong, Y. Zhu "Self-Assembled PDINH Supramolecular System for Photocatalysis under Visible Light", *Adv. Mater.* **2016**, *28*, 7284.

[310]   Y. Sheng, W. Li, L. Xu, Y. Zhu "High Photocatalytic Oxygen Evolution via Strong Built-In Electric Field Induced by High Crystallinity of Perylene Imide Supramolecule", *Adv. Mater.* **2022**, *34*, e2102354.

[311]   Y. Sun, D. Wang, Y. Zhu "Deep degradation of pollutants by perylene diimide supramolecular photocatalyst with unique Bi-planar π-π conjugation", *Chem. Eng. J.* **2022**, *438*, 135667.

[312]   A. S. Weingarten, R. V. Kazantsev, L. C. Palmer, M. McClendon, A. R. Koltonow, A. P. S. Samuel, D. J. Kiebala, M. R. Wasielewski, S. I. Stupp "Self-assembling hydrogel scaffolds for photocatalytic hydrogen production", *Nat. Chem.* **2014**, *6*, 964.

[313]   S. R. D. Gamelas, J. P. C. Tomé, A. C. Tomé, L. M. O. Lourenço "Advances in photocatalytic degradation of organic pollutants in wastewaters: harnessing the power of phthalocyanines and phthalocyanine-containing materials", *RSC Adv.* **2023**, *13*, 33957.

[314] V. Iliev, A. Mihaylova, L. Bilyarska "Photooxidation of phenols in aqueous solution, catalyzed by mononuclear and polynuclear metal phthalocyanine complexes", *J. Mol. Catal. A: Chem.* **2002**, *184*, 121.

[315] Z. Xiong, Y. Xu, L. Zhu, J. Zhao "Photosensitized Oxidation of Substituted Phenols on Aluminum Phthalocyanine-Intercalated Organoclay", *Environ. Sci. Technol.* **2005**, *39*, 651.

[316] O. Dumele, L. Đorđević, H. Sai, T. J. Cotey, M. H. Sangji, K. Sato, A. J. Dannenhoffer, S. I. Stupp "Photocatalytic Aqueous CO2 Reduction to CO and CH4 Sensitized by Ullazine Supramolecular Polymers", *J. Am. Ceram. Soc.* **2022**, *144*, 3127.

[317] M. Xu, K. Kong, H. Ding, Y. Chu, S. Zhang, F. Yu, H. Ye, Y. Hu, J. Hua "Quinacridone-pyridine dicarboxylic acid based donor–acceptor supramolecular nanobelts for significantly enhanced photocatalytic hydrogen production", *J. Mater. Chem. C* **2020**, *8*, 930.

[318] B. Srikanth, R. Goutham, R. B. Narayan, A. Ramprasath, K. P. Gopinath, A. R. Sankaranarayanan "Recent advancements in supporting materials for immobilised photocatalytic applications in waste water treatment", *J. Environ. Manage.* **2017**, *200*, 60.

[319] S. Sun, M. Li, Y. Xue, H. Yang "Immobilized photocatalysts with varied macroscopical supports of different morphologies: A review", *J. Environ. Chem. Eng.* **2024**, *12*, 113636.

[320] A. Yousef, N. am Barakat, S. S. Al-Deyab, R. Nirmala, B. Pant, H. Y. Kim "Encapsulation of CdO/ZnO NPs in PU electrospun nanofibers as novel strategy for effective immobilization of the photocatalysts", *Colloids Surf., A* **2012**, *401*, 8.

[321] Y. Fan, W. Ma, D. Han, S. Gan, X. Dong, L. Niu "Convenient recycling of 3D AgX/graphene aerogels (X= Br, Cl) for efficient photocatalytic degradation of water pollutants", *Adv. Mater.* **2015**, *27*, 3767.

[322] N. E. Salim, J. Jaafar, af Ismail, M. H. Othman, M. A. Rahman, N. Yusof, M. Qtaishat, T. Matsuura, F. Aziz, W. N. Salleh "Preparation and characterization of hydrophilic surface modifier macromolecule modified poly (ether sulfone) photocatalytic membrane for phenol removal", *Chem. Eng. J.* **2018**, *335*, 236.

[323] X. Xin, S.-H. Li, N. Zhang, Z.-R. Tang, Y.-J. Xu "3D graphene/AgBr/Ag cascade aerogel for efficient photocatalytic disinfection", *Appl. Catal., B* **2019**, *245*, 343.

[324] Yuxiang Xue, Na Li, Boqiang Gao, Hu Yang "Selective photocatalysis degradation of dyes using CdS composited with a cationic starch film", *Sci. Sin.: Chim.* **2020**, *50*, 707.

[325] M. M. Rahman, D. Huang, C. M. Ewulonu, C. Wang, S. Kuga, M. Wu, Y. Huang "Preparation of multifunctional cellulosic fabric based on graphene/TiO 2 nanocoating", *Cellulose* **2021**, *28*, 1153.

[326] J. C. Lopes, M. J. Sampaio, J. L. Faria, C. G. Silva "Synthesis and performance of a composite photocatalyst based on polyester-supported carbon nitride nanosheets for selective oxidation of anisyl alcohol", *Surf. Interfaces* **2022**, *30*, 101938.

[327] A. P. Shah, S. Jain, V. J. Mokale, N. G. Shimpi "High performance visible light photocatalysis of electrospun PAN/ZnO hybrid nanofibers", *J. Ind. Eng. Chem. (Amsterdam, Neth.)* **2019**, *77*, 154.

[328]   W. Wang, T. An, G. Li, Y. Li, C. Y. Jimmy, P. K. Wong "Free-standing red phosphorous/silver sponge monolith as an efficient and easily recyclable macroscale photocatalyst for organic pollutant degradation under visible light irradiation", *J. Colloid Interface Sci.* **2018**, *518*, 130.

[329]   C.-J. Chang, P.-Y. Chao, K.-S. Lin "Flower-like BiOBr decorated stainless steel wire-mesh as immobilized photocatalysts for photocatalytic degradation applications", *Appl. Surf. Sci.* **2019**, *494*, 492.

[330]   A. Uheida, H. G. Mejía, M. Abdel-Rehim, W. Hamd, J. Dutta "Visible light photocatalytic degradation of polypropylene microplastics in a continuous water flow system", *J. Hazard. Mater.* **2021**, *406*, 124299.

[331]   C. Sarantopoulos, E. Puzenat, C. Guillard, J.-M. Herrmann, A. N. Gleizes, F. Maury "Microfibrous TiO2 supported photocatalysts prepared by metal-organic chemical vapor infiltration for indoor air and waste water purification", *Appl. Catal., B* **2009**, *91*, 225.

[332]   J. H. Kim, M. K. Joshi, J. Lee, C. H. Park, C. S. Kim "Polydopamine-assisted immobilization of hierarchical zinc oxide nanostructures on electrospun nanofibrous membrane for photocatalysis and antimicrobial activity", *J. Colloid Interface Sci.* **2018**, *513*, 566.

[333]   D. M. Lee, H. J. Yun, S. Yu, S. J. Yun, S. Y. Lee, S. H. Kang, J. Yi "Design of an efficient photocatalytic reactor for the decomposition of gaseous organic contaminants in air", *Chem. Eng. J.* **2012**, *187*, 203.

[334]   W. Chairungsri, A. Subkomkaew, P. Kijjanapanich, Y. Chimupala "Direct dye wastewater photocatalysis using immobilized titanium dioxide on fixed substrate", *Chemosphere* **2022**, *286*, 131762.

[335]   P. Chen, L. Zhang, Q. Wu, W. Yao "Novel synthesis of Ag3PO4/CNFs/silica-fiber hybrid composite as an efficient photocatalyst", *J. Taiwan Inst. Chem. Eng.* **2016**, *63*, 506.

[336]   X. Lv, M. Cao, W. Shi, M. Wang, Y. Shen "A new strategy of preparing uniform graphitic carbon nitride films for photoelectrochemical application", *Carbon* **2017**, *117*, 343.

[337]   A. Sugunan, V. K. Guduru, A. Uheida, M. S. Toprak, M. Muhammed "Radially Oriented ZnO Nanowires on Flexible Poly-l-Lactide Nanofibers for Continuous-Flow Photocatalytic Water Purification", *J. Am. Ceram. Soc.* **2010**, *93*, 3740.

[338]   F. Kayaci, S. Vempati, C. Ozgit-Akgun, N. Biyikli, T. Uyar "Enhanced photocatalytic activity of homoassembled ZnO nanostructures on electrospun polymeric nanofibers: A combination of atomic layer deposition and hydrothermal growth", *Appl. Catal., B* **2014**, *156-157*, 173.

6 Danksagung

Als Erstes möchte ich meinem Doktorvater, Herrn Prof. Dr. Hans-Werner Schmidt, dafür danken, dass ich meine Forschung und die daraus resultierende Doktorarbeit bei ihm am Lehrstuhl für Makromolekulare Chemie I der Universität Bayreuth durchführen konnte. Besonders habe ich die Freiheit, die er mir in meiner Forschung gewährt hat und die Unterstützung beim Verfolgen von neuen Projekten, wertgeschätzt. Deine Ideen, konstruktiven Ratschläge und dein wissenschaftliches Engagement haben maßgeblich zum Gelingen dieser Arbeit beigetragen.

Für die finanzielle Unterstützung bedanke ich mich beim Bayerischen Staatsministerium für Wissenschaft und Kunst im Rahmen des Verbundprojektes „*Solar Technology go Hybrid*" und für die Förderung durch den Elitestudiengang „*Macromolecular Science*" im Rahmen des Elitenetzwerks Bayern, sowie der Graduate School der Universität Bayreuth für partielle Unterstützung während meines Auslandsaufenthaltes.

Ein ganz besonderer Dank gilt Dr. Klaus Kreger, mit dem ich kilometerweit, zahllose „Besprechungs-Spaziergänge" zu meiner Forschung und angrenzenden Themen hatte. Deine Ratschläge, Hilfestellungen und fachliche Expertise haben diese Arbeit und meinen Werdegang maßgeblich geprägt.

Bedanken möchte ich mich außerdem bei Dr. Christian Neuber für die Einweisung in die Aufdampfanlage und stehts mit Rat und Tat zur Seite stand, wenn es um das Thema PVD ging. Bei Dr. Rainer Giesa möchte ich mich für die Unterweisung und Hilfestellung im Bereich der Polmerverarbeitung und Characterisierung bedanken.

Ein ganz besonderer Dank gilt Petra Weiss und Christina „Wundi" Frank die immer wundervolle Mutmacher waren, unterstützt haben bei allem was organisatorisch angefallen ist und immer gute Laune versprüht haben. Weiter Dank gilt dem Dreamteam aus Labor 569, Jutta Failner und Sandra Opel. Ihr beide habt maßgeblich zum Erfolg meiner Arbeit beigetragen und für Eure Hilfe beim Synthetisieren und Charakterisieren aber auch für ein Offenes Ohr und das versprühen von guter Laune möchte ich euch Danken.

Bedanken möchte ich mich auch bei Felix Bretschneider, Maximilian Rist, Jutta Eckert und Jannik Thanner für deren Messungen und Hilfestellung. Bei Dr. Ulrich Mansfeld und Martina Heider möchte ich mich für die Hilfestellungen bei der Raster Elektronen Mikroskopie, bedanken. Bei

7 (Eidesstattliche) Versicherungen und Erklärungen

(§ 9 Satz 2 Nr. 3 PromO BayNAT)

Hiermit versichere ich eidesstattlich, dass ich die Arbeit selbstständig verfasst und keine anderen als die von mir angegebenen Quellen und Hilfsmittel benutzt habe (vgl. Art. 97 Abs. 1 Satz 8 BayHIG).

(§ 9 Satz 2 Nr. 3 PromO BayNAT)

Hiermit erkläre ich, dass ich die Dissertation nicht bereits zur Erlangung eines akademischen Grades eingereicht habe und dass ich nicht bereits diese oder eine gleichartige Doktorprüfung endgültig nicht bestanden habe.

(§ 9 Satz 2 Nr. 4 PromO BayNAT)

Hiermit erkläre ich, dass ich Hilfe von gewerblichen Promotionsberatern bzw. -vermittlern oder ähnlichen Dienstleistern weder bisher in Anspruch genommen habe noch künftig in Anspruch nehmen werde.

(§ 9 Satz 2 Nr. 7 PromO BayNAT)

Hiermit erkläre ich mein Einverständnis, dass die elektronische Fassung meiner Dissertation unter Wahrung meiner Urheberrechte und des Datenschutzes einer gesonderten Überprüfung unterzogen werden kann.

(§ 9 Satz 2 Nr. 8 PromO BayNAT)

Hiermit erkläre ich mein Einverständnis, dass bei Verdacht wissenschaftlichen Fehlverhaltens Ermittlungen durch universitätsinterne Organe der wissenschaftlichen Selbstkontrolle stattfinden können.

………………………………………………………………………………….
Ort, Datum, Unterschrift